MECHANICALLY INTELLIGENT ELONGATE LIMBLESS ROBOTS FOR LOCOMOTION IN COMPLEX LAND AND WATER ENVIRONMENTS

A Dissertation
Presented to
The Academic Faculty

By

Tianyu Wang

In Partial Fulfillment
of the Requirements for the Degree
Doctor of Philosophy in the
Institute for Robotics and Intelligent Machines
and George W. Woodruff School of Mechanical Engineering

Georgia Institute of Technology

December 2025

© Tianyu Wang 2025

MECHANICALLY INTELLIGENT ELONGATE LIMBLESS ROBOTS FOR LOCOMOTION IN COMPLEX LAND AND WATER ENVIRONMENTS

Thesis committee:

Dr. Daniel I. Goldman
School of Physics
Georgia Institute of Technology

Dr. Hang Lu
School of Chemical and Biomolecular Engineering
Georgia Institute of Technology

Dr. David L. Hu
George W. Woodruff School of Mechanical Engineering
Georgia Institute of Technology

Dr. Howie Choset
School of Computer Science
Carnegie Mellon University

Dr. Tony G. Chen
George W. Woodruff School of Mechanical Engineering
Georgia Institute of Technology

Date approved: December 1, 2025

Mechanics defines motion; curiosity shapes science.

To my beloved family, for their unwavering love and support.

ACKNOWLEDGMENTS

First and foremost, I would like to express my deepest gratitude to my advisor, Dr. Daniel I. Goldman, for his exceptional guidance and support throughout my Ph.D. journey. When I joined the lab during the pandemic, I could hardly imagine that my doctoral years would become such an enjoyable and fulfilling experience. Dan has taught me not only how to think rigorously but also how to think creatively as a scientist. I am deeply grateful for his accessibility, dedication, and genuine care, from which I have learned much about both science and character. His creation of a truly multidisciplinary environment has allowed me to explore research at the intersection of biology, physics, and robotics, an experience that has profoundly shaped my scientific vision. Beyond research, his mentorship and education, both inside and outside the lab, have been invaluable in helping me grow as an independent researcher and as a person.

I would like to thank my committee members for their guidance and support throughout my Ph.D. studies. I am grateful to Dr. Howie Choset for introducing me to the world of biorobotics and for his generous guidance and education over the years, which laid the foundation for much of my Ph.D. work. I am also deeply thankful to Dr. Hang Lu for her collaboration and insightful biological perspective on my work, and for always providing thoughtful and detailed feedback that greatly improved my research. I would like to thank Dr. David Hu for his valuable advice and help over the years, and for the many thoughtful questions that helped sharpen my thinking and deepen my understanding. I am sincerely thankful to Dr. Tony Chen, who has been not only a mentor but also a genuine friend, for his many valuable suggestions on my research and career, and for the opportunities to discuss and co-organize workshops together around our shared interests.

I am also grateful to many professors whose insights and collaborations have greatly enriched my research. I would like to thank Dr. Grigoriy Blekherman, Dr. Zeb Rocklin, Dr. John Dabiri, Dr. Andrew Zangwill, Dr. Simon Sponberg, Dr. Frank L. Hammond

III, Dr. Feifei Qian, Dr. Chen Li, and Dr. Perrin Schiebel for the many discussions, suggestions, and collaborations that have influenced my work over the years and broadened my understanding across disciplines.

Special thanks to my colleagues in the CRAB Lab, which I have been fortunate to call home. I am especially grateful to Dr. Baxi Chong, my long-term collaborator, whose hard work and dedication have continuously inspired me, and whose insight has complemented my work in ways that shaped many of our shared projects. I would also like to thank Dr. Christopher Pierce, Dr. Shengkai Li, Dr. Kelimar Diaz, Dr. Deniz Kerimoglu, Dr. Yasemin Ozkan Aydin, Jianfeng Lin, Zhaochen Xu, Juntao He, Zhexin Shen, Jiyeon Maeng, and Daniel Soto for working closely with me on various projects and papers. Their collaboration, insight, and support have been integral to the progress of my research. I am also thankful to Dr. Laura Treers, Dr. Hosain Bagheri, Enes Aydin, Dr. Akash Vardhan, Madison Hales, Aradhya Rajanala, Steven Tarr, Wesley Dyar, Malaika Taylor, and many others whose friendship and support have made the lab a truly special place. I would also like to thank my mentees, Venny Kojouharov, Matthew Fernandez, Dmitri Kalinin, Galen Tunnicliffe, Donoven Dortilus, Nishanth Mankame, Anushka Bhumkar, Valerie Zborovsky, Pranav Muthukrishnan, Haitong Lian, Niko Cornell, Miles Schuler, Justin Duong, Sean Lublinsky, Darsh Parikh, Salome Jibladze, and many others, whose contributions have been essential to my research. None of the work presented in this thesis would have been possible without their efforts.

I am also grateful to Dr. Xiangyu Chu, Dr. Ryuki Sato, Dr. Elio Challita, Dr. Bo Lin, Dr. Daniel Irvine, Dr. Peter Gunnarson, Dr. Wenzhong Yan, Dr. Qiyuan Fu, Bangyuan Liu, and many others, whose collaboration and friendship have made my academic journey both productive and enjoyable. I have greatly appreciated the opportunities to work together and exchange ideas, which have continually inspired me and broadened my perspective.

I would like to thank my former colleagues from the Biorobotics Lab at Carnegie Mellon University, Dr. Julian Whitman, Dr. Guillaume Sartoretti, Dr. Chaohui Gong, Dr. Matt

Travers, Dr. Shuo Yang, Shuoqi Chen, Ruijie Fu, Lu Li, Yuelin Deng, Zhaoyuan Gu, and many others for their guidance, support, and friendship during my early graduate school years.

I would also like to thank Dr. Guoying Gu, Dr. Lisen Ge, and Dr. Ningbin Zhang from the Soft Robotics and Biodesign Lab at Shanghai Jiao Tong University for guiding my early research during my undergraduate years. I am deeply appreciative of their mentorship, which first sparked my interest in robotics.

I would like to thank my friends for making my Ph.D. years filled with joy and unforgettable memories. Baxi Chong, Xiaoxiao Sun, Ji Yin, Hongzhe Yu, Runze Zhang, Yuntian Xia, Jianfeng Lin, Zhaochen Xu, Xinze Wang, Shuting Lin, Rongzhi Zhang, Yitong Li, Hanlong Li, Yuan Tian, Kerr Ding, and many others made Atlanta feel home through countless family gatherings, board games, and shared celebrations. Xinze Wang, Rongzhi Zhang, Hanlong Li, Kerr Ding, Jason Taylor, Ian Graham, and many other basketball friends shared wins and losses on the court with me, and through those games we became close friends beyond it. I am also grateful to Zhijian Ren, Yu Yang, Xiaochen Zhou, Yijian Duan, Jiaqi Li, Yuchen Wang, Zhuo Chen, Jiafeng Lang, Zheng Chen, Pu Li, Yuze Wang, and many others for their companionship and support in life. Their friendship has brought me joy, strength, and balance throughout this journey.

Finally, I owe my deepest thanks to my family, whose constant love, patience, and encouragement have carried me through every challenge along this journey. I would like to thank my parents, Yongjun Wang and Jian He, for their unconditional love and selfless support, and for always believing I am the best kid, even though I know I am not. I am also deeply grateful to my grandmother, Guilan Li, for the early education and values she instilled in me, which have shaped who I am today. I want to thank my uncle, Han Ding, for his constant encouragement and valuable advice. I would also like to thank my big family, including my grandparents, aunts, uncles, and cousins, for their continuous care and support over the years. I would like to thank my parents-in-law, Xiaohua Han and

Ye Zhang, for their kindness, understanding, and support for our young family. I would also like to thank my dog, Hammer Han, for her companionship and the warmth she has brought me. Most importantly, I want to thank my dear wife, Minxi Han. I cannot imagine life without you. Time has passed so quietly that I hardly noticed how many years we have already shared together. Your love, understanding, and strength have been my greatest source of comfort and motivation. You are a friend, a family, an ally, and the other half of my life. Every accomplishment in this journey belongs as much to you as it does to me.

TABLE OF CONTENTS

LIST OF FIGURES

LIST OF ACRONYMS

AquaMILR Aquatic Mechanically Intelligent Limbless Robot

CI computational intelligence

MI mechanical intelligence

MILR Mechanically Intelligent Limbless Robot

NDC negative directional compliance

OAL obstacle-aided locomotion

PCA principal component analysis

PDC positive directional compliance

SUMMARY

Limbless animals such as snakes and nematodes exhibit remarkable capability in navigating complex environments, inspiring the development of limbless robotic systems. However, most existing designs consist of rigid segments actuated by rotational motors and often face limitations in mobility and adaptability within heterogeneous or unstructured terrains. This thesis introduces a new design paradigm centered on mechanical intelligence (MI). A novel actuation mechanism is presented, featuring bilateral actuation along a flexible spine that models the musculoskeletal systems of animals. This mechanism enables effective open-loop locomotion in complex environments through the exploitation of passive body mechanics and body-environment interactions, thereby reducing reliance on complex control algorithms while guaranteeing adaptability. Building on this foundation, computational intelligence (CI) techniques such as gait optimization, tactile sensing, and closed-loop control are incorporated to achieve enhanced performance across both terrestrial and aquatic environments. The thesis is organized around three aims: (1) to develop bilaterally actuated limbless robots to identify and quantify the principles of MI, (2) to design and optimize gaits that take advantage of MI for improved performance, and (3) to extend established MI principles and discover new ones in aquatic environments, exploring the synergy between MI and CI for robust, adaptive amphibious autonomy. This work contributes to the development of versatile limbless robots with enhanced autonomy and resilience, supporting applications in search-and-rescue operations, industrial inspections, precision agriculture, and planetary exploration.

CHAPTER 1
INTRODUCTION AND BACKGROUND

1.1 Overview

Locomotion in complex and dynamic environments presents a fundamental challenge for both biological organisms and engineered robotic systems [1]. From the flapping of hawkmoths [2] to the prancing of gazelles [3], and from the undulation of snakes [4] to the crawling of nematodes [5], these organisms achieve directed movement through a sophisticated interplay of neural and mechanical control. Neural circuits play a crucial role by integrating sensory input and generating locomotor commands through intricate signaling networks, allowing organisms to navigate ever-changing environments by adjusting motor actions based on external cues. Significant progress has been made in unraveling the neural aspects of locomotor control, including the structure, function, and dynamics of neural circuits, particularly with well-studied genetic models such as *Caenorhabditis elegans* [6], *Drosophila melanogaster* [7], and mice [8].

Beyond neural control, the concept of "neuromechanical" integration has emerged, describing how active neural commands and passive mechanical processes interact within body-environment systems. These approaches, primarily explored in flying and walking systems, demonstrate how organisms utilize reflexive or passive responses to maintain stability in unpredictable conditions [9, 10]. In limbless locomotion, studies have shown that many limbless organisms move through bilateral actuation, where muscles on opposite sides of the body contract and relax in coordinated wave patterns. This combination of active force generation and passive compliance facilitates efficient movement over uneven terrains. For example, the Mojave shovel-nosed snake (*Chionactis occipitalis*) navigates sandy, obstacle-rich environments using a characteristic sinusoidal motion, bending pas-

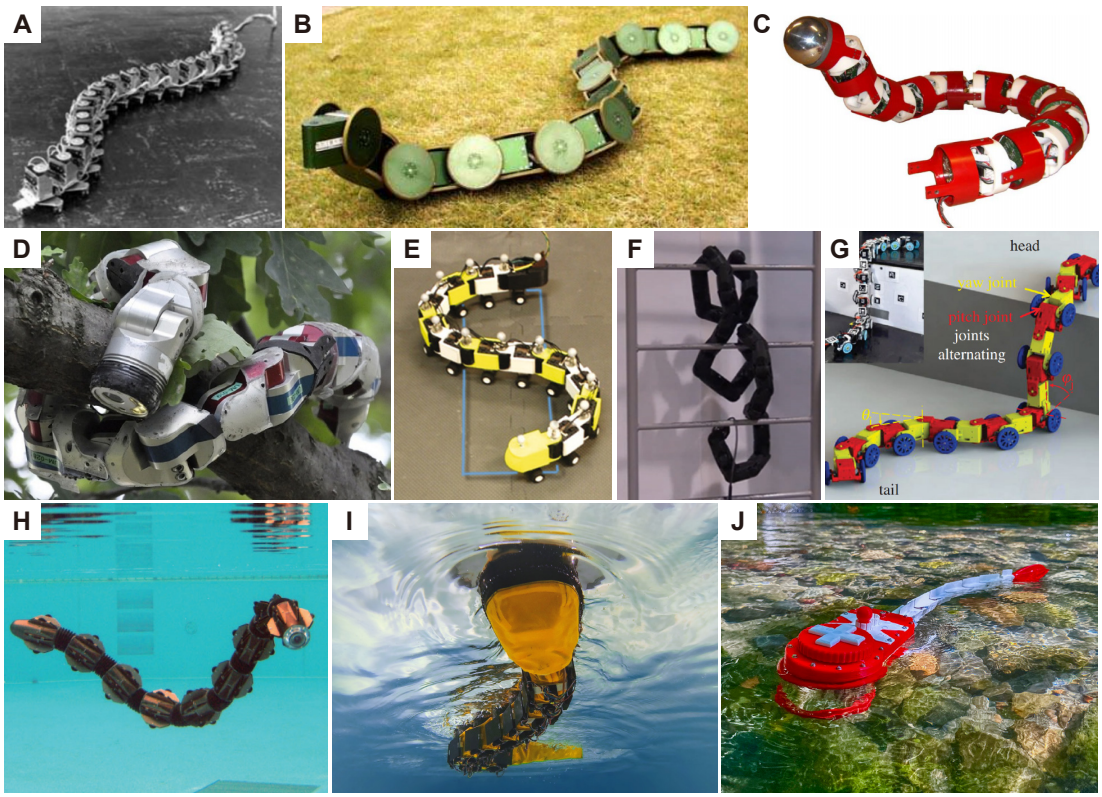

Figure 1.1: **Diverse limbless robot designs composed of serially chained rigid links and joints in the limbless robotics literature for versatile tasks and environments.** From (**A**) to (**J**): [11, 12, 13, 14, 15, 16, 17, 18, 19, 20].

sively around obstacles rather than relying on active sensing.

Motivated by the remarkable ability of limbless organisms like snakes and nematodes to adapt and move through complex terrains [21, 22, 23, 4, 24, 25, 26], researchers have developed limbless robots aimed at traversing challenging environments. These robots show potential in applications where traditional wheeled and legged systems struggle, such as search-and-rescue missions, industrial inspections, precision agriculture, and planetary exploration. However, despite often being referred to as snake-like [12, 13, 27, 28], these robots have yet to match the locomotion capabilities of even the simplest limbless organisms like nematodes, particularly in complex environments. Most existing limbless robots employ rigid, rotary-actuated modules [11, 12, 13, 28, 15, 16, 17, 18, 19, 20], which lack passive mechanical adaptability and struggle to cope with unpredictable terrains that natural counterparts navigate with ease (Figure 1.1). While soft limbless robots with com-

pliant bodies have emerged over the past decade [29, 30, 31], challenges related to air/fluid handling mechanisms and the complexity of modeling intrinsic material properties have limited their practical applications. Hence limbless robots have yet to fulfill their promised potential.

To address these challenges, this thesis proposes a new class of limbless robots that employ bilateral actuation along a flexible spinal structure, modeling the actuation mechanisms of biological musculature. By adopting a decentralized cable-driven musculoskeletal system, this design introduces programmable body compliance, significantly reducing the reliance on computationally intensive control algorithms for terrain adaptation. This approach enables the robot to spontaneously react to terrain heterogeneities through passive environmental interactions, mirroring the effectiveness observed in biological systems while enhancing the robot's navigation capabilities in diverse and dynamic environments.

Current approaches to limbless locomotion in complex environments only emphasize computational intelligence (CI)—the utilization of sensing, reasoning, and decision-making to process information, recognize patterns, and adapt behavior for effective perception, control, and autonomy. In contrast, our approach relies fundamentally on mechanical intelligence (MI)—exploiting the robot's physical properties to facilitate movement and stability in natural, unpredictable environments, thereby reducing computational load. This paradigm shift offloads the complexities of sensorimotor control to MI, freeing onboard resources for higher-level CI tasks such as objective-oriented motion planning and control.

The primary aim of this proposal is to advance the development of bilaterally actuated limbless robots that capitalize on MI principles for locomotion in complex, cluttered, and unpredictable environments. The research is structured around three key aims: (1) to develop bilaterally actuated limbless robots to identify MI principles, (2) to develop models for gait optimization and explore diverse bilateral actuation morphologies to maximize terrestrial capabilities, and (3) to validate the bilateral actuation strategy in aquatic environments and explore the synergy between MI and CI for robust, adaptive amphibious

multimodal locomotion. Achieving these aims will enhance the robot's ability to navigate diverse environments, advancing the practical applications of limbless robots in agriculture, aquaculture, planetary exploration, and search-and-rescue operations.

1.2 Related work, state of the field

1.2.1 Limbless robot morphology and design

The development of limbless robots dates back to Hirose's 1972 design [11], which introduced a serially actuated articulated body with rotary motors at its joints, enabling movement in the horizontal plane. This early design, like many subsequent limbless robots, relied on passive wheels to create anisotropic friction, facilitating forward movement on flat surfaces. Over the years, numerous advancements have refined this approach, leading to serially connected modular robots designed for planar movement using passive wheels, such as those in [27, 32, 33, 34].

To expand beyond planar motion, a class of limbless robots incorporated yaw and pitch joints, allowing three-dimensional locomotion. These robots, often retaining passive wheels [12, 17, 35, 36], could generate anisotropic friction for effective movement on flat surfaces and transitions between smooth surfaces but remained limited in uneven and cluttered environments, where passive wheels became ineffective. To address this, researchers explored wheel-free designs [28, 13, 16] that rely on environmental contact forces to generate thrust, such as pushing against obstacles [37, 13] for planar motion or employing intermittent contact strategies [38, 39, 40, 41, 42, 43].

In recent years, the emergence of soft limbless robots has introduced an alternative paradigm, leveraging functional soft materials powered by pneumatic, hydraulic, or electroactive actuators [44, 29, 45, 46, 47, 48]. These robots naturally conform to their surroundings, offering whole-body compliance that traditional rigid robots lack. However, soft robots suffer from low actuation bandwidth (< 10 Hz), and limited motion precision and controllability, restricting their practical applications where higher actuation speed and

force generation are necessary.

1.2.2 Forms of locomotion and development of gaits

While the hyper-redundancy of limbless robots enables high flexibility, coordinating their many degrees of freedom for effective locomotion remains a significant challenge. Researchers have extensively studied *gait* (the sequencing of body movements) design to achieve efficient forward motion, turning, and terrain adaptation. One of the most widely used bio-inspired gaits in 2D limbless robots is lateral undulation, modeled after snake undulatory movement [49]. By commanding joints to follow sinusoidal waves propagating from head to tail, robots can generate propulsion under anisotropic ground friction conditions [11, 50]. Robots with yaw and pitch actuation have enabled more complex 2.5D and 3D locomotion modes, such as sidewinding [39, 38, 40, 41], sinus lifting [51, 52], crawling [53, 54, 55], and concertina [56, 57] gaits, which are particularly useful for navigating uneven and structured terrains. Beyond biologically inspired motions, engineered gaits such as rolling [58, 59] and climbing [60, 61] have demonstrated effective movement in specific environments.

To optimize locomotion performance, geometric mechanics [62] has emerged as a key tool for linking body shape changes to locomotion velocity. By mapping the relationship between joint velocity in shape space and resulting displacement in global position space, geometric mechanics enables the systematic optimization of gait templates [63, 64, 65]. This framework has been instrumental in optimizing gait template parameters, and developing new locomotion strategies for diverse environments. Despite these advances, most gait optimization studies have been conducted on rigid-body robots without significant consideration for MI. This proposed research aims to integrate compliance into geometric mechanics frameworks, optimizing MI-driven gaits that enhance agility and robustness across heterogeneous substrates. To complement geometric mechanics, other modeling approaches include dynamical system modeling [66, 67] and pure geometry-based curve

fitting [43, 68, 69, 70]. These methods provide parallel strategies for gait analysis and optimization and have contributed significantly to the field.

1.2.3 Motion planning and control in complex environments

Building on fundamental locomotion strategies such as lateral undulation and sidewinding, researchers have developed high-level motion planning techniques to enable limbless robots to operate in diverse and dynamic environments. Two primary challenges in motion planning involve path following in structured spaces and target-oriented exploration in unknown environments [71].

In homogeneous, obstacle-free settings, motion planning focuses primarily on modulating locomotive direction to reach a target [72, 73]. However, in cluttered and unstructured environments, robots must interact with obstacles, leading to two major planning approaches: obstacle-avoidance and obstacle-aided locomotion. Obstacle-avoidance strategies use precomputed routes to navigate around obstacles [74, 75], but these methods often fail in real-world scenarios where prior environmental knowledge is limited. Obstacle-aided locomotion, on the other hand, actively leverages environmental contacts to generate propulsion, allowing robots to maneuver through confined or obstacle-rich spaces [13]. While more adaptable, this approach requires designing the body shape to precisely match the density and distribution of obstacles, which must be determined in advance. Otherwise, improper contact may occur, potentially trapping the robot between obstacles.

Most existing motion planning strategies rely heavily on CI—using sensing, mapping, and control algorithms to continuously adjust the robot's body shape based on environmental feedback [37, 76, 71, 77, 78]. While effective in structured environments, these approaches struggle in unpredictable terrains where sensory input may be unreliable or computationally expensive. Motion planning for specialized environments, such as climbing ladders, rolling through pipes, and transitioning between substrates, has also been explored [16, 59, 79]. However, these methods typically assume that the robot's rigid body

can precisely achieve the planned geometry, overlooking the role of MI in adapting to environmental uncertainties.

1.2.4 Tendon-/cable-driven mechanisms in other types of robot platforms

Cable-driven robots encompass a wide range of robotic systems that utilize cables for actuation, offering advantages such as flexibility, lightweight construction, and the ability to generate complex motions. Continuum robots [80, 81] are designed primarily for manipulation tasks. They employ centralized actuation from a fixed base to bend a continuous, flexible structure, making them well-suited for applications requiring dexterity and precision, such as minimally invasive surgery [82, 83] and industrial manipulation [84, 85]. The continuous and smooth bending motion of these robots allows for intricate manipulation within constrained environments. Cable-driven parallel robots (CDPRs) [86, 87] are another class of cable-actuated systems designed to manipulate or position a rigid end-effector. These robots consist of multiple cables attached from fixed anchor points to a mobile platform, which moves by precisely controlling cable tension. CDPRs are particularly advantageous for large workspace manipulation and tasks requiring high stiffness, such as heavy load handling and precise positioning.

While both continuum robots and CDPRs are primarily designed for manipulation and positioning, the proposed cable-driven limbless robots are fundamentally different in their use of cable actuation. Instead of focusing on manipulation, they employ distributed actuation along the robot's body to achieve self-propelled locomotion for traversing complex and unstructured terrains.

1.3 Biological inspiration of bilateral actuation

Many limbless organisms achieve locomotion through bilateral actuation, in which muscles on opposite sides of the body contract and relax in coordinated traveling waves (Figure 1.2A, B). This coordination integrates longitudinal and oblique muscle groups along

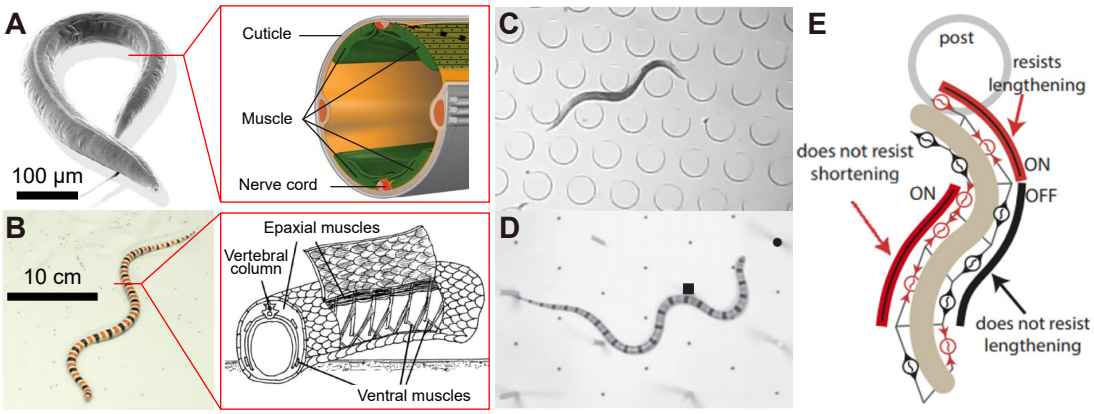

Figure 1.2: **Versatile limbless locomotion facilitated by bilateral actuation.** Nematode *Caenorhabditis elegans* (**A**) and Mojave shovel-nosed snake *Chionactis occipitalis* (**B**), along with cross-sectional anatomy [88, 89, 90]. *C. elegans* (**C**) and *Chionactis occipitalis* (**D**) move on obstacle terrains. (**E**) A schematic of snake muscle activation during obstacle negotiation [4].

the axial skeleton, producing curvature waves that propagate from head to tail. Snakes possess a bilaterally symmetric axial musculature, where paired epaxial and hypaxial muscles contract antagonistically to generate undulatory bending [22, 88]. The axial system consists of three major longitudinal columns of epaxial muscles: the *spinalis-semispinalis*, *longissimus dorsi*, and *iliocostalis*. Each column contains overlapping segments that extend across multiple ribs and vertebrae, forming a continuous series along the trunk. These muscle bundles are interconnected by tendinous linkages that transmit forces between adjacent segments. Ventral and hypaxial muscles occupy the lower body wall and connect to the ribs and abdominal structures. Together, this bilateral musculoskeletal architecture forms a continuous, segmented framework surrounding the vertebral axis and providing the primary structural basis of the body wall in snakes [88].

Beyond vertebrates, the nematode *Caenorhabditis elegans* provides a complementary model at the millimeter scale. Its body-wall musculature is arranged into four longitudinal quadrants along the dorsal and ventral surfaces [90]. Each quadrant contains spindle-shaped muscle cells that attach to the cuticle through dense bodies and M-line analogs, forming obliquely striated sarcomeres with actin and myosin filaments. Alternating con-

traction of dorsal and ventral muscles generates curvature that propagates as a traveling wave along the body. Muscle cells extend arms toward the nerve cords, forming neuromuscular junctions and gap junctions that synchronize contractions between quadrants [91]. This bilateral arrangement, together with the compliant cuticle and hypodermis, forms an integrated body-wall structure in which muscles, extracellular matrix, and epidermal layers are mechanically coupled.

The biological mechanisms described above manifest clearly in observed locomotor behaviors (Figure 1.2C, D). The nematode *C. elegans* generates traveling curvature waves through alternating activation muscle bands, producing smooth undulations in homogeneous media and adaptive gait changes in structured environments. Similarly, the Mojave shovel-nosed snake *Chionactis occipitalis* moves through obstacle-rich terrains using a stereotyped sinusoidal waveform that allows the body to buckle passively around posts or obstacles [4]. This passive accommodation arises from the bilateral activation of muscles that resist shortening while yielding to lengthening, enabling smooth deflection and forward progress (Figure 1.2E). Together, these examples demonstrate how bilateral actuation integrates active force production with passive mechanical compliance, allowing limbless organisms to maintain propulsion and stability across heterogeneous terrains.

1.4 Concepts of mechanical intelligence (MI) and computational intelligence (CI)

Locomotion in animals and robots arises from the coordination of body mechanics, sensing, and control. Two complementary forms of intelligence contribute to this coordination: mechanical intelligence (MI) and computational intelligence (CI).

Mechanical intelligence (MI) is a concept proposed and discussed in recent works that explore how physical structure, material properties, and passive dynamics can simplify perception and control in robotic systems [92, 93, 94, 95, 96]. In this thesis, MI refers to mechanisms that make challenges for perception, control, and autonomy easier or more robust for natural, unstructured, and often unpredictable environments by virtue of their

physical properties. This perspective emphasizes that the body's morphology and intrinsic mechanics can contribute directly to adaptive behavior, allowing the system to stabilize motion, absorb perturbations, and interact effectively with complex terrains without relying entirely on computation or sensing. MI therefore captures the functional role of physical embodiment, in which mechanical design performs part of the control and decision-making normally handled by algorithms.

Computational intelligence (CI) has been widely used in robotics and control to describe processes that involve sensing, reasoning, and decision-making to process information, recognize patterns, and adapt behavior in response to perturbations for effective perception, control, and autonomy [97, 98, 99]. In this thesis, CI captures the capability of a system to sense, reason, and make decisions that enable perception, planning, and adaptive control for goal-directed behavior. CI includes both feedforward (offline) form, which involves motion planning and gait optimization based on predicted/known environmental conditions, and feedback (online) form, which governs real-time decision-making and closed-loop control. Together, these forms of CI provide the ability to interpret sensory information, plan trajectories, and continuously adjust actions to achieve specific objectives.

Although MI and CI arise from different mechanisms, they are most effective when integrated. MI provides robustness and adaptability, whereas CI supplies precision and autonomy. Effective locomotion depends on their hierarchical coordination, in which mechanical mechanisms handle fast, local adaptation and computational processes manage higher-level planning and decision-making.

This thesis follows the hierarchical framework shown in Figure 1.3, progressing from MI as the foundation for spontaneous adaptation, through feedforward CI for environment-specific gait optimization, to feedback CI for high-level real-time capability and autonomy. The integration of these levels defines a pathway toward full-body intelligence, enabling robust and effective locomotion across complex and unpredictable terrains.

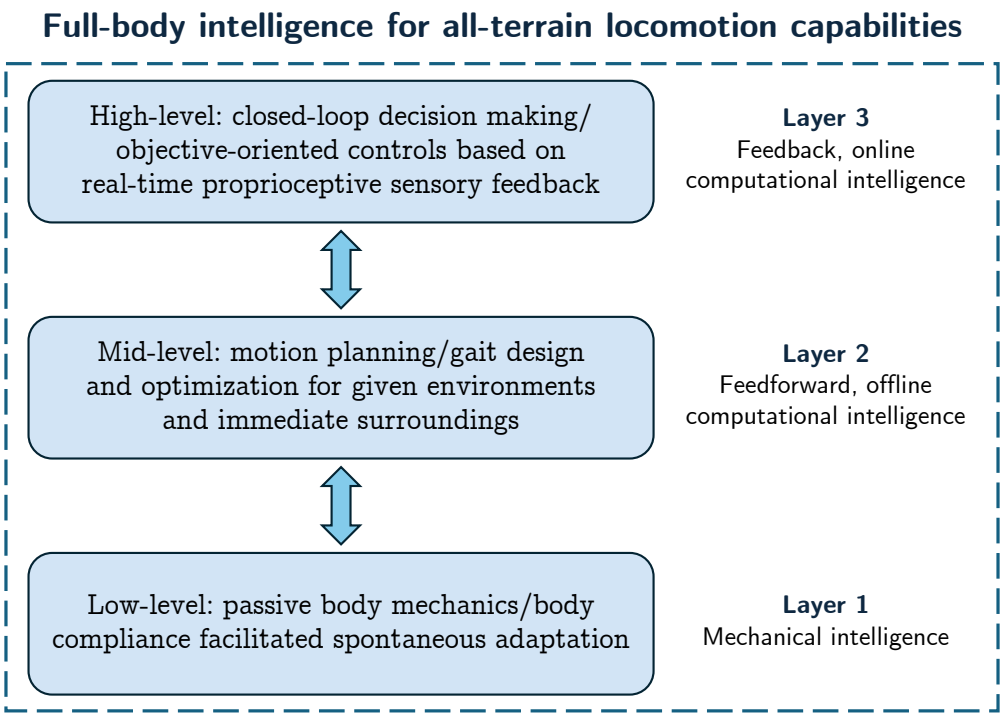

Figure 1.3: **A hierarchical framework for limbless locomotion.** Locomotor intelligence emerges through the integration of mechanical and computational intelligence layers. Low-level adaptation arises from body compliance and passive mechanics (mechanical intelligence, Layer 1). Mid-level gait optimization encodes offline, feedforward planning based on environmental context (computational intelligence, Layer 2). High-level online feedback control and decision-making enable task-oriented autonomy (computational intelligence, Layer 3). Together, these layers form a unified framework for full-body intelligence and all-terrain locomotion.

1.5 Outline of chapters and thesis organization

This thesis consists of three parts and thirteen chapters, organized to follow a progressive framework of full-body intelligence. As illustrated in Figure 1.3, full-body intelligence emerges from the synergy between mechanical and computational mechanisms operating across different levels of physical and algorithmic abstraction. Together, the three parts complete this hierarchy by moving from local-level body adaptation to mid-level motion planning and optimization and, ultimately, to high-level closed-loop control for environmentally responsive locomotion across diverse terrains.

Part I focuses on identifying and implementing the principles of MI that enable limb-

less robots to achieve robust and adaptive locomotion via pure passive body mechanics alone.

- **Chapter 2** introduces the bilaterally cable-driven limbless robot MILR, establishing programmable body compliance as a quantitative measure of MI. This chapter is adapted from [89].

- **Chapter 3** demonstrates how passive body compliance and environmental interactions produce emergent open-loop locomotion without sensing or feedback. This chapter is adapted from [89].

- **Chapter 4** extends MI principles to a sidewinding variant of MILR, showing that mechanical intelligence stabilizes sidewinding motion on complex terrains. This chapter is adapted from [100].

- **Chapter 5** upgrades MILR into a morphology-varying variant, which adds out-of-plane rolling joints to realize three-dimensional, multimodal gaits.

Together, these chapters define the physical foundation of mechanical intelligence and show how passive body mechanics can generate stable and versatile terrestrial locomotion on complex terrains.

Part II builds upon the mechanically intelligent platforms developed in Part I to introduce computational frameworks that enhance their performance through modeling, control, and optimization.

- **Chapter 6** formulates a cable-driven model within a geometric-mechanics framework to predict locomotor behavior and optimize actuation patterns. This chapter is adapted from [101].

- **Chapter 7** develops omega-turn gaits, demonstrating effective in-place turning behaviors inspired by nematode motion. This chapter is adapted from [102, 103].

- **Chapter 8** expands gait modeling to obstacle-aided locomotion, mapping environmental constraints into shape-space dynamics to improve the ability to utilize surrounding obstacles. This chapter is adapted from [104].

- **Chapter 9** explores sidewinding gait optimization, revealing how frequency and contact modulation balance speed and stability. This chapter is adapted from [105, 106].

Collectively, these chapters show that computational modeling and optimization can achieve globally improved locomotor performance while preserving the system's ability to exploit mechanical intelligence for handling local environmental perturbations.

Part III extends the study of mechanical intelligence to aquatic environments and integrates sensing and control strategies toward amphibious autonomy. It revisits MI principles under hydrodynamic conditions, and explores decentralized feedback mechanisms for adaptive interaction with complex media.

- **Chapter 10** introduces the AquaMILR series, extending mechanical intelligence to underwater environments through waterproofed, untethered designs. This chapter is adapted from [107].

- **Chapter 11** investigates mechanical intelligence in aquatic contexts, exploring how compliance and hydrodynamics jointly shape movement under varied environmental conditions. This chapter is adapted from [108, 107].

- **Chapter 12** incorporates sensing and decentralized feedback control, bridging mechanical and computational intelligence for context-responsive behavior and advancing toward amphibious autonomy. This chapter is adapted from [89, 108].

Together, these chapters demonstrate how the integration of mechanical and computational principles broadens the operational envelope of limbless robots and drives their evolution toward fully autonomous amphibious locomotion.

Collectively, the three parts realize the complete hierarchy of locomotor intelligence envisioned in Figure 1.3 and establish a unified framework for full-body intelligence and all-terrain locomotion in limbless robots.

Part I

Developing bilaterally actuated limbless robots to identify mechanical intelligence principles for versatile terrestrial locomotion in complex environments

Part I of this thesis focuses on identifying and implementing the principles of mechanical intelligence that enable limbless robots to achieve robust locomotion in complex and unpredictable terrestrial environments. Mechanical intelligence refers to mechanisms that, through their inherent physical properties, simplify challenges associated with perception, control, and autonomy in natural, unstructured settings. With a focus on bilaterally actuated systems that model the bilateral actuation morphology in organisms such as snakes and nematodes, this part explores a substantially different locomotor strategy designed for environments where traditional wheeled, bipedal, or even myriapod robots struggle.

Building upon this foundation, the following chapters develop a family of bilaterally actuated robots that embody mechanical intelligence through symmetric antagonistic actuation and tunable body compliance. These include the baseline MILR platform, along with the sidewinding and morphing variants that extend mechanical intelligence to diverse and three-dimensional terrestrial motions. Together, they establish the physical basis of mechanical intelligence and demonstrate how passive body mechanics alone can facilitate stable, adaptive, and versatile locomotion.

CHAPTER 2
DEVELOPMENT OF A NOVEL CLASS OF BILATERALLY CABLE-DRIVEN LIMBLESS ROBOTS

2.1 Introduction

To model the bilateral actuation mechanisms of organisms such as snakes and nematodes [88, 109, 90], we developed a cable-driven limbless robot, Mechanically Intelligent Limbless Robot (MILR) [89]. MILR (Figure 2.1) is a hybrid hard-soft robot featuring an 86 cm long body with seven single-degree-of-freedom passive bending joints. Each joint is actuated by two non-elastic cables on opposite sides, with independent control over each cable's length through a cable-pulley-servo system. By coordinating the cable lengths to generate angular oscillations of the joints along the body, MILR replicates the undulatory locomotion observed in natural limbless organisms. The design allows for programmable and quantifiable body compliance through cable actuation, which is essential for enabling passive body mechanics and effective body-environment interactions. This programmable compliance represents a physical manifestation of mechanical intelligence (MI) in the proposed limbless robotic system.

Building upon this design, this chapter establishes the foundation for implementing and quantifying MI in bilaterally actuated limbless robots. We first describe the detailed structure of the cable-driven mechanism, emphasizing how the bilateral cable architecture enables distributed control of joint angles and stiffness. We then formulate a generalized compliance parameter G that regulates the tightening and relaxation of the cable pairs. This parameter provides a simple yet powerful means to describe and modulate the robot's body compliance, allowing the emergence of passive mechanical behaviors during undulatory motion.

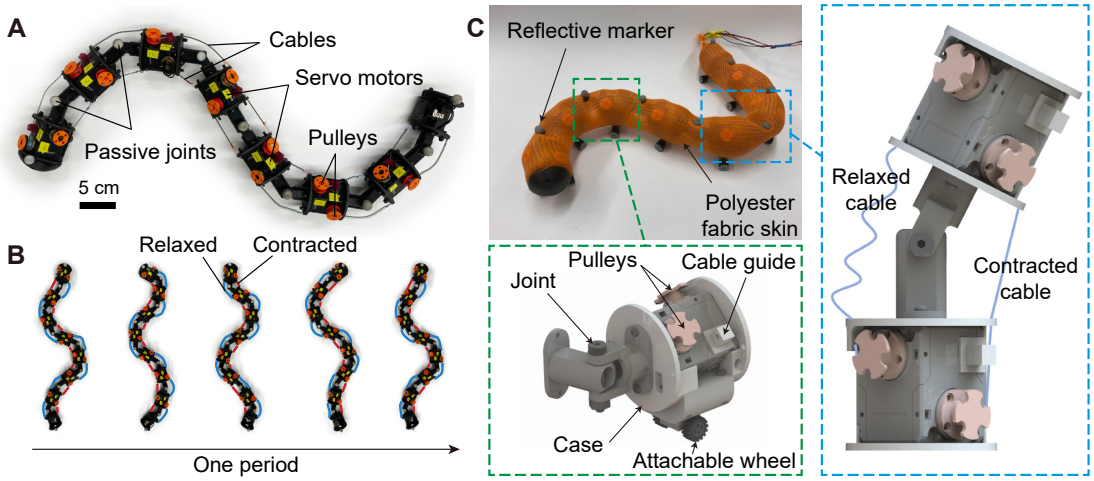

Figure 2.1: **The mechanically intelligent limbless robot, MILR**. (**A**) The robot features a bilateral actuation mechanism. (**B**) A conceptual illustration of body postures and antagonistic cable activities over one gait period in MILR. (**C**) An example of MILR fully equipped for experiments and computer-aided design drawings detailing the components. Figures are adapted from [89].

Through a combination of static deformation tests and dynamic wave generation experiments, we characterize how G governs the effective stiffness, torque response, and deformation symmetry of the system. These analyses demonstrate that body compliance can be precisely tuned and exploited. The resulting framework establishes the mechanical foundation for subsequent chapters, extending the concept of programmable compliance to locomotion across varied terrestrial and aquatic environments.

This chapter is adapted from my previously published peer-reviewed work [89].

2.2 Robot design

MILR is constructed from a chain of linked identical modules. Each individual module consists of a two-axis servo motor housed inside a case. The cases are attached to one another with a unilaterally bending joint linkage. Pulleys are then attached to each axis of the motor, and the pulleys are spooled with strings, which are referred to as cables. To complete the design, the cables are unspooled through the case and fixed onto the case ahead of the current one.

Each module contains a Dynamixel 2XL430-W250-T servo motor (ROBOTIS), which has two axes that can be controlled independently. This feature enables the left and right cables to be adjusted to different lengths as needed. With a stall torque of 1.4 Nm, the motor provides ample support for the cable tension resulting from body-environment interactions. Additionally, the motor offers precise and continuous position control, with small enough resolution for multiple rotations. This feature allows for accurate cable length controls, where it is assumed that the cable length was approximately proportional to the motor position within the range between the maximum and minimum cable lengths.

The case that houses the servo motor serves as the main structural component and skeleton of the body. It is custom designed (55 mm length, 68 mm diamater) and manufactured to fit the motor's geometry and is 3D printed using PLA material. To attach the case to other components, such as the joint and wheels, heat-insets are inserted into all the holes. All the cases are identical, except for the one at the anterior end (head) of the robot, which has a spherical surface for smoother head-obstacle interactions.

The joint (28 mm length) connecting adjacent modules in the system provides one degree of freedom rotation, with the axis of rotation perpendicular to the ground surface. We 3D print joints with PLA material. Each joint allows a full range of 180 degrees of rotation, from -90 to $+90$ degrees, with the neutral position at 0 degrees where the two links align. The joints are secured to the cases with two screws that connect directly to the heat insets, facilitating easy rearrangement and replacement.

The cables are the component that drives the movement of the robot. To achieve this, we utilize nonelastic fishing lines (Rikimura) that boast high tensile strength of up to 180 pounds and demonstrate negligible deformation and shape memory upon stretching. To control the shortening and lengthening of the cables, we employ pulleys (9.5-mm diameter) that are 3D printed using PLA material and attached to each rotational shaft of the servo motor. One end of each cable is fixed to the pulley, whereas the rest is tightly wound around it. This configuration allows the length of the cable to vary proportionally with the rotation

angle of the pulley, which can be accurately controlled by the servo motor. The other end of each cable is threaded through a small guiding hole on the edge of the case and attached to the other case linked by the joint. For each joint, two cables are present on either side, controlling the full range of motion of the joint. A cable shortens when it is taut and under tension, whereas it lengthens when it is slack and has no tension.

Our robot is controlled using code developed with the Dynamixel SDK library and programmed in MATLAB. Control signals are transmitted to the robot from a PC via U2D2 (ROBOTIS). We power the motors using a DC power supply with a voltage setting of 11.1 V. As the servo motors are connected in a daisy chain configuration for both power and communication, we connect the U2D2 and power supply to the last motor in the series.

In some experiments and applications settings, we use an mesh sleeve (1.75-inch ID polyester fabric expandable sleeving, McMaster-Carr) to wrap around the robot body. Note that the sleeve cannot create anisotropy to provide any extra propulsion. The benefit of using an isotropic sleeve is twofold. The robot is made of discretized hard modules and joints; therefore, it can get wedged unexpectedly in the heterogeneities because of the irregular structures, such as edges of the case. The sleeve can smooth the discretization of the body to allow for more continuous body contact with the environment. The sleeve also provides weak passive elasticity, facilitating a weak but inherent "potential" for the robot to return to the straight posture.

In some experiments and applications settings, we equip the robot with wheels. The wheels are attachable components that can be attached or removed from the bottom of each case. To attach wheels onto the case, a base is 3D printed using PLA and screwed to the base. Then, the wheel frame (LEGO) is screwed into the base. The wheels are passive, non-actuated.

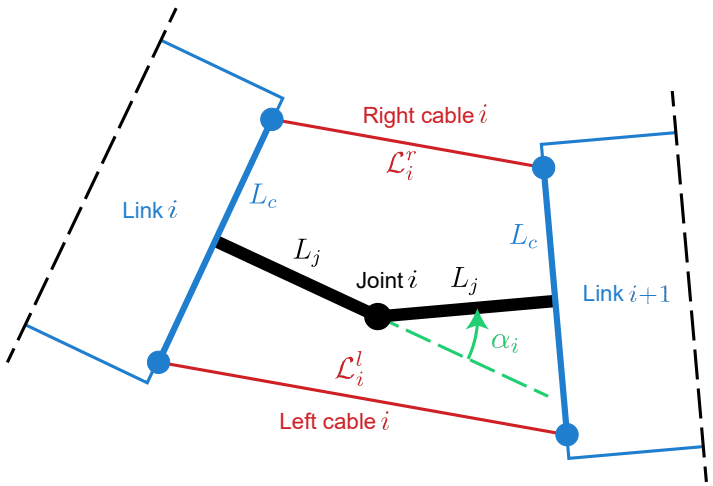

Figure 2.2: **Illustration of a single MILR joint.** Geometry of the joint mechanical design for the calculation of exact lengths of cables $\mathcal{L}_i^l$ and $\mathcal{L}_i^r$ to strictly form a suggested angle α_i. The figure is adapted from [89].

2.3 Basic shape-based control

To implement a basic traveling-wave locomotion pattern on MILR, we developed a shape-based control scheme based on the "serpenoid" template [11]. The template can generate a central pattern that enables a wave to propagate from head to tail, if the i-th joint angle α_i in the spine at time t follows

$$\begin{aligned}\alpha_i(t) &= A\sin(2\pi\xi\frac{i}{N} - 2\pi\omega t) \\ &= A\cos(2\pi\omega t)\sin(2\pi\xi\frac{i}{N}) - A\sin(2\pi\omega t)\cos(2\pi\xi\frac{i}{N}) \\ &= w_1(t)\beta_1^\alpha(i) + w_2(t)\beta_2^\alpha(i),\end{aligned} \tag{2.1}$$

where A, ξ and ω are the amplitude, the spatial and temporal frequencies of the wave, i is the joint index, and N is the total number of joints. The joint angle α given by this template will be further referred to as the "suggested" angle (the angle that would be realized absent all external and internal forces apart from those applied by the cables). Thus, the suggested gait path (the trajectory of $w_1(t)$ and $w_2(t)$) forms a perfect circle in the shape space spanned by w_1 and w_2.

We calculated the exact lengths of the left and right cables that can form a joint angle α, $\mathcal{L}^l(\alpha_i)$ and $\mathcal{L}^r(\alpha_i)$, based on the geometry of the joint mechanical design (Figure 2.2). "Exact length" means the cable is in a shortened state, forming a straight line. Thus, $\mathcal{L}^l$ and $\mathcal{L}^r$ follow

$$\begin{aligned}\mathcal{L}^l(\alpha_i) &= 2\sqrt{L_c^2 + L_j^2}\cos\left[-\frac{\alpha_i}{2} + \tan^{-1}\left(\frac{L_c}{L_j}\right)\right], \\ \mathcal{L}^r(\alpha_i) &= 2\sqrt{L_c^2 + L_j^2}\cos\left[\frac{\alpha_i}{2} + \tan^{-1}\left(\frac{L_c}{L_j}\right)\right].\end{aligned} \tag{2.2}$$

Considering design parameters of MILR, the equations simplify to

$$\begin{aligned}\mathcal{L}^l(\alpha_i) &= 79.2\cos\left(-\frac{\alpha_i}{2} + \frac{\pi}{4}\right)\text{mm}, \\ \mathcal{L}^r(\alpha_i) &= 79.2\cos\left(\frac{\alpha_i}{2} + \frac{\pi}{4}\right)\text{mm}.\end{aligned} \tag{2.3}$$

Thus, by controlling the length of each cable in MILR following Equation 2.3, the robot can accurately form any desired body shape, thus can achieve any capability that a conventional serially actuated limbless robot can achieve.

2.4 Shape space kinematics

To simplify the analysis of locomotion kinematics, we employed dimensionality reduction techniques. Previous studies have applied principal component analysis (PCA) to undulatory systems such as nematodes and snakes, showing that most body postures can be represented as linear combinations of sine-like shape-basis functions, despite the inherently high dimensionality of postural data [110, 111]. By considering the first two dominant principal components, we assume that the body curvature profile κ at time t and position s ($s = 0$ denotes the head and $s = 1$ denotes the tail) can be approximated by:

$$\begin{aligned}\kappa(s,t) &= w_1(t)\sin(2\pi\xi s + \phi) + w_2(t)\cos(2\pi\xi s + \phi) \\ &= w_1(t)\beta_1(s) + w_2(t)\beta_2(s),\end{aligned} \tag{2.4}$$

where ξ is the spatial frequency of body undulation obtained from direct fitting, and ϕ is the emergent phase. $w_1(t)$ and $w_2(t)$ are the reduced shape variables describing the instantaneous posture of the locomotor at time t. By projecting curvatures onto the shape-basis functions $\beta_{1,2}(s)$, locomotion can be visualized as a trajectory in a two-dimensional "shape space" defined by w_1 and w_2 (Figure 2.3A).

However, robots such as MILR are composed of a finite number of discrete joints. To understand how the shapes of a discretized, jointed body correspond to a continuously curving undulator, we first evaluate the curvature of a continuous body at a discrete set of points along its length:

$$\kappa(i,t) = A\sin(\omega t + k_d i), \tag{2.5}$$

where i is the index of the discretized points.

We further decompose the serpenoid traveling wave into temporal and spatial components:

$$\begin{aligned}\kappa(i,t) &= \underbrace{A\sin(\omega t)}_{w_1(t)}\underbrace{\cos(k_d i)}_{\beta_1(i)} + \underbrace{A\cos(\omega t)}_{w_2(t)}\underbrace{\sin(k_d i)}_{\beta_2(i)} \\ &= w_1(t)\beta_1(i) + w_2(t)\beta_2(i),\end{aligned} \tag{2.6}$$

where $\beta_1(i)$ and $\beta_2(i)$ are time-invariant shape-basis functions that describe a serpenoid traveling wave.

Next, we apply the serpenoid curve to a robot composed of discretized joints and links. Define $\vec{T}(i)$ as the tangent vector evaluated at the i-th point along the curve. Note that $\vec{T}(i)$ has unit length, $|\vec{T}(i)| = 1$. Let $\vec{T}(i+1)$ denote the unit tangent vector at the $(i+1)$-th point. The distance between two consecutive points is $\Delta s = L/N$, where L is the total length of the curve and N is the total number of points. The curvature $\kappa(i)$ is defined as

$$\kappa(i) = \lim_{N\to\infty} \frac{|\vec{T}(i+1) - \vec{T}(i)|}{\Delta s}. \tag{2.7}$$

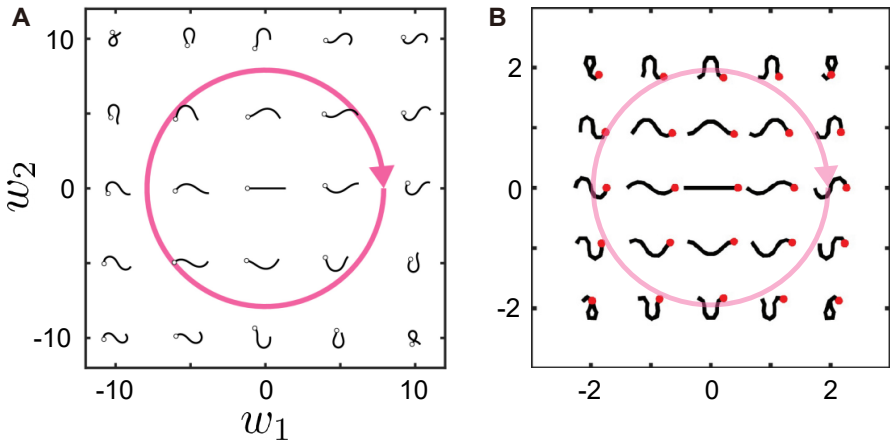

Figure 2.3: **Visualization of waveforms in the 2D shape space.** (**A**) An undulator with a continuous body (*C. elegans*). (**B**) A 9-link limbless robot with a discretized body. Figures are adapted from [112].

We define $\alpha(i)$ as the joint angle between the tangent vectors $\vec{T}(i+1)$ and $\vec{T}(i)$. From geometry,

$$|\vec{T}(i+1) - \vec{T}(i)| = |\Delta\vec{T}| = 2\sin(\alpha(i)/2). \tag{2.8}$$

Substituting Equation 2.8 into Equation 2.7, we obtain

$$\kappa(i) = \lim_{N\to\infty} \frac{2\sin(\alpha(i)/2)}{L/N}. \tag{2.9}$$

Since $\lim_{N\to\infty} 2\sin(\alpha(i)/2) = \alpha(i)$, we have $\kappa(i) = N\alpha(i)/L$ as $N \to \infty$. Therefore, in a discretized system (such as a robot), the joint angle $\alpha(i,t)$ serves as a discrete analog of curvature in the continuous case, describing the system kinematics:

$$\alpha(i,t) = w_1(t)\beta_1^\alpha(i) + w_2(t)\beta_2^\alpha(i), \tag{2.10}$$

as in Equation 2.1. Projecting the joint-angle trajectories $\{\alpha_1(t), \alpha_2(t), ..., \alpha_N(t)\}$ onto the shape bases $\{\beta_1^\alpha(i), \beta_2^\alpha(i)\}$ yields $w_1(t)$ and $w_2(t)$ in the shape space, which describe the robot's kinematics (Figure 2.3B).

2.5 Generalized compliance, definition of programmable and quantifiable body compliance

The bilateral cable actuation mechanism enables body compliance in MILR. However, in contrast to soft limbless robots that inherit compliance from soft materials which are usually hard to modulate, cables in our robot are non-elastic, and thus their lengths can be explicitly controlled. This allows the body compliance in our robot to be quantifiable, programmable, inhomogeneous, and anisotropic, simply by appropriately coordinating the lengthening and shortening of cables.

To implement programmable body compliance in MILR, we developed a cable length control scheme based on the suggested angle template, where the lengths of the left and right cables (L_i^l and L_i^r) for the i-th joint following

$$L_i^l(\alpha_i) = \begin{cases} \mathcal{L}_i^l(\alpha_i) & \text{if } \alpha_i \leq -(2G_i - 1)A \\ \mathcal{L}_i^l[-A \cdot \min(1, 2G_i - 1)] + l_0 \cdot [(2G_i - 1)A + \alpha_i] & \text{if } \alpha_i > -(2G_i - 1)A \end{cases}$$
$$L_i^r(\alpha_i) = \begin{cases} \mathcal{L}_i^r(\alpha_i) & \text{if } \alpha_i \geq (2G_i - 1)A \\ \mathcal{L}_i^r[A \cdot \min(1, 2G_i - 1)] + l_0 \cdot [(2G_i - 1)A - \alpha_i] & \text{if } \alpha_i < (2G_i - 1)A \end{cases} \tag{2.11}$$

where α_i is the suggested angle, A is the wave amplitude as in Equation 2.1, $\mathcal{L}_i^l$ and $\mathcal{L}_i^r$ are the exact lengths of left and right cables to form α_i. l_0 is a design parameter that determines how much a cable will be lengthened and is fixed throughout this work. G_i is the generalized compliance for the i-th joint, a key controller parameter to enable programmable body compliance. Notice that unless specifically stated, we keep the generalized compliance value to be the same throughout all joints, $G_1 = \cdots = G_N = G$. The generalized compliance $G \in [0, +\infty)$ is a parameter that expands the range of possible angles that can occur for a given suggested angle by altering the lengths of the cables on alternate sides; thus G intuitively works as a standalone "knob" in the control that allows for programmable body compliance—increasing G leads to more compliance. Moreover, G is a dimension-

less quantity that quantifies body compliance and not related to the robot's geometry and characteristics of the environment that the robot locomotes in.

We followed Equation 2.11 to control the lengths of the left and right cables $L_i^{l/r}$ for the i-th joint. We converted the linear motion of shortening and lengthening cables to the rotary motion of pulleys by spooling cables onto them. Since arc length is proportional to the center rotational angle, which we can directly control via servo motor (4096 positions per full rotation, 0.088° resolution), we commanded the motor position P to achieve the shortening and lengthening of cable length L using

$$P(L) = P_0 - \gamma L, \tag{2.12}$$

where P_0 is the position of the motor when the cable length is 0 (calibrated for each cable), and $\gamma = \frac{\text{Motor positions per full rotation}}{\text{Cable coil length per full rotation}} = \frac{4096}{\pi D_{\text{pulley}}} = 137.2$ mm^{-1}. Note that $L \geq 0$ and we regulated the positive direction of motor rotation corresponds to the shortening of the cable, according to our mechanical design, thus P_0 is the maximum motor position and γ is positive. Also note that, we neglected the change of pulley radii due to the thickness of the cable (< 0.5 mm). By substituting Equation 2.11 into Equation 2.12, we obtained the control policy in terms of motor position that we directly programmed to run the robot. Practically, we set γl_0 to be a constant with a magnitude of 100 throughout this work, yielding $l_0 = 0.73$ mm/degree.

To provide a better understanding of the generalized compliance G, we narrate the robot's compliant states under three representative generalized compliance values below. At $G = 0$ the robot is bidirectionally non-compliant (Figure 2.4A), where all cables are shortened ($L_i^l(\alpha_i) = \mathcal{L}_i^l(\alpha_i)$ and $L_i^r(\alpha_i) = \mathcal{L}_i^r(\alpha_i)$) so that joints are non-compliant. When $G = 0$, joint angles can precisely track the suggested angles. The projection of joint angle trajectories in the configuration space to the shape space (following the method given by Equation 2.10) then is a perfect circular orbit. Specifically, at $G = 0$ the robot behaves as a

conventional rigid limbless robot; all joints can resist forces from either sides.

At $G = 0.5$ the robot is directionally compliant (Figure 2.4B), where either the left or right cable of a joint is lengthened (L_i^l or L_i^r departs from $\mathcal{L}_i^l$ or $\mathcal{L}_i^r$) so that the joint is directionally (anisotropically) compliant, thus can admit forces to bend further but reject forces from the other side which would otherwise cause the bend to decrease. In the directionally compliant state, a joint is allowed to form an angle (the emergent angle ζ) with a larger absolute value than the suggested angle (α): when a joint is suggested to bend to the right ($\alpha > 0$), the left cable will be lengthened (with an amount of $l_0\alpha_i$) so that the joint can be bent further to the right direction, thus its emergent angle ζ can be larger than the suggested angle α, $\zeta \geq \alpha$; and vice versa, the right cable will be lengthened when $\alpha < 0$ so that $\zeta \leq \alpha$. Note that when $\alpha = 0$, $L_i^l(0) = \mathcal{L}_i^l(0)$ and $L_i^r(0) = \mathcal{L}_i^r(0)$ so $\zeta = 0$. As a result, the projections of all feasible joint trajectories of ζ into the shape space yield a feasible region for gait paths to be perturbed by external forces, where the inner boundary is the "suggested" circular gait orbit.

At $G = 1$ the robot is bidirectionally compliant (Figure 2.4C), where both the left and right cables of a joint are lengthened (L_i^l and L_i^r departs from $\mathcal{L}_i^l$ and $\mathcal{L}_i^r$) so that the joint is bidirectionally compliant, thus can admit forces from either side. In the bidirectionally compliant state, the emergent angle ζ of a joint can vary in both directions around α: at any given α, the left and right are both lengthened (with amounts of $l_0(A + \alpha)$ and $l_0(A - \alpha)$). Note that when $\alpha = A$, $L_i^r(A) = \mathcal{L}_i^r(A)$ so $\zeta \geq A$, and similarly, when $\alpha = -A$, $L_i^l(-A) = \mathcal{L}_i^l(-A)$ so $\zeta \leq -A$, meaning the joint will only be directionally compliant when the suggested angle hits its maximum and minimum. In this state, the feasible region of the gait path in the shape space correspondingly expands as the inner boundary shrinks.

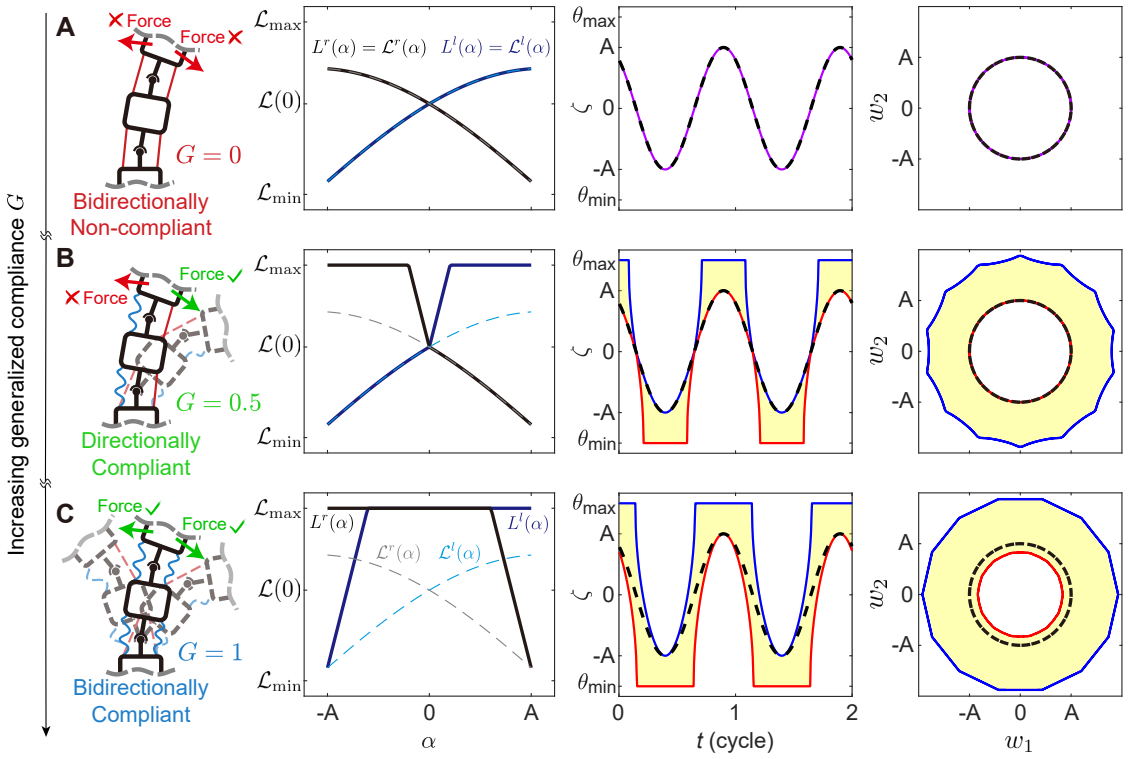

Figure 2.4: **Programmable and quantifiable body compliance in MILR.** Three representative compliant states of the robot under varied generalized compliance G: (**A**) bidirectionally non-compliant, (**B**) directionally compliant and (**C**) bidirectionally compliant. The first column illustrates schematics of cable activation, where red cables are shortened whereas blue cables are lengthened. The second column shows how cables are lengthened at varied suggested angles according to the control scheme, where solid lines represent implemented cable lengths whereas dashed lines represent "exact" lengths of cables to form the suggested angle. The third column shows how much a feasible emergent angle ζ (yellow region) is allowed to deviate from the suggested angle α (dashed line), where solid blue and red lines represent upper and lower boundaries of ζ. The last column shows the how much a feasible emergent gait path in the shape space (yellow region) is allowed to deviate from the suggested circular gait path (dashed line), where solid blue and red lines represent outer and inner boundaries of feasible emergent gait paths. Figures are adapted from [89].

As a continuous quantity, when the generalized compliance value falls between representative values described above, the joint can exhibit a hybrid state. For example, when $G = 0.75$, the joint will be bidirectionally compliant when $\alpha \in (-0.5A, 0.5A)$, and be directionally compliant otherwise.

Note that although the three representative values of G ($G = 0, 0.5, 1$) are not related

to the robot's geometry and gait parameter selection, the fully passive value, the value over which G exceeds the robot will become fully passive, is related to the geometry and parameter selection. The accurate fully passive value can be calculated using the fourth equation given in Equation 2.11,

$$\mathcal{L}^r[A \cdot \min(1, 2G-1)] + l_0 \cdot [(2G-1)A - A] = \mathcal{L}_{max}, \tag{2.13}$$

meaning that when the commanded angle is set to the maximum amplitude ($\alpha = A$), the right cable is loosened to the maximum length such that the joint can freely bend to the minimum amplitude ($-A$); thus the joint is fully passive. Note that without the loss of symmetry, using the left cable equation (the second equation in Equation 2.11) will lead to the same result. Given $G > 0.5$, it can be simplified as

$$\mathcal{L}^r(A) + 2l_0A(G-1) = \mathcal{L}_{max}. \tag{2.14}$$

Solveing for G, we get $G = 1 + \frac{\mathcal{L}_{max} - \mathcal{L}^r(A)}{2l_0A}$, the fully passive value. $\mathcal{L}_{max}$ and $\mathcal{L}^r(A)$ can be directly calculated using Equation 2.3, by letting $\alpha = \pi/2$ and $\alpha = A$. Practically, in the robophysical experiments we varied G value with a 0.25 interval, $G = 1.75$ works as a general approximated fully passive value throughout the work.

To sum up, generalized compliance G works as a "knob" that we tuned to "program" how strongly the robot is driven by the suggested shape, regulating the level of mechanical intelligence. A full schematic of properties that the robot displays under different G see Figure 2.5. Figure 2.5 provides a detailed explanation of the behaviors that one single joint and the whole robot can display when G falls in different ranges. The first schematic in each row shows the state of the joint (either bidirectionally non-compliant, directionally compliant, or bidirectionally compliant) and the state of left and right cables (either shortened or lengthened) depending on which region the suggested joint angle falls into. The second plot in each row illustrates the actual lengths comparing with the exact lengths of

left and right cables on either sides of the joint as a function of the suggested joint angle, where overlaps of actual and exact lengths means the cable is shortened, whereas the discrepancy between actual and exact lengths shows how much the cable is lengthened. Note that $\mathcal{L}(0)$ on the y-axis means the exact length of a cable when joint angle is 0, $\mathcal{L}_{\text{max}}$ and $\mathcal{L}_{\text{min}}$ mean the exact length of the left (right) cable when the joint angle is 90° and -90° (-90° and 90°), respectively. The third plot in each row illustrates the feasible range of all possible emergent joint angle, showing how much a single joint angle could depart the suggested joint angle by perturbation of external forces, enabled by lengthening of cables. The last figure in each row depicts the feasible region of all possible emergent gait paths of the robot, taking all joints as a whole, in the shape space spanned by w_1 and w_2. We projected the collection of upper bounds for all joints onto the $\sin$ and $\cos$ shape basis functions to acquire the outer bound of the possible gait paths. And similarly we projected lower bounds of joint angle to acquire the inner bound of the possible gait paths. The region bounded by inner and outer bounds then illustrates how much the robot could depart the suggested gait path by perturbation of external forces.

Generalized Compliance G

Joint state diagram

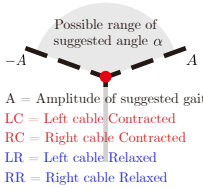

A = Amplitude of suggested gait
LC = Left cable Contracted
RC = Right cable Contracted
LR = Left cable Relaxed
RR = Right cable Relaxed

Cable lengths

- Exact length of left cable to form suggested angle α, $\mathcal{L}^l(\alpha)$
- Exact length of right cable to form suggested angle α, $\mathcal{L}^r(\alpha)$
- Employed length of left cable at suggested angle α, $L^l(\alpha)$
- Employed length of right cable at suggested angle α, $L^r(\alpha)$

Feasible range of deployed joint angle

- Suggested joint angle α
- Upper bound of deployed joint angle ζ
- Lower bound of deployed joint angle ζ
- Feasible range of deployed joint angle ζ

Feasible region of gait path in the shape space

- Suggested gait path
- Outer bound of feasible gait paths
- Inner bound of feasible gait paths
- Feasible region of feasible gait paths

$G = 0$

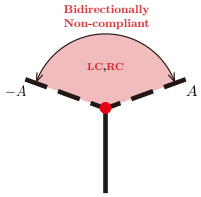

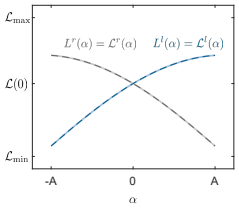

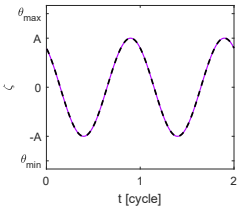

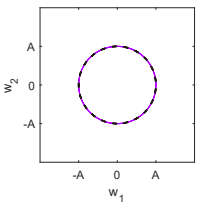

$G \in (0, 0.5)$

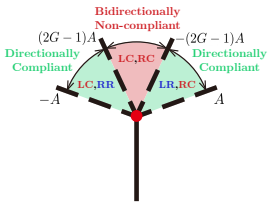

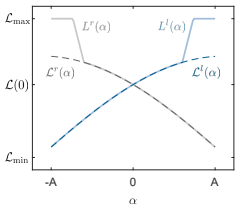

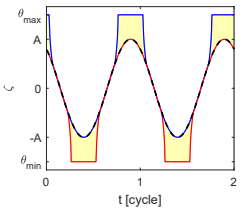

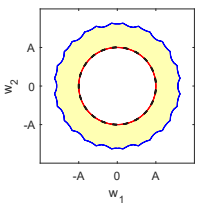

$G = 0.5$

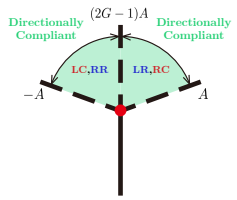

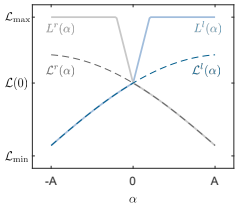

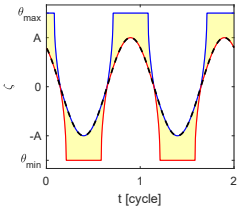

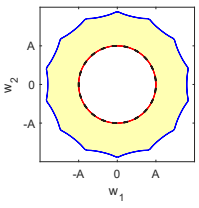

$G \in (0.5, 1)$

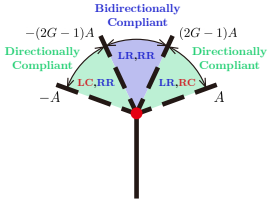

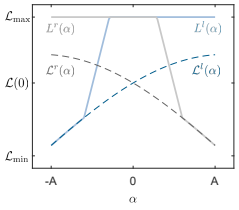

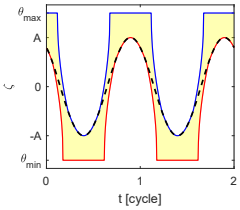

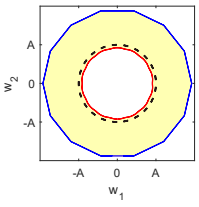

(Con'd)

$G = 1$

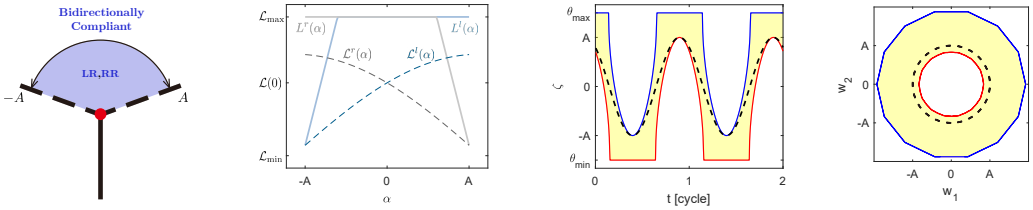

$G \in \left(1, 1 + \dfrac{\mathcal{L}(0) - \mathcal{L}^r(A)}{2l_0 A}\right)$

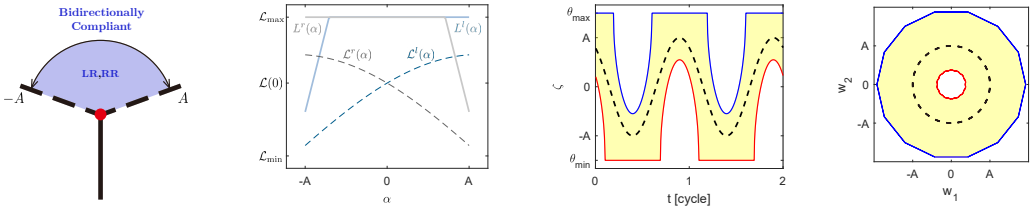

$G = 1 + \dfrac{\mathcal{L}(0) - \mathcal{L}^r(A)}{2l_0 A}$

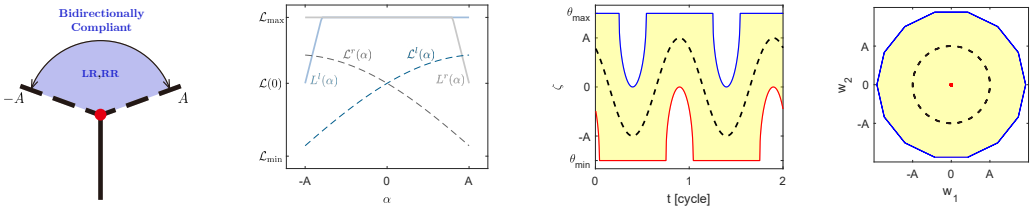

$G \in \left(1 + \dfrac{\mathcal{L}(0) - \mathcal{L}^r(A)}{2l_0 A}, 1 + \dfrac{\mathcal{L}_{max} - \mathcal{L}^r(A)}{2l_0 A}\right)$

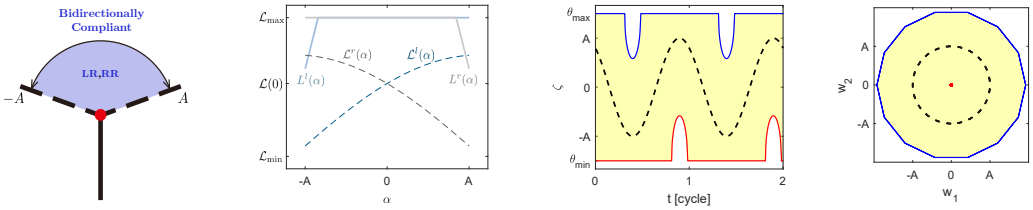

$G \in \left[1 + \dfrac{\mathcal{L}_{max} - \mathcal{L}^r(A)}{2l_0 A}, +\infty\right)$

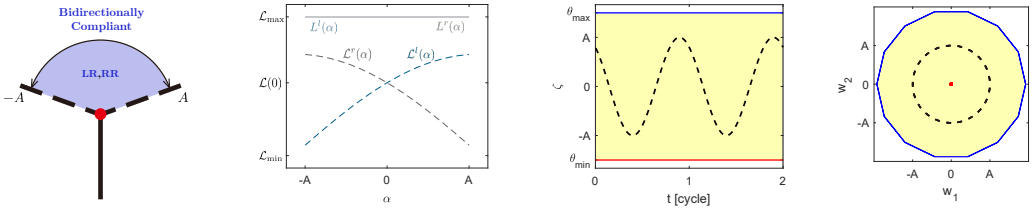

Figure 2.5: **An overview of behaviors that one single joint and MILR can display with varied generalized compliance value G.** The first schematic in each row shows the state of the joint, left and right cables depending on which region the suggested joint angle falls into. The second plot in each row illustrates the actual lengths according to the control scheme comparing with the exact lengths of left and right cables on either sides of the joint as a function of the suggested joint angle. The third plot in each row illustrates the feasible range of all possible emergent joint angle, showing how much a single joint angle could deviate from the suggested joint angle by perturbation of external forces. The last figure in each row depicts the feasible region of all possible emergent gait paths of the robot in the shape space. Figures are adapted from [89].

2.6 An extension of the generalized compliance definition and discussion

In the current definition of generalized compliance G, a joint can only *increase* its local curvature when subject to external forces within the region of directional compliance. This means the body is allowed to bend further in the same direction as the commanded angle, forming what we refer to as positive directional compliance (PDC) [76]. In other words, the local curvature can increase but not decrease, a behavior analogous to the passive buckling observed in limbless organisms such as worms and snakes [4]. We adopted this convention because such buckling and yielding are frequently observed in biological systems, which tend to accommodate external perturbations by bending further rather than resisting or straightening. This property was hypothesized to be the most beneficial form of compliance for terrain negotiation.

From an engineering perspective, however, this definition is not unique. One can define an alternative type of compliance, negative directional compliance (NDC) [76], where the body curvature is only allowed to decrease. In this case, a joint yields in the opposite direction, effectively "flattening" rather than "buckling." Although this behavior is rarely exhibited by biological organisms, the corresponding formulation is straightforward.

We define the extended form of generalized compliance G as:

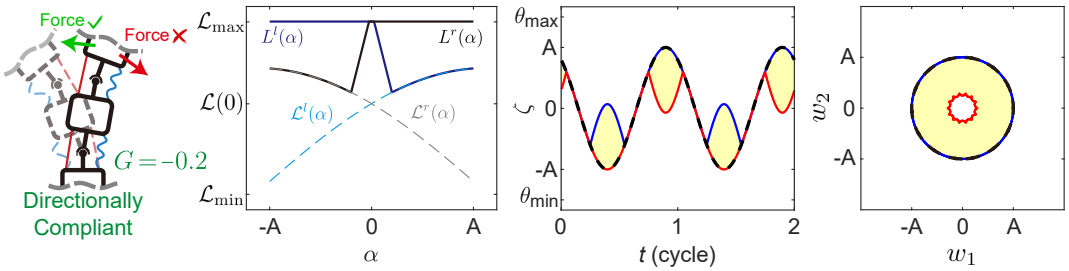

Figure 2.6: **Extended definition of negative generalized compliance** G**.** A representative compliant states of the robot with $G = -0.2$.

If $G \geq 0$, use Equation 2.11; otherwise,

$$L_i^l(\alpha_i) = \begin{cases} \mathcal{L}_i^l(\alpha_i) & \text{if } \alpha_i \geq (-2G_i - 1)A \\ \mathcal{L}_i^l[A \cdot \min(1, -2G_i - 1)] + l_0 \cdot [(-2G_i - 1)A - \alpha_i] & \text{if } \alpha_i < (-2G_i - 1)A \end{cases}$$

$$L_i^r(\alpha_i) = \begin{cases} \mathcal{L}_i^r(\alpha_i) & \text{if } \alpha_i \leq -(-2G_i - 1)A \\ \mathcal{L}_i^r[-A \cdot \min(1, -2G_i - 1)] + l_0 \cdot [(-2G_i - 1)A + \alpha_i] & \text{if } \alpha_i > -(-2G_i - 1)A \end{cases} \tag{2.15}$$

where $G_i < 0$ corresponds to the implementation of NDC (Figure 2.6).

Conceptually, this extension allows compliance to reduce the local body curvature rather than increase it. The governing equations Equation 2.11 and Equation 2.15 together form a complete definition of generalized compliance encompassing both PDC and NDC domains. In essence, PDC ($G > 0$) allows local curvature to increase, corresponding to the passive buckling behavior widely observed in limbless organisms. NDC ($G < 0$) instead allows curvature to decrease, leading to straightening under external forces. Although both are defined for completeness, the remainder of this thesis focuses primarily on PDC, as it better captures the adaptive and obstacle-accommodating behaviors seen in biological locomotion, except where NDC is explicitly tested for comparison.

CHAPTER 3
MECHANICAL INTELLIGENCE FACILITATES EMERGENT OPEN-LOOP LOCOMOTION IN COMPLEX TERRESTRIAL ENVIRONMENTS

3.1 Introduction

Locomotion through heterogeneous terrains often challenges traditional limbless robot control paradigms that rely heavily on sensing, feedback, and centralized computation. In this chapter, we demonstrate that mechanical intelligence (MI) alone can facilitate effective and adaptive locomotion without explicit environmental perception or closed-loop control. Using the mechanically intelligent limbless robot (MILR) introduced in Chapter 2, we show that an appropriate level of body compliance enables the robot to spontaneously exploit physical interactions with the environment for propulsion and obstacle negotiation. The results presented here reveal how passive body mechanics can simplify control architectures, allowing open-loop gaits to generate robust and adaptive behaviors across complex terrestrial settings.

To investigate the function of mechanical intelligence systematically, we prescribe a lateral undulation gait and vary the generalized compliance parameter G to modulate the robot's effective stiffness. Through a series of locomotion experiments conducted on substrates with different levels of heterogeneity, we quantify how compliance influences body kinematics, locomotor speed, and energy efficiency. We further examine whether the advantages associated with intermediate G values depend on specific gait parameters by conducting a parametric survey over wave amplitude and spatial frequency.

Together, these experiments establish a quantitative relationship between compliance and locomotor robustness. They demonstrate that appropriate mechanical design can replace complex control policies with passive dynamics that naturally adapt to environmental

variations. The findings presented in this chapter provide direct experimental evidence for MI as an emergent property arising from bilateral actuation, forming the foundation for subsequent chapters that extend this principle to diverse locomotion modes and environmental contexts.

This chapter is adapted from my previously published peer-reviewed work [89].

3.2 A biological model: Locomotion of *C. elegans* in obstacle terrains

To evaluate how mechanical intelligence may manifest in living systems and to establish biological relevance for the robot introduced in Chapter 2, we examined locomotion in the nematode *Caenorhabditis elegans*. Despite possessing only 302 neurons, *C. elegans* exhibits notable agility when navigating confined and irregular terrains such as the interior of rotten fruit, which makes it a useful model for studying undulatory locomotion in heterogeneous environments. Using microfluidic lattices with varying post densities as controlled model terrains, we quantified the worm's body kinematics and locomotor performance (detailed methods see [89]). As shown in Figure 3.1, principal component analysis of body curvature data shows that worm postures can be represented as near-sinusoidal traveling waves in a low-dimensional shape space (as introduced in Chapter 2), maintaining stable orbits even under perturbations. Locomotion speed tends to increase in moderately cluttered environments, suggesting that body-environment interactions may contribute positively to propulsion. These observations hint that passive mechanical effects could play an important role in how *C. elegans* maintains locomotor stability and effectiveness, motivating the development of a robophysical model to test this possibility directly.

Building on these biological observations, we next used the mechanically intelligent limbless robot (MILR) introduced in Chapter 2 as a robophysical model [113] of *C. elegans*. By scaling up the system and isolating body mechanics from neural control, we can directly test whether mechanical intelligence alone is sufficient to reproduce the locomotor patterns and performance trends observed in the worm. The MILR allows precise control of body

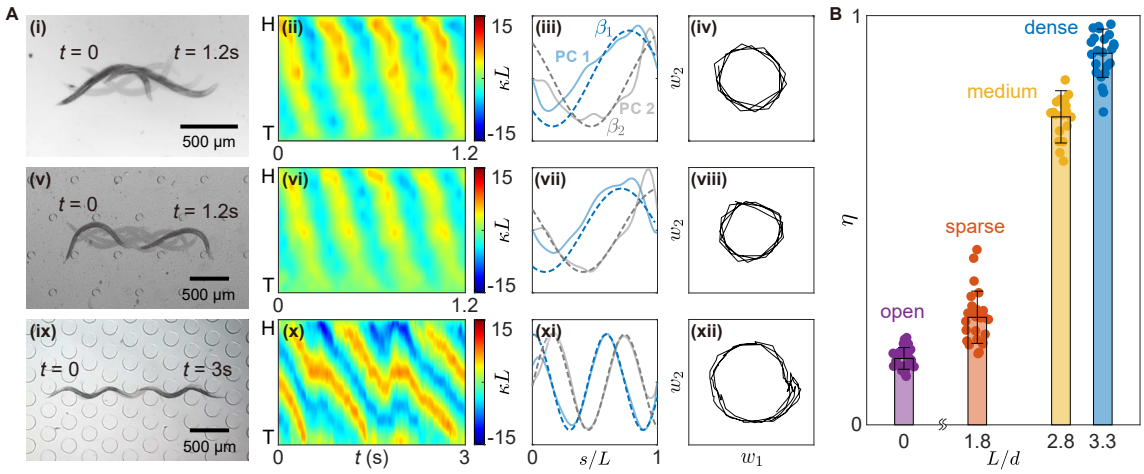

Figure 3.1: **Nematode kinematics and performance imply the role of mechanical intelligence.** (**A**) Overlaid snapshots, effective body curvature, gait paths in the shape space, the first two dominant modes (solid lines are the principal components and dashed lines are the best fits to $\sin$ and $\cos$ shape bases) of nematode locomotion in laboratory environments with varied pillar density. (**B**) Locomotion speed (wave efficiency η) as a function of obstacle density (measured as the ratio of body length and obstacle spacing L/d) for nematodes. Error bars represent SDs (n = 26 individuals in open and sparse lattices, n = 20 individuals in the medium lattice, and n = 24 individuals in the dense lattice). Figures are adapted from [89].

compliance and actuation symmetry, enabling systematic exploration of how passive body-environment interactions contribute to locomotion across varying terrain heterogeneities.

3.3 Spontaneous obstacle navigation with MILR

To test the role of mechanical intelligence in limbless locomotion and its effect on locomotor performance, we conducted robophysical experiments with MILR in four scaled-up environments (from open to dense) corresponding to the nematode study. Similar to the lattices for nematodes, pillars in the lattices for robophysical experiments cannot move and deform upon collision with the robot. In each environment, the robot was under open-loop control, executing a suggested traveling-wave gait as in Equation 2.1, with the shape parameters approximated directly from nematode kinematics in the corresponding environment so that the robot used the same gaits as nematodes did (more specifically, the ratio of the body wavelength and the lattice spacing was kept the same between the robot and

nematodes). We varied G to access the locomotion displayed by the robot in each environment. Quantifying locomotor performance (the wave efficiency η, the ratio of forward center of mass speed to backwards wave propagation speed) across the full range of G revealed that an appropriate G becomes necessary to facilitate open-loop traversal as heterogeneities arise (Figure 3.2B). In flat terrain, η was inversely correlated to G. However, when obstacles were introduced, low G (≤ 0.5) resulted in frequent jams and becoming irreversibly stuck. At high G (≥ 1.5), the model failed to generate sufficient self-propulsion. $G = 0.75$ emerges as an appropriate G value for locomotion in all heterogeneous environments, as local maxima of η display at $G \approx 0.75$. Further, η in the robot with $G = 0.75$ increased as the obstacle density increased, well approaching η that displayed in nematodes (Figure 3.2C).

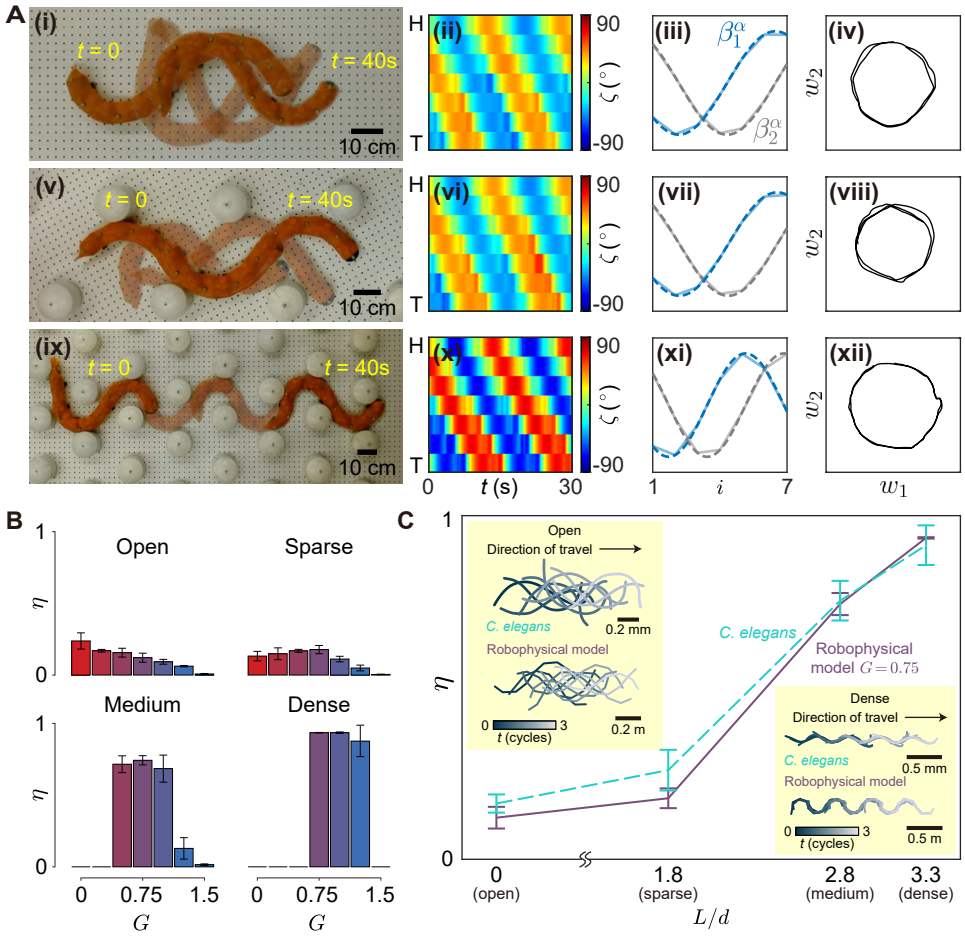

Figure 3.2: **Open-loop robot performance reveals the importance of mechanical intelligence.** (**A**) Overlaid snapshots, emergent joint angles, gait paths in the shape space and shape basis of robophysical locomotion ($G = 0.75$) in laboratory environments with varied obstacle density. (**B**) Locomotion speed (wave efficiency η) of the robot as a function of generalized compliance G in environments with varied obstacle density (open, sparse, medium and dense). Error bars represent SD across three repetitions per experiment. (**C**) Comparison of locomotion speed as a function of obstacle density between the biological model *C. elegans* and the robot with $G = 0.75$, accompanied with example time traces of splined points along the body as the nematode and the robot move in the open and dense environments (insets). Error bars represent the SD across three repetitions per experiment. Figures are adapted from [89].

To investigate the emergent robot body kinematics, we tracked emergent joint angles ζ of the robot, which are comparable to nematode emergent curvatures (detailed reasoning is provided Supplementary Methods). We then projected ζ onto the shape-basis functions $\beta^\alpha_{1,2}$ to extract the shape space gait path formed by $w_1(t)$ and $w_2(t)$ as we did for nema-

todes. For $G = 0.75$ in the robot, the body kinematics and gait orbits in the shape space (Figure 3.2A) closely resembled those observed in nematodes (Figure 3.1A). The model performed an approximate traveling wave motion in flat terrain and sparser lattices, which resulted in nearly circular orbits in the shape space. In the dense lattice, analogous to the nematodes, we also observed small deviations from ideal traveling wave shapes, which converged quickly back to the circular orbit. Thus, the robot can serve as an effective robophysical model of nematode locomotion, well capturing both overall performance and detailed body kinematics.

The emergent match between *C. elegans* and the robot kinematics and the enhancement of performance at $G = 0.75$ compared to other G values resulted completely from body compliance—simply by programmatically and anisotropically loosening the physical constraints on the joints in a way that mirrors the geometry of organismal patterns of activity, which allows joints to passively deform under external forces. Such a seemingly counter-intuitive result (improving performance via relaxing controls) verified our hypothesis that the appropriate level of mechanical intelligence (purely passively, mechanically controlled emergent body-environment interactions) can facilitate heterogeneity navigation, and is sufficient to reproduce organismal lattice traversal performance.

3.4 MILR force-deformation characterization

We used the force-deformation properties of MILR to identify how interactions with obstacles lead to deformations to the suggested traveling wave kinematics that enable successful lattice traversal. By characterizing the relation between the external force F and the emergent joint angle ζ at suggested angles α, we achieved maps of force-deformation properties of the robot with varied G values (Figure 3.3). For low G, external forces produced minimal deformation of the joint for all parts of the cycle (unless they are sufficiently high to break the cable) (Figure 3.3B-i, C-i). For high G, large deformations can be created in response to external forces in either direction (Figure 3.3B-iii, C-vii). However, at $G = 0.75$,

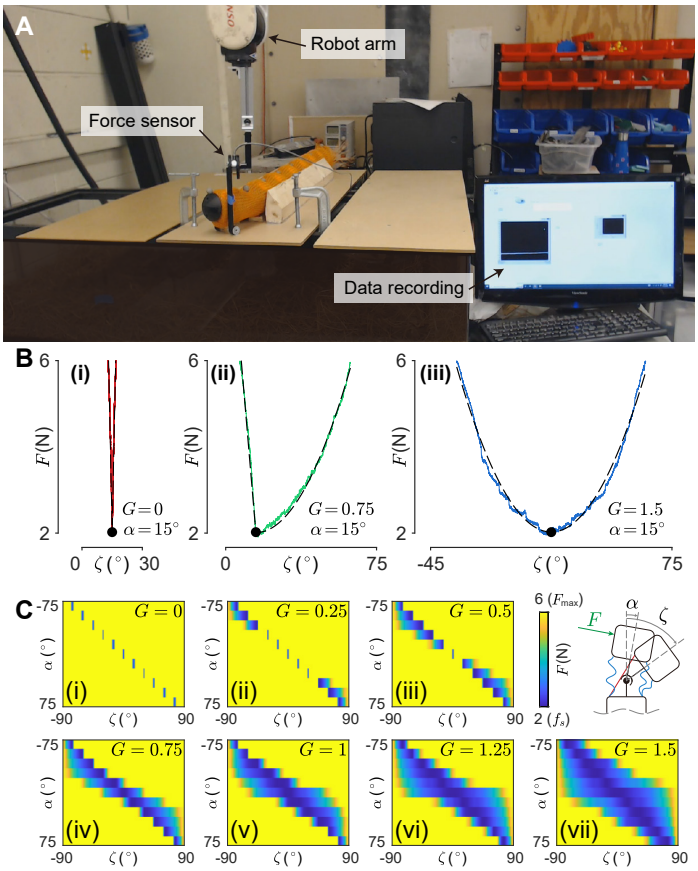

Figure 3.3: **Force-deformation characterization for the robot.** (**A**) The experiment setup. (**B**) External force versus emergent joint angle curves that show behaviors of a joint reacting to external forces under different compliance states. (**C**) Force-deformation maps of the robot with varied G that show the robot body compliance can be programmatically tuned. Figures are adapted from [89].

force-deformation responses displayed a hybrid state (Figure 3.3B-ii, C-iv): for small angles, force was admitted in both directions (bidirectionally compliant); for large angles, force was admitted in the direction of the bend but stiffly opposed in the opposite direction (directionally compliant).

We hypothesized that such hybrid compliance allows the selective exploitation of thrust-producing interactions through rigid responses and deformations that prevent jamming in detrimental interactions, such as head-on collisions. Our robot and many other limbless undulators move through space by passing body waves from head to tail with wave velocity v_{wave} anti-parallel to the center of mass velocity v_{CoM} (Figure 3.4A). External forces F_{ext}

from collisions that lie parallel to v_{wave} inhibit the center of mass motion, whereas collisions that produce forces parallel to v_{CoM} produce thrust. Figure 3.4B shows the deflection from the suggested angle in response to a point force ($\approx$ 3 N) parallel or anti-parallel to v_{CoM} for a range of suggested joint angles at $G = 0.75$. At small suggested joint angles ($|\alpha| < 0.5A$), the joint displays a bidirectional compliant state, in which deflection is permitted more symmetrically ($F_{\text{ext}} \parallel v_{\text{CoM}}$ and $F_{\text{ext}} \parallel v_{\text{wave}}$) to produce a similar magnitude of deformation. However, as the suggested angle increases ($|\alpha| > 0.5A$), the joint becomes directionally compliant, such asymmetry produces an "easy" high compliance axis and "hard" low compliance axis. The direction of the easy and hard axes depends on the shape of the organism. When the "easy axis" is aligned with inhibitory interactions and the "hard axis" with thrust producing interactions, organisms can resist buckling while maintaining forward progress. Figure 3.4C shows the orientation of the "easy"/high compliance direction (black triangles) and the "hard" low compliance (orange triangles) direction for 3 values of G (0, 0.75 and 1.5) and for the various joints along the body of an example 8-link undulator. Small arrows show point forces acting along the body either parallel to v_{CoM} or to v_{wave}. At $G = 0$, all joints are non-compliant, hence point forces produce either jamming interactions (small red arrows) or thrust (green red arrows). At $G = 0.75$ the distribution of easy and hard axes is arranged such that would-be jamming interactions are converted into body deformations which lead to deflection and therefore successful obstacle traversal, while still maintaining rigidity (non-compliance) in thrust-producing interactions. At $G = 1.5$ all interactions permit substantial deformations (all joints are highly bidirectionally compliant). Although jamming is avoided entirely, there is no ability to produce coherent thrust. Experimentally, the geometry of contacts closely follows the curvature profile of the gait (Figure 3.5). Would-be jamming interactions, for example near the head, often lead to longer durations of contact, governed by the dynamics of the deformation under locally compliant joints, whereas thrust-producing interactions at higher curvature near the mid-body typically follow regular contact patterns with shorter duration contacts, matching

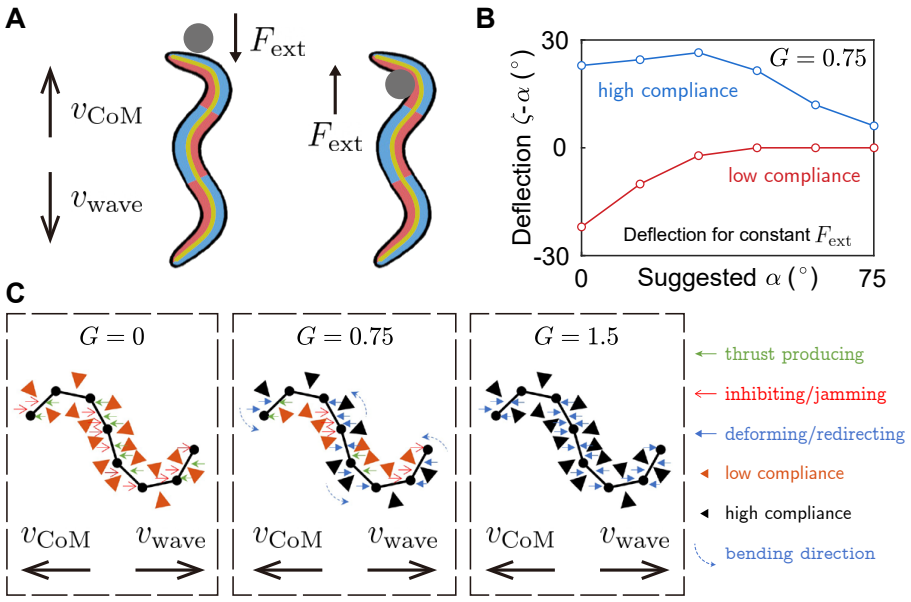

Figure 3.4: **A simplified model to understand the functional mechanism of mechanical intelligence.** (**A**) Schematic illustration of an undulator facing inhibitory interactions (left) and thrust producing interactions (right). (**B**) Deflection angle in response to a point force F_{ext} either parallel or anti-parallel to v_{CoM} at $G = 0.75$ for different commanded angles, showing the response of the "easy" or high compliance direction and the "hard" low compliance direction. (**C**) The geometry of easy (black triangles) and hard directions (orange triangles) for a single posture across three representative values of G. Small arrows show point forces that are thrust producing (green arrows), are jamming (red arrows), or result in deformation of the undulator from the commanded shape (blue arrows), with bend directions indicated by the dashed blue lines. Figures are adapted from [89].

the propagation of curvature along the body.

This simplified model (Figure 3.4) revealed that for certain, intermediate values, of G, the robot spontaneously converted inhibitory interactions into soft deflections while maintaining rigidity and thrust production in advantageous collisions without any explicit computation. The coordinated shortening and lengthening of the cables served therefore not only to realize an approximate traveling wave body shape sequence, but also to dynamically modulate the compliance properties of the robot to buffer the motion to external collisions.

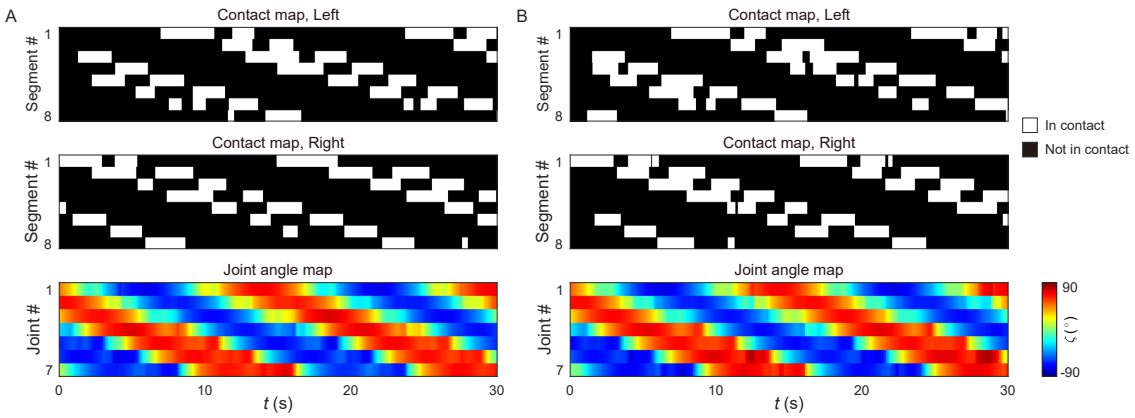

Figure 3.5: **Lattice collisions match the symmetry of the gait.** Contact maps and curvature map for a wheeled (**A**) and wheelless (**B**) robot, both with $G = 0.75$. Contact maps of collisions of the robot and lattice points on the left (top row) and right (middle row) side of the body show at what body point and at what times contact with the lattice occurs (contact shown in white, absence of contact in black). These contact patterns show similar patterns to the gait, as visualized in a curvature map (bottom row) with collisions on the left-hand side of the robot corresponding with regions of positive curvature and right-hand side collisions with negative curvature. Wheeled and wheelless robots show qualitatively similar contact patterns, highlighting the dominance of lattice collisions in producing thrust (relative to ground contact) in dense lattices. Note that the head often shows longer durations of contact relative to the rest of the body, a result of the dynamics of buckling and gliding collisions. Figures are adapted from [89].

3.5 Robot performance in diverse laboratory complex environments

Limbless organisms not only perform well in heterogeneous, collision-dominated environments. They also encounter a diverse array of substrates, including Newtonian fluids of varying viscosity and other flowable substances with complex, non-Newtonian rheologies. Hence, body compliance that enables lattice traversal, may also improve performance in less structured environments or, at a minimum not disrupt performance. We, therefore, hypothesized that MILR can also display good performance without major changes in control in a diversity of terrain with properties similar to those encountered during search and rescue and other applications. Indeed, we found that beyond functioning as a model for discovering and understanding emergent principles in limbless locomotion that cannot be directly tested with organisms, the bilaterally actuated limbless robot displayed substantial

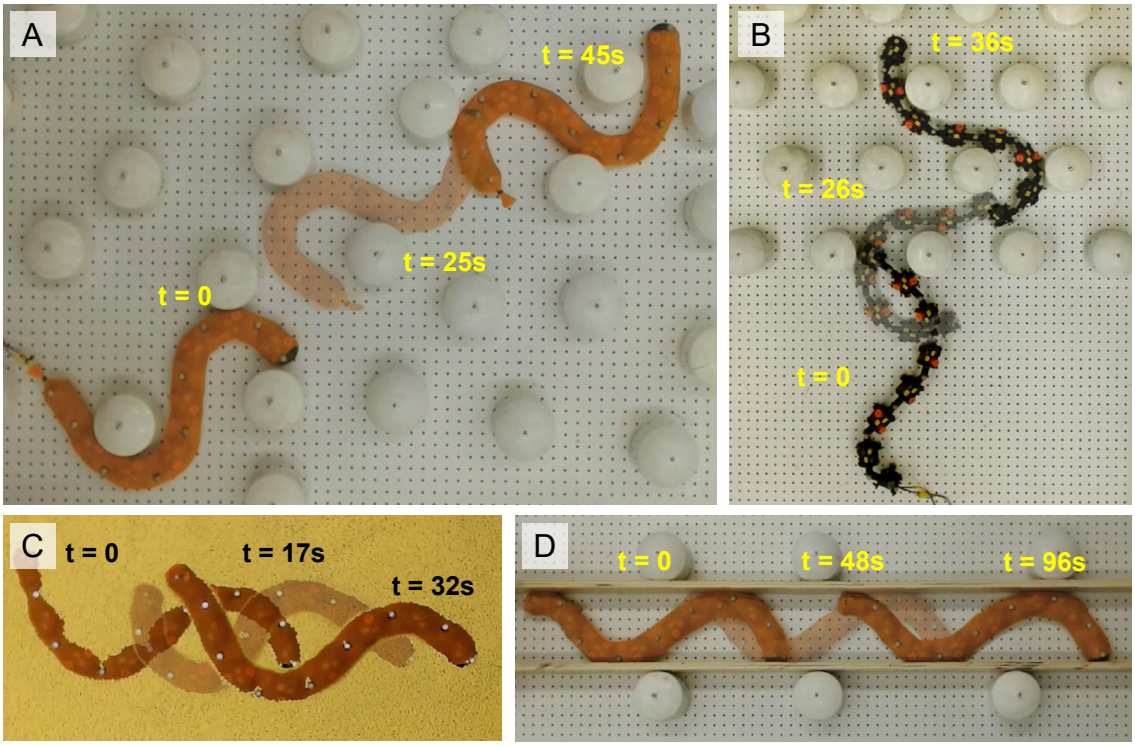

Figure 3.6: **Open-loop robotic terrestrial capabilities in various types of complex environments facilitated by mechanical intelligence.** (**A**) The robot traverses a randomly distributed obstacle array. (**B**) The robot transitions from flat ground to a densely distributed obstacle array. (**C**) The robot locomotes in granular media (5 mm plastic spheres). (**D**) The robot moves in a narrow channel (18 cm width) formed with two parallel rigid walls. Figures are adapted from [89].

terrestrial mobility in diverse, complex, and more challenging environments.

We tested the robot in a range of laboratory environments (Figure 3.6). Beyond regular lattices, the robot demonstrated effective traversal in randomly distributed obstacle terrains (Figure 3.6A) and agile transitions from open terrain to obstacle terrain (Figure 3.6B), where the robot was under open-loop controls with $G = 0.75$. Without the need for active adaptation of body shapes [76, 114, 37] or selection of paths [78, 115, 116] based on the awareness of internal states (such as instantaneous joint angles or torques) or knowledge of the surrounding environment (for example, via contact sensing or visual feedback) as proposed in previous works, the mechanical intelligence in this robot enables compliant body-environment interactions, facilitating the spontaneous locomotion. Further, we

conduct tests of locomotion speeds and cost of transport in other types of environment.

Evaluation metrics and methods

In addition to the wave efficiency η (which is the ratio of the center of mass velocity to the wave propagation velocity) that we used to describe the robot's locomotion speed, we also calculated the mechanical cost of transport c_{mt}. This dimensionless quantity, widely used in the study of legged animals and robots [117, 118, 119, 120], gives the work required to move a unit body weight a unit distance and allows us to analyze the robot's locomotion efficiency in a more comprehensive manner.

To calculate the mechanical cost of transport, we used the formula $c_{\text{mt}} = W/mgd$, where W is the work done by cables, mg is the robot's weight, and d is the distance traveled. We estimated the tension T exerted by each cable using the torque sensor embedded in the servo motor (ROBOTIS 2XL430-W250-T). During an experiment, we recorded the torque readings τ from the motor with a time interval of $\Delta t = 10$ ms. To obtain the nominal torque readings τ_0, which represent the "metabolic" torques required to enable the shaft to rotate without moving the robot, we ran a calibration experiment with the same motor running the same trajectory without tying the cable to the pulley. We then estimated the tension at each time step using the formula $T = (\tau - \tau_0)/R_{\text{pulley}}$, where R_{pulley} is the radius of the pulley. To estimate the distance traveled Δl, we measured the rotation angle difference $\Delta\zeta$ of the servo motor via its internal encoder within the time interval Δt times R_{pulley}. By summing up the products of the tension and distance for each time step, we calculated the work done by one cable during an experiment. We then summed up the work done by all cables to obtain the total work done by cables. The traveled distance d was measured using tracking data by summing up the distance traveled by the robot's center of geometry during each time interval.

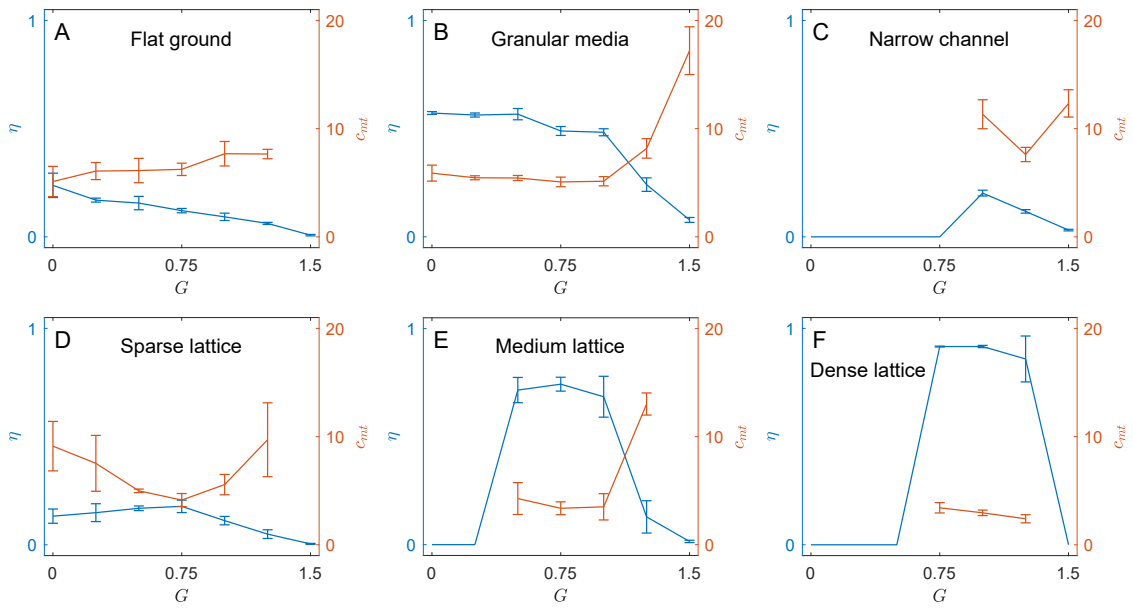

Figure 3.7: **Robot locomotion speed (wave efficiency, η) and mechanical cost of transport (c_{mt}) in different environments**: (**A**) flat ground, (**B**) granular material (5 mm plastic spheres), (**C**) a narrow channel (18 cm width), (**D**) a sparse lattice, (**E**) a medium lattice, and (**F**) a dense lattice. Error bars represent standard deviations across three repetitive trials of each experiment. Figures are adapted from [89].

Flat ground

Figure 3.7A shows the robot's wave efficiency η and mechanical cost of transport c_{mt} on a wood-surface flat ground, where the robot was equipped with wheels to generate a $\sim$1.6:1 drag anisotropy and move forward with retrograde wave propagation along the body. Gait parameters were fixed as $A = 46^{\circ}$ and $\xi = 0.82$ as discussed in Materials and Methods. As the generalized compliance G increases, we observed a nearly proportional decrease in η and increase in c_{mt}. We omitted data points where $c_{\mathrm{mt}} > 20$ in all the plots. The robot's performance on the flat ground serves as a benchmark for comparison with other environments that we tested.

Granular media

As demonstrated in previous work, a limbless robot can generate forward thrust in granular media with retrograde wave [121, 122], thus the robot was not equipped with wheels for tests in granular media. The experiments were conducted in a pool of plastic spheres with a diameter of 5 mm, which could not enter the motor and potentially damage the robot. Gait parameters were fixed as $A = 60^\circ$ and $\xi = 1$. At the range of $0 \leq G \leq 1$, η shares a similar decreasing trend as on the flat ground (Figure 3.7B). Surprisingly, we observed a more dramatic decrease in the work done by cables, yielding a decreasing c_{mt} with a local minima at $G = 0.75$. From this result we posit that, with lower body compliance, much of the active work done by the robot cannot effectively transfer into thrusting forces in such environments, and is wasted instead. By increasing the body compliance to let the robot "flow" with the environment (react to it), we reduce energy consumption without sacrificing locomotion speed. However, when G is too high, the locomotion speed drops notably, leading to an increase in c_{mt}. Such a result suggests that by leveraging the mechanical intelligence in locomotion, the robot has the potential to move efficiently within granular media.

Channel

Channels were set up to function as models for pipes and other environments where body shapes of the robot in lateral direction are highly constrained. Previous work has modeled and demonstrated that a limbless robot can gain thrust forces purely from its interactions with walls without the need of wheels for creating drag anisotropy [104]. Differing from nematodes using retrograde waves to move in channels [123, 124] where we posit their thrusts primarily result from the drag anisotropy of the fluid interactions, the robot with isotropic friction needs to use direct waves to produce forward motion, solely through forces experienced on the wall. In our experiments, the robot was not equipped with wheels and we commanded the robot with a direct wave (change "$-$" into "$+$" in Equation 2.11) with

parameters $A = 60^\circ$ and $\xi = 1$. Specifically, the width of the robot body while employing this gait was measured as 23 cm. To make the channel a challenging environment, we set the width of the channel as 18 cm such that the robot need to "squeeze" its body to adapt to it, which is usually the case in applications such as pipe inspection. As a result (Figure 3.7C), our robot cannot fit into the environment until $G = 1$. When $G \geq 1$, the robot generated effective forward locomotion in the channel and the local minima of c_{mt} emerged at $G = 1.25$. This result suggests that the generalized compliance G enables spontaneous shape adaptation to the channel without the need of probing channel width in advance, and reduced c_{mt} meanwhile. Notably, this conclusion holds true even for a wheeled limbless robot employing a retrograde wave with drag anisotropy.

Lattice

We evaluated c_{mt} for all lattices with different densities (Figure 3.7D to E). The robot was in the same condition as in experiments on the flat ground (with wheels), and executing open-loop gaits with fixed parameters obtained from direct fitting from nematode kinematics in biological experiments, $A = 48^\circ, 51^\circ, 72^\circ$ and $\xi = 0.80, 0.58, 1.02$ in sparse, medium and dense lattices, respectively.

Firstly, the obstacles in the sparse lattice impede locomotion of the robot with low G, resulting in reduced η compared to that on the flat ground. However, with an increasing G, the more compliant robot emerged to utilized the obstacles to generate thrust by pushing off of them, leading to an improved η, known as obstacle-aided locomotion. The local minimum of c_{mt} emerged at $G = 0.75$, where we observed both increased locomotion speed and decreased energy consumption compared to lower G values.

In the medium lattice, the robot started to become "stuck" on obstacles, where the robot cannot traverse the lattice with the commanded gait while the body was relatively rigid ($G = 0$ and 0.25). However, under the same open-loop control for the basic pattern of head-to-tail wave propagation, locomotion emerged when the body was more compliant,

where η and c_{mt} also reached their maximum and minimum in the range of $0.5 \leq G \leq 1$. When the body is too compliant ($G > 1$), the robot cannot generate sufficient thrust, leading to a dramatic drop in η and increase c_{mt}.

In our experiments, we observed a similar result in the dense lattice, where only intermediate values of G led to effective and efficient locomotion. Interestingly, we also noted a slight shift in the effective range of G from $0.5 \leq G \leq 1$ (medium lattice) to $0.75 \leq G \leq 1.25$ (dense lattice). We posit that, with lower G values, the robot is better able to generate thrust by utilizing drag anisotropy, but may struggle with adapting to the environment. On the other hand, with higher G values, the robot is more compliant to the environment, but may have reduced capabilities for generating thrust (as also demonstrated by the flat ground data). As the obstacle density increases from medium to dense lattice, the constraints on body shapes become stronger, requiring the robot to be more compliant. On the other hand, in such environments, the contact forces between the robot body and the obstacles play a more dominant role in the robot's forward motion, surpassing the contribution of drag anisotropy (as evident from the robot's ability to move in the dense lattice without wheels). Therefore, higher values of G are preferred in denser lattices, which explains the slight shift in the effective range of G from the medium lattice to the dense lattice.

Further discussion

In summary, our findings indicate that in highly constrained environments where interactions between the robot body and the environment play a dominant role in locomotion, an intermediate range of generalized compliance ($0.75 \leq G \leq 1.25$) enables the robot to be compliant enough to adapt to the environment, while minimizing the work required to maintain the wave propagation pattern. This results in local minima of c_{mt}, indicating an optimal balance between compliance and wave propagation efficiency. This insight sheds light on the importance of generalized compliance in enabling effective locomotion in chal-

lenging environments such as non-movable obstacles in medium/dense lattices and channels, where the robot needs to adapt its body shape to the environment while minimizing energy expenditure.

3.6 Robot performance in natural complex environments

To determine the potential benefits of mechanical intelligence in practical limbless robot applications and the generalizability of principles derived from two-dimensional laboratory environments to complex three-dimensional natural environments, we conducted open-loop locomotion experiments in a mechanically complex environment. Specifically, we tested the robot's performance in a randomly distributed and tightly packed pile of rocks (Figure 3.8), simulating the terradynamic challenges that a limbless robot may face during search-and-rescue or planetary exploration tasks. Our quantitative analysis of robot locomotion performance demonstrated that, with an appropriate amount of generalized compliance ($G = 0.75$), mechanical intelligence facilitates effective negotiation with irregularities, ensuring successful locomotion. Conversely, inadequate compliance ($G = 0$) hindered obstacle traversal, whereas excessive compliance ($G = 1.5$) resulted in insufficient thrust generation. Notably, the cost of transport exhibited local minima at intermediate values of G, consistent with our findings from laboratory tests.

Overall, laboratory and outdoor tests demonstrated that intermediate values of G enable effective locomotion in the largest range of environments and provide reduced costs of transport. This suggests mechanical intelligence not only facilitates obstacle negotiation, but also can improve locomotion speed and efficiency.

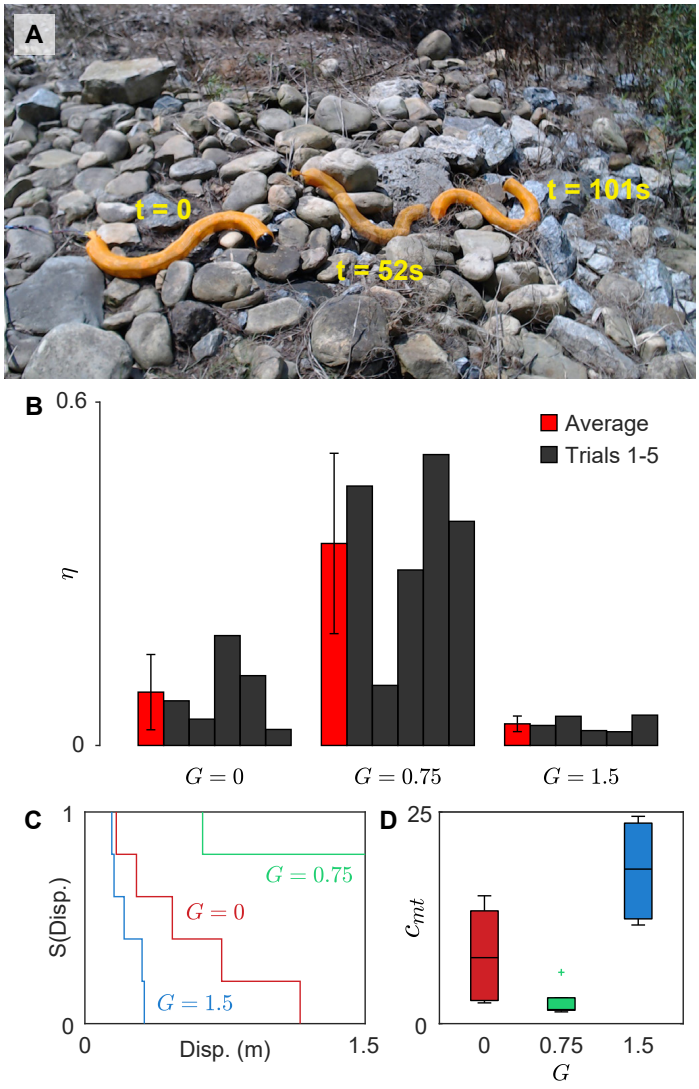

Figure 3.8: **Open-loop robot capabilities in real-world complex environments.** (**A**) Time-lapse photos of the open-loop robot traversing over a tightly packed rock pile with an intermediate generalized compliance value ($G = 0.75$). (**B**) Comparison of locomotion speed (wave efficiency η) with varied G on the rock pile. Error bars represent SDs. (**C**) The survivor function for varied G with respect to displacement, measuring the robot's traveling distance before getting stuck or failing in motors. (**D**) Mechanical cost of transport (c_{mt}) for varied G on the rock pile, measuring the robot's energy efficiency of locomotion. Box central mark indicates the median, edges indicate the 25-th and 75-th percentiles. The whiskers cover data points within a range of 1.5 times the interquartile range, whereas outliers outside of this range are marked with a + symbol. Figures are adapted from [89].

3.7 Robustness of locomotor performance across gait parameters

The previous sections focus on locomotion using a suggested gait that is approximated from *C. elegans* [89]. Although this provides a biologically grounded reference, the observed benefits of intermediate G values could, in principle, depend on the specific gait choice. To examine whether the improvement in performance arises from a special case or reflects a more general effect of mechanical intelligence, we systematically sweep gait parameters including body wave amplitude A and spatial frequency ξ across the patterned lattice environment while varying G. This survey evaluates how programmable compliance influences locomotor robustness over a wide range of preselected gaits.

For each combination of $A \in [55°, 85°]$, $\xi \in [0.4, 1.6]$, and $G \in [0, 1.5]$, we measure two key performance metrics: the average forward speed normalized by body length per cycle and the mechanical cost of transport (c_{mt}). If the robot fails to progress, its speed is recorded as zero and c_{mt} is treated as infinite. To compute an effective average c_{mt} across all gaits, we use a four-step process: first, we calculate c_{mt} for each individual trial; second, we take the inverse of each value ($1/c_{\text{mt}} = 0$ for failed trials); third, we average these inverse values across all tested gaits; and finally, we take the inverse of the averaged inverse to obtain the group mean. Figure 3.9A summarizes the averaged speed and c_{mt} across all gaits for each G value. Locomotion speed reaches its maximum at $G = 1$, while c_{mt} is minimized (corresponding to the highest energetic efficiency) at $G = 1$ and $G = 1.25$. Figure 3.9B presents the detailed c_{mt} distributions across gait parameters for $G = 0$ and $G = 1$, showing that the introduction of compliance substantially enlarges the region of low-cost, high-performance gaits.

Together, these results indicate that intermediate levels of mechanical compliance not only enhance locomotion efficiency but also reduce sensitivity to precise gait tuning. In heterogeneous or disordered environments, where terrain structures cannot be pre-characterized to determine an optimal gait, an appropriate level of G allows the robot to maintain effective

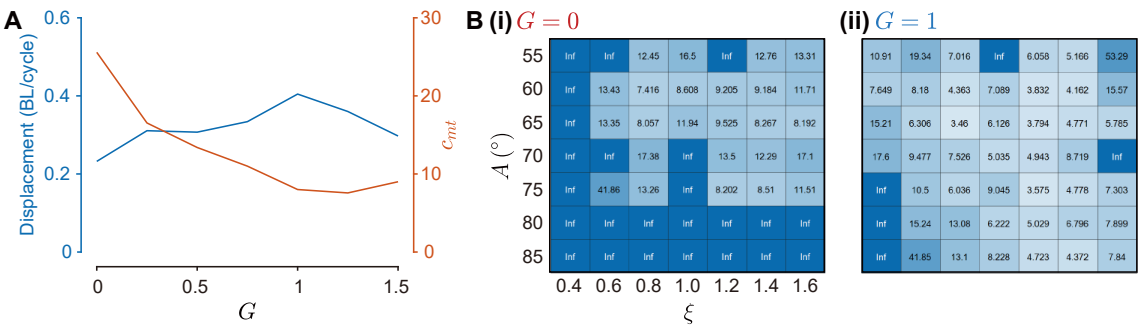

Figure 3.9: **Robustness of locomotor performance across gait parameters.** (**A**) Averaged speed and mechanical cost of transport (c_{mt}) across all combinations of amplitude A, spatial frequency ξ, and compliance G. Speed peaks at $G = 1$, while c_{mt} is minimized at $G = 1$ and $G = 1.25$. (**B**) Heatmaps of c_{mt} as functions of A and ξ for $G = 0$ and $G = 1$, illustrating that compliance expands the region of low-cost, high-performance gaits. These results demonstrate that appropriate mechanical compliance can enhance locomotion efficiency and robustness across diverse gait parameters.

movement even when commanded with suboptimal open-loop parameters.

3.8 Discussion

In summary, our integrative and comparative study of biological and robophysical limbless locomotors reveals that mechanical intelligence, the general collection of emergent adaptive behaviors that arise from passive body-environment interactions, simplifies control in terrestrial limbless locomotion, especially in heterogeneous environments, and is sufficient to reproduce organismal lattice traversal performance. The robot, once programmed with an appropriate level of compliance, not only accurately models undulatory organisms in terms of locomotor performance and body kinematics, but also in terms of dynamic force-deformation relationships (similar force-deformation relationships have been established for vertebrate undulators [125]). Dynamic force-deformation relationships are non-trivial for an organism of the scale of *C. elegans* (only passive viscoelastic properties have been determined for *C. elegans* [126]). Thus, our robot is a useful tool for understanding the functional mechanism of mechanical intelligence in the organism—by identifying and understanding the mechanically intelligent control regimes of the robot that accurately repro-

duce *C. elegans* kinematics in lattices, we can generate hypotheses about what underlying physiological and anatomical details are required to produce the emergent effective locomotion. Broadly, model organisms like *C. elegans* have an important role to play in connecting neural dynamics to behavior. Our results suggest that mechanics also play a substantial role in shaping behavior via processes that occur outside the nervous system, and therefore must be understood and accounted for to reach a comprehensive understanding of animal behavior in general.

Robotic limbless locomotion in confined environments presents challenges in generating adequate thrust and preventing jamming caused by obstacles. Prior research has confronted this challenge through gait design and online parameter turning approaches [13, 71, 76, 104]. Essentially, if provided with sufficient foreknowledge of the environment or precise real-time proprioceptive sensory feedback (such as visual or internal body forces), it is possible that an "optimal" gait template can be carefully designed, or "optimal" parameters within a template can be tuned online so that even a non-compliant robot can move effectively. In the case of lattices, optimal gaits will have wavelengths, amplitudes and phasing that allow geometric conformity to the lattice (in other words, the wavelength and lateral displacement, determined by the amplitude, will be an integer multiple of the lattice spacing). However, developing and implementing such controllers and sensing modalities requires considerable effort and computational resources. Our approach of exploiting mechanical intelligence can replace these complicated processes, enabling the robot to move in complex environments with open-loop controls, utilizing a simple traveling wave template with low sensitivity to the chosen wave parameters (so that slightly mismatched parameters do not fail to produce locomotion because of mechanical modulation of commanded shapes). Further, we verified in laboratory and natural complex environments that mechanical intelligence (in the form of the appropriate compliant actuation scheme) can even improve locomotion speed and efficiency. For nematodes, who rely on mechanical and chemical cues to navigate, gait selection based on foreknowledge of the environment is

not possible; hence the mechanical control scheme is likely important in traversing dense terrain. Even in organisms with vision, like snakes, the speed of locomotion often makes gait planning ineffective, and passive mechanisms again become substantial [4]. Moreover, our results hint at mechanisms that govern the trade-off between active neural controls and passive body mechanics in nematodes. Our comparative exploration of mechanical intelligence could potentially offer a perspective that complements existing approaches to the question of the general role of neural versus mechanical control [127, 128, 129, 130, 131].

Further, our demonstration of the advantages arising from our implementation of mechanical intelligence through the bilateral actuation mechanism presents several promising research avenues. As we observed in experiments that the performance of the robot operating at a certain G value can vary in different environments, we posit that developing a full mechanistic model of the dynamics of the system in various environments could further help determine "optimal" G based on terrain properties. As G can be dynamically tuned, we posit that adding sensory capabilities could enable the robot to learn or select the "optimal" G value in real-time that accommodate best with the current environment. As each joint is controlled in a decentralized manner, we posit that locally varying G based on local sensing feedback would enable the system to maximize the utility of surrounding environment to generate thrust and thus to locomote more effectively.

Finally, to conclude Part I, the bilateral actuation scheme suggests a design and control paradigm for limbless robots. Contrasting the lack of mechanical intelligence in limbless robots to date, the bilateral actuation mechanism offloads complex sensorimotor controls for handling body-environment interactions to mechanical intelligence, improving locomotion efficiency and freeing up onboard hardware and computational bandwidth for advanced sensing and motion planning techniques [71, 78, 103, 106, 59, 132, 19, 133, 134, 135]. This represents a paradigm shift in limbless robotics that could pave the way for the future development of more agile, intelligent and capable limbless robots that fulfill their promised potential of maneuverability in extremely complex environments, finding diverse

applications such as search and rescue, industrial inspection, agricultural management, and planetary exploration.

CHAPTER 4
SIDEWINDING MILR: COMPLIANT SIDEWINDING LOCOMOTION ON COMPLEX SUBSTRATES

4.1 Introduction

Sidewinding represents a distinct mode of limbless locomotion characterized by coordinated vertical and lateral body undulations (Figure 4.1) that generate alternating regions of body contact and lift, enabling robust motion even under isotropic friction conditions [136, 137, 138, 38, 40]. This gait, frequently observed in desert-dwelling vipers and other species that traverse deformable substrates [21, 139], provides an effective strategy for maintaining traction and stability across complex terrains. For limbless robots, replicating sidewinding offers a pathway toward efficient and versatile 3D locomotion [140, 141, 142, 143]. However, while sidewinding gaits have been successfully implemented on homogeneous surfaces, navigating heterogeneous environments with obstacles or rheological variability remains a major challenge [144].

In biological sidewinders, compliant body deformations are often observed during obstacle negotiation [144], suggesting that compliance facilitates passive shape adaptation and reduces the need for explicit sensing or feedback control. Inspired by this observation, we hypothesize that MI, embodied in the robot's physical compliance, can enhance robotic sidewinding by offloading control demands to passive body-environment interactions. Building upon the bilateral cable-driven architecture introduced in Chapter 2 and the generalized compliance framework developed in Chapter 3, we designed a 3D cable-driven limbless robot capable of programmable, anisotropic body compliance for sidewinding. By embedding compliance directly into the robot's mechanical design, this system extends MI principles into non-planar locomotion, enabling adaptive contact modulation without

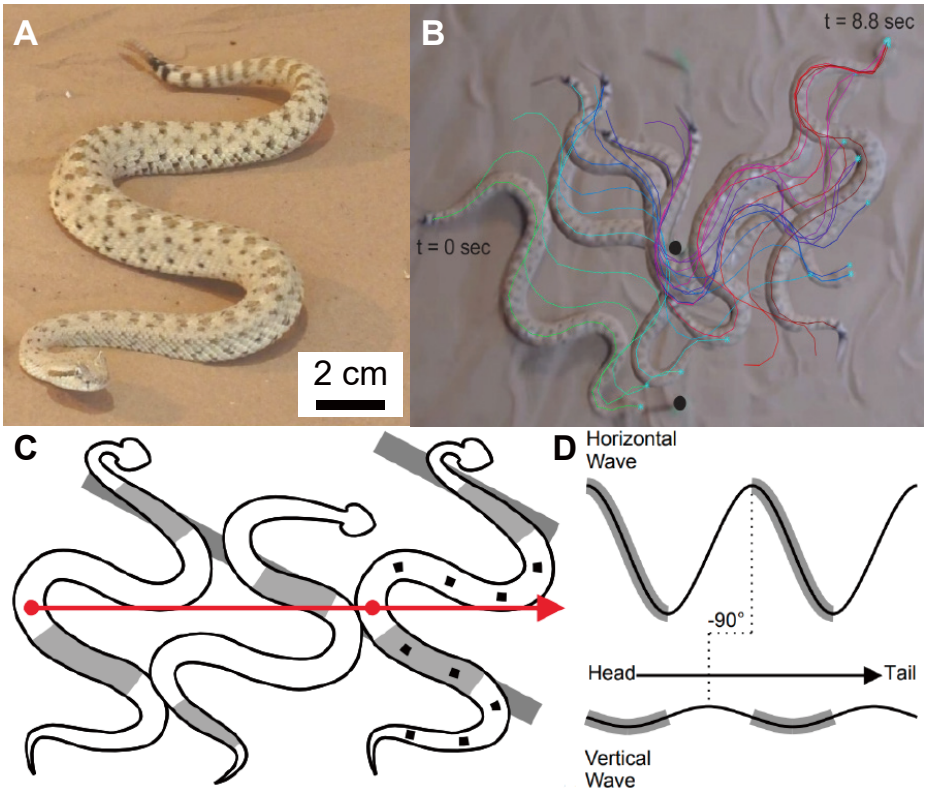

Figure 4.1: **Sidewinding snakes capable of performing sidewinding locomotion in diverse, rheologically complex terrestrial environments.** (**A**) The sidewinding behavior observed in rattlesnakes. (**B**) Sequential images showing a snake sidewinding through a row of posts. (**C**) A diagram of sidewinding motion. Gray areas in the body indicate static contact with the substrate, and white areas represent body segments lifted and in motion. Gray rectangles denote tracks. The red arrow shows the center of mass direction of motion. (**D**) A diagram of the vertical and horizontal waves propagating from head to tail in sidewinding, characterized by a $\pi/2$ phase difference. Grey areas denote static contact. Figures are adapted from [144, 100].

feedback control.

This chapter is adapted from my previously published peer-reviewed work [100].

4.2 Robot design and control

Building on MILR introduced in Chapter 2, the sidewinding variant (Figure 4.2) extends the same bilateral cable-driven architecture into three dimensions to enable coordinated horizontal and vertical bending. The robot consists of a series of 12 modules connected by 11 passive hinge joints (total length 1.31 m). There are two types of joints on the robot: ver-

tical bending joints and lateral bending joints, each with one rotational degree of freedom rotation in their respective planes. The combination of these two bending joints allows the robot to simultaneously propagate waves in the horizontal and vertical planes—necessary to produce a sidewinding gait. The vertical and lateral joints are evenly spaced along the body, where joints 3, 6, and 9 are vertical bending with the remaining 8 being lateral bending (Figure 4.2A). The higher number of lateral bending joints allows us to achieve much higher curvature in the horizontal plane compared to the vertical plane, similar to what has been observed in sidewinding rattlesnakes [145]. This gives this robot an advantage in replicating the snake's gaits compared to previous sidewinding limbless robots that use alternating vertical and lateral bending modules [146, 106].

Sidewinding MILR's modular design, bilateral cable actuation, and electronic architecture follow the design of MILR introduced in Chapter 2, with only minor adaptations for vertical bending joints. This design preserves the core mechanical intelligence mechanism (programmable body compliance via differential cable length control) while extending it to allow combined horizontal and vertical actuation required for sidewinding locomotion.

4.3 Sidewinding gait template for Sidewinding MILR

To implement a sidewinding gait on our robot, we implemented a two-wave template that is widely used in sidewinding robots [145, 146, 144],

$$\begin{aligned} \alpha_H(i,t) &= A_H \sin\left(2\pi\xi_H \frac{i}{N_H} - 2\pi\omega t\right), \\ \alpha_V(i,t) &= A_V \sin\left(2\pi\xi_V \frac{i}{N_V} - 2\pi\omega t - \frac{\pi}{2}\right), \end{aligned} \tag{4.1}$$

where subscripts H and V refer to horizontally and vertically oriented motors, respectively; α represents joint angle; i is joint index; t is time; A, ξ and ω is the amplitude, the spatial and temporal frequencies of the corresponding wave; and N is the total number of joints in the corresponding plane. Note that the horizontal and vertical waves are out of phase.

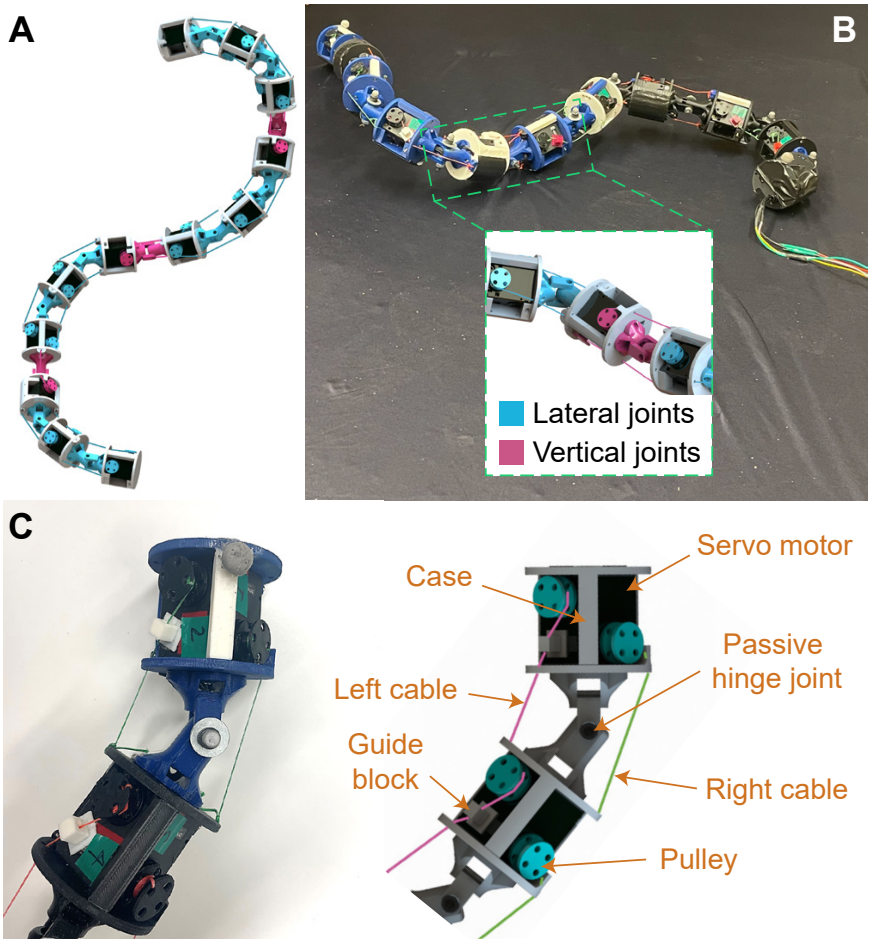

Figure 4.2: **Design of Sidewinding MILR, inspired by sidewinding snakes.** (**A**) Computer-aided design representation of the robot. The design features 8 lateral bending joints (cyan) and 3 vertical bending joints (pink) (**B**) Picture of the robot with zoomed-in view of 2 joints – one vertical bending and one lateral bending. (**C**) Picture and labeled schematic of a single robot module. Figures are adapted from [100].

To accurately form a joint angle α as defined in Equation 4.1, we need to adjust the lengths of the left and right cables around the joint so that they both are shortened following Equation 2.2 as in MILR.

Based on Equation 2.2, we can implement accurate body postures for sidewinding gaits on our robot. Bilateral actuation allows us to program body compliance via coordinately loosening cables. Extending the implementation of the generalized compliance variable (G) defined in Equation 2.11 to Sidewinding MILR, the cable length control scheme is

then given by:

$$
\begin{aligned}
L^l_{H,i}(\alpha_{H,i}) &= \begin{cases} \mathcal{L}^l_{H,i}(\alpha_{H,i}), & \text{if } \alpha_{H,i} \leq -\gamma \\ \mathcal{L}^l_{H,i}[-\min(A_H, \gamma)] & \\ \quad +l_0 \cdot [\gamma + \alpha_{H,i}], & \text{if } \alpha_{H,i} > -\gamma \end{cases} \\
L^r_{H,i}(\alpha_{H,i}) &= \begin{cases} \mathcal{L}^r_{H,i}(\alpha_{H,i}), & \text{if } \alpha_{H,i} \geq \gamma \\ \mathcal{L}^r_{H,i}[\min(A_H, \gamma)] & \\ \quad +l_0 \cdot [\gamma - \alpha_{H,i}], & \text{if } \alpha_{H,i} < \gamma \end{cases} \\
L^l_{V,i}(\alpha_{V,i}) &= \mathcal{L}^l_{V,i}(\alpha_{V,i}) \\
L^r_{V,i}(\alpha_{V,i}) &= \mathcal{L}^r_{V,i}(\alpha_{V,i})
\end{aligned}
\tag{4.2}
$$

where superscripts l and r refer to left and right, respectively; γ is short for $(2G-1)A_H$; and l_0 is a design parameter which we maintain the value we used in MILR, 0.73 mm/degree. Thus, each joint in Sidewinding MILR can achieve the same representative compliance states as in MILR (Figure 2.5).

4.4 Robust sidewinding on diverse terrains

Flat terrain

As suggested in previous work where body compliance can improve lateral undulation locomotion efficiency in diverse environments [89], we started with testing the robot's sidewinding performance on flat terrain with varied generalized compliance G. In this experiment, we fixed the parameters in Equation 4.1 as $A_H = 75°, \xi_H = 1, A_V = 25°, \xi_V = 1$, with which the robot's body shape can approximate that observed from rattlesnakes [145]. We quantify the performance using locomotion speed and mechanical cost of transport, the same metrics used in the previous chapter.

We set up an experiment shown in Figure 4.3 by running the sidewinding gait on the robot on a flat surface with Coulomb friction ($\mu \approx 0.7$). We varied the generalized com-

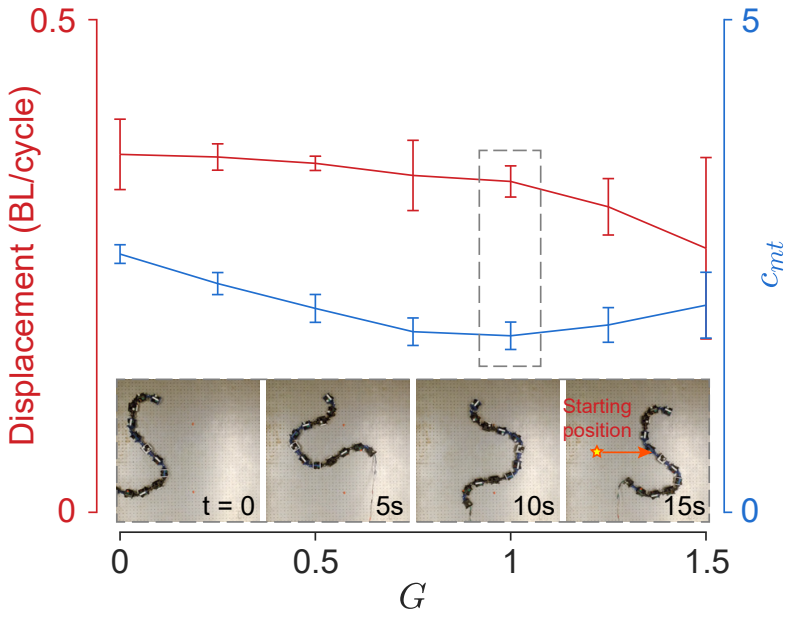

Figure 4.3: **Sidewinding locomotion speed (red) and mechanical cost of transport c_{mt} (blue) as a function of body compliance G.** Locomotion speed is measured by the averaged center of mass displacement normalized by the body length of the robot over a gait cycle. Mechanical cost of transport is a unit-less quantity calculated by the work done by cables divided by the product of the robot's weight and distance traveled. Error bars represent standard deviations. The inset shows a time lapse of the bilaterally compliant ($G = 1$) robot sidewinding on hard ground. Figures are adapted from [100].

pliance of the robot in the lateral bending joints, from $G = 0$ (fully rigid) to $G = 1.5$ (very compliant) with an increment of 0.25. We ran three trials for each G value and in each trial the robot sidewinds two gait cycles. We attached 13 markers evenly on the robot's body and recorded the robot's motion using OptiTrack motion tracking system. We then averaged each marker's displacement to calculate the robot's center of geometry displacement. To calculate mechanical cost of transport (c_{mt}), we used the equation $c_{\text{mt}} = W/mgd$, where W is the work done by cables which is estimated using the torque sensor reading from the servo motor, mg is the robot's weight, and d is the displacement.

We found that unlike in lateral undulation, when sidewinding in an open environment, having compliance in the body can decrease the mechanical cost of transport in open, hard-ground environments. While the fully rigid body results in a slightly higher displacement (0.48 m/cycle) compared to the $G = 1$ robot (0.4 m/cycle), the work done by the pulleys in

the $G = 1$ is less, resulting in a consistent decrease in the mechanical cost of transport as G increases. The value of $G = 1$ was the local minima of the cost of transport. After $G = 1$, the robot can no longer maintain the desired contact pattern for effective sidewinding, resulting in much lower displacements per body cycle (for $G = 1.5$, the robot only translates 0.351 m/cycle). This result gave us the basis for selecting what generalized compliance parameters to use in later experiments. Given that sidewinding efficiency tends to break down after $G = 1$, for the following experiments, we will be comparing three G values: 0, 0.5, and 1.

Obstacle terrain

To verify our hypothesis that mechanical intelligence induced by the body compliance can enhance obstacle navigation in sidewinding, we set up a model heterogeneous environment for the robot: a level pegboard base ($L = 2.4$ m, $W = 1.2$ m) with a row of obstacles (5 cm diameter PVC pipes) as depicted in Figure 4.4A. In this series of experiments, we fixed the parameters in Equation 4.1 as $A_H = 75^\circ, \xi_H = 1, A_V = 25^\circ, \xi_V = 1$. The parameters were selected so that the ratio of the wavelength displayed in robot and the obstacle spacing roughly matches with that observed from rattlesnakes ($\sim$0.8) [145]. Further, the robot is wrapped with a mesh skin to create a smoother contact surface between the robot and the environment.

A total of 15 sets of trials were conducted—5 different obstacle spacings (60, 65, 70, 75, and 80 cm) each with 3 different generalized compliance values ($G = 0, G = 0.5, G = 1$). These specific G values are chosen because they are representative of the three different states of compliance: no compliance, directional compliance, and bidirectional compliance. Given that the attack angle and initial condition of the body may affect the robot's ability to pass through the obstacles, we selected five different initial positions and orientations for each set of trials. For our experiments, the criterion for success was to have the entire body clear the line connecting centers of obstacles. If the robot does not clear the center line of

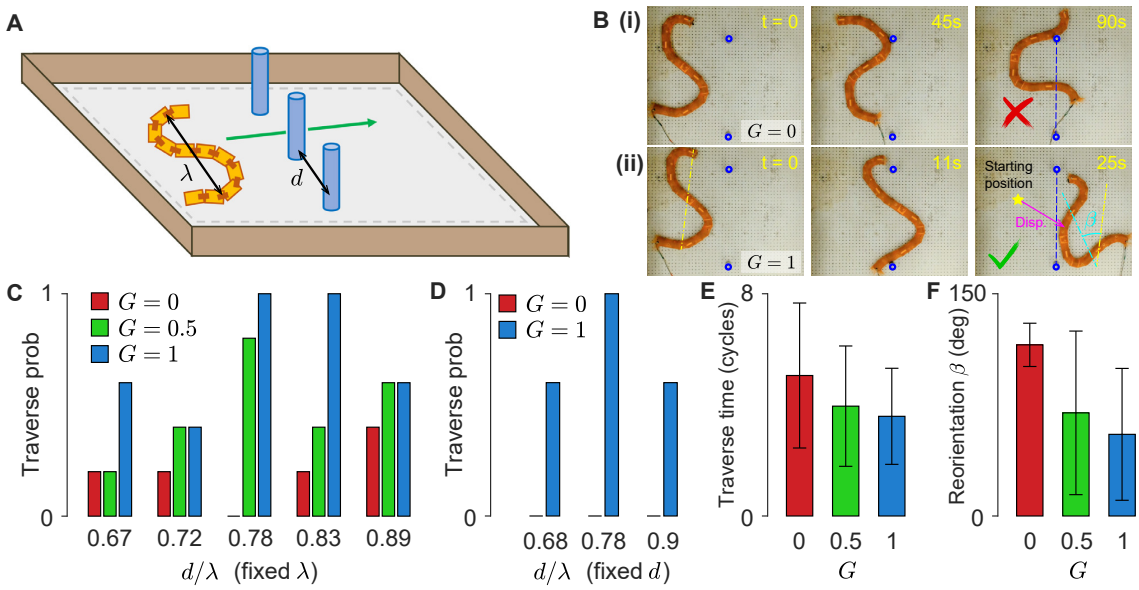

Figure 4.4: **Robot performance when sidewinding through an array of obstacles.** (**A**) Diagram of the experimental setup. Obstacle spacing d, robot initial condition, robot wavelength λ and the generalized compliance parameter G were varied for different experiments. (**B**) Time-lapse photos of (i) a failure ($G = 0$) and (ii) a success ($G = 1$). Success counts when the entire robot body passing the center line intersecting the obstacles. (**C**) The traverse (success) probability of the robot for different (G) values across different obstacle spacing (normalized by the robot's wavelength). (**D**) The traverse (success) probability of the robot for different (G) values with different robot wavelengths and fixed obstacle spacing of 70 cm (the axis is obstacle spacing normalized by the robot's wavelength). We tested three different gaits with $A_H = 82.5°, 75°, 67.5°$ and $\xi_H = 1.1, 1.0, 0.9$, respectively, which are noted by their corresponding wavelengths of the robot body shape $\lambda = 79, 91, 104$ cm. (**E**) The average traverse time (in number of cycles) to traverse through the obstacles for each successful trial, sorted by G value. (**F**) The average robot reorientation angle (in degrees) for each successful trial, sorted by G value. Figures are adapted from [100].

the obstacles after 10 gait cycles or if the robot became jammed between two obstacles, the experiment was classified as a failure. In every set of trials, the traverse probability represents the percentage of successful outcomes out of five initial positions.

Our experiment results indicate that, across different obstacle spacings, having a more compliant body led to a higher traverse probability Figure 4.4C. Moreover, the robot that has anisotropic bidirectional compliance outperforms others because it allows body joints to comply with the obstacles in different directions. We observed that in the bidirectionally compliant robot 1) the interactions with the obstacles led to less drastic deviations from the

robots initial trajectory, and 2) the body compliance allowed the robot to deform its body to squeeze through obstacles that are tighter than the robot's body length before deformation. The two primary failure modes that were observed with the non-compliant robot were: 1) the robot was not able to deform its body enough to squeeze between two obstacles or 2) because the robot cannot absorb the impact of obstacle collisions, it rapidly reorients its body into an undesirable position, causing it to jam. Both of the failure modes are mitigated by increased compliance. Figure 4.4F shows the average reorientation angle in successful trials for different G parameters of the robot. With $G = 0$, the average reorientation angle was 115.5 ± 14.6 degrees, with $G = 0.5$ it was 69.6 ± 55.2 degrees, and with $G = 1$ it was 55.1 ± 44.5 degrees. The average reorientation angle was lower for the more compliant robot because it locally deforms its bodies to mitigate harsh obstacle contacts that cause re-orientation. Further, across all trials, the robot with bilateral compliance ($G = 1$) had lower a average number of cycles to traverse (3.59 ± 1.73 cycles to traverse, in the success trials) compared to both the directionally compliant (3.96 ± 2.17 cycles to traverse, in successful trials) and the non-compliant robot (5.07 ± 2.61 cycles to traverse, in the success trials) as shown in Figure 4.4E. Overall, increased body compliance helps to prevent and mitigate reorientation due to obstacle interaction and decreases the number of cycles necessary for the robot to traverse through the obstacle array.

Note that while body compliance shows its advantages across experiments with varied obstacle spacings, by far the highest traverse probability for the robot was at 70 and 75 cm obstacle spacing, the same obstacle spacing ratio as what was observed in the biological experiments. We hypothesize that having compliance alone is not exclusively sufficient for obstacle-rich environments when sidewinding. Instead, choosing the "appropriate" gait parameters based on the heterogeneities present in the environment is also important. For the scope of this paper, appropriate gaits were chosen based on analyzing videos from [146, 145] and matching the wavelength to peg spacing ratio This gave a starting point for gait selection, but appropriate gait parameters alone cannot guarantee traversal, as the traverse

probability for the $G = 0$ trials consistently remained below 20%. Thus, our results indicate that in order to achieve effective locomotion within complex environments, a sidewinding robot needs the synergy of computational intelligence (to select appropriate parameters) and mechanical intelligence (for passive body mechanics and compliant body-environment interactions).

To further validate that the effect of body compliance is not exclusive to specific gait parameter choices, we varied the spatial frequency and amplitude of the horizontal wave and ran experiments at the 70 cm obstacle spacing. Without the loss of generality, we chose $A_H = 82.5^\circ, 75^\circ, 67.5^\circ$ and $\xi_H = 1.1, 1, 0.9$, respectively, while A_V and ξ_V remained unchanged. As in the previous tests, each experiment was repeated with 5 different initial conditions, and we compared the robot's performance with no compliance ($G = 0$) and with anisotropic bidirectional compliance ($G = 1$).

Remarkably, the bidirectionally compliant robot produced traverse probabilities larger than 60% for all parameter combinations as shown in Figure 4.4D. While for all three gait parameter combinations, the non-compliant robot failed to get through in every trial. This result suggests that with an appropriate level of body compliance G, robot performance can remain robust for an increased range of parameters. Even without an "optimal" choice in gait parameters for a particular environment, body compliance can help facilitate effective locomotion.

Natural terrain

Lastly, we conducted a series of open-loop outdoor experiments to examine the potential applications of sidewinding with anisotropic bidirectional compliance in complex natural terrains. We tested the robot in two different terrains: 1) pine straw with small ferns and 2) coarse granular media (Figure 4.5). These environments imitate what the robot could encounter during future applications such as planetary exploration, environmental monitoring, and open-field search-and-rescue tasks. Each of the trials was performed with bidi-

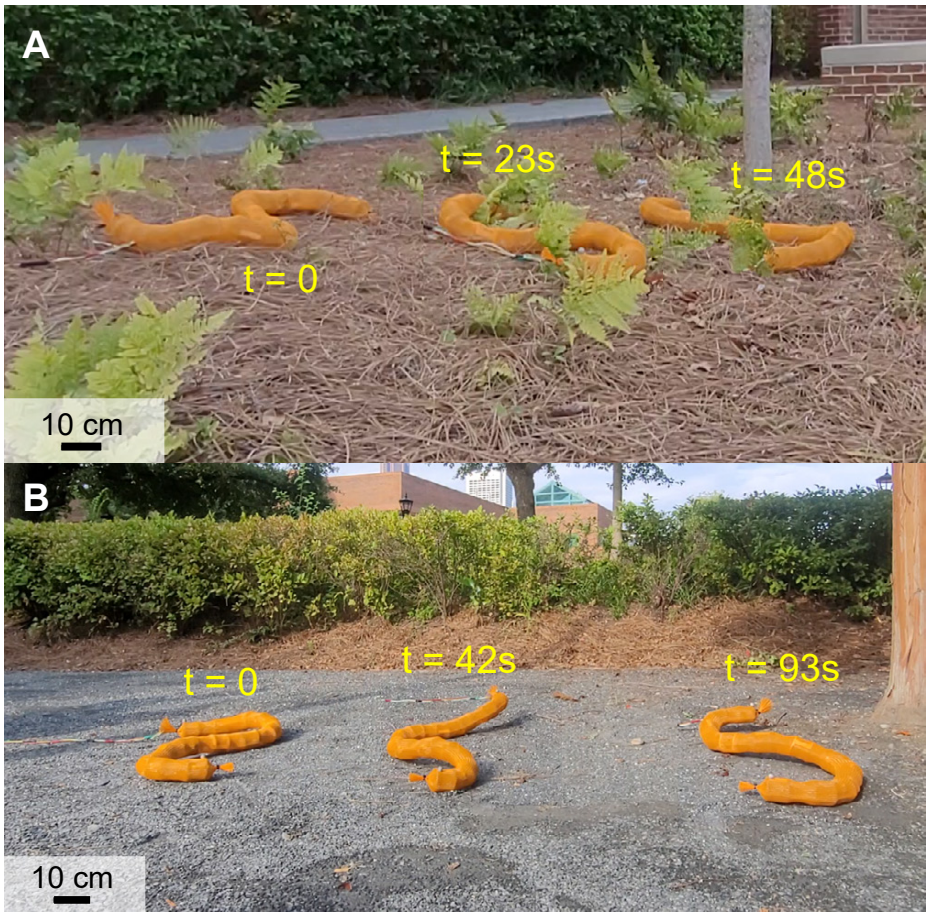

Figure 4.5: **The robot demonstrates its capability of sidewinding in complex natural environments with bidirectional compliance ($G = 1$).** (**A**) Time-lapsed images of the robot traversing pine straw and fern environment. (**B**) Time-lapsed images of the robot traversing coarse granular media environment. Figures are adapted from [100].

rectional compliance ($G = 1$) in the horizontal bending joints and non-compliant vertical bending joints. Similar to the observations in indoor experiments, bidirectional compliance allowed for effective negotiation of irregularities, as the robot body is more likely to deform and deflect from the harsh contact with surrounding obstacles. Our outdoor experiments demonstrated the robot's locomotion capability and potential for practical applications.

4.5 Discussion

In this work, we focused on introducing compliance to sidewinding to simplify the control needed in complex terrains. By incorporating compliance into the robot, we simplify the

control process, enabling the robot to sidewind effectively with open-loop controls over a range of heterogeneities in the environment. Our approach utilizes a traveling wave template for both vertical and horizontal waves that exhibits low sensitivity to variations in wave parameters. We observed that across the various robot sidewinding experiments, by introducing compliance we achieve both more energetically efficient locomotion on hard ground, and improved navigation through heterogeneities in both lab and outdoor terrains. We hypothesize that when sidewinding obstacle-rich environments, having compliance in the lateral wave helps minimize the effect of harsh robot-environment interactions, allowing the robot to either 1) squeeze through obstacles or 2) brush by them without having large changes in body orientation. The robot's ability to exploit its compliance to improve open-loop sidewinding performance across these various terrains makes it mechanically intelligent.

Notice that in this work, the generalized compliance parameter (G) was only varied in the lateral joints, not the vertical joints. Sidewinding requires careful coordination of horizontal and vertical waves along the body to establish and break contact with the substrate. Implementing the same compliance strategy in the vertical direction negatively affected the robot's ability to sidewind. We hypothesize that this is because the contact pattern determined by the suggested gait is disturbed by unwanted ground contact brought by vertical compliance. Instead of remaining above the ground, vertical bending joints tended to sag. However, we assume there could be better compliant strategies for vertical waves during sidewinding so that the contact pattern can be preserved while the energy consumption can go down.

This work also builds a strong foundation for designing multi-modal compliant limbless robots capable of multiple modes of limbless locomotion (e.g., sidewinding, lateral undulation, etc.). By designing a robot capable of exploiting body compliance to be mechanically intelligent in both sidewinding and lateral undulation, we can get closer to creating agile, robust, and capable limbless robots for real-world applications.

More generally, modeling mechanics and interactions involved in biological limbless locomotion are challenging, making limbless robots good tools (as "robophysical" models) for revealing fundamental principles underlying limbless locomotion. To this end, this robot has the potential to serve as a model to study snake sidewinding. With a bilaterally cable-driven robot we can systematically test locomotor performance with varied gait parameters and level of body compliance, which is impossible to carry out with animals. Through comparison across robotic and biological systems, this robot can help us learn sidewinding snakes' kinematics, dynamics, and even physiology, deepening our understanding of their locomotion in complex terrains.

CHAPTER 5
MORPHING MILR: DEVELOPING ROLLING JOINTS TO EXPAND 3D MULTIMODAL CAPABILITIES

5.1 Introduction

Limbless organisms achieve extraordinary mobility across diverse terrains by coordinating body bending and reorientation without appendages. Yet, while MILR has demonstrated environment-adaptive compliance and robust planar locomotion, their movement remains largely constrained within a single plane. Such restriction limits their ability to navigate cluttered three-dimensional terrains where body reorientation and climbing are required. To address this gap, we developed a rolling-enhanced Mechanically Intelligent Limbless Robot (Morphing MILR), a modular platform that integrates programmable body compliance with continuous axial rotation at each joint. This design allows the robot to dynamically reorient its body wave planes and generate multimodal gaits such as lateral undulation, sidewinding, and rolling within a unified architecture.

Morphing MILR builds directly upon the cable-driven compliant framework established in previous chapters, extending it through a rolling cable-driven joint that introduces a new rotational degree of freedom. Each module couples a worm-gear-based rolling module with a bilaterally actuated compliant joint, forming a compact and energy-efficient system capable of non-backdrivable 360 degrees rotation under load. The worm gear maintains orientation passively, while antagonistic cables provide programmable stiffness and motion, enabling both precision and adaptability. Together, these features form a foundation for multimodal, three-dimensional limbless locomotion.

5.2 Robot design and control

Morphing MILR extends the modular cable-driven framework described in previous chapters by introducing a rolling joint that enables active reorientation of each segment about its longitudinal axis (Figure 5.1A). This additional degree of freedom allows the robot to morph its joint orientation in real time, converting planar bending into fully three-dimensional shape control. The system consists of six modules: four identical body modules, a rounded head module, and a tail module. Each active body module provides one degree of freedom through a revolute joint mounted on a rotating base. The cable-driven compliant mechanism remains identical to that of the original MILR (Figure 5.1B), consisting of antagonistic cable pairs that generate programmable compliance.

Mechanical design

Each rolling joint integrates a worm-helical-spur gear transmission positioned between two compliant joint housings (Figure 5.1C). The worm gear is driven by a compact Dynamixel XC330-T288-T servo motor coupled to a helical and spur-gear stage that together provide an effective reduction ratio of approximately 1:13.3. This gearing multiplies torque sufficiently to lift adjacent modules while preserving smooth motion and compact form. The worm-helical arrangement also introduces a non-backdrivable property, allowing the joint to hold orientation without power. Such mechanical locking is essential when the robot must maintain a specific morphology during locomotion.

Each module's housing is composed of two PLA sections joined around a central metal plate. The upper section houses the ball bearing, spur gear, and helical gear assembly that reduce friction and support rotational actuation. This portion also integrates the slip ring into one half of the joint, preventing cable entanglement during continuous operation. The lower section contains the dual-servo that actuates the bilateral cables controlling joint angles. Both halves of the joint are linked by a shoulder bolt through precision-matched holes,

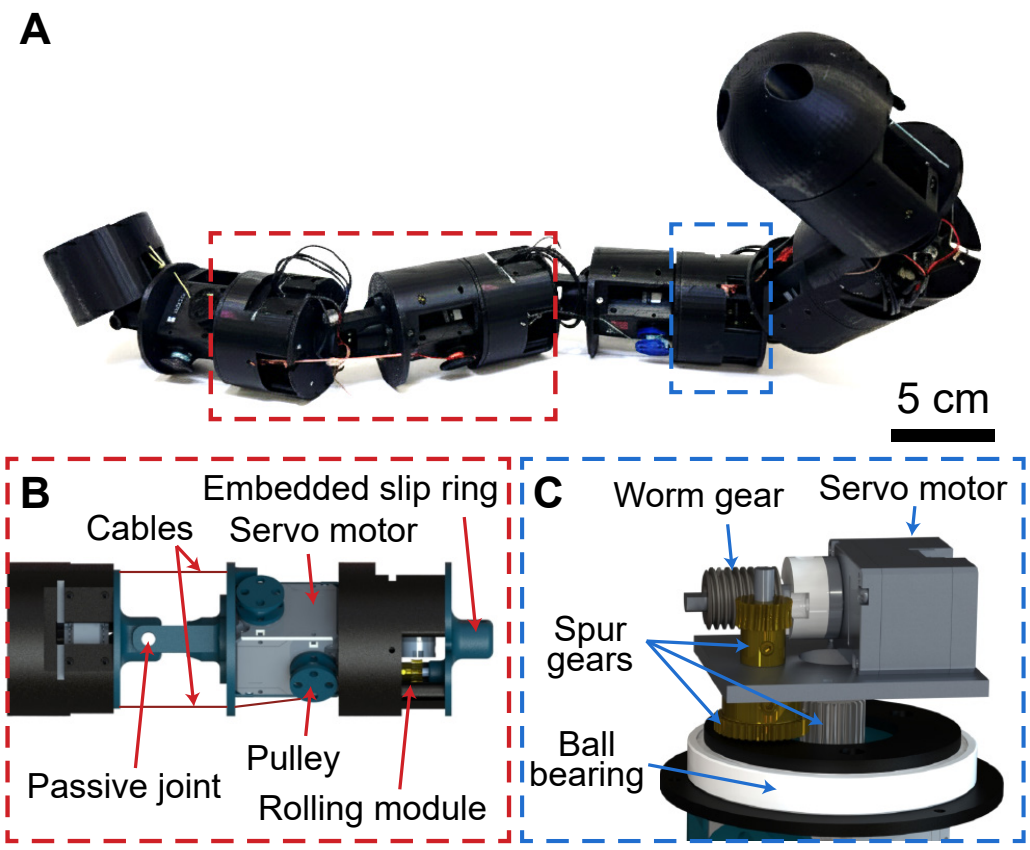

Figure 5.1: **Design of Morphing MILR and rolling joint module.** (**A**) Assembled Morphing MILR composed of six rolling-compliant modules capable of three-dimensional body morphing. (**B**) Structural layout of one module that preserves the MILR actuation principle while enabling continuous axial rotation. (**C**) Sectional view of the rolling module that provides non-backdrivable 360-degree rotation for morphing capability.

providing smooth articulation and alignment. Press-fit bearings and locking caps maintain structural rigidity, and the modular housing allows rapid maintenance and replacement.

A slip ring is incorporated into the center of the rolling module to transmit electrical power and control signals across the rotating interface. This feature ensures that all internal cables remain correctly oriented relative to the joint housing, allowing unrestricted continuous rotation while preserving signal integrity and mechanical reliability throughout extended operation. A pair of radial bearings supports the rotating output plate, reducing friction and preventing lateral wobble during dynamic maneuvers. The output plate serves as the mounting interface for the compliant joint above it, while the lower half houses the

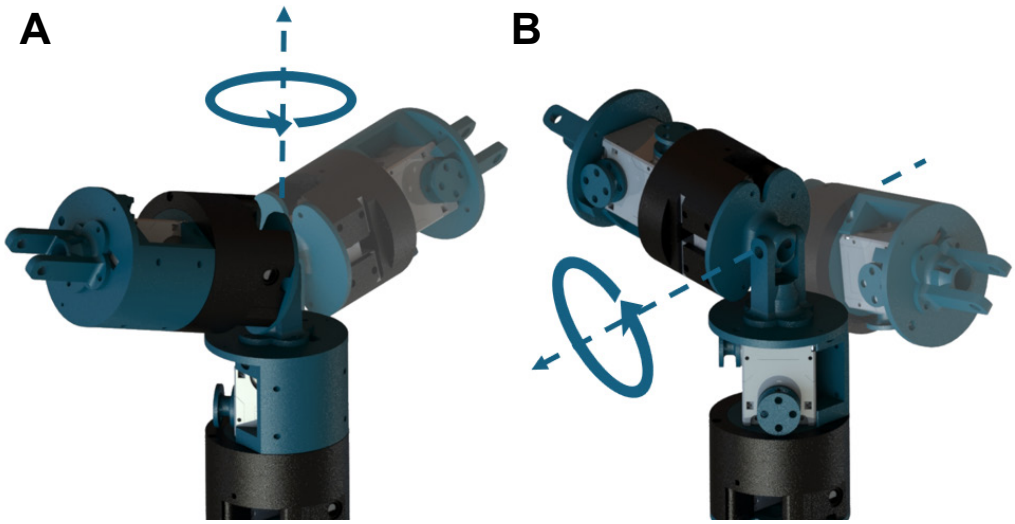

Figure 5.2: **Rolling and bending motions of a single Morphing MILR module.** (**A**) Rolling motion about the longitudinal axis generated by the worm-helical-spur gear transmission, enabling 360-degree reorientation for body morphing. (**B**) Bending motion driven by bilateral cable actuation. Together these two degrees of freedom provide independent control of orientation and curvature, forming the mechanical foundation of the morphing capability.

motor, worm, and gear assembly inside a compact cylindrical shell. This geometry preserves the slender profile required for limbless locomotion.

Above each rolling module sits the bilaterally actuated compliant joint originally developed for the MILR. A Robotis 2XL430-W250-T dual-axis servo controls two opposing 9.5-mm pulleys that pull or release high-tensile Rikimaru 800 N braided cables to adjust joint angles. The cables are routed symmetrically through PLA-based guides that distribute tension evenly and minimize stress concentrations. They are anchored to connection rings on adjacent modules, forming antagonistic pairs for controlled bidirectional motion. This design yields smooth, reversible actuation and allows the robot to maintain continuous bending without backlash. Because the joint's compliance characteristics remain unchanged during rotation, this decoupling allows independent control of bending and rolling motions. The robot therefore combines programmable compliance for environmental adaptability with rolling morphing for gait transitions. The two degrees of freedom provided by each module (axial rolling and lateral bending) are illustrated in Figure 5.2.

Electronics and control

The robot currently operates in a tethered configuration, powered and commanded through a U2D2 interface via TTL communication. All Dynamixel actuators share a single serial line, minimizing wiring complexity. Slip rings between modules prevent wire twisting during rotation and maintain uninterrupted electrical connection. The Dynamixel motors operate at 12 V supplied directly from the U2D2 interface, with negligible communication latency.

Control of Morphing MILR separates the actuation of the rolling joints from that of the cable-driven bending joints. The rolling joints configure the robot's morphology, while the cable-driven joints generate the locomotor waves that produce movement. For a predetermined gait, the control process first commands each rolling joint to rotate into its designated orientation, establishing the spatial configuration of joint planes along the body. Once the morphology is set, the same actuation pattern used in previous chapters is applied to produce bending-based locomotion such as lateral undulation or sidewinding. When a gait transition is required, the system pauses the cable actuation sequence and rotates the rolling joints to a new configuration corresponding to the next desired gait. After rotation is complete, the cable actuation resumes under the same control laws as before. This decoupled control structure enables smooth reorientation of the robot's joint bending axes without disturbing the ongoing cable-driven motion. All parameters and control schemes related to cable actuation, curvature modulation, and generalized compliance G remain consistent with those described in earlier chapters.

Gear selection

Although the raw motor torque is limited, the combined worm, helical, and spur gearing provides adequate torque multiplication to sustain complex configurations. A torque ratio of approximately 1:11 was identified from static load analysis as optimal for lifting two adjacent modules, and a practical ratio of 1:13.33 was implemented. This transmission not

only amplifies torque but also provides the inherent non-backdrivable property necessary for power-efficient posture holding. The worm gear is mounted to the motor shaft using a clamping collar, ensuring minimal play and precise torque transfer. This compact and reliable transmission enables smooth, controlled actuation of each joint under dynamic loading conditions.

5.3 Multi-modal locomotion and gait transition

Lateral undulation

In the lateral undulation mode, all rolling joints were fixed at zero degrees, keeping the robot body within a single plane. The cable-driven joints followed the sinusoidal gait template introduced in Chapter 2, where curvature along the body was defined by amplitude A, spatial frequency ξ, and temporal frequency ω. This configuration produced a smooth traveling wave that propagated from head to tail and generated forward propulsion by pushing against obstacles. During demonstrations in the same lattice environment used in Chapter 2 (Figure 5.3A), Morphing MILR maintained consistent undulatory motion and effective obstacle negotiation. The results confirmed that the addition of rolling joints does not alter the bending dynamics or the gait's mechanical stability. The robot's programmable compliance continued to facilitate adaptation around obstacles, demonstrating that Morphing MILR preserves the mechanical intelligence of the original MILR design.

Sidewinding

Sidewinding is achieved by assigning fixed orientations to the rolling joints in a repeating sequence of $0°$, $90°$, $180°$, $-90°$, and $0°$ along the body axis. This configuration divides the body into alternating bending planes that are perpendicular to each other, enabling the superposition of vertical and horizontal body waves. The cable-driven joints follow the same spatiotemporal phase pattern defined in Chapter 4 (Equation 4.1). The combination of these two orthogonal undulations produces a motion in which body segments lift and

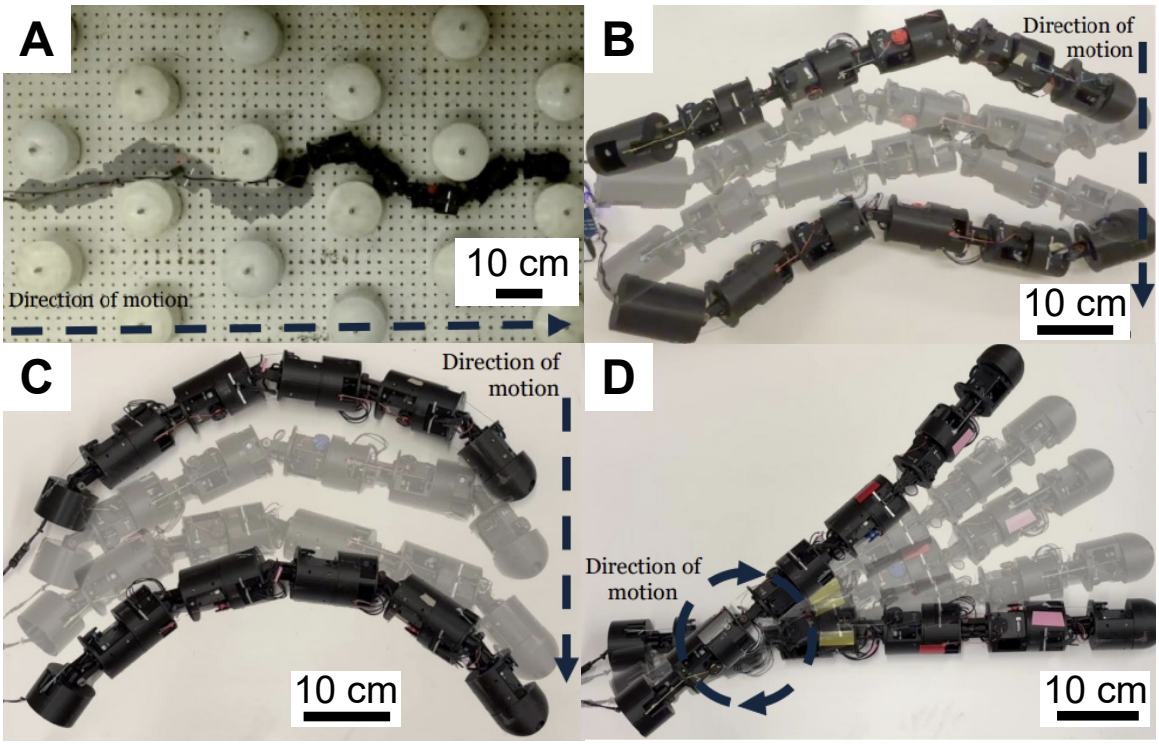

Figure 5.3: **Versatile gaits of Morphing MILR.** Lateral undulation (**A**), sidewinding (**B**), rolling (**C**), and screwing (**D**).

contact the ground sequentially. In demonstrations (Figure 5.3B), Morphing MILR generated clear lifting and sliding cycles and maintained directional stability across smooth and rough surfaces. The compliance of each segment allowed partial body support while minimizing drag, showing that the jointed morphology can effectively redistribute body contact to achieve controlled lateral displacement.

Rolling

The rolling gait extends the same morphological configuration used in sidewinding but applies a modified control sequence to the bending joints. The rolling joints are fixed at orientations of $0°$, $90°$, $180°$, $-90°$, and $0°$ along the body, while the cable-driven joints

follow two perpendicular sinusoidal functions with a phase difference of $\pi/2$:

$$\alpha_i(t) = \begin{cases} A\sin\left(2\pi\xi\dfrac{i}{N} - 2\pi\omega t\right), & i \text{ is odd,} \\ A\sin\left(2\pi\xi\dfrac{i}{N} - 2\pi\omega t - \dfrac{\pi}{2}\right), & i \text{ is even.} \end{cases} \tag{5.1}$$

Here A is the curvature amplitude, ξ is the spatial frequency in waves per body which we fixed at 1, and ω is the temporal frequency. All control parameters for the cable-driven joints, including the implementation of generalized compliance G, remain consistent with those defined in earlier chapters.

This phase-shifted control generates a traveling helical deformation that converts bendings into rotational displacement. During laboratory demonstrations (Figure 5.3C), Morphing MILR exhibited continuous rolling, maintaining a stable trajectory and consistent rotation rate.

Screwing

In the screwing mode, all cable-driven bending joints are mechanically locked to maintain straight, while only the rolling joints are actuated. The actuation sequence commands consecutive modules to rotate at constant but slightly offset angular velocities, producing a helical motion similar to a corkscrew. In physical demonstrations (Figure 5.3D), Morphing MILR successfully rotates in place on a flat surface. This mode illustrates how the same mechanical components can be reconfigured to perform both compliant undulatory motion and rigid rotational propulsion, underscoring the versatility achieved through the combination of rolling and cable-driven actuation.

Gait transition

To validate the ability of Morphing MILR to reconfigure between distinct locomotor modes, we conducted a demonstration that transitions from lateral undulation to sidewinding as

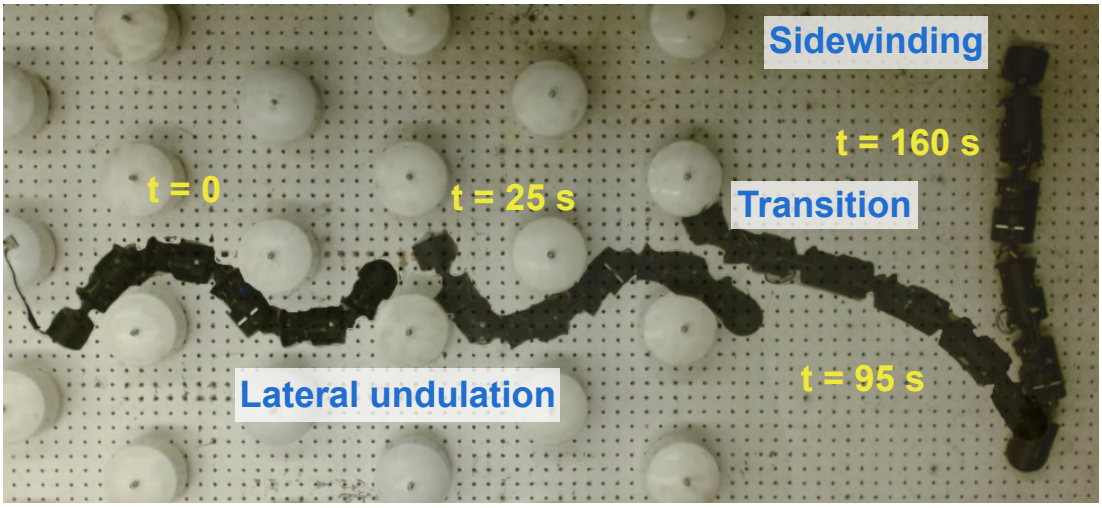

Figure 5.4: **Gait transition demonstration in Morphing MILR.** Sequential snapshots showing Morphing MILR transitioning from lateral undulation in the obstacle lattice to sidewinding on flat terrain.

the robot moves from an obstacle terrain to flat ground (Figure 5.4). Initially, the robot performed lateral undulation within the obstacle field, where programmable compliance allowed its body to conform around posts and maintain forward progress through passive obstacle negotiation. At $t = 95$ s, the cable-driven actuation sequence was paused and each rolling joint was commanded to rotate into the sidewinding configuration ($0°$, $90°$, $180°$, $-90°$, $0°$). After this reorientation, the bending control resumed with the sidewinding gait template, enabling the robot to continue movement across the flat surface with diagonal displacement. This demonstration confirms that robot morphology can be changed mechanically in real time while preserving stable locomotion. This experiment highlights the potential of Morphing MILR to adapt between gaits in response to environmental changes using its modular rolling-bending architecture.

5.4 Discussion

Morphing MILR demonstrates a new level of morphological capability through the integration of programmable compliance and body-axis rotation. Although the present study focused on independently executing each gait, the robot's modular control structure already

enables transitions between them. By separating rolling and bending actuation, the robot can reconfigure its body-wave orientation in real time without interrupting the ongoing locomotion sequence. Future work will further develop continuous gait-transition control, allowing the robot to smoothly shift among lateral undulation, sidewinding, rolling, and screwing in response to terrain feedback. This capability will provide a physical platform for studying how mechanical intelligence can support dynamic adaptation and behavioral diversity in limbless systems.

Beyond the demonstrated gaits, Morphing MILR also provides a framework for synthesizing new three-dimensional motion patterns. Because each joint can bend and rotate independently, it becomes possible to approximate arbitrary spatial curves along the robot's backbone. By defining curvature and torsion profiles directly from target trajectories, future controllers can map desired three-dimensional paths into coordinated joint commands. Such an approach would generalize the design of limbless locomotion from a small set of canonical gaits to a continuous family of spatial body deformations governed by geometric principles.

Together, these results highlight how mechanical intelligence can be extended to support a wide range of gaits and operating environments. Morphing MILR shows that mechanical design itself can encode versatility, enabling a single robot architecture to exhibit planar, volumetric, and rotational modes of movement without additional limbs or actuators. This unification of structure, compliance, and control establishes Morphing MILR as a comprehensive physical platform for future limbless robotic research and applications. It represents a system approaching a complete form of adaptable locomotion in which morphology and intelligence function as an integrated whole.

Part II

Exploiting mechanical intelligence with mid-level computational intelligence to design and optimize gaits for maximum terrestrial performance

Part II of this thesis focuses on developing computational intelligence that leverages the mechanical intelligence established in bilaterally actuated limbless robots. This part builds upon the mechanically intelligent platforms developed in Part I to explore how modeling, control, and gait optimization can further enhance their performance in complex terrestrial environments.

We integrate tools from geometric mechanics and compliance-aware modeling to establish systematic frameworks for gait design and optimization. These computational approaches operate primarily in an offline, feedforward manner, generating control templates that exploit the robot's intrinsic mechanical intelligence rather than relying on real-time feedback. In doing so, they enable systematic improvement of gait performance and stability while preserving the simplicity and physical robustness inherent to mechanically intelligent systems. Through this integration of modeling and computation, Part II demonstrates that these frameworks can achieve globally optimized locomotor performance while maintaining the system's inherent capacity to exploit mechanical intelligence in responding to local environmental perturbations.

CHAPTER 6
CABLE ACTUATION MODELING AND OPTIMIZATION

6.1 Introduction

Locomotion in limbless systems arises from the coupled interactions among actuation, body mechanics, and environmental resistance. The preceding chapters demonstrated how programmable body compliance via cable actuation and morphing structures embed mechanical intelligence (MI) directly into the body, allowing passive mechanisms to shape and benefit locomotion. In this chapter, we shift the focus from morphological embodiment to actuation modeling, developing a quantitative framework that links cable actuation, body compliance, and locomotor performance.

We begin by formulating a cable-driven model that captures how the realized body shape emerges from the interactions between commanded actuation and internal elasticity. By integrating geometric mechanics with cable-driven dynamics, we establish a unified representation of the relationship between actuation space and shape space, where joint-level compliance filters motor commands into emergent body shapes. This approach enables direct prediction of locomotor displacement, providing a physics-based foundation for understanding how compliant actuation affects gait generation.

Building upon this model, we introduce an optimization framework that searches for motor commands maximizing performance under varied compliance conditions. The optimization combines geometric mechanics, resistive-force modeling, and inverse dynamics to identify actuation patterns that exploit compliance. Experimental validation with a simplified 3-link cable-driven limbless robot (Mini MILR, as shown in Figure 6.1) confirms that the framework accurately predicts both emergent body shapes and locomotor outcomes. Results further show that optimized gaits leverage compliance to enhance robustness and

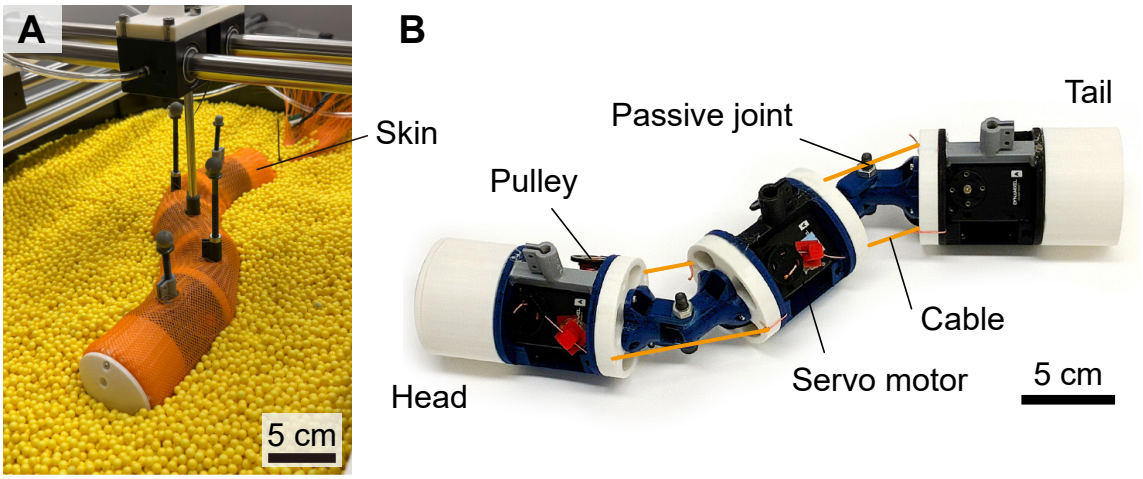

Figure 6.1: **Mini MILR, a cable-driven three-link limbless robot (swimmer).** (**A**) Mini MILR mounted on a gantry and immersed in a granular medium. (**B**) Mini MILR (skin off), with bilateral cables routed through pulleys and actuated by servo motors to produce in-plane bending and body compliance. Figures are adapted from [101].

performance.

Together, this chapter extends the concept of morphology-control co-design into a modeling-optimization framework, where body compliance becomes a controllable resource for mechanical intelligence. The methods developed here provide a general foundation for modeling and optimizing compliant actuation across diverse environments, offering new tools for gait design and motion planning with cable-driven limbless robots.

This chapter is adapted from my previous work [101].

6.2 Review of geometric mechanics

Geometric mechanics provides a general framework for describing locomotion in systems whose movement results from internal shape changes. It establishes a kinematic relationship between the deformation of a body and the net displacement generated by that deformation. This framework has been widely applied to analyze undulatory systems moving in environments dominated by resistive interactions. In highly damped environments where

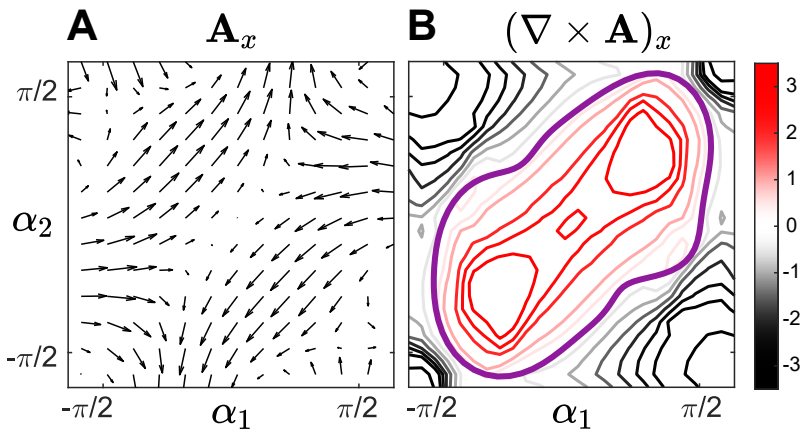

Figure 6.2: **Tools from geometric mechanics for modeling and optimization.** (**A**) An example of local connection vector field, which maps joint velocities to body velocities and provide the foundation for displacement prediction. (**B**) An example of height function, the curl of the local connection vector field. The net displacement from a gait (purple) corresponds to the areas it encloses on the height function. The unit of the height function is body length/rad^2, and its values are scaled by a factor of 100. Figures are adapted from [101].

the locomotion is approximated as quasi-static, the kinematics can be estimated as

$$\boldsymbol{\xi} = \boldsymbol{A}(\boldsymbol{\alpha})\dot{\boldsymbol{\alpha}} = \begin{bmatrix} \boldsymbol{A}_x(\boldsymbol{\alpha}) \\ \boldsymbol{A}_y(\boldsymbol{\alpha}) \\ \boldsymbol{A}_\theta(\boldsymbol{\alpha}) \end{bmatrix} \dot{\boldsymbol{\alpha}}, \tag{6.1}$$

where $\boldsymbol{\xi} = [\xi_x, \xi_y, \xi_\theta]^T$ refers to the body velocity in forward, lateral and rotational directions, $\boldsymbol{\alpha}$ is the actual joint angles as mentioned before, and $\boldsymbol{A}(\boldsymbol{\alpha})$ is the 3×2 local connection matrix which maps the joint angular velocity with body velocity linearly. Each row of matrix represents the direction of body velocity and can be visualized as a connection vector field in shape space (Figure 6.2A).

For viscous fluid or granular media, the local connection matrix can be analytically or numerically solved by the following force $F_{x,y}$ and torque M balance.

$$\sum_i \boldsymbol{F}_i(\boldsymbol{\xi}, \boldsymbol{\alpha}, \dot{\boldsymbol{\alpha}}) = \sum_i [F_x^i, F_y^i, M_i]^T = 0, \tag{6.2}$$

where $\boldsymbol{F}_i$ denotes the environmental force applied on each link. Solving this quasi-static equilibrium yields the mapping $\boldsymbol{A}(\boldsymbol{\alpha})$ that encodes how local shape changes generate body motion.

When a system executes a periodic cycle in its shape space, termed a *gait*, the total body displacement $\Delta \boldsymbol{q} = [\Delta x, \Delta y, \Delta \theta)]^T$ can be approximated by integrating the local connection along the closed trajectory,

$$\Delta \boldsymbol{q} \approx \int_{\partial \phi} \boldsymbol{A}(\boldsymbol{\alpha}) \dot{\boldsymbol{\alpha}} \, dt, \tag{6.3}$$

where $\partial \phi$ denotes the closed path traced by the gait in shape space. According to Stokes' theorem, this line integral can be expressed as a surface integral over the area enclosed by the gait,

$$\Delta \boldsymbol{q} \approx \iint_{\varphi} \nabla \times \boldsymbol{A}(\boldsymbol{\alpha}) \, d\alpha_1 d\alpha_2. \tag{6.4}$$

The term $\nabla \times \boldsymbol{A}(\boldsymbol{\alpha})$ defines a *height function* (Figure 6.2B), which quantifies how much net displacement results from an infinitesimal closed path around each point in shape space. The sign and magnitude of this function directly indicate how efficiently a local gait produces motion in a given direction.

This geometric representation provides an intuitive and quantitative tool for analyzing locomotion. Instead of solving the complete dynamic equations, one can evaluate how the geometry of the shape trajectory, such as its amplitude and phase relationship, maps to locomotor performance.

6.3 Modeling and optimization framework

Building on the foundation of geometric mechanics introduced in the previous section, this part develops a modeling and optimization framework that connects cable actuation, gait, and locomotor performance. The formulation captures how motor commands are filtered through compliant body dynamics and environmental interactions to generate emergent

body shapes and net displacement. The framework provides both predictive and prescriptive capability: it allows locomotor performance to be estimated from model parameters, and optimal actuation patterns to be identified for the compliant robot.

System Dynamics

The model is based on Purcell's classic three-link swimmer model [147], comprising three rigid segments connected in series. Body compliance is incorporated by introducing a spring in series with each motor (Figure 6.3). For locomotion in highly damped environments (also referred to as low-coasting environments [110]), where inertial effects are typically negligible, environmental forces are assumed to be balanced by internal body compliance (spring forces). Under these assumptions, the governing equations describing system dynamics are:

$$\underbrace{\boldsymbol{K}(\boldsymbol{\alpha})(\boldsymbol{\psi}-\boldsymbol{\alpha})}_{\text{body torque}} = \boldsymbol{\tau}_{\text{env}}(\boldsymbol{\alpha}, \dot{\boldsymbol{\alpha}}), \tag{6.5}$$

where $\boldsymbol{\alpha} = [\alpha_1, \alpha_2]^{\mathrm{T}}$ represents the emergent shape of the robot (joint angles that the robot realize, hereafter we call α as "emergent" joint angles); $\boldsymbol{\psi}$ denotes the shape we command the robot to form by actuating the cables, hereafter we call ψ as "suggested" joint angles; $\boldsymbol{K}(\boldsymbol{\alpha})$ is the 2×2 joint stiffness matrix; and $\boldsymbol{\tau}_{\text{env}}(\boldsymbol{\alpha}, \dot{\boldsymbol{\alpha}})$ represents environmental torques acting on each joint. In this study, the joint stiffness can either be constant or state-dependent explicitly on the actual joint angles (Figure 6.3).

The environmental forces acting on each link are modeled using resistive force theory (RFT), which decomposes forces into local normal and tangential components relative to the link surface. We consider two distinct highly damped environments: a viscous fluid and a 6-mm granular medium. In viscous fluids, resistive forces are proportional to link velocities, with a higher drag coefficient in the normal direction than the tangential direction—a phenomenon known as drag anisotropy. Similarly, locomotion within granular media is captured using granular resistive force theory (granular RFT), an effective

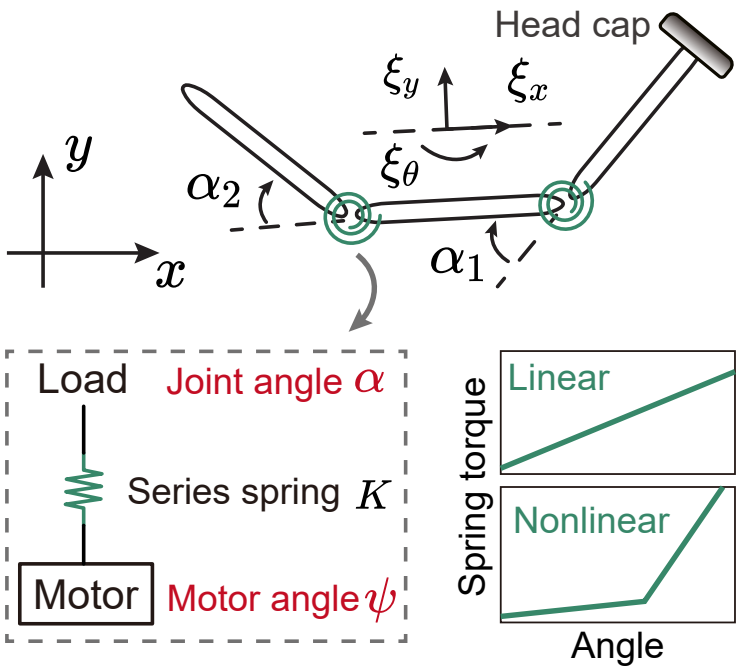

Figure 6.3: **Analytical model of Mini MILR.** Analytical three-link model with a body frame corresponding to a weighted average of the link positions and orientations. Each joint includes a motor connected in series with a spring. Insets illustrate both linear and nonlinear springs, which can be captured by the model. Figures are adapted from [101].

rate-independent force model that accounts for the dependence of forces on velocity direction and has successfully described undulatory locomotion in granular media [113]. To more accurately represent the real-world robophysical system, introduced in the following section, we model the body as a series of connected links without accounting for width, while incorporating a "T"-shaped element at the first link to represent the head (Figure 6.3).

Geometric mechanics formulation

The system dynamics described above are integrated within the geometric mechanics framework introduced earlier (section 6.2). Geometric mechanics provides a reduced-order representation that relates shape changes to body displacement through a local connection matrix. Once this mapping is derived from force balance, it can predict the net displacement $\Delta \boldsymbol{q} = [\Delta x, \Delta y, \Delta \theta]^T$ produced by any prescribed gait in shape space.

Rather than solving the full dynamics, the geometric formulation visualizes locomo-

tor performance using a height function defined over the joint-angle space. This function quantifies the efficiency with which each region in shape space contributes to overall displacement. Gait optimization can then be viewed as identifying a closed path that encloses regions of maximal height-function magnitude, subject to the robot's mechanical limits. This approach reduces a complex dynamic search into a geometric problem defined directly by the interaction between body shape and environment.

Optimization of Actuation Gaits

To identify actuation commands that maximize performance, we search for the optimal joint trajectory in motor space ($\boldsymbol{\psi}$) that results in an emergent trajectory in shape space ($\boldsymbol{\alpha}$) producing the largest net displacement. We prescribed the commanded motor angles ψ_i for two joints ($i = 1, 2$) motor space as 10th-order Fourier series

$$\psi_i = \sum_{p=1}^{10} a_p^i \cos(\frac{2\pi pt}{T}) + b_p^i \sin(\frac{2\pi pt}{T}), \tag{6.6}$$

where T is the temporal period of gait. The optimization flow is described in Figure 6.4. To simplify the calculation we incorporate the height function from geometric mechanics. After deriving the height function from the certain medium (viscous fluid or granular media), the optimal gait can be easily identified from the height function. With the optimal gait in shape space, we can directly solve the motor space parameters $\{a_1^i, ..., a_{10}^i, b_1^i, ..., b_{10}^i\}$ from Equation 6.5.

6.4 Robot development and robophysical experiment setup

Robot development

The robot Mini MILR (Figure 6.1) used in this study is a three-link (two-joint) version of MILR (as developed in Chapter 1). Both joints allow in-plane rotational bending, enabling the robot to execute planar undulatory motions. All three modules are mechani-

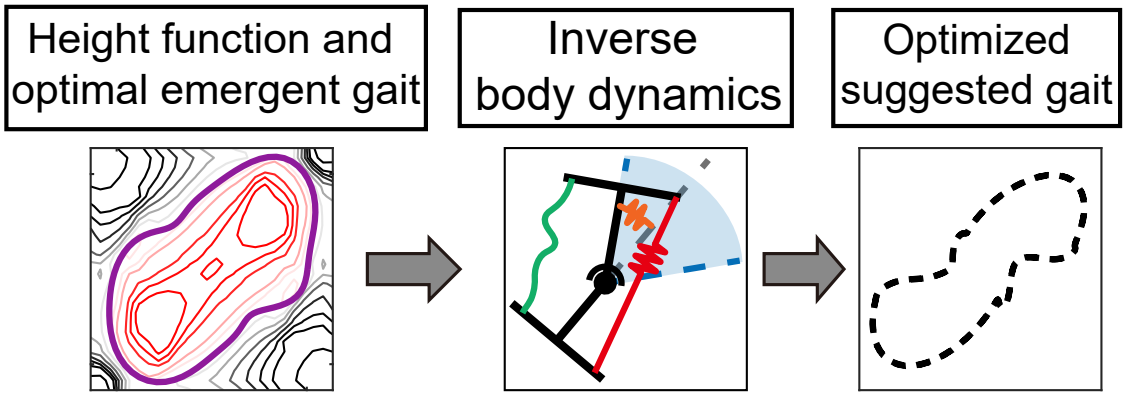

Figure 6.4: **Optimization flow for identifying optimal gaits under body compliance.** First, the optimal emergent gait is identified by deriving the height function. Then, by incorporating the inverse body dynamics, the corresponding optimized gait is obtained. Figures are adapted from [101].

cally identical. Each module consists of a 3D-printed PLA outer shell that houses one DYNAMIXEL 2XL430-W250-T (ROBOTIS) actuator. This actuator contains two independently controlled servo motors, each driving a pulley. Non-elastic cables are spooled around the pulleys to form antagonistic pairs on two sides of the joint. These cables exhibit negligible shape memory and minimal elongation under load, ensuring accurate and consistent transmission of actuation. The distal ends of the cables are anchored to the adjacent module, enabling joint motion via differential cable retraction. The robot is wrapped in a mesh skin made of 4 cm inner diameter expandable sleeving (McMaster-Carr). This outer layer smooths the body profile and prevents granular particles from entering the joint gaps, which could otherwise cause jamming or hindered motion.

Cable actuation scheme

To verify the modeling and optimization scheme, we follow the method of programming body compliance in MILR through a bilateral cable-driven scheme [89]. Specifically, each joint is actuated by two cables, whose lengths can be independently controlled as L_i^r and L_i^l for the right and left cables, respectively, with the geometric relationship illustrated in Figure 6.5. We define a generalized compliance parameter G to control the simultaneous

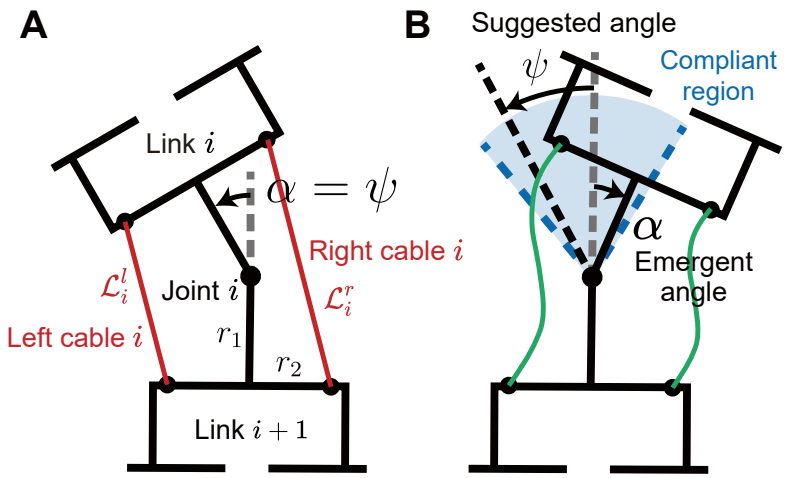

Figure 6.5: **Cable actuation and joint compliance mechanism.** Schematic of bilateral cable actuation at a single joint, where left and right cables tensioned to form the exact suggested joint angle (**A**), and left and right cable slacked to form a compliant region, so that the emergent joint angle can deviate from the suggested angle (**B**). Figures are adapted from [101].

contraction of cables at each joint, governed by the following equations:

$$L_i^l(\psi_i) = \begin{cases} \mathcal{L}_i^l(\psi_i), & \text{if } \psi_i \leq -\gamma \\ \mathcal{L}_i^l[-\min(A_\psi, \gamma)] + l_0[\gamma + \psi_i] & \text{if } \psi_i > -\gamma \end{cases}$$
$$L_i^r(\psi_i) = \begin{cases} \mathcal{L}_i^r(\psi_i), & \text{if } \psi_i \geq \gamma \\ \mathcal{L}_i^r[\min(A_\psi, \gamma)] + l_0[\gamma - \psi_i] & \text{if } \psi_i < \gamma \end{cases}, \tag{6.7}$$

where $\mathcal{L}_i^l$ and $\mathcal{L}_i^r$ denote the exact lengths of the left and right cables corresponding to the suggested motor angles (Equation 2.2), based on the geometry (Figure 6.5A). Here, A_ψ is the commanded gait amplitude, l_0 is a fixed design parameter related to cable tightness, and $\gamma = (2G-1)A_\psi$.

Within this scheme, by varying the generalized compliance G, cables can become loose as illustrated in Figure 6.5(b). The loose cables define a compliant region of the joint that can rotate freely. With the generalized compliance G, the equivalent joint stiffness becomes state dependent. When the actual joint angle remains within the compliant region,

the robot's skin acts as a weak spring, restoring the joint toward the zero position (Figure 6.6B). When the joint angle reaches the rigid boundary, the cable tightens and introduces an additional spring in series (Figure 6.6C). The state-dependent body compliance can therefore be expressed as

$$K(\alpha) = \begin{cases} k_{\text{skin}} & \text{if } \alpha \in \text{compliant region} \\ k_{\text{skin}} + k_{\text{cable}} & \text{if } \alpha \in \text{rigid boundary} \end{cases}, \tag{6.8}$$

where k_{skin} and k_{cable} are the stiffness values of the skin and the cable, respectively, as measured in Chapter 1.

Robophysical experiments

Experiments were conducted in a testbed filled with plastic spheres (6 mm diameter), which served as the granular environment. To constrain Mini MILR's motion to a horizontal plane and maintain a consistent depth, we designed a custom gantry system incorporating air bearings. The system includes two orthogonal linear air bearings (New Way Air Bearings) that provide frictionless translation along the X and Y axes, and a rotational ball bearing enabling smooth in-plane rotation (Figure 6.7). The robot is attached to the gantry via a vertical shaft whose lower end is fixed to a rigid connector mounted at the center of the middle link. This mechanical coupling ensures that the robot remains suspended at a constant height while allowing free planar motion. The overall setup minimizes mechanical resistance, eliminates vertical drag or sinkage, and enables repeatable locomotion trials within the granular bed.

To track the motion of the robot during experiments, we uniformly attached four infrared reflective markers along its body: one at head, two at joints, and one at tail. An OptiTrack motion capture system with six OptiTrack Flex 13 cameras was used to track the three-dimensional positions of the markers at a frame rate of 120 FPS. We recorded trajectories of robot movement and calculated displacements and body shape patterns to

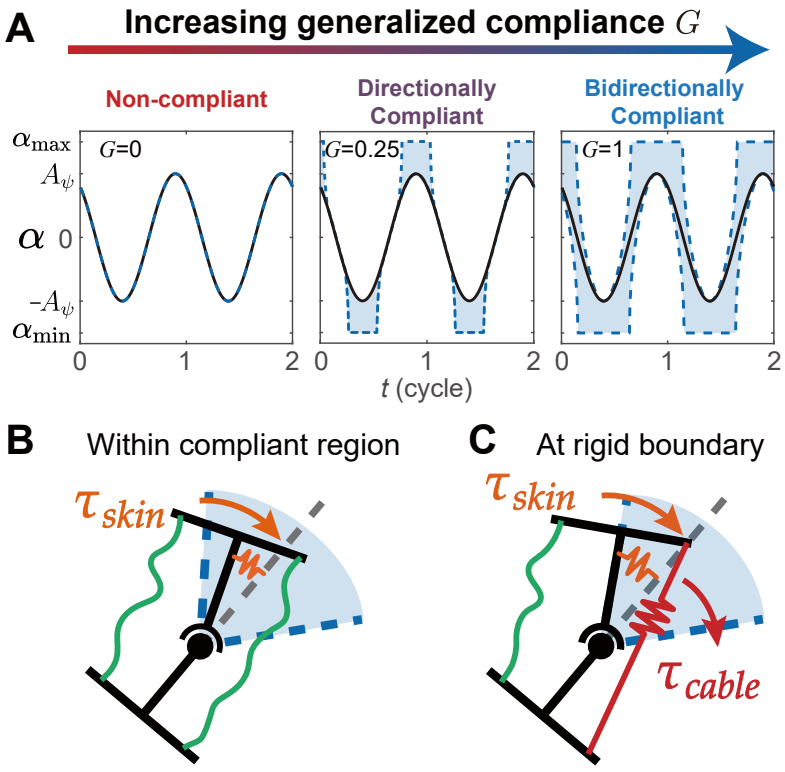

Figure 6.6: **Effect of generalized compliance G on joint behavior.** (**A**) Emergent joint angle trajectories (α) across different compliance regimes: rigid (non-compliant, $G = 0$), directionally compliant ($G = 0.25$), and bidirectionally compliant ($G = 1$). Compliance enlarges the range of joint motion within which the suggested angle (ψ) can deviate, illustrated by shaded blue regions. (**B**) Within the compliant region, the joint is governed primarily by the skin's restoring torque (τ_{skin}). (**C**) At the rigid boundary, cable tension engages, introducing an additional restoring torque (τ_{cable}) that stiffens the joint response. Figures are adapted from [101].

evaluate locomotor performance.

In each experiment, the robot was positioned such that its entire body was fully immersed in the granular medium, with the top edge maintained at a depth of 1 cm beneath the surface. For every gait tested, the robot executed seven full cycles. To eliminate the effects of transient dynamics, only the final five cycles were included in the analysis. Each experiment was repeated five times, and we report averaged results with standard deviation across trials. Additionally, we conducted friction characterization tests by dragging the robot in a static configuration (i.e., without any active joint motion) through the granular bed. These tests provided baseline measurements of resistive forces and supported

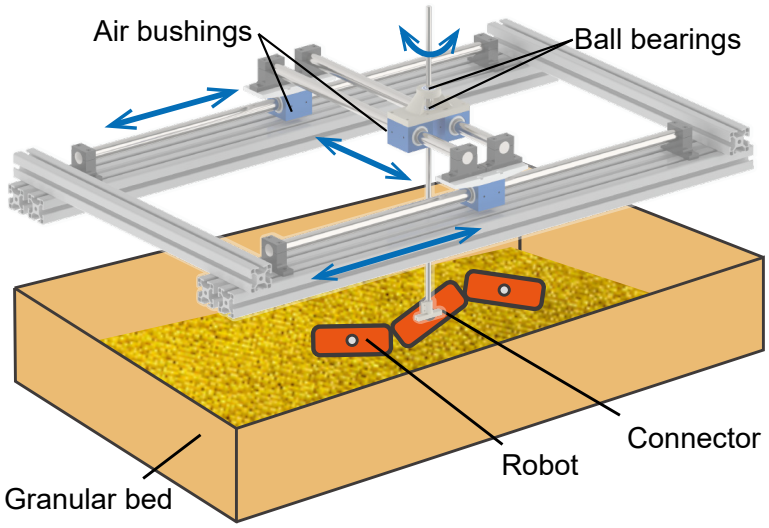

Figure 6.7: **Experimental setup for robophysical experiments in granular media.** Mini MILR is immersed in granular media and mounted on a gantry, which constrains its motion to the horizontal plane while allowing both translation and rotation. The figure is adapted from [101].

interpretation of locomotion performance.

6.5 Verification of system dynamics for shape prediction

A critical first step in validating our framework is to confirm that the system dynamics model (Equation 6.5) correctly predicts the actual body shapes that emerge when motor commands are filtered through compliance and environmental interactions. To test this, we prescribed a nominal circular gait in motor space, following the gait equation

$$\begin{aligned} \psi_1(t) &= A_\psi \cos(2\pi\omega t), \\ \psi_2(t) &= A_\psi \sin(2\pi\omega t). \end{aligned} \tag{6.9}$$

Specifically, we selected $A_\psi = 60°, \omega = 0.1$ Hz (one gait cycle takes 10 sec). We then examined the resulting trajectories in shape space under different levels of generalized compliance G. Representative cases are shown in Figure 6.8.

With no compliance ($G = 0$), Mini MILR can accurately execute the prescribed gait

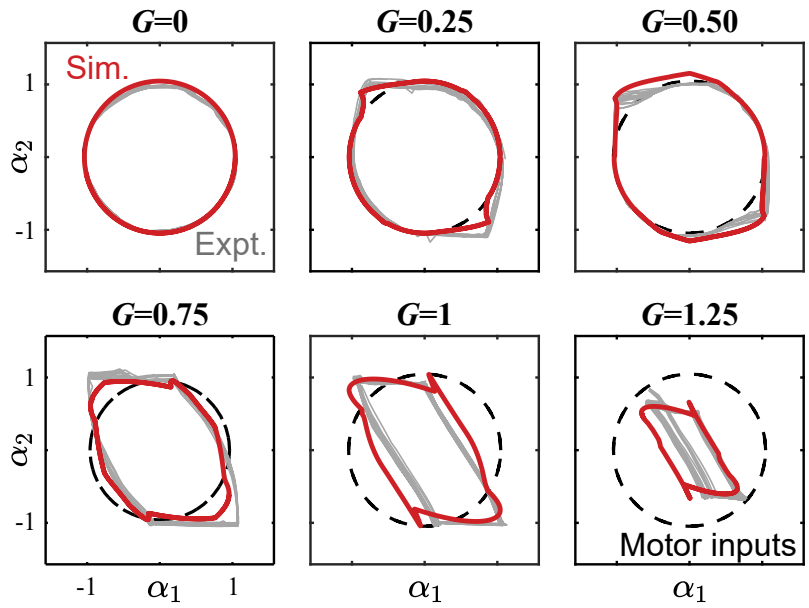

Figure 6.8: **Validation of system dynamics for predicting emergent shapes under compliance.** Emergent gait trajectories in shape space (α_1-α_2) for increasing generalized compliance G. Dashed circles indicate prescribed circular motor inputs, gray lines show experimental measurements, and red lines denote simulation predictions. With no compliance ($G = 0$), emergent gaits closely follow the commanded circular inputs, while body compliance causes distorted and collapsed trajectories. Simulation results capture the deformation trends observed in experiments across all compliance regimes. Figures are adapted from [101].

commands where its trajectory in the shape space (α_1-α_2 space) forms a perfect circle. At low compliance ($G = 0.25$), the emergent gait closely followed the commanded circle, indicating that the motor commands were faithfully transmitted to the joints with little deformation. At moderate compliance ($G = 0.75$), the emergent gait deviated substantially from the nominal circular path, reflecting the growing influence of environmental torques relative to joint stiffness. At high compliance ($G = 1.25$), the emergent gait collapsed into a much smaller, distorted loop, demonstrating that environmental forces dominate the effective shape dynamics when the joints are highly compliant.

Across all conditions, the predicted shape trajectories generated by our dynamics model (red) showed excellent agreement with experimentally observed trajectories (gray), capturing both the degree and direction of gait deformation as compliance increased. This

agreement demonstrates that the system dynamics model accurately encodes the interaction between motor commands, joint compliance, and environmental resistance. In effect, the model provides a quantitative description of how compliance reshapes commanded motor gaits into realized body motions in shape space.

6.6 Verification of the full framework for performance prediction

While the dynamics model captures how commanded gaits are transformed into emergent trajectories, locomotor performance depends on how these trajectories interact with environmental forces to generate net displacement. To assess whether our framework can also predict performance outcomes, we quantified the displacement per cycle as a function of generalized compliance G (Figure 6.9).

Two complementary theoretical tools were employed. First, resistive force theory (RFT, blue) was used to compute the net forces and torques acting on the body as it executed the realized gait, providing a direct estimate of displacement. Second, geometric mechanics was used to derive the height function (red), which encodes the geometric phase associated with a closed trajectory in shape space and predicts the net displacement resulting from each gait cycle.

The relationship between compliance and performance was not strictly monotonic. In the low-compliance regime ($G \approx 0.25$), performance was nearly unchanged compared to the non-compliant case and in some conditions even slightly higher. This occurred because environmental perturbations naturally distorted the commanded circular gait in a way that favored forward locomotion; in terms of the height function, the deformed trajectory enclosed more positive area, which increased net displacement. At higher compliance levels, however, performance declined sharply. As gait amplitude collapsed, the enclosed area in the height function shrank, leading to reduced displacement per cycle.

Experimental measurements (black) closely matched both the RFT and height-function predictions, reproducing the initial plateau or slight improvement at low compliance and the

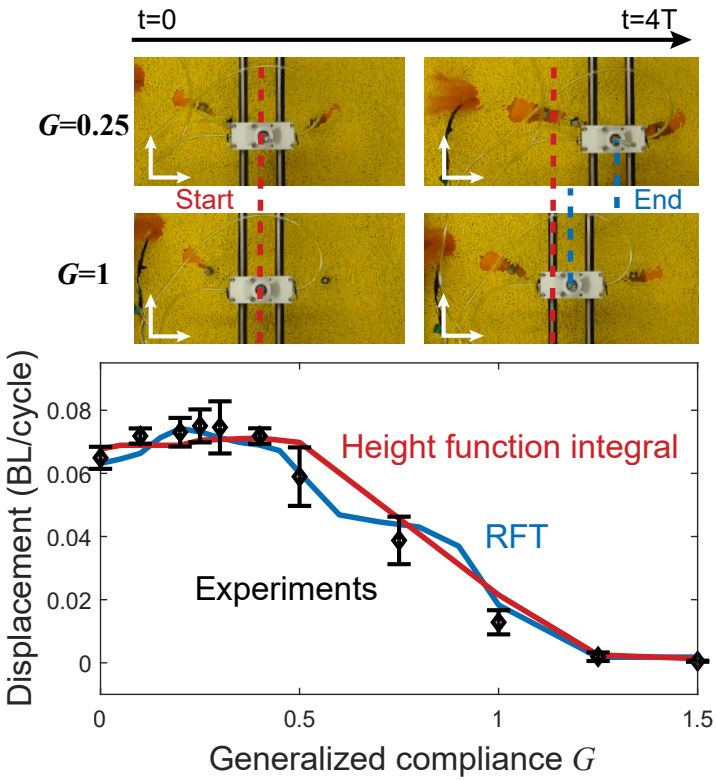

Figure 6.9: **Verification of locomotor performance predictions under varied body compliance.** (*Top*) Experimental snapshots of Mini MILR displacement after four gait cycles for moderate compliance ($G = 0.25$) and high compliance ($G = 1$). Red and blue dashed lines indicate start and end positions, respectively. At higher compliance, displacement per cycle decreases markedly. (*Bottom*) Quantitative comparison of displacement per cycle (in body lengths, BL) as a function of generalized compliance G. Predictions from resistive force theory (RFT, blue) and geometric mechanics height-function integral (red) closely match experimental measurements (black points with error bars representing standard deviation), capturing the initial plateau at low compliance and sharp performance drop at high compliance. Figures are adapted from [101].

drop-off at higher compliance. These results confirm that our framework predicts not only the deformation of gait trajectories but also their performance consequences. They also show that a moderate amount of compliance can sometimes improve locomotion, while excessive compliance ultimately reduces effectiveness in viscous fluid and granular media. In particular, Figure 6.8 demonstrates that the system dynamics model captures the detailed deformation of gait trajectories across compliance regimes, with predicted emergent shapes (red) aligning closely with experimentally measured ones (gray). This agreement under-

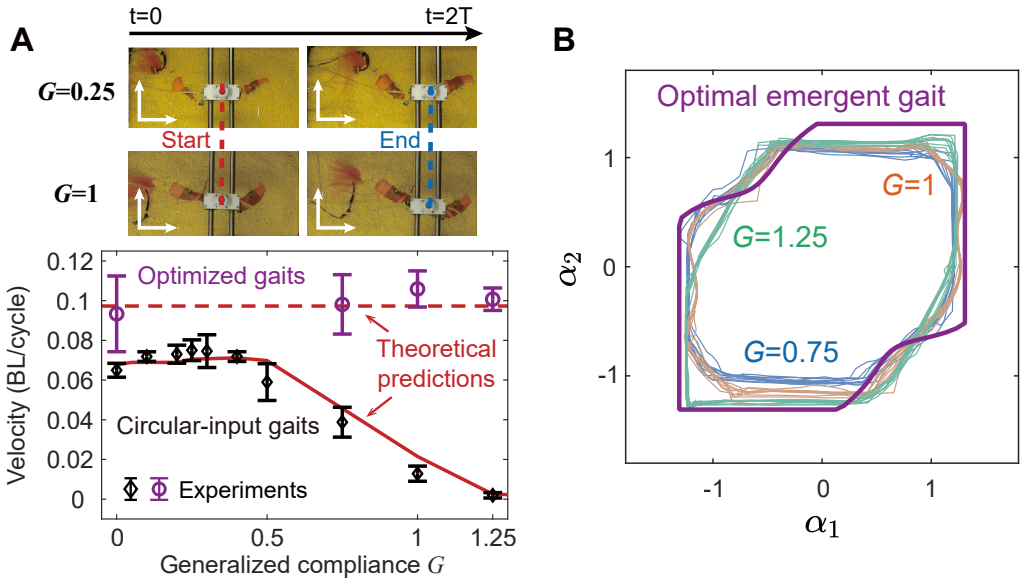

Figure 6.10: **Gait optimization maximizes performance in Mini MILR.** (**A**) Displacement per cycle as a function of generalized compliance G. Circular-input gaits (black points) show rapid performance degradation with increasing compliance, consistent with geometric mechanics predictions (red). Optimized gaits (purple points), identified through the proposed optimization framework, maintain consistently high performance across all compliance levels. (**B**) Emergent gait trajectories in shape space for high compliance levels ($G = 0.75, 1, 1.25$). Despite variations in compliance, the optimized motor inputs yield emergent gaits that closely match the theoretical optimal trajectory (purple), enabling robust high performance. Figures are adapted from [101].

scores the ability of our framework to predict how motor commands generates emergent body shapes under compliance in granular media.

6.7 Gait optimization with the proposed framework

While circular-input gaits provided a convenient baseline to test our model, they did not achieve optimal locomotor performance across different compliance levels. In particular, performance declined sharply as compliance increased, even though the underlying system dynamics were accurately predicted. To address this limitation, we employed our proposed optimization framework, which combines system dynamics, resistive force theory, and geometric mechanics to search for the input (commanding) gaits that maximize displacement given Mini MILR's compliance.

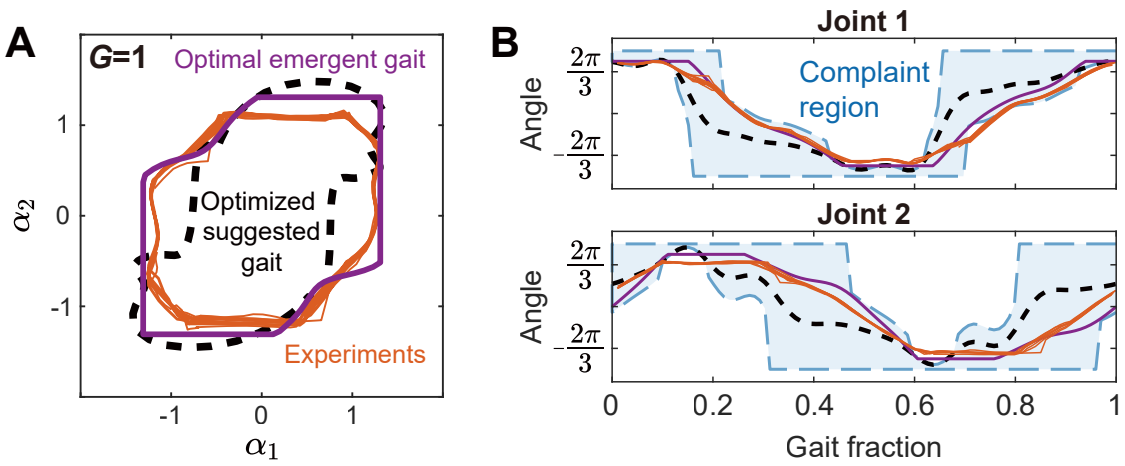

Figure 6.11: **Execution of optimized gaits in Mini MILR.** (**A**) Shape-space trajectories $G = 1$. The optimized suggested gait (black dashed) differs substantially from the theoretical optimal emergent gait (purple), and by executing the optimized suggested gait, the robot can successfully realize the optimal emergent gait (orange). (**B**) Joint angle traces over one gait cycle. The emergent joint angles (orange) follow the optimal trajectories (purple), demonstrating that environmental perturbations and compliance are exploited to reinforce performance. Figures are adapted from [101].

Overall, Figure 6.10A compares the displacement of circular suggested gaits (black points, red curve) with that of optimized suggested gaits (purple points). Circular gaits exhibited performance that was high only in the rigid or near-rigid regime and degraded rapidly with increasing compliance. In contrast, optimized suggested gaits maintained consistently high performance, nearly doubling the displacement relative to circular gaits in the compliant regime. Theoretical predictions and experimental measurements were in close agreement, confirming that the optimization framework successfully identifies gaits that recover performance otherwise lost to compliance.

In detail, we first identified the theoretical optimal emergent gait using the RFT and geometric mechanics models, and then applied the inverse system dynamics to determine the corresponding suggested motor commands for each compliance value G. Deploying these optimized suggested gaits on Mini MILR enabled it to realize the optimal emergent gait and maintain high performance. Figure 6.10B presents a collection of emergent gait trajectories across different G values. Taking $G = 1$ as an example, the optimized suggested gait

(black dashed) differs substantially from the circular input, and the robot reliably executed the optimal emergent gait trajectory in experiments (Figure 6.11A). Joint angle traces further confirm that the optimized suggested gait effectively leverages compliant regions of the dynamics (Figure 6.11B), shaping motor inputs so that environmental perturbations naturally reinforce forward locomotion.

Together, these results demonstrate that optimization does not simply "fix" the limitations introduced by compliance but instead co-designs gaits with compliance. Without optimization, compliance might appear as a disadvantage, since naive circular gaits collapse and lose performance. With optimization, however, compliance becomes a resource. Unlike rigid robots, which transmit environmental disturbances directly to their actuators and therefore require complex sensing and control to remain stable, compliant robots can passively absorb shocks, adapt their body shape when moving through granular media or clutter, and reduce the burden on active control. In this way, compliance provides a built-in form of mechanical intelligence that improves robustness across environments. Beyond robotics, incorporating compliance also increases the biological relevance of our robophysical models, since animals rely on body elasticity for effective locomotion. Thus, optimization enables compliant robots to achieve high performance while simultaneously establishing them as powerful physical models for studying the role of compliance in biological systems.

6.8 Optimized compliant locomotion for fast obstacle navigation

While the previous sections demonstrated how compliance reshapes motor commands and how optimization can recover performance in homogeneous environments, the true advantage of compliance becomes evident in cluttered settings. To test this, we introduced a row of rigid pillars embedded in granular media (Figure 6.12A), where Mini MILR was required to pass through the openings between pillars.

When operated with no compliance ($G = 0$), the robot jammed upon its contacts with

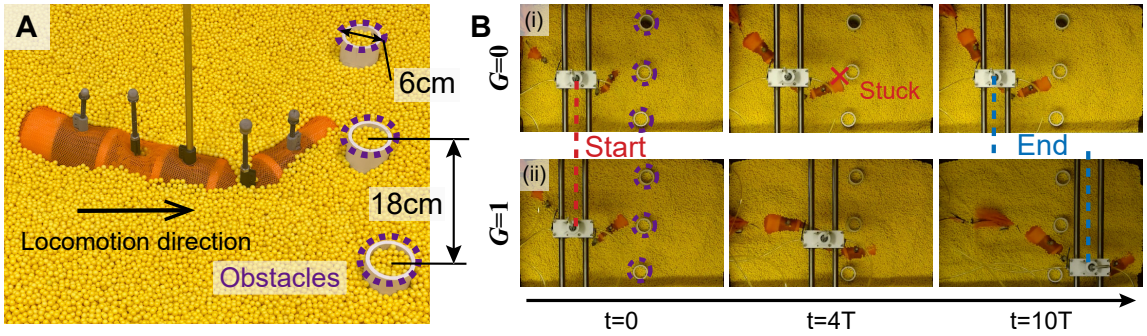

Figure 6.12: **An optimized gait with body compliance enables the robot to traverse obstacles.** (**A**) Three cylindrical rigid obstacles immersed in the granular medium. (**B**) When operating the optimized gait without body compliance ($G = 0$), the robot becomes stuck by obstacles in the granular medium (i). With body compliance ($G = 1$), the robot executing the optimized gait successfully passes through the obstacles while maintaining the speed (ii). Figures are adapted from [101].

the obstacles (Figure 6.12B-i). With a rigid body configuration, the robot was unable to reconfigure its shape to exploit the available openings. In some cases, external contact forces were transmitted directly to the actuators, potentially driving them toward torque limits and further preventing forward progression. By contrast, with high compliance ($G = 1$), the robot was able to negotiate the obstacles smoothly (Figure 6.12B-ii). Passive joint flexibility allowed the body to bend around the pillars and "flow" through the available gaps without requiring explicit sensing or contact modeling. To further explain the role of body compliance in facilitating obstacle traversal, we examined the joint-level responses of the robot executing the optimized gait. Figure 6.13A shows at the head, compliance allows the joint to adapt passively upon contact with an obstacle, producing a hooking behavior that effectively leverages the obstacle to aid forward motion. This behavior is reflected in the joint angle trajectory, which deviates from the prescribed optimal gait during contact. At the tail (Figure 6.13B), compliance enables passive deflection as the segment encounters an obstacle, thereby reducing resistive forces that would otherwise impede motion.

It is worth noting that compliance alone is not sufficient for obstacle navigation. Without gait optimization, the robot could not achieve effective forward speed in this homogeneous media, and thus would also fail to make useful progress in cluttered environments.

Our optimization framework resolves this limitation by identifying motor commands that maximize displacement with varied G. With optimized gaits, the robot maintains high free-space speed, and compliance then naturally takes over the task of negotiating unpredictable obstacle contacts.

This result illustrates a practical control principle: in real-world environments, it is impossible to explicitly model every unknown contact. Instead, robots should be optimized for performance with compliance in homogeneous media, and then rely on compliance to handle unmodeled obstacle interactions. This approach exemplifies the philosophy of mechanical intelligence, in which passive body mechanics are deliberately leveraged to offload control and enhance robustness. In this way, compliance transforms from a performance liability into a "robustifier", allowing robots to move effectively through clutter where purely rigid ones fail.

6.9 Discussion

In this work, we developed and experimentally validated a unified framework for modeling, analyzing, and optimizing the locomotion of compliant cable-driven limbless robots in highly damped environments. We introduced body compliance by incorporating series elastic elements into the system dynamics, which allowed us to map from suggested joint angles (input body shape sequence) to emergent joint angles (realized body shape sequence). Coupled with resistive force theory and geometric mechanics, this framework enabled us to predict how compliance reshapes commanded gaits and how these emergent trajectories interact with the environment to generate locomotion. Through robophysical experiments with a three-link robot Mini MILR in granular media, we verified that the framework accurately predicts both gait deformation and locomotor performance. Finally, we applied the optimization pipeline to identify gaits that maximize displacement under different levels of compliance and showed that the robot executing these optimized gaits achieve consistently high performance across compliance regimes. Our results extend the

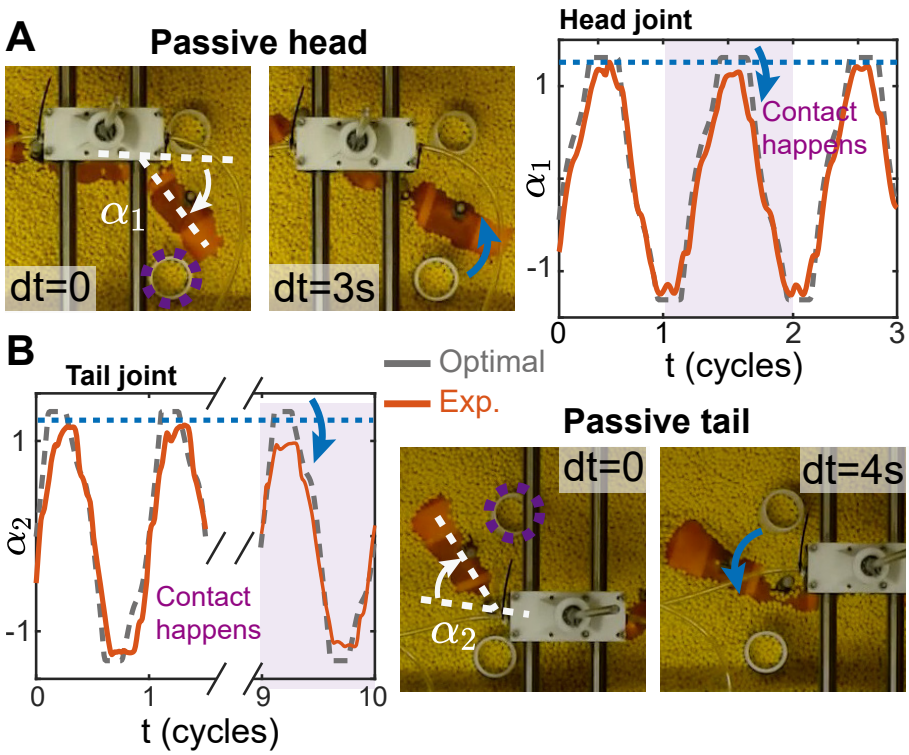

Figure 6.13: **Passive responses from compliance augment locomotion capabilities.** (**A**) Compliance in the head joint enables a passive hooking behavior that aids locomotion upon contact with obstacles. (**B**) Compliance in the tail joint allows passive deflection, reducing resistance from obstacles. Figures are adapted from [101].

gait design framework of geometric mechanics from systems with prescribed shape control to those in which shape emerges from interactions between the environment and body elasticity. Furthermore, geometric mechanics plays a vital role in simplifying the search for optimal control strategies.

Beyond these, this study provides deeper insight into the role of compliance in limbless locomotion. Our findings reveal that, beyond its well-recognized benefits for interacting with environmental heterogeneity, compliance should not be viewed solely as a constraint or deficiency even in homogeneous environments. While naive circular gaits degrade with increasing compliance, optimized gaits exploit compliance to enhance robustness and adaptability. Unlike rigid robots, which transmit external disturbances directly to actuators and therefore require sophisticated sensing and control to maintain stability, compliant robots can passively absorb contacts, adapt their body shape to cluttered or granular terrain,

and reduce control complexity. This passive adaptability represents a form of mechanical intelligence that allows robots to offload part of the locomotor "control problem" to their body mechanics. This work further contributes to showing how compliance can be implemented while still achieving optimal performance, allowing compliance to become a free bonus rather than a drawback. Moreover, embedding compliance into robotic platforms strengthens their connection to biology, since animals universally rely on body elasticity for effective movement.

This work opens up several new directions for advancing the study of compliant undulatory locomotion. First, the framework can be extended to more diverse robot morphologies, such as robots with additional joints as different MILR morphologies as mentioned in previous chapters, and to more complex three-dimensional gaits that better capture the richness of limbless locomotion. Second, while this study focused on displacement performance, future efforts should investigate the energetic consequences of compliance, examining whether compliant bodies enable more energy-efficient locomotion by reducing actuation effort or exploiting passive body dynamics. Third, by applying this framework in conjunction with comparative biological studies, compliant robophysical models could serve as powerful experimental platforms for testing biomechanical hypotheses and exploring how animals leverage compliance for robustness and efficiency. Together, these directions highlight the potential of compliance-aware geometric mechanics not only to advance the development of resilient robots but also to deepen our understanding of limbless locomotion in the natural world.

CHAPTER 7
THE OMEGA TURN: A BIOLOGICALLY INSPIRED TURNING GAIT FOR LIMBLESS ROBOTS

7.1 Introduction

Building on the modeling framework developed in Chapter 6, where cable-driven mechanism was formulated and optimized, the next three chapters (Chapters 7-9) focus on gait design for general elongate limbless robots. These chapters explore locomotor strategies that do not depend on cable actuation but can later be incorporated into the framework established in Chapter 6. In this way, the principles developed here serve as higher-level gait templates that can be physically realized through cable-driven actuation while remaining broadly applicable to common limbless robots.

Inspired by undulatory animals such as snakes and worms, the translational locomotion of limbless robots has been widely studied. In these systems, traveling waves of body bending propagate from head to tail to produce propulsion [13, 148, 149]. Such body waves can be expressed through simple sinusoidal equations [11], which, when combined with passive body mechanics [89] or sensory feedback such as vision [71] and torque sensing [150, 76], enable adaptive locomotion on uneven terrains.

By contrast, effective turning gaits for limbless robots have received considerably less attention and are often studied only in simplified settings [151, 145]. Hirose [11] first proposed an "offset turning" strategy by adding a constant curvature bias to the body wave, which allows steering through offset regulation [152]. Later, Dai *et al.* [153] applied geometric mechanics tools to design an in-place "geometric turn," while Astley *et al.* [145] introduced "frequency turning" by modulating vertical-wave frequency [106]. Although effective in open space, these strategies rely heavily on environmental homogeneity and

lose efficiency in cluttered or confined terrains.

Interestingly, the nematode *C. elegans* achieves remarkable turning performance [154, 24, 155]. Its signature turning strategy, the *omega turn*, features the head sweeping near the tail to form an "Ω"-shaped body configuration (Figure 7.1A). Given this elegance and simplicity, we hypothesize that omega turns offer a robust and efficient template for robotic reorientation. In this chapter, we model the omega turn as the superposition of two traveling waves, reconstruct it experimentally on a limbless robot, and systematically compare its performance to existing turning gaits. Our results show that the omega turn provides larger angular displacement, smaller swept area, and improved robustness across environments. Finally, we introduce a compliance-based amplitude modulation mechanism that allows adaptive turning in complex terrains such as pillar arrays, grass, and natural rock piles.

This chapter is adapted from my previously published peer-reviewed work [102] and [103].

7.2 The two-wave gait family and omega turns

Turning behavior in C. elegans

While thought of as simple organism, *C. elegans* exhibits behaviors and performances in complex environments not seen in robots. One of these behaviors is the worm's turning strategy, known as omega (Ω) turns [154]. These worms generate a high curvature bend such that the head touches body and outlines an omega (Ω) shape, allowing the worms to turn in place. The worms were observed to use omega turns to explore unknown environments, avoid navigational bias, and to escape painful external stimuli [156, 155, 157]. Note that the omega turn can produce effective turning performance in a variety of environments with different drag anisotropy. These turns are advantageous when navigating and traversing complex heterogeneous terrain that the worms encounter throughout their lifetime. Stephens *et al.* [24] showed that the *C. elegans* kinematics during free crawling can be described with more than two principal components. Two principal components are observed to characterize a traveling wave for the forward motion. Surprisingly, an-

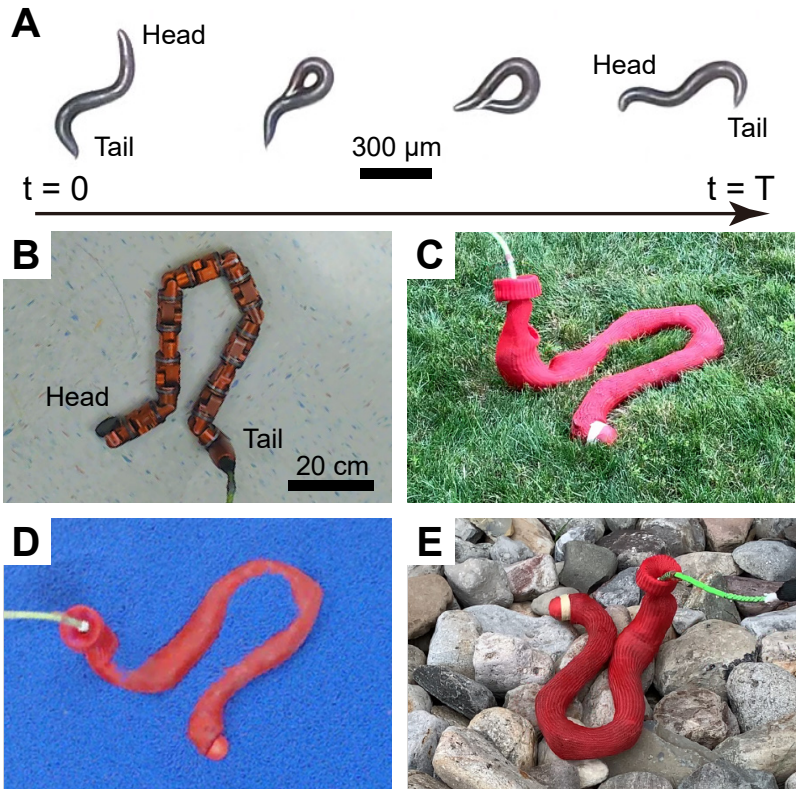

Figure 7.1: **The bio-inspired omega turn allows agile limbless robot in-place and in-plane reorientation.** (**A**) The omega (Ω) shaped turning behavior of the nematode worm *C. elegans* in a gait cycle. Limbless robot reorientation on various types of terrain: (**B**) flat hard ground, (**C**) rough grassland, (**D**) granular media, and (**E**) a pile of rocks. Figures are adapted from [103].

other principal component is observed to drive the turning motion. This suggests that a single traveling sinusoidal wave is not sufficient to describe turning behaviors. Based on this observation, and our further examination of the motions of *C. elegans*, we propose that omega turns can be represented by two planar sinusoidal waves with different spatial frequencies.This is a higher-dimensional gait representation than those in most prior snake robot gaits, but remains structured and low-dimensional while enabling a richer set of behaviors.

A family of two-wave turning gaits

Inspired by the body waves on the *C. elegans*, in this section we describe a template for a family of in-plane turning gaits. The template is a superposition of two coplanar traveling sinusoidal waves: a *forward wave* and a *turning wave*, with joint angles prescribed by

$$\theta_i(t) = A_f(t)\sin\left(2\pi\omega t + 2\pi k_f\frac{i}{N}\right) + A_o(t)\sin\left(2\pi\omega t + 2\pi k_o\frac{i}{N} + \psi\right), \tag{7.1}$$

where $A_{f,o}, \omega_{f,o}$ and $k_{f,o}$ represent the amplitude, the temporal frequency and the spatial frequency for the forward wave and the omega wave, t is the time, i is the index of the joint, N is the total number of joints, and ψ is the phase difference between two waves. Note that ω_f is kept the same as ω_o, and phases of the waves are defined as $\tau_f = 2\pi\omega_f t$ and $\tau_o = 2\pi\omega_o t + \psi$.

With the gait template in Equation 7.1, we fixed $k_f = 1.5$ and found omega turning motion emerging at $k_o = 1$, generating effective rotational displacement compared to other turning gaits. Thus the gait with $k_o = 1$ in Equation 7.1 was denoted by the omega turn for limbless robot. Using tools from geometric mechanics, we found the optimal phases for two waves in the template that maximize the turning angle of the robot body. We briefly review the process of optimization using geometric mechanics tools in the next section.

Geometric Mechanics

We apply the hierarchical geometric framework [158] to design omega turn gaits. Specifically, we propose to reconstruct omega turn by superposition of two traveling waves as in Equation 7.1. By defining $\tau_f = 2\pi\omega_f t$ and $\tau_o = 2\pi\omega_o t + \psi$, we form a four-dimensional shape variable $m = [A_f, \tau_f, A_o, \tau_o]^T$. The set of all shape variables is then defined as M. The gait path in the shape space can then be described as: $f : t \mapsto m, t \in S^1, m \in M$.

Some internal shapes lead to self-collision, which are not desired in robot implementation. Further, as we will discuss later, we modulate the turning by implementing joint

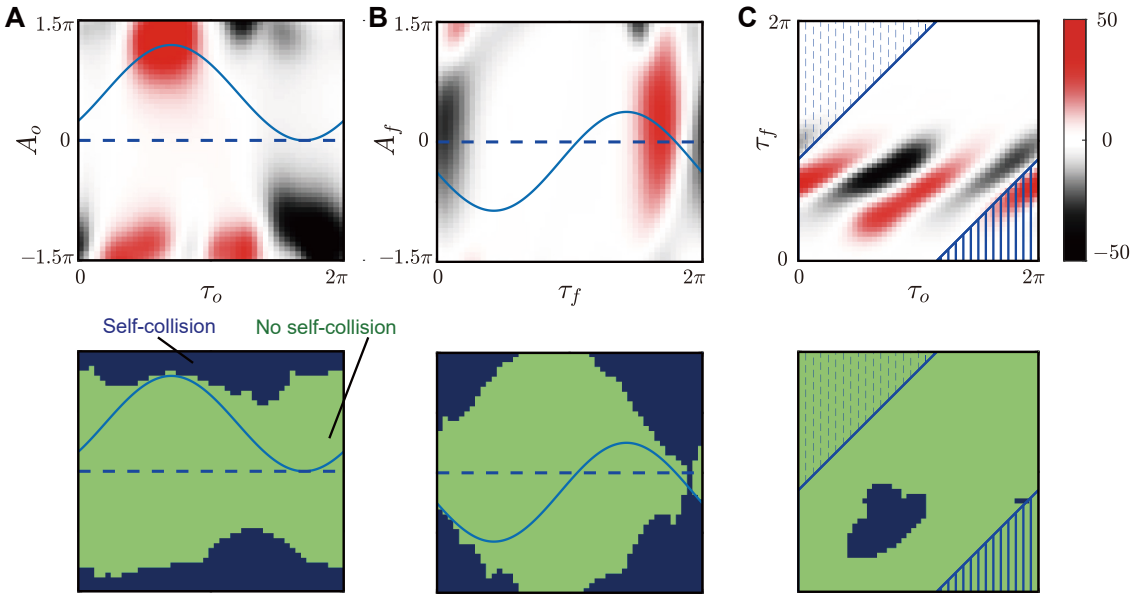

Figure 7.2: **The height functions on three 2-dimensional sub-shape spaces.** The height function (*top*) and self-collision region (*bottom*) on the shape space (**A**) $\{[\tau_o\ A_o], \tau_o \in S^1, A_o \in \mathbb{R}^1\}$, (**B**) $\{[\tau_f\ A_f], \tau_f \in S^1, A_f \in \mathbb{R}^1\}$, and (**C**) $\{[\tau_f\ \tau_o], \tau_f \in S^1, \tau_o \in S^1\}$. The red and black colors represent the positive and negative values of the height function on the top figures. The dark blue regions in the bottom figures represents the shapes that lead to self-collision. The blue curve shows the gait paths f_1, f_2 and f_3, designed to maximize the surface integral while not passing through the collision regions. The surface integrals in (A) and (B) is the integral of surface enclosed by the gait path and the dashed line; in (C) is the integral of surface enclosed in the lower right corner (shadow by solid line) minus the surface enclosed in the upper left corner (shadow by dashed line). Figures are adapted from [103].

angle limit, which also introduces infeasible regions in the shape space. In this way, with the geometry of each module (width: 5 cm, length: 7 cm, N = 8 unless otherwise stated), we construct a feasibility map on the shape space. We thus add the constraints that the gait path of f cannot pass through the infeasible region.

Note that τ_f and τ_o are cyclic. In this way, we can simplify the gait path in the four-dimensional shape space to three simple functions in the two-dimensional sub-shape spaces [158]: $f_1 : \tau_f \mapsto A_f$, $f_2 : \tau_o \mapsto A_o$, and $f_3 : \tau_f \mapsto \tau_o$ ($f_3^{-1} : \tau_o \mapsto \tau_f$). Given any two simple functions, we can reduce the shape space dimension to two. For example, given f_1, and f_3, Equation 7.1 becomes

$$\begin{aligned}\theta_i =& f_1(f_3^{-1}(\tau_o))\sin\left(f_3^{-1}(\tau_o) + 2\pi k_f \frac{i}{N}\right) \\ &+ A_o \sin\left(\tau_o + 2\pi k_o \frac{i}{N}\right) = \theta_i(A_o, \tau_o).\end{aligned} \tag{7.2}$$

Given Equation 7.2, we can reduce the original shape space to $\{[\tau_o\ A_o], \tau_o \in S^1, A_o \in \mathbb{R}^1\}$, from which we can numerically calculate the height function to optimize for f_2. Similarly, given f_1 and f_2, the height functions on $\{[\tau_f\ \tau_o], \tau_f \in S^1, \tau_o \in S^1\}$ can be numerically calculated; given f_2 and f_3 the height functions on $\{[\tau_f\ A_f], \tau_f \in S^1, A_f \in \mathbb{R}^1\}$ can be numerically calculated. In the optimization, we iteratively optimize the three simple functions f_1, f_2 and f_3 until a local maximum in turning angle per gait cycle is reached.

For computational simplicity, we reduce the search space of f_1, f_2 and f_3 by prescribing the functions below:

$$\begin{aligned}&f_1 : \tau_f \mapsto A_f, A_f = a_f(\gamma + \sin(\tau_f + \phi_f)), \\ &f_2 : \tau_o \mapsto A_o, A_o = a_o(1 + \sin(\tau_o + \phi_o)), \\ &f_3 : \tau_o \mapsto \tau_f, \tau_f = \tau_o - \psi.\end{aligned} \tag{7.3}$$

The converged height functions and gait paths are shown in Figure 7.2. It may be possible to obtain slightly higher performing gaits by using more complex functions to describe the trajectory through shape space, e.g. as in [159]. However, simpler functions of paths through the shape space are correspondingly easier to optimize and execute on the robot, while still nearing the performance from such complex functions.

Reference turning gaits

To validate the performance of the advanced omega turn gait in complex environments, we compare it with other commonly employed turning gaits in limbless robots, such as the offset turn [11, 160], the geometric turn [153], and the frequency turn [145, 106]. We give a brief review of these turning gaits that works as reference gaits in this work.

Offset turn: To achieve lateral undulation motion, limbless robots can actuate their joints following the *serpenoid curve* [11], an effective single sinusoidal wave template which is identical to the forward wave in Equation 7.1. A simple way to initiate turning motion while lateral undulating is to add a constant offset κ in the body curvature onto the sinusoidal wave, yielding

$$\theta_i(t) = A \sin\left(2\pi\omega t + 2\pi k \frac{i}{N}\right) + \kappa. \tag{7.4}$$

By tuning the offset parameter κ in Equation 7.4, the locomotion direction can be altered. Note that the offset turn can be achieved using the two-wave template in Equation 7.1 by letting $k_o = 0$.

Geometric turn: Dai *et al.* [153] engineered a turning gait using tools from geometric mechanics. Their work described the serpenoid curve Equation 7.4 as a weighted sum of sine and cosine modes, where weights served as the parameters of the shape space. By experimentally determining the local connection [161] relating trajectories in the shape space to those in the robot position space, a trajectory in the shape space was found to generate maximum displacement in the rotational position space. We refer to the gait that realizes the maximum displacement as the "geometric turn." Note that the geometric turn can be achieved using the two-wave template in Equation 7.1 by letting $k_o = k_f$.

Frequency turn: The frequency turn was developed while studying the sidewinding motion for limbless robots [145, 106]. In sidewinding motion, two sinusoidal traveling waves were separately implemented in the horizontal and the vertical planes, where the horizontal wave altered locomotion direction and the vertical wave governed the contact between the body and the environment. By modulating the ratio of spatial frequencies of the two waves, turning motion could be achieved, and was called as a "frequency turn." Compared to the in-plane turning gaits, the frequency turn allows the robot to partially lift its body out of the plane.

7.3 Numerical and experimental analysis

To evaluate the effectiveness of omega turn gaits, we performed numerical simulations and robophysical experiments.

In numerical simulations, under the assumption of quasi-static motion, we determined the instantaneous body velocity from the force and torque balance in ground reaction forces. The we obtain the body trajectory of the robot in the position space by integrating the body velocity throughout one period [161, 162]. We use kinetic Coulomb ground friction [163] ($F = -\mu\frac{v}{|v|}$, where F is the ground reaction force, and v is the body velocity) to model the ground reaction force on hard ground. Note that under the quasi-static assumption, the net displacement will be independent of the choices of μ. Then the angular displacement is determined by the orientation change of the averaged main body axis over one gait cycle.

In robophysical experiments, we used a limbless robot composed of 16 identical alternative pitch-yaw arranged rotary joints (CMU SEA snake robot [164]). The gaits were executed by controlling the positions of joints to follow a sequence of joint angle commands. Note that for 2D in-plane motion, we only command odd (yaw) joints to move with even (pitch) joint angle maintains zero. For each gait tested, we repeated the experiment three times. In each trial, we commanded the robot to execute three cycles of the gait. The motion of the robot was tracked by an OptiTrack motion capture system at a 120 FPS frequency with eight reflective markers affixed along the backbone of the robot.

7.4 Omega turn performance evaluation

Simulation-experiment comparison of an omega turn

We measured the rotation angle of the snake robot during a complete gait cycle using the positions tracked by the motion capture system, and compare them to the trajectory calculated in the numerical simulation. We observe close agreement between the simulation

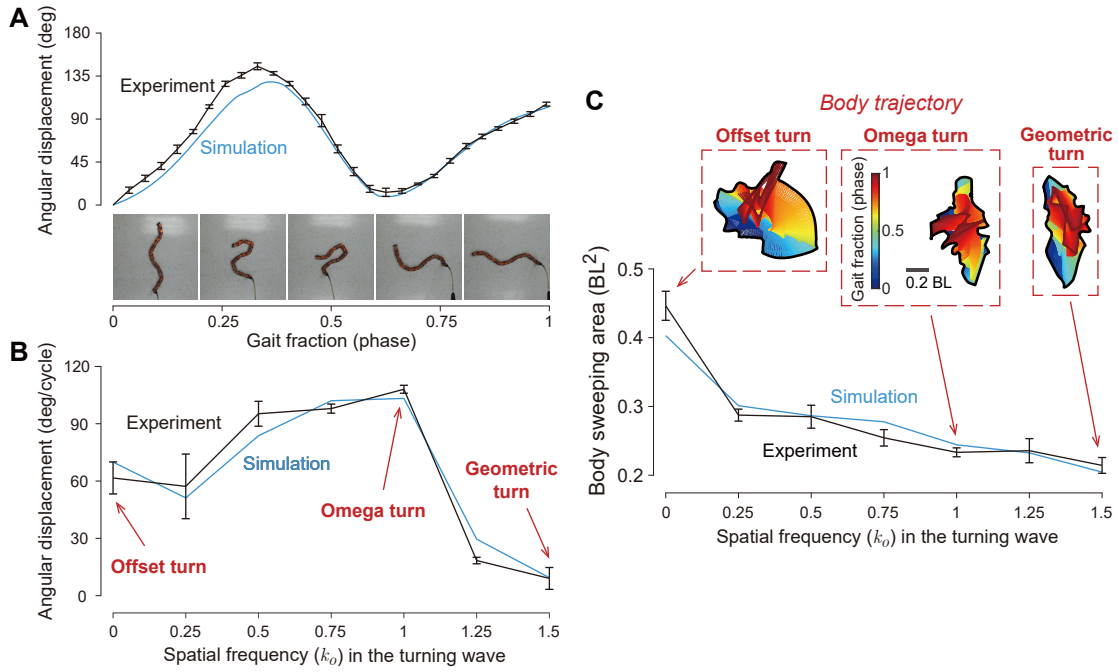

Figure 7.3: **Effectiveness of omega turn.** (**A**) Time evolution of the angular displacement in the simulation and the robot experiments during an omega turn. Each point represents the average over three trials. Error bars correspond to standard deviation in all plots/graphs. A sequence of video frames of the robot depicts the time evolution of the robot's body shape in 10 seconds. (**B**) The angular displacement for the turning gaits over a range of turning wave spatial frequencies (k_o) on flat ground. Error bars indicate the standard deviation. Omega turns have the largest angular displacement both in simulation and reality. (**C**) The area swept by the body for the turning gaits with varied turning wave spatial frequency k_o. The results are normalized by the robot body length squared (BL^2). The time evolution of robot's configurations executing the designed gaits over a period are shown in the red dashed boxes, where the gait fraction is indicated by colors from the beginning (blue) to the end (red). Figures are adapted from [102].

and the experimental results, as shown in Figure 7.3A. We illustrate a sequence of video frames depicts the time evolution of the robot's body shape. During the progression of an omega turn, the body first folds so that the anterior end of the body comes close to the posterior end of the body to form an omega (Ω) shape, and then unfolds to complete the turn.

Turning performance

Next, we compared the turning performance of the omega turn gait with other gaits in the two-wave gait family defined by Equation 7.1. With fixed temporal frequency $2\pi\omega = 0.1Hz$, we tested a range of gaits by sampling the spatial frequency of the turning wave k_o from $[0, 1.5]$ with a 0.25 stride, and conducted three trials for each gait. Notice that the gait with $k_o = 0$ is the offset turn, $k_o = 1.0$ is the omega turn, and $k_o = 1.5$ is the geometric turn. Figure 7.3B shows the results of the angular displacement per gait cycle for each gait. The simulation and experiment results share similar trends, in which the omega turn outperforms other gaits in the turning gait family. The average angular displacement of the omega turn is 105.7° ± 2.1°, while the average angular displacement of the offset turn and the geometric turn are 61.6° ± 8.4° and 9.0° ± 5.7°, respectively. The larger angular displacement per gait cycle implies that the omega turn is a more efficient turning strategy on flat ground.

Note that the offset turn we tested in these comparisons was optimized with a time-variant offset. The optimized time-varying offset turn consistently outperformed the constant offset turn, and so the latter was not included in our comparisons.

Area swept by the body

To evaluate the potential effectiveness of these turning gaits in confined spaces, we quantified the body-swept area per gait cycle. Assuming obstacles are randomly distributed throughout the environment, a smaller swept area corresponds to a lower likelihood of encountering obstacle interference. The body swept areas were obtained by computing the convex hull of all points the tracked positions on the robot passed through over the course of a cycle. These areas were averaged over three trials, and normalized by the body length squared (BL^2). Figure 7.3C depicts the body swept areas for the gaits tested. The body swept area for the omega turn is 0.25 ± 0.01 BL^2, while the body sweeping area for the offset turn is 0.46 ± 0.02 BL^2. As turning gaits with $k_o = 1.25$ and $k_o = 1.5$ (the geo-

metric turn) are the least effective on flat ground, swept areas for these settings are small because they did not generate as much turning motion on the robot. The omega turn has the smallest swept area per degree angular displacement achieved over the cycle. Smaller swept areas imply that the omega turn reduces the possibility of the robot colliding with obstacles, potentially allowing the robot to turn in narrower spaces.

7.5 Robustness of omega turn under varied conditions

Amplitude modulation

For highly maneuverable limbless locomotion in confined spaces, fine-tuning of the locomotive direction is often needed in order to follow a designated path or avoid jamming in between obstacles. Thus, it is important to modulate the turning gait to execute exact turning angles in limbless robot agile motion. To this end, we varied the parameters of the two-wave template Equation 7.1 to explore a simple way to modulate the rotational displacement of the robot.

We modulated the turning angle by controlling the joint angle limit, θ_{max}. In other words, we define a configuration to be infeasible if $\exists\, i \in \{1\ 2\ ...\ N\}$ such that $|\theta_i| > \theta_{max}$. In this way, we can numerically calculate the infeasible region on each sub-shape space and design gait path to avoid passing through it.

In amplitude modulation experiments, we fixed forward wave spatial frequency $k_f = 1.5$ and tested the gaits with omega wave spatial frequency k_o ranging from 0 to 1.5 on the flat hard ground. Figure 7.4 depicts the angular displacement per gait cycle as a function of k_o for three different joint angle amplitudes.

The robophysical experiments result shows that the omega turn gait ($k_o = 1$) is capable of producing $20.0° \pm 4.7°$, $64.2° \pm 2.7°$ and $108.0° \pm 2.1°$ of angular displacement per cycle under $\theta_{max} = 60°, 75°$ and $90°$, respectively. The modulation of joint angle amplitude between $60°$ and $90°$ can yield a turning angle within the range of $88°$, which is approximately 2 times larger than the range offset turn ($k_o = 0$) and geometric turn ($k_o = 1.5$) can

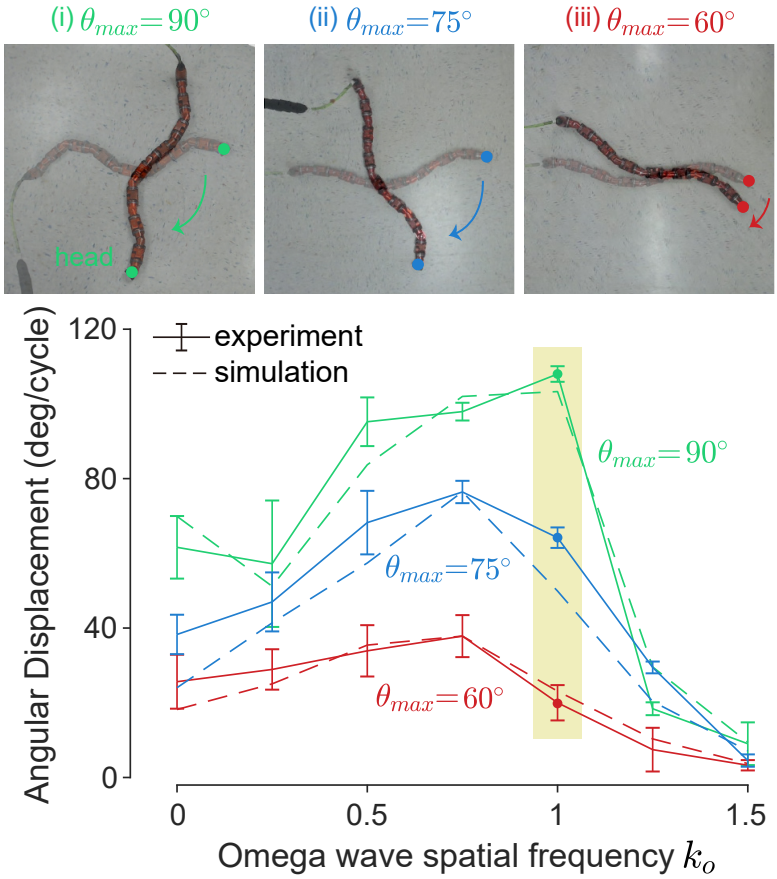

Figure 7.4: **Amplitude modulation of turning gaits.** The omega turn ($k_o = 1$, highlighted) displays the largest tunable range of angular displacement. Three time-lapse frames of robophysical experiments depicts the courses of turning with joint amplitude $60°, 75°$ and $90°$ in one gait cycle. Figures are adapted from [103].

produce ($36.1°$ and $5.8°$). This experiment demonstrates that the omega turn gait is capable of generating a continuous range of angular displacement via amplitude modulation, thus is a good candidate for applications in which high maneuverability is required.

Spatial frequency variation

In the previous sections, we fixed the spatial frequency of the forward wave (k_f) at 1.5. However, in practical applications, limbless robots must modulate k_f to better adapt to different environmental conditions. In this section, we explore how to design omega turn strategies when varying the spatial frequency of the forward wave.

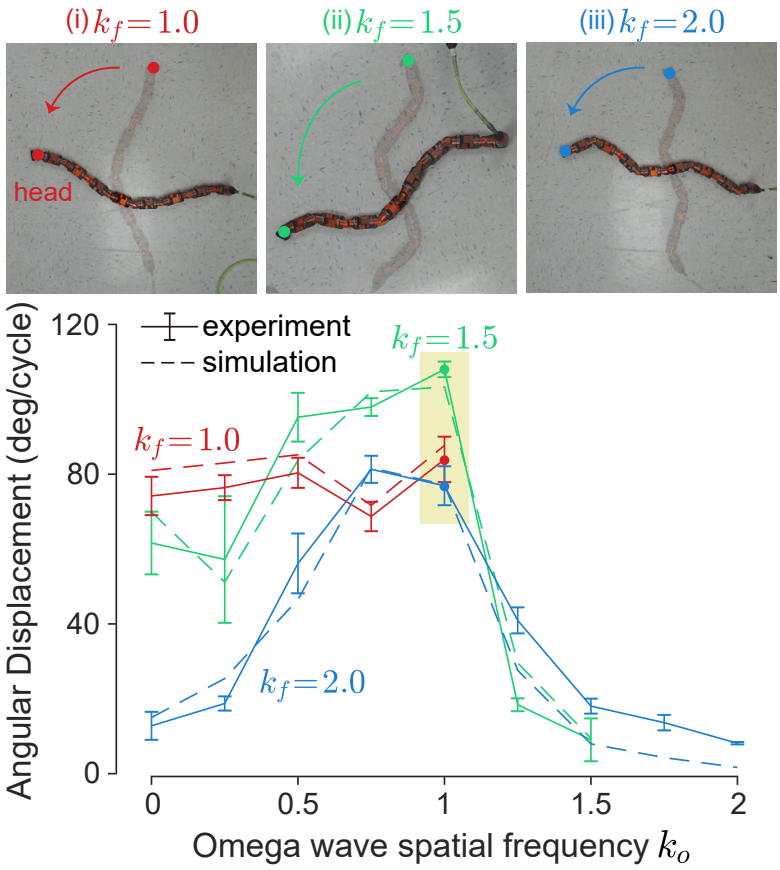

Figure 7.5: **Turning gaits with spatial frequency variation.** The omega turn ($k_o = 1$) performs robustly over different spatial frequencies of the forward wave k_f (number of waves on the body). Starting and ending positions of the omega turn with varied k_f are shown in the robot pictures. Figures are adapted from [103].

In this set of experiments, we fixed joint angle amplitude $\theta_{max} = 90°$, and tested a series of turning gaits with $k_o \in [0, k_f]$ on the flat hard ground over three forward wave spatial frequencies, $k_f = 1, 1.5$ and 2. The gaits are designed using the same methods as discussed in previous sections. Figure 7.5 illustrates the simulated and experimental result, while the robot images show the starting and ending positions of omega turns with different k_f.

The result verifies that the omega turn ($k_o = 1$) can provide consistent turning performance over k_f: $83.9° \pm 6.1°$, $108.0° \pm 2.1°$ and $76.9° \pm 5.2°$ angular displacement per cycle when $k_f = 1, 1.5$ and 2, respectively. Given the offset and the geometric turning gaits cannot maintain consistent turning performance, the omega turn is a better turning

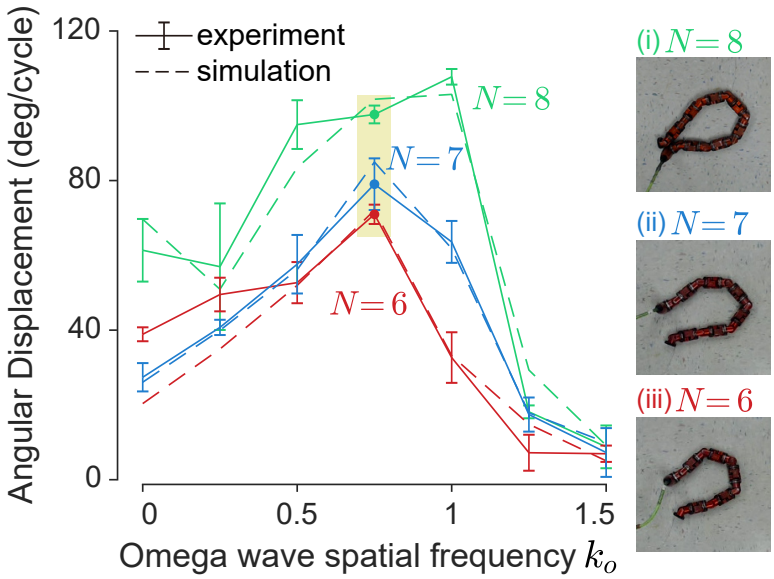

Figure 7.6: **Omega turn with different numbers of joints.** The omega turn can be generalized to different body lengths with fine tuning of omega wave spatial frequency, as the local maximum of angular displacement shifts to $k_o = 0.75$ as the joint number decreases. Robot pictures show the key frames when the robot has the largest local body curvature to form the "Ω" shape. Figures are adapted from [103].

strategy that can be employed conveniently in tasks when the limbless robot is operated with varying body shapes. Note that the omega turn and the geometric turn are identical when $k_f = 1$.

Omega turn with different numbers of joints

Based on needs of the task and constraints created by the environment, limbless robots are used with varying number of rotary joints. To expand the applicability of the omega turn strategy, we explored the omega turn for limbless robots with different numbers of joints.

We tailored the omega turn gait for different number of joints (N) and tested them on three limbless robots with 6, 7 and 8 of yaw joints. Figure 7.6 shows the result of turning performance for the family of gaits with $k_o \in [0, 1.5]$ with k_f fixed at 1.5 and θ_{max} fixed at $90°$. The gaits are designed using the same methods as discussed in previous sections. The turning performance of the omega turn ($k_o = 1$) drops modestly as number of joints decreases, and local maximum of turning performance shifts to $k_o = 0.75$ for the cases

of $N = 6$ ($71.2^\circ \pm 2.6^\circ$) and $N = 7$ ($79.3^\circ \pm 6.9^\circ$). We posit that this shift of local maximum results from that the head of the robot is no longer able to touch the tail with a shorter body length. For the robots with shorter body length, gaits with $k_o = 0.75$ allow a shorter distance between head and tail during the course of turn, enable a larger local body curvature, and thus larger angular displacement. When $N = 8$, $k_o = 0.75$ and $k_o = 1$ both ensure the head to touch the tail when turning. The result implies that, the omega turn gait is applicable to a wide range of limbless robots with varied body lengths through an alternation in the omega wave spatial frequency k_o, and offers improved turning performance compared to reference gaits.

7.6 Omega turn in complex environments

Omega turn in granular media

Limbless locomotion is not only employed on hard surfaces, but also has been demonstrated to be useful in granular substrates such as sand [146]. Therefore, we studied the turning motion in granular media using a test pool filled with 6mm plastic spheres.

We tested a series of turning gaits on the surface of granular media. Figure 7.7 depicts experiment data and a series of time-lapse key frames for the omega turn in granular media. In granular media, the omega turn ($k_o = 1$) can generate $78.5^\circ \pm 6.5^\circ$ angular displacement per cycle, while the offset turn and the geometric turn were ineffective ($2.9^\circ \pm 2.7^\circ$ and $4.8^\circ \pm 2.1^\circ$). This comparison indicates that, in granular media, the omega turn is capable of producing effective turning motion which is comparable to the performance on the flat hard ground, while other common turning strategies do not work well.

Compliant omega turn in a pillar array

Interacting with obstacles using proprioceptive torque sensors and deforming the body shape to comply to obstacles has been studied for limbless robot forward locomotion [150, 76]. We hypothesized that the application of the compliant control framework [150] on the

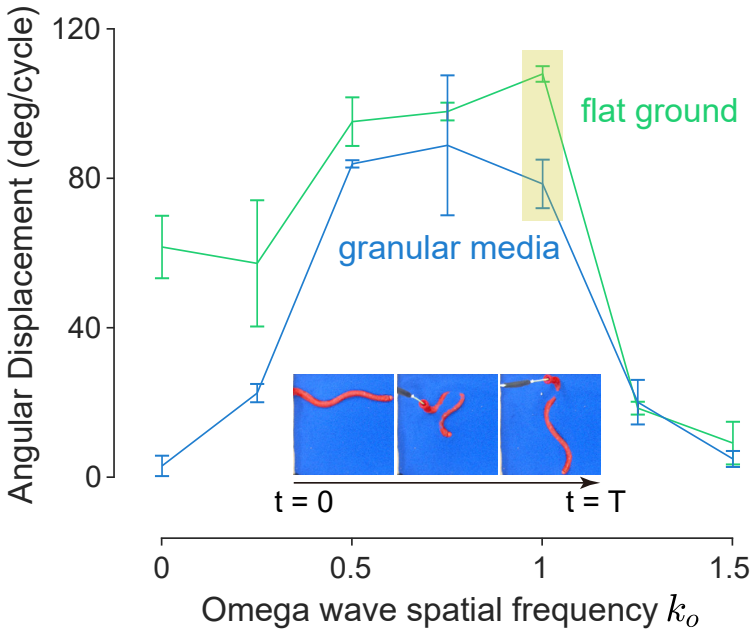

Figure 7.7: **Omega turns in granular media.** The omega turn ($k_o = 1$) produces the angular displacement that approaches that on the flat ground. A series of robot pictures show the course of omega turning in granular media. Figures are adapted from [103].

omega turn motion could enable the robot to compliantly negotiate obstacles during the course of turning.

As an extension of admittance control [165] to articulated locomotion, the compliant control framework for limbless locomotion assigns spring-mass-damper-like dynamics to the shape parameters in the gait equation to allow them to vary according to the sensed joint torques. In this work, we built the compliant control system on wave amplitudes $A = [A_f, A_o]^T$ in the two-wave template Equation 7.1 by

$$M\ddot{A} + B\dot{A} + K(A - A_0) = J\tau_{\text{ext}}, \tag{7.5}$$

where $M = \begin{bmatrix} 1 & 0 \\ 0 & 1 \end{bmatrix}$, $B = \begin{bmatrix} 8 & 0 \\ 0 & 8 \end{bmatrix}$, and $K = \begin{bmatrix} 8 & 0 \\ 0 & 8 \end{bmatrix}$ are positive-definite tuning matrices (2×2) that govern the dynamic response, $A_0 = [45°, 45°]^T$ is the nominal amplitude, τ_{ext} is the vector of external torques $(N \times 1)$ measured by the joint torque sensors, and $J =$

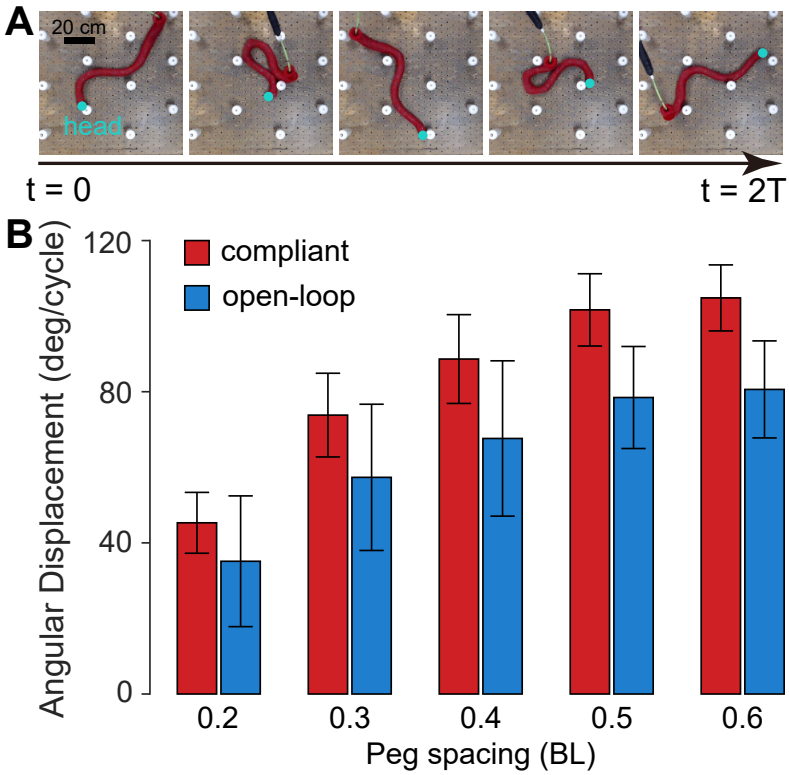

Figure 7.8: **Omega turn in a pillar array.** (**A**) Time-lapse images of a limbless robot executing the compliant omega turn in a pillar array with 0.3 BL spacing. (**B**) The omega turn with the compliant control applied in the pillar array with varied pillar spacing (in body lengths, BL). The compliant omega turn generates larger averaged turning angle compared to the open-loop turn, as well as performs more consistently (smaller error bars). Figures are adapted from [103].

$[\sin(2\pi\omega_f t + 2\pi k_f \frac{i}{N}), \sin(2\pi\omega_o t + 2\pi k_o \frac{i}{N})]^T$ is the Jacobian $(2 \times N)$ that maps the external torques onto the amplitude. We solved Equation 7.5 for $\ddot{A}$ and double integrated $\ddot{A}$ using Newton-Euler method for the amplitude. We refer readers to [150] for detailed explanation and demonstration of the compliant control framework on limbless robot locomotion.

We tested the compliant omega turn on an indoor artificial obstacle-rich environment—a board with a hexagonal array of pillars, and compared with open-loop omega turn in the same environment. Figure 7.8A illustrates the comparison of turning performance between open-loop and compliant omega turns, where the angular displacement increased by $\sim$30% with the compliant omega turn in all tested environments with various pillar spacing ranging from 0.2 body lengths (BL) to 0.6 BL. Furthermore, the compliant omega turn per-

formed more robustly with smaller variance in angular displacement in all environments, reflected by shorter error bars (standard deviation) than the open-loop variant. Figure 7.8B captures some key body shapes during two cycles of turning in a pillar array with 0.3 BL spacing.

Compliant omega turn on a rock pile

Finally, to test if our lab robophysical studies could show benefit in field robot application, we carried out field experiment by running the omega turn gait with compliance on an outdoor pile of rocks (diameter $\sim$0.3 BL) where distribution of obstacles and contact between body and environment are nondeterministic. We also tested the offset turn gait, the geometric turn gait, and the frequency turn gait [146] as references.

Figure 7.9A presents the averaged angular displacement on the rock pile for each of tested gaits, as well as their turning performance on the flat hard ground. Although performance of all the gaits drops when executed on the rock pile, the omega turn was still capable of generating a $\sim 100^{\circ}$ of angular displacement per cycle. Also, the performance of the omega turn was robust on the rock pile, given a small standard deviation of 6.4°. Selected key frames of the limbless robot executing an omega turn on the rock pile are presented in Figure 7.9B.

This set of experiments demonstrated that, with proper modulation and coordination of parameters in the gait template, the omega turn is able to outperform other turning strategies, which makes it a promising approach for effective and robust turning motion in agile limbless locomotion in complex environments.

7.7 Discussion

The results presented in this chapter demonstrate that the omega turn provides an effective and broadly applicable turning strategy for elongate limbless robots. By formulating the turn as a superposition of two traveling waves, we established a continuous extension of

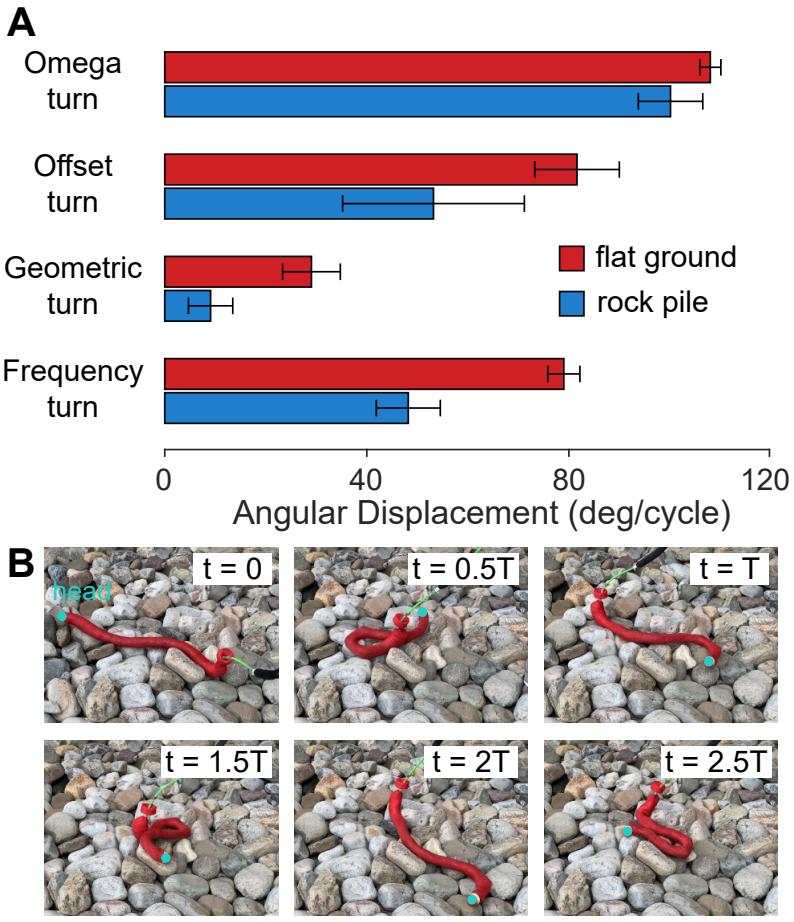

Figure 7.9: **Field test of omega turn.** (**A**) Comparison of different turning strategies on hard ground and on an outdoor rock pile. The omega turn outperforms other common turning strategies in both environments, and its performance on the rock pile ($100.1° \pm 6.4°$) approaches that on hard ground ($108.0° \pm 2.1°$). (**B**) Time-lapse frames show the omega turn enables agile reorientation of a limbless robot on the rock pile. Figures are adapted from [103].

the classic serpenoid template traditionally used for lateral undulation. This formulation allows turning and straight translation to be treated within a unified mathematical family of gaits, enabling smooth transitions between straight locomotion and reorientation without the need for additional control layers or discrete gait switching. Such continuity simplifies motion planning in cluttered or confined environments.

Implementation of the compliant controller on the CMU SEA snake robot further highlights the potential of embedding compliance into the omega turn framework. By assigning spring-mass-damper–like dynamics to the gait amplitudes, the robot was able to sense and

respond to environmental interactions through torque feedback, maintaining effective turning even when encountering obstacles. This demonstrates that compliance, if introduced at the actuation level, can offload substantial control complexity for sensing and feedback control. When translated to a cable-driven mechanism such as the MILR, this principle can be physically embodied within the actuation system itself. In this way, the compliant actuation mechanism can serve as the physical substrate for the control law realized in the SEA snake, achieving mechanical intelligence through the body rather than sensing and computation.

Together, these findings establish the omega turn as both a powerful locomotor template and a bridge between geometric mechanics-based gait design and compliance-assisted implementation.

CHAPTER 8
GAIT DESIGN FOR OBSTACLE-AIDED LOCOMOTION

8.1 Introduction

This chapter extends our study from mechanically intelligent implementations to the optimization of gait templates in obstacle-rich environments. In previous chapters, we demonstrated how mechanical intelligence enables limbless robots to navigate cluttered terrains through compliant body mechanics with serpenoid gaits. The results confirmed that appropriately tuned compliance facilitates obstacle negotiation without requiring active sensing or feedback. However, such performance was based on a prescribed gait pattern and thus did not guarantee optimality at the gait-design level.

In this chapter, we aim to determine how gaits themselves can be optimized when obstacles are taken explicitly into account. This analysis does not contradict the concept of mechanical intelligence; rather, it complements it by identifying how intelligent body–environment interactions can be further enhanced through optimized gait templates. Importantly, the approach developed here is general and can be applied to all limbless robots, regardless of their actuation mechanisms (e.g., cable-driven, servo-driven, or soft-bodied systems).

Elongate limbless locomotors have advantages in navigating confined spaces. For instance, the adaptation to cluttered environments is believed to be a source of evolutionary pressure for limblessness in Squamates (lizards and snakes) [166, 167]. To move through such cluttered environments, these animals have evolved the capability to push off their surroundings to locomote, a phenomenon known as obstacle-aided locomotion (OAL) [168, 131, 169]. Many biological limbless locomotors can even achieve higher speeds with OAL than in obstacle-free environments [131, 169], whereas legged locomotors often slow down

as heterogeneity increases [9, 170, 171, 172].

To replicate biological OAL in robotic systems, prior work has examined robot-obstacle interactions and their effects on locomotor performance. [13] developed physical models to quantitatively predict robot motion in obstacle fields, while [168] highlighted that obstacle forces are only beneficial when aligned with the desired direction of motion. Accordingly, obstacles can be classified as "beneficial" or "detrimental" depending on their geometric relation to the robot. More recently, shape-based compliant control has been introduced to improve locomotor performance among obstacles [150, 76]. However, most prior OAL studies have been based on predetermined traveling-wave gait templates, without designing gaits specifically for obstacle exploitation.

Geometric mechanics provides a powerful framework for gait design by decoupling locomotor motion into a shape space (internal joint angles) and a position space (world-frame displacement and orientation) [147, 173, 122]. However, existing geometric mechanics formulations have been restricted to obstacle-free environments, leaving gait design for heterogeneous settings an open problem.

In this chapter, we expand the scope of geometric mechanics to obstacle-rich terrains by integrating explicit robot–obstacle interactions into the framework. Specifically, we model obstacles as vertical posts randomly distributed on flat ground and map their presence from position space into constraints in shape space. This integration enables us to identify whether obstacles are beneficial or detrimental and to embed these constraints into gait optimization. By reformulating gait design as a discrete optimization problem on a graph, we identify a new class of elliptical gait templates that combine amplitude and phase modulation, specialized for sparsely distributed obstacle-rich environments. In contrast, traditional traveling-wave gait templates are found to perform best in densely distributed environments, consistent with prior experimental observations [168, 150]. These results are validated through robophysical experiments (Figure 8.1), confirming that body compliance and contact exploitation can together enable mechanically intelligent locomo-

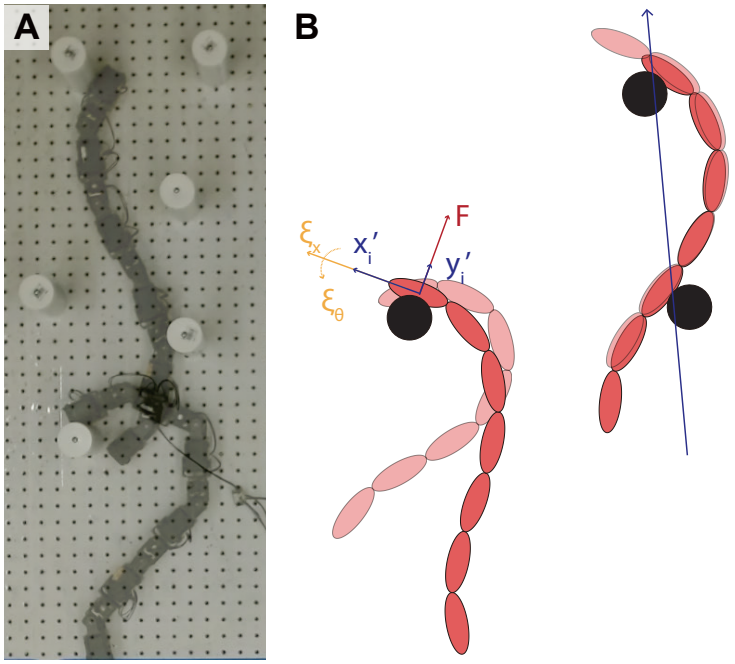

Figure 8.1: **Obstacle-aided locomotion of a robot and a theoretical model.** (**A**) Top view of the robot navigating among multiple obstacles. (**B**) The theoretical model for obstacle-aided locomotion with (*left*) a single obstacle and (*right*) multiple obstacles. Figures are adapted from [104].

tion in cluttered terrains.

This chapter is adapted from my previously published peer-reviewed work [104].

8.2 Geometric mechanics framework

In Chapter 6, we introduced the geometric mechanics framework as a tool to relate internal shape change to body displacement through the local connection matrix [147, 173, 122]. There, we derived the reconstruction equation, described the numerical derivation of the local connection matrix using resistive force theory [174, 175, 176]. Here, we briefly summarize the essential concepts to establish notation and then extend geometric mechanics to include the effect of obstacles.

In systems where inertial effects are negligible ([177]), geometric mechanics gives the

so-called reconstruction equation for computing body velocities from shape velocities.

$$\boldsymbol{\xi} = \boldsymbol{A}_r(\boldsymbol{r})\dot{\boldsymbol{r}}, \tag{8.1}$$

where $\boldsymbol{\xi} = [\xi_x, \xi_y, \xi_\theta]$ denotes the body velocity in the forward, lateral, and rotational directions; $\boldsymbol{r}$ denotes the internal shape variables (joint angles); $\boldsymbol{A}_r(\boldsymbol{r})$ is the local connection matrix, which encodes environmental constraints and the conservation of momentum. The analysis and visualization power of geometric mechanics is particularly effective when the shape variable is 2-dimensional, i.e., $\boldsymbol{r} \in \mathbb{R}^2$. In the applications where there are more than 2 joints (e.g. N degrees-of-freedom), we use two shape basis functions [178] to reduce the dimensionality of the system:

$$\boldsymbol{r} = [\boldsymbol{\beta}_1,\ \boldsymbol{\beta}_2]\,\boldsymbol{w},\ \ \boldsymbol{\xi} = \boldsymbol{A}_r\Big(\boldsymbol{r}(\boldsymbol{w})\Big)\dot{\boldsymbol{w}} = \boldsymbol{A}(\boldsymbol{w})\dot{\boldsymbol{w}} \tag{8.2}$$

where $\boldsymbol{\beta}_1,\ \boldsymbol{\beta}_2 \in \mathbb{R}^N$ are shape basis functions, $\boldsymbol{w} \in \mathbb{R}^2$ is the reduced shape variable, and $\boldsymbol{A}$ is the local connection matrix expressed with respect to reduced shape variables. In applications to limbless robots with N joints, the shape basis functions are often chosen to be:

$$\boldsymbol{\beta}_1(i) = \sin\left(2\pi f_s \frac{i}{N-1}\right),\ \ \boldsymbol{\beta}_2(i) = \cos\left(2\pi f_s \frac{i}{N-1}\right) \tag{8.3}$$

where f_s is the number of spatial waves, i denotes the joint index.

The local connection matrix $\boldsymbol{A}(\boldsymbol{w})$ is obtained numerically using resistive force theory (RFT) to model ground reaction forces [174, 175, 176]. In this formulation, each body segment experiences tangential and normal reaction components $\boldsymbol{F}_\parallel$ and $\boldsymbol{F}_\perp$, which depend on body velocity $\boldsymbol{\xi}$, shape $\boldsymbol{w}$, and shape velocity $\dot{\boldsymbol{w}}$ [163, 165]. Assuming quasi-static motion, the net force on the system satisfies

$$\boldsymbol{F} = \sum_{i=1}^{N} \left[\boldsymbol{F}_\parallel^i(\boldsymbol{\xi}, \boldsymbol{w}, \dot{\boldsymbol{w}}) + \boldsymbol{F}_\perp^i(\boldsymbol{\xi}, \boldsymbol{w}, \dot{\boldsymbol{w}})\right] = 0, \tag{8.4}$$

which implicitly relates $\dot{\boldsymbol{w}}$ and $\boldsymbol{\xi}$. Applying the implicit function theorem and linearization yields the local connection matrix $\boldsymbol{A}(\boldsymbol{w})$, computed in practice using the MATLAB function *fsolve*. Detailed derivations and validation procedures are presented in Chapter 6.

Each row of $\boldsymbol{A}(\boldsymbol{w})$ defines a connection vector field describing how shape change contributes to translation and rotation. The displacement of the body over one gait cycle with shape path $\partial\phi$ is obtained by integrating these vector fields [161]:

$$\begin{pmatrix} \Delta x \\ \Delta y \\ \Delta\theta \end{pmatrix} \approx \int_{\partial\phi} \boldsymbol{A}(\boldsymbol{w})\,\mathrm{d}\boldsymbol{w} = \iint_{\phi} -\mathrm{d}\boldsymbol{A}(\boldsymbol{w})\,\mathrm{d}w_1\mathrm{d}w_2, \tag{8.5}$$

where ϕ denotes the area enclosed by the gait loop in shape space. The term $-\mathrm{d}\boldsymbol{A}(\boldsymbol{w})$ represents the curl of the connection vector field, and its distribution defines a height function whose extrema correspond to efficient gait regions.

To account for noncommutative effects between rotation and translation, a Lie-bracket correction term $[\boldsymbol{A_1}, \boldsymbol{A_2}]$ may be included [161, 179], giving the corrected displacement field

$$D\boldsymbol{A}(\boldsymbol{w}) = -\mathrm{d}\boldsymbol{A}(\boldsymbol{w}) + [\boldsymbol{A_1}, \boldsymbol{A_2}]. \tag{8.6}$$

The three rows of $D\boldsymbol{A}(\boldsymbol{w})$ form height functions for the forward, lateral, and rotational directions, respectively. Full derivations and explanation can be found in [104].

Limbless locomotors typically show limited mobility on hard ground [180, 181], indicating a geometric symmetry that restricts net displacement. The presence of obstacles can break this symmetry and thus enhance locomotion. To examine this effect, we compared height functions $D\boldsymbol{A}(\boldsymbol{w})$ across different spatial wave numbers ($f_s = \{1,\, 0.5\}$ in Equation 8.3). Although both produce negligible intrinsic propulsion in smooth environments, their geometric properties differ: at $f_s = 1$, neither the forward velocity integral nor the Lie bracket term contributes significantly to translation, while at $f_s = 0.5$, these two terms

have opposite directions and comparable magnitudes. This suggests that when lateral reaction forces are introduced, such as through obstacle contacts, they can be redirected into forward motion for certain spatial frequencies. To generalize this observation, We used the Frobenius norm to approximate the magnitude of the vector field across spatial frequencies and found that gaits with $f_s \approx 0.5$ are most sensitive to lateral forces. This geometric interpretation reveals how obstacle interactions can be leveraged to assist motion and motivates the extension of geometric mechanics in the following section to explicitly include obstacle effects in gait optimization.

8.3 Gait design with single obstacle in contact

Geometric model

In this section, we establish a new method to numerically calculate the connection vector field, respecting the interactions between the robot and obstacles in its environment. Note that to simplify our analysis, we assume that the friction between the robot and the obstacle is negligible.

Consider one obstacle in contact with the robot. Index i_0 denotes the link of contact. We further assume that i_0 does not change in each obstacle-interaction instance. This assumption is later justified in robot experiments.

For simplicity, our analysis below assumes that the obstacle resides on the left hand side (LHS) of link i_0. The analysis for the right hand side (RHS) obstacle will be symmetric to our analysis below. Existence of the obstacle will restrict the lateral body velocity $\xi_y \geq 0$. In this way, there are two mutually exclusive conditions for the lateral body velocity:

1) $\xi_y = 0$: In this case, the robot will remain in contact with the obstacle. If we assume that the friction between the robot and the obstacle is negligible, then the net force from obstacle to robot (F) will align with the lateral direction (y_i') of the body frame in link i_0. In the body frame of link i_0, the interaction between the obstacle and the robot only contributes in the lateral direction. In other words, the force and torque balance in forward

and rotational directions are independent from the interactions with obstacles. In this way, we can rewrite Equation 8.4 into:

$$\boldsymbol{F} = \sum_i \left(\boldsymbol{F}^i_{\parallel}(\begin{pmatrix} \xi_x \\ 0 \\ \xi_\theta \end{pmatrix}, \boldsymbol{w}, \dot{\boldsymbol{w}}) + \boldsymbol{F}^i_{\perp}(\begin{pmatrix} \xi_x \\ 0 \\ \xi_\theta \end{pmatrix}, \boldsymbol{w}, \dot{\boldsymbol{w}}) \right) = \begin{pmatrix} 0 \\ F \\ 0 \end{pmatrix}. \tag{8.7}$$

In Equation 8.7, there are two variables and two equality constraints, allowing us to determine the local connection vector field.

In the case where there is non-negligible friction, we can also calculate the frictional force as a function of the known friction coefficient and normal-direction reaction force between the obstacle and the robot:

$$\boldsymbol{F} = \sum_i \left(\boldsymbol{F}^i_{\parallel}(\begin{pmatrix} \xi_x \\ 0 \\ \xi_\theta \end{pmatrix}, \boldsymbol{w}, \dot{\boldsymbol{w}}) + \boldsymbol{F}^i_{\perp}(\begin{pmatrix} \xi_x \\ 0 \\ \xi_\theta \end{pmatrix}, \boldsymbol{w}, \dot{\boldsymbol{w}}) \right) = \begin{pmatrix} \mu F \\ F \\ 0 \end{pmatrix}. \tag{8.8}$$

where μ is the friction coefficient. Equation 8.8 has three variables and three equality constraints, also allowing us to determine the local connection vector field.

2) $\xi_y > 0$: In this case, the robot will leave the obstacle. In this way, original force and torque balance in Equation 8.4 are still valid to determine the local connection vector field.

Inequality constraints

With the two mutually exclusive interactions conditions, it is thus important to establish a criterion to evaluate the direction of ξ_y. We first explore the conditions where the robot leaves the obstacle. Specifically, from the equation of motion (Equation 8.2), the lateral velocity ξ_y can be approximated by:

$$\xi_y = \boldsymbol{A}_y(\boldsymbol{w})\dot{\boldsymbol{w}}, \tag{8.9}$$

where $\boldsymbol{A}_y(\boldsymbol{w})$ is the second row of the local connection matrix $\boldsymbol{A}(\boldsymbol{w})$. On the one hand, if $\boldsymbol{A}_y(\boldsymbol{w})\dot{\boldsymbol{w}} > 0$, the robot will leave the obstacle, which is consistent with our assumed condition. In this case, Equation 8.9 is valid in accordance with Equation 8.4, where we use condition (2) to determine the local connection matrix. On the other hand, if $\boldsymbol{A}_y(\boldsymbol{w})\dot{\boldsymbol{w}} \leq 0$, the robot will keep engaging with the obstacle, which contradicts our assumption. In this case, Equation 8.9 is not valid, and we will use Equation 8.7 and condition (1) to determine local connection matrix.

Gait Design

With the above model, we can now design gaits. With the optimal gait, the robot should take the best advantage of each obstacle-interaction and leave the obstacle only when necessary. Consider the joint angle limit being θ_m ($w_1, w_2 \in [-\theta_m, \theta_m]$. Let $\Phi = \{\phi : [0,T] \rightarrow [-\theta,\theta] \times [-\theta,\theta]\}$ be the collection of all paths in the shape space; let V_1 be the local connection vector field generated from condition 1 (Equation 8.7); and $V_2 = \boldsymbol{A}_y(\boldsymbol{w})$. The gait optimization problem becomes a line integral subject to direction constraints:

Problem 1. *Find the path $\phi \in \Phi$, subject to: $\frac{d\phi(t)}{dt} \cdot V_2\Big(\phi(t)\Big) > 0 \; \forall \; t \in [0,T]$, such that $\int_0^T \frac{d\phi(t)}{dt} \cdot V_1\Big(\phi(t)\Big)\mathrm{d}t$ is maximized.*

Assuming $i_0 = 1$, we showed an example of V_1 and V_2 in Figure 8.2.

Numerical Optimization

In practice, we discretize the shape space into a $(n+1) \times (n+1)$ lattice grid, where n is a suitable positive integer. The values of V_1 and V_2 are then numerically calculated at the grid points: $V_i(x,y) = \Big[V_{i,1}(x,y), V_{i,2}(x,y)\Big]$ where $i = 1, 2$ and (x,y) is a discretized element in the shape space. We optimize ϕ among lattice paths with horizontal and vertical line segments. V_2 is one part of the vector fields for locomotion in isotropic environment; thus it is reasonable to assume that V_2 is a conservative vector field. Then we can compute a potential function $P(x,y)$ defined on the shape space such that V_2 is the gradient of $P(x,y)$.

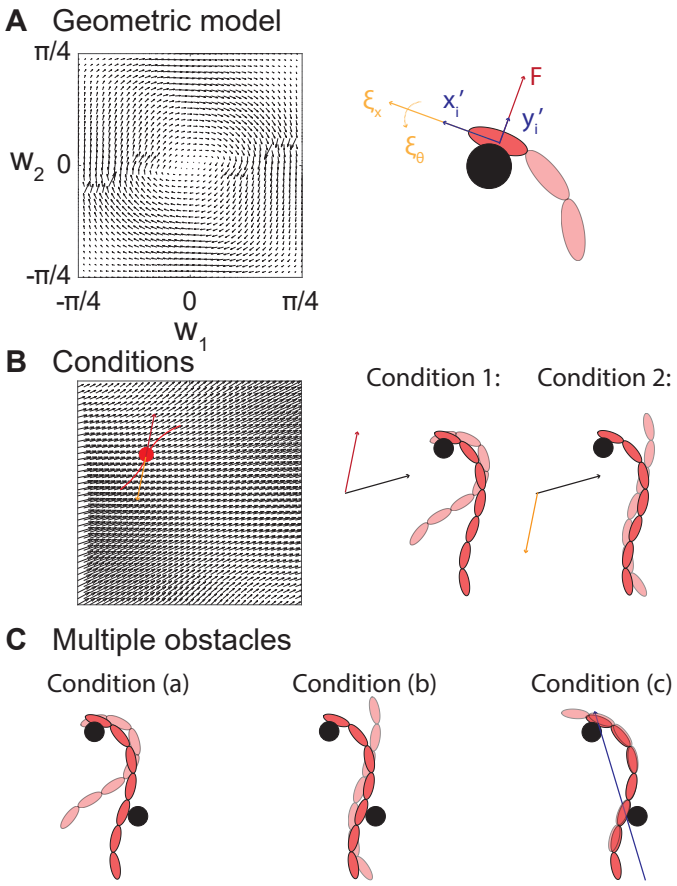

Figure 8.2: **Modeling interactions between the robot and obstacles.** (**A**) (*Left*) The vector field V_1 assuming the obstacle has interactions with the head link ($i_o = 1$). (*Right*) Force relationship illustrations for interactions between robot and obstacle. (**B**) (*Left*) The vector field V_2 assuming the obstacle has interactions with the head link ($i_o = 1$). (*Right*) Two conditions are compared. (**C**) OAL with multiple obstacles. Three conditions are compared. Note that in condition (c), obstacles constrain the lateral and rotational oscillation of robot's central body axis (blue arrow). Figures are adapted from [104].

We consider a weighted directed graph $G = (U, A)$, where the set of vertices U consists of the $(n + 1) \times (n + 1)$ lattice points (We chose the letter U (instead of V) to represent collections of vertices to avoid notation confusion with $V_{1,2}$ as in vector fields). In this way, at each vertex $u = (x, y) \in U$, there are 4 adjacent vertices: $\{(x \pm 1, y), (x, y \pm 1)\}$. The arcs are constructed in the following way:

a) If $P(x + 1, y) > P(x, y)$, then we add an arc from (x, y) to $(x + 1, y)$ with weight $V_{1,1}(x, y)$ to A;

b) If $P(x-1,y) > P(x,y)$, then we add an arc from (x,y) to $(x-1,y)$ with weight $V_{1,1}(x,y)$ to A;

c) If $P(x,y+1) > P(x,y)$, then we add an arc from (x,y) to $(x,y+1)$ with weight $V_{1,2}(x,y)$ to A;

d) If $P(x,y-1) > P(x,y)$, then we add an arc from (x,y) to $(x,y-1)$ with weight $V_{1,2}(x,y)$ to A;

Thus, the existence of an arc $a_{ij} \in A$ (from vertex u_i to u_j, $u_i, u_j \in U$) indicates that the move from u_i to u_j has positive dot product in V_2. The weight of a_{ij} denotes the line integral from u_i to u_j along V_1.

Lemma 2. *G is a directed acyclic graph (DAG).*

Proof of Lemma 2. Let C be a directed cycle in G. From our previous assumptions, every arc in C has positive dot product in V_2. Thus, the sum of all dot product of arcs in C and V_2 must be strictly positive. This indicates that there exists a path in a conservative vector field (V_2) with positive strictly line integral, which violates our assumption. Therefore, there is no directed cycle in G. □

With the aforementioned notation, a discretized version of Problem 1 becomes

Problem 3. *Find a simple directed path in $G = (U, A)$ with maximal weight.*

It is well-known that Problem 3 in a DAG has a linear-time algorithm if the starting point is fixed [182, p. 661]. So we can run this algorithm once for each vertex in U to solve Problem 3. Since $|U| = (n+1)^2$, our algorithm has time complexity $O(n^4)$. We implemented this algorithm in MATLAB and found optimal paths in our lattice grid.

Gait identification

From the algorithms introduced before, we solve Problem 1 and identify the effective gait paths ϕ_{LHS} with link of contact varying from 1 (head) to 3 (mid-body) in Figure 8.3A. We

define a gait path to be effective if it can cause net displacement greater than 0.1 body length (BL). Note that ϕ_{LHS} (colored red) denotes gait paths designated for robot interacting with an obstacle on the left-hand-side. From symmetry, we can identify ϕ_{RHS} with an obstacle on the right-hand-side (colored blue). Note that no gait path can lead to displacement higher than 0.1 BL when interacting with obstacles on mid-body links ($i_0 = 3$). In Figure 8.3A (right), we illustrate the optimal gait path which causes displacement of 0.06 BL.

From Figure 8.3A, we notice that the number of effective gait paths decreases as the link of contact transitions from head to mid-body links. Further, the properly designed gait path can cause up to 0.35 BL (per cycle) when interacting with the head link; whereas it can only cause 0.12 and 0.06 BL when i_0 changes to 2 and 3 respectively. Therefore, our results indicate that it is desired to interact with obstacles from head link rather than mid-body links.

We further observe from Figure 8.3A (left) that almost all effective gait paths emerge to be (at least a part of) elliptical paths. To quantify this observation, we fit the collection of effective gaits with an oriented ellipse. An ellipse with flatness (defined as the ratio of short-axis and long-axis) around 0.5 can reasonably fit effective gait paths. The ellipse oriented at angle of $\pi/4$ with respect to the horizontal axis.

8.4 Gait design with multiple obstacles in contact

Now we consider multiple obstacles in contact with the robot. Similar to our analysis before, there are three conditions with respect to the status of robot leaving/engaging obstacles:

a) Robot only interacts with one obstacle. In this case, the robot will only remain contact with one of the obstacle. This condition is similar to condition (1) in the previous section.

b) Robot leaves all obstacles. In this case, the robot will leave all obstacles, which is similar to condition (2) in the previous section.

c) Robot interacts with multiple obstacles. In this case, the robot will remain contact with

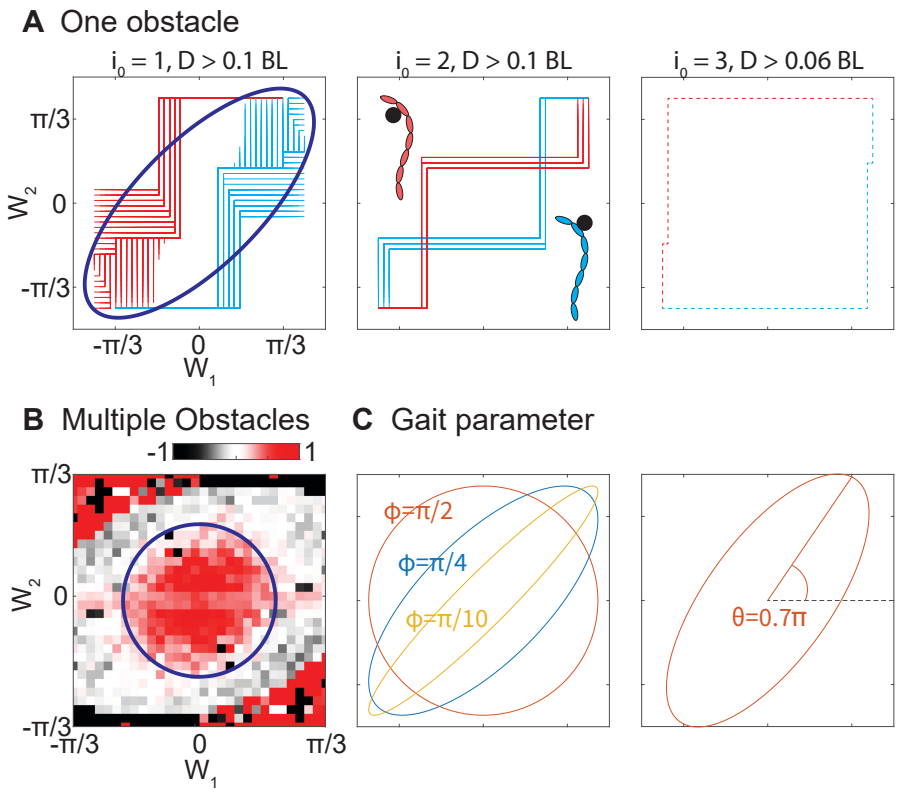

Figure 8.3: **Identification of gait templates.** (**A**) Collection of effective OAL gaits for (*left*) $i_0 = 1$, (*middle*) $i_0 = 2$, and (*right*) $i_0 = 3$. We consider a gait to be effective if it can produce displacement greater than 0.1 BL (body length). Note that there is no effective gait for $i_0 = 3$. We illustrate the optimal gait with $D = 0.05$ for $i_0 = 3$. (**B**) Height function for OAL among densely-distributed obstacles. (**C**) Parameter variation. (*Left*) An illustration of ellipse eccentricity variation by manipulating ϕ. (*Right*) An illustration of ellipse orientation variation by manipulating θ. Figures are adapted from [104].

more multiple obstacles. As illustrated in Figure 8.2C, the presence of multiple obstacles restricts the lateral oscillation and rotational oscillation of the central body axis on robot (assuming the friction is negligible). The definition of central body axis frame can be found in [178, 163]. In other words, in the body reference frame of central body axis, we have:

$$\boldsymbol{F} = \sum_i \left(\boldsymbol{F}^i_{\parallel}(\begin{pmatrix} \xi_x \\ 0 \\ 0 \end{pmatrix}, \boldsymbol{w}, \dot{\boldsymbol{w}}) + \boldsymbol{F}^i_{\perp}(\begin{pmatrix} \xi_x \\ 0 \\ 0 \end{pmatrix}, \boldsymbol{w}, \dot{\boldsymbol{w}}) \right) = \begin{pmatrix} 0 \\ F_y \\ F_\tau \end{pmatrix}. \tag{8.10}$$

In Equation 8.10, there is only one variable and one equality constraint, allowing us to determine the local connection vector field.

Note that the condition determination for when the robot is in contact with multiple obstacles can be challenging, which likely requires sensing and compliance as indicated in prior work. However, consider the case where the obstacles are so densely distributed that the robot will inevitably interact with multiple obstacles. In this case, we can simply assume that condition (c) is always valid and calculate the height functions to determine the optimal gaits. We illustrate the height function in Figure 8.3B. We notice that a traveling-wave gait path emerges as an optimal gait in environments with densely-packed obstacles.

8.5 Obstacle-aided locomotion with sparsely distributed obstacles

In robophysical experiments, we used a limbless robot composed of 11 identical alternative pitch-yaw arranged rotary joints using Dynamixel AX-12a motors. The gaits are executed by controlling the positions of joints to follow a sequence of joint angle commands. Note that for 2D in-plane motion, we only command odd (yaw) joints to move while the even (pitch) joint angles are held at zero. For each gait tested, we repeat the experiment at least six times. In each trial, we commanded the robot to execute three cycles of the gait. The motion of the robot is tracked by an OptiTrack motion capture system at a 120 FPS frequency with eight reflective markers affixed along the midline of the robot.

From our framework, we predicted that elliptical gaits can have the best performance among sparsely distributed obstacles. To test our prediction, we constructed a sparsely-distributed obstacle-rich environments. Note that in our experiments, the friction between our robophysical model and the obstacles can be considered negligible. The obstacles are randomly positioned in the track (Figure 8.4). We then conduct robophysical experiments and evaluate the OAL performance of various gaits.

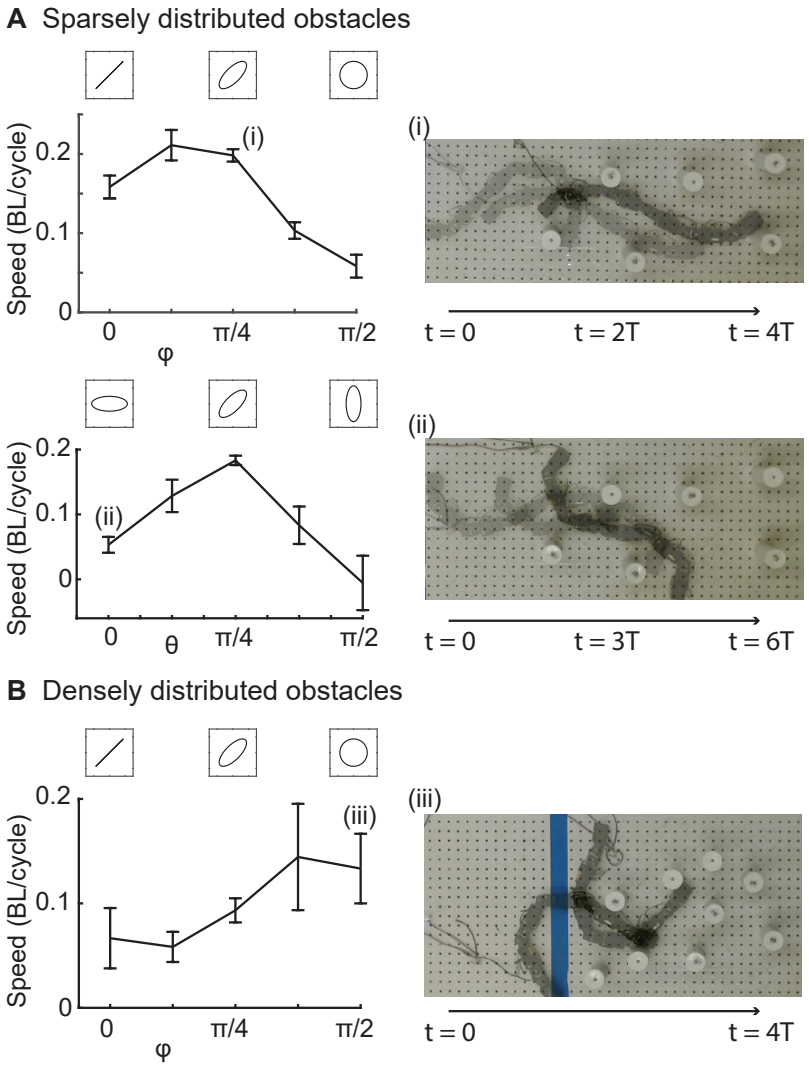

Figure 8.4: **Robophysical OAL experiments.** (**A**) Sparsely distributed obstacles. (*Top*) OAL performance as a function of ϕ (for fixed $\theta = \pi/4$). Elliptical gaits ($\phi \sim \pi/4$) leads to the best OAL performance. (i) Snapshots of robot execute elliptical gaits ($\phi = \pi/4$) among sparsely distributed obstacles. (*Bottom*) OAL performance as a function of θ (for fixed $\phi = \pi/4$). Elliptical orientation ($\theta = \pi/4$) lead to the best OAL performance. (ii) Snapshots of robot execute uncoordinated elliptical gaits ($\theta = 0$) among sparsely distributed obstacles. (**B**) Densely distributed obstacles. OAL performance as a function of ϕ. Circular gaits ($\phi = \pi/2$) leads to the best OAL performance. (iii) Snapshots of robot execute traveling-wave gaits ($\phi = \pi/2$) among densely distributed obstacles. Figures are adapted from [104].

Varying ellipse eccentricity

We first test gaits with varied eccentricity. Specifically, prescribe the reduced shape variable by $w_1(t) = w_m \sin(\omega t),\ w_2(t) = w_m \cos(\omega t + \phi)$, where ω is the temporal frequency, w_m

is the amplitude, and ϕ controls the eccentricity. As illustrated in Figure 8.3C, varying ϕ can facilitate the transition from standing wave ($\phi = 0$) to traveling wave ($\phi = \pi/2$) in the shape space. In our theoretical analysis, we predicted that $\phi = \pi/4$ can have the best OAL performance. We test gaits with different ϕ among sparsely-distributed obstacles. We notice that $\phi = \pi/4$ indeed outperforms other gaits, including standing wave and traveling wave (Figure 8.4).

To explore the principle behind the advantage of the elliptical gaits, we measured the duration of obstacle-contact in these experiments. Here, we defined the duration of contact by the average fraction that the robot is interacting with obstacles τ/T, where τ is empirically measured average contact duration (Figure 8.5) and T is the gait period. We notice the contact duration in the standing-wave gait is significantly lower than the elliptical-wave and traveling-wave gaits, indicating that the standing-wave gait has the lowest duration of beneficial contact between robot and obstacle. We also measured the attack angle between the robot and the obstacle. It is defined as the angle between the head link and the obstacle at the end of the robot-obstacle interaction, where larger attack angle indicates greater push from the obstacle to robots. As shown in Figure 8.5, the attack angles in the traveling-wave gait are significantly lower than the elliptical and standing wave gaits, indicating that the traveling wave gait can take the least advantage of the obstacle.

Varying ellipse orientation

We further explore the optimal ellipse eccentricity. Consider an elliptical gait with $\phi = \pi/4$. We define (θ) as the angle between the long axis and the horizontal axis. We illustrate an example gait with $\theta = \{0.45\pi,\ 0.7\pi\}$ in Figure 8.3C. From our theoretical analysis, we predict that $\theta = \pi/4$ can cause the optimal OAL performance. Robophysical experiments verified our prediction that $\theta = \pi/2$ causes the best OAL performance.

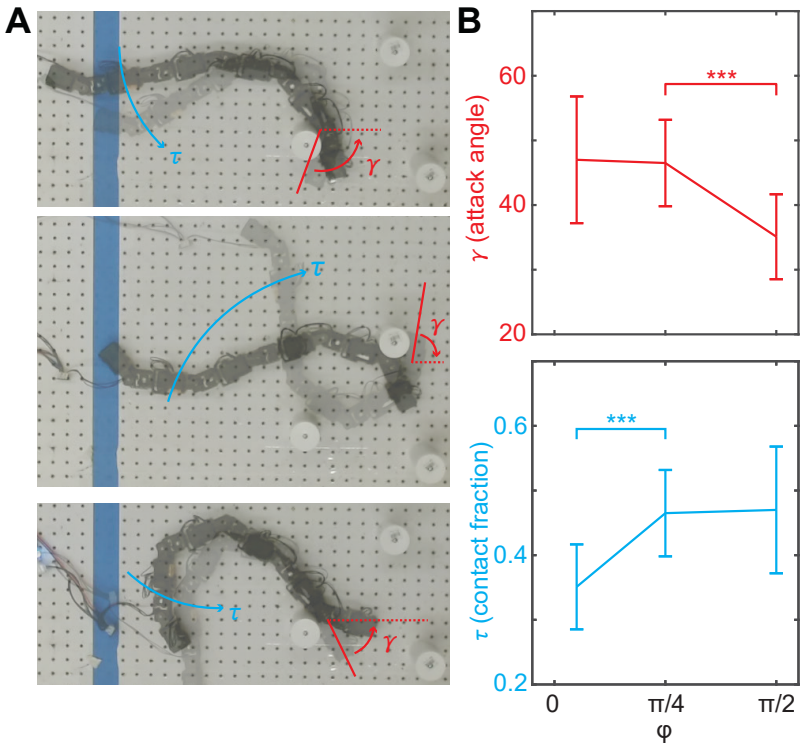

Figure 8.5: **Advantage of elliptical gaits.** (**A**) Snapshots of robots executing (*top*) standing wave, (*mid*) elliptical wave, and (*bottom*) traveling wave locomotion among sparsely-distributed obstacles. Attack angle and contact duration are labelled. (**B**) (*top*) Attack angle as a function of ϕ. Traveling wave ($\phi = \pi/2$) have significantly lower attack angle than standing wave ($\phi = 0$) and elliptical wave ($\phi = \pi/4$). (*Bottom*) Contact fraction as a function of ϕ. Standing wave have significantly lower attack angle than traveling wave and elliptical wave. *** denotes statistical significance with $p < 0.001$. Figures are adapted from [104].

8.6 Obstacle-aided locomotion with densely distributed obstacles

We next explore OAL among densely distributed obstacles. We constructed a densely-distributed obstacle-rich environments where robot will inevitably encounter with multiple obstacles. We tested gaits with varying ϕ on densely-distributed obstacles and observed that traveling-wave gaits ($\phi = \pi/2$) can cause the best OAL performance (Figure 8.4). Since our analysis is limited to open-loop gait-level design, the large variation in our experiments (Figure 8.4B) is expected.

To explore the physical principles behind the advantage of traveling-wave gaits, we examine the interaction profile between the robot and the obstacles. As predicted in our

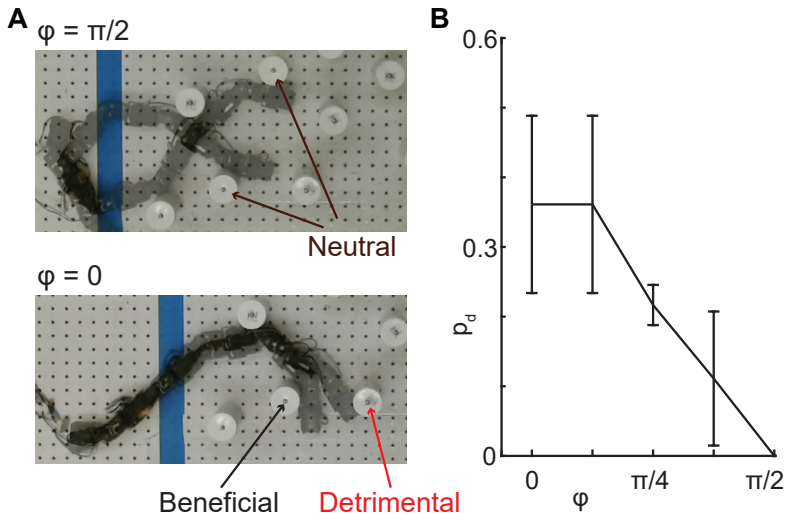

Figure 8.6: **Different types of contacts with obstacles.** (**A**) Snapshots of traveling wave (*top*) and standing wave (*bottom*) locomotion among densely-distributed obstacles. Beneficial, detrimental, and neutral obstacles are labeled. (**B**) p_d, the probability of encountering detrimental obstacles, plotted as a function of ϕ. p_d decreases as ϕ increases. Figures are adapted from [104].

theoretical analysis, effective OAL in traveling-wave gaits results from the combined effects of multiple obstacles restricting the lateral/oscillation of central body axis. Therefore, there is no clear definition of "beneficial" or "detrimental" obstacles in traveling-wave gaits. As illustrated in Figure 8.6, interactions between the robot and obstacles are mostly perpendicular to the direction of motion (therefore considered as "neutral") in traveling-wave gaits. On the other hand, effective OAL for elliptical and standing wave relies more on the interaction with a single obstacle. Therefore, OAL performance of elliptical and standing wave are sensitive to the distribution of obstacles.

Following this idea, we record the probability of robot interacting of "detrimental" obstacle (p_d) for traveling, elliptical, and standing gait templates. We notice that p_d increases as ϕ increases (Figure 8.6). Moreover, once interacting with the detrimental obstacles, the probability of escaping decreases as ϕ decreases.

8.7 Discussion

This chapter expanded the geometric mechanics framework to heterogeneous environments by explicitly incorporating obstacle interactions into gait design. Through this extension, we established a model that maps the presence of obstacles in position space to constraints in shape space, enabling systematic gait optimization for obstacle-aided locomotion (OAL). Our analysis and robophysical experiments revealed several key insights. First, there exists a threshold obstacle spacing below which effective OAL cannot occur. Second, lateral forces from obstacles can contribute to forward displacement through the Lie bracket effect, allowing lateral contacts to be utilized for propulsion. Third, elliptical-wave gaits ($\phi = \pi/4$, $\theta = \pi/4$) are specialized for locomotion among sparsely distributed obstacles, while traveling-wave gaits ($\phi = \pi/2$) perform better in densely packed environments. Together, these findings establish a geometric foundation for understanding and exploiting obstacle interactions in limbless locomotion.

While this study focused on open-loop gait-level design, we acknowledge that gait optimization alone may not be sufficient for effective OAL, particularly in highly cluttered terrains. However, appropriate gait design can significantly reduce the control burden by aligning body kinematics with environmental structure. When integrated with compliant actuation and passive body dynamics brought by cable actuation, the optimized gait templates developed here can complement mechanical intelligence and facilitate locomotion without reliance on extensive sensing or feedback control. In this way, geometric optimization and mechanical intelligence act synergistically: one providing global structure, the other providing local adaptability.

Beyond forward locomotion, the framework presented here can also be extended to analyze and optimize turning behaviors in cluttered environments. Given the kinematic similarity between the omega turn and elliptical wave gaits, it is likely that such turning behaviors also exploit obstacle-aided effects predicted by our analysis.

CHAPTER 9

GAIT STABILIZATION AND OPTIMIZATION FOR SIDEWINDING

9.1 Introduction

Building upon gait level design frameworks established in previous chapters, this chapter investigates how limbless robots can regulate body-environment contact to achieve stable and controlled sidewinding motion. Biological limbless locomotors are particularly adept at traversing complex terrains, partly due to their ability to adjust contact patterns along the body. Among these, sidewinding snakes provide a compelling example: by coordinating undulations in the horizontal plane (the horizontal wave) with vertical lifting of body segments (the vertical wave), they generate smooth, directed motion with minimal slip and high maneuverability [149, 146, 151, 145].

However, the same lifting mechanism that grants sidewinding agility can also introduce instability. When portions of the body are lifted without proper coordination, the center of mass may fall outside the support polygon defined by ground contacts, resulting in the loss of static stability. At high speeds, this loss can be mitigated dynamically, as brief unstable configurations are averaged out by momentum. Yet at the low speeds typical of limbless robots, the loss of static stability often leads to unintended body contacts and irregular ground reaction forces, causing deviations from the desired trajectory.

While adjusting the parameters of the horizontal wave can improve stability, such modulation often reduces locomotion speed or alters the direction of motion [145, 148]. Therefore, it is preferable to stabilize sidewinding gaits through modulation of the vertical wave. For example, [146] demonstrated that increasing vertical-wave amplitude on granular slopes enhances body contact and stability, though this method has limited effect on flat or rigid terrain where contact distribution is less sensitive to amplitude. These obser-

vations highlight the need for alternative mechanisms to achieve gait stabilization without sacrificing speed or controllability.

Inspired by contact planning in legged locomotion [183, 184, 185, 186], this chapter introduces a contact pattern based approach to stabilize statically unstable sidewinding gaits. Unlike legged robots, where contacts can be explicitly defined and sequenced, limbless robots face additional challenges because contact states emerge from the coupled body configuration rather than independent appendages. Furthermore, modifying contact patterns not only affects stability but also redistributes ground reaction forces, influencing the direction and efficiency of motion [145].

To address these challenges, we develop a three-dimensional configuration optimization framework [187] that enables precise control of contact distribution during sidewinding. This framework allows systematic generation of contact-stabilized gaits, which are then coordinated with horizontal-plane motions through geometric mechanics analysis. The resulting family of sidewinding gaits exhibits both static stability and directional controllability, encompassing translational and rotational movements. These predictions are verified through numerical simulations and experiments.

This chapter is adapted from my previously published peer-reviewed work [105] and [106].

9.2 Sidewinding gait and contact pattern realization

Sidewinding gait template

Biological sidewinding motion has been described as the superposition of two traveling waves: one in the horizontal plane and another in the vertical plane [145, 146, 110]. The horizontal wave of body curvature is described by:

$$\kappa(s,t) = \kappa_m \sin(\omega_t t + \omega_s s), \tag{9.1}$$

where $s \in [0\ 1]$ indicates the position along the arc length of the body ($s = 0$ denotes head and $s = 1$ denotes tail); $\kappa(s,t)$ denotes the local body curvature at position s and time t; κ_m, ω_s and ω_t denote the amplitude, the spatial frequency, and the temporal frequency of body curvatures respectively.

The vertical wave is often reconstructed as a time-dependent contact state:

$$c(s,t) = \sigma[\sin(\omega_s t + \omega_s s + \phi_0)], \tag{9.2}$$

where $\sigma[x] = \frac{1}{1+e^{-\gamma x}}$, with the parameter γ approximating the sharpness of the contact state transition; and ϕ_0 is the phase difference between the horizontal wave and the vertical wave. Note that $\gamma \to \infty$ indicates a step-wise transition in contact state; to allow the continuity and the differentiability in Equation 9.2, we take $\gamma = 4$ in this chapter unless otherwise stated. Previous work [145] revealed that $\phi_0 = \pm\pi/2$ yields to effective sidewinding motion.

In our robotic implementation (CMU SEA snake robot [164]), adjacent rotary modules are rotated by 90° such that successive joints alternately actuate in the horizontal and vertical planes. This configuration allows the robot to achieve three-dimensional body shapes through the superposition of a horizontal wave and a vertical wave.

For an N-joint limbless robot, joints are labeled 1 to N, and links are labeled from 0 to N, where joint j connects link $j-1$ and link j. Odd-numbered joints are *yaw* joints that produce motion in the horizontal plane (their rotation axes are vertical), while even-numbered joints are *pitch* joints that produce motion in the vertical plane (their rotation axes are horizontal). The joint angles are prescribed using the following functions:

$$\theta(2j-1,t) = A_l \sin\left(2\pi K_l \frac{2j-1}{N} + 2\pi f t\right), \tag{9.3}$$

$$\theta(2j,t) = A_v \sin\left(2\pi K_v \frac{2j}{N} + 2\pi f t + \phi_0\right), \tag{9.4}$$

where $\theta_l(2j-1,t)$ and $\theta_v(2j,t)$ refer to the yaw (odd) and pitch (even) joint angles, respectively; K_l and K_v are the spatial frequencies of the horizontal and vertical waves; A_l and A_v are the corresponding amplitudes; f defines the temporal frequency; and ϕ_0 is the phase lag between the two waves.

The contact state of link i is represented by $c(i)$, where $c(i) = 1$ indicates that link i is in contact and $c(i) = 0$ indicates that link i is not in contact. The links between two consecutive vertical joints have the same contact state, i.e., $c(2j) = c(2j-1)$. Therefore, the contact state in robots can be approximated by [110]:

$$\begin{aligned} c(2j-1,t) &= c(2j,t) \\ &= \sigma\left[\sin\left(2\pi K_v \frac{j}{2N} + 2\pi f t + \phi_0\right)\right]. \end{aligned} \tag{9.5}$$

Contact pattern realization

For 3D limbless robots, sidewinding locomotion is composed of a continuous sequence of 3D configurations. Each 3D configuration is a "sum" of a 2D configuration in the horizontal plane and a 2D configuration in the vertical plane [145]. Ideally, the projections of the 3D configuration onto the horizontal and vertical planes are identical to the desired 2D horizontal configuration and the desired 2D vertical configuration. When fitting a mechanism to a backbone curve, 3-degrees-of-freedom joints are practically preferred since they are easier to capture pitch, roll and yaw. However, our snake robot, along with many others [164, 16, 17], only has pitch and yaw degrees of freedom. If the robot's yaw and pitch joints directly employ the horizontal and vertical joint angle equations (as Equation 9.3 and Equation 9.4), the composed 3D configuration of the robot fails to capture the twist features in the desired 3D configuration [187]. The inaccuracy of the 3D configuration can, in turn, cause an inaccurate contact pattern realization. Previous studies hypothesised

that the vertical joint angle prescribed by Equation 9.4 can lead to the contact pattern in Equation 9.5 [146, 110]. While in many cases such correspondence is reasonable, in some cases the discrepancy in the correspondence can lead to unexpected locomotion behavior. Therefore, we apply a 3D configuration optimization tool [187] to implement an accurate mapping from the desired contact pattern to the robot joint angles.

To achieve the desired configuration for an N-joint robot, we first denote the 3D Cartesian coordinates of the anterior endpoint of the robot by P_0, the posterior endpoint of the robot by P_{N+1}, and N joints by $P_1, P_2, ..., P_N$. We define the xy-plane as the horizontal plane and the xz-plane as the vertical plane.

We first obtain the coordinates of links in the xy-plane by iteratively solving $[P_{i,x}, P_{i,y}]^T$ by varying j from 0 to $N/2$ following:

$$
\begin{aligned}
g\left(\begin{bmatrix} P_{2j+1,x} \\ P_{2j+1,y} \\ P_{2j+1,\theta} \end{bmatrix}\right) &= g\left(\begin{bmatrix} P_{2j,x} \\ P_{2j,y} \\ P_{2j,\theta} \end{bmatrix}\right) D \\
g\left(\begin{bmatrix} P_{2j+2,x} \\ P_{2j+2,y} \\ P_{2j+2,\theta} \end{bmatrix}\right) &= g\left(\begin{bmatrix} P_{2j+1,x} \\ P_{2j+1,y} \\ P_{2j+1,\theta} \end{bmatrix}\right) R\left(\theta(2j+1)\right) D,
\end{aligned}
\tag{9.6}
$$

where

$$g\left(\begin{bmatrix} x \\ y \\ \theta \end{bmatrix}\right) = \begin{bmatrix} \cos(\theta) & -\sin(\theta) & x \\ \sin(\theta) & \cos(\theta) & y \\ 0 & 0 & 1 \end{bmatrix};$$

$$D = \begin{bmatrix} 1 & 0 & L \\ 0 & 1 & 0 \\ 0 & 0 & 1 \end{bmatrix};$$

$$R(\theta) = \begin{bmatrix} \cos\theta & -\sin\theta & 0 \\ \sin\theta & \cos\theta & 0 \\ 0 & 0 & 1 \end{bmatrix};$$

$\theta(2j-1)$ is the yaw joint angle defined in Equation 9.3; $P_{i,\theta}$ is a dummy variable introduced to obtain the coordinates (with initial condition defined as $P_{0,\theta} = 0$); L is the link length.

Next, we obtain the coordinates in the xz-plane:

$$P_{i,z} = \left(1 - c\left(i - \frac{1}{2}\right)\right) h, \tag{9.7}$$

where $c\left(i - \frac{1}{2}\right)$ is the contact state of joint i (we use $i - \frac{1}{2}$ to indicate the relative position of joint i which connects link $i-1$ and link i along the body) defined in Equation 9.2, and h is amplitude of body lifting, which we empirically relate to A_v by $\sin(A_v) = h/L$. Note that under Equation 9.7, the contact pattern is realized by lifting the modules not in contact with the ground by h.

Finally, we performed a 3D spline fitting to the discrete coordinates $P_0, ..., P_{N+1}$ to achieve a continuous curve. We then uniformly re-sample the curve with $N+2$ sample points $P'_0, ..., P'_{N+1}$ such that distances between any two consecutive points P'_i and P'_{i+1} are equal, i.e., if we denote the $N+1$ links by vectors $l_i = P'_{i+1} - P'_i$ for $0 \leq i \leq N$, all l_is have the identical length.

We use $N+2$ coordinates $Q_0, Q_1, ..., Q_{N+1}$ to denote the optimized positions for the anterior endpoint of the robot, N joints of the robot, and the posterior endpoint of the robot. Thus, the optimal robot configuration (which is as close to the desired configuration as possible) is found by minimizing the objective function

$$\sum_{i=0}^{N+1} \left\| P_i' - Q_i \right\|^2 . \tag{9.8}$$

We denote the $N+1$ links in the optimized robot configuration by vectors $l_i' = Q_{i+1} - Q_i$ for $0 \leq i \leq N$. Since each joint possesses a single rotational degree of freedom, the two links l_{i-1}' and l_i' at joint i should lie in the same rotational plane α_i ($1 \leq i \leq N$). We associate a unit normal vector $n_i \in \mathbb{R}^3$ to plane α_i ($\|n_i\| = 1$) to describe its direction. The alternating pitch and yaw joints robot geometry draws the constraint that any two consecutive rotation planes should be orthogonal in $\mathbb{R}^3$, yielding $n_i \cdot n_{i+1} = 0, \forall 1 \leq i \leq N-1$.

Given that the two links l_{i-1}' and l_i' both belong to the plane α_i and the normal vector n_i is orthogonal to α_i, n_i is orthogonal to both l_{i-1}' and l_i'. It follows that the three vectors l_{i-1}', n_i, n_{i-1} are pairwise orthogonal. In other words, l_{i-1}' is parallel to the cross product $n_{i-1} \times n_i$ for $2 \leq i \leq N$.

Assuming the internal shape of the robot is fixed, i.e., relative positions of all Q_i are determined, the value of the objective function will only depend on the choice of absolute positions of Q_i. We let $d_i = P_i' + (Q_0 - Q_i)$, where d_i are constants under the assumption,

then the objective function can be expressed as

$$\begin{aligned}
&\sum_{i=0}^{N+1} \|P_i' - Q_i\|^2 = \sum_{i=0}^{N+1} [(Q_0 - d_i) \cdot (Q_0 - d_i)] \\
&= \sum_{i=0}^{N+1} [Q_0 \cdot Q_0 - 2Q_0 \cdot d_i + d_i \cdot d_i] \\
&= (N+2) Q_0 \cdot Q_0 - 2Q_0 \cdot \left(\sum_{i=0}^{N+1} d_i \right) + \sum_{i=0}^{N+1} (d_i \cdot d_i) \\
&= (N+2) \left(Q_0 - \frac{\sum_{i=0}^{N+1} d_i}{N+2} \right) \cdot \left(Q_0 - \frac{\sum_{i=0}^{N+1} d_i}{N+2} \right) \\
&\quad + \left[\sum_{i=0}^{N+1} (d_i \cdot d_i) - \frac{1}{N+2} \left(\sum_{i=0}^{N+1} d_i \right) \cdot \left(\sum_{i=0}^{N+1} d_i \right) \right].
\end{aligned}$$

Note that the last term in the square bracket is a constant. Thus, the objective function attains the minimum if and only if $Q_0 = \frac{1}{N+2} \sum_{i=0}^{N+1} d_i$, which is equivalent to $\sum_{i=0}^{N+1} Q_i = \sum_{i=0}^{N+1} P_i'$. Also note that this constraint is derived purely mathematically, but an intuitive interpretation of the constraint is that the centroid of the actual robot configuration should coincide with the centroid of the desired configuration.

We now arrive at the final formulation the optimization problem which exploits the geometric structure of the robot

$$\begin{aligned}
\underset{Q_i}{\text{minimize}} \quad & \sum_{i=0}^{N+1} \|P_i' - Q_i\|^2, \\
\text{subject to} \quad & \text{(i) } \|n_i\| = 1, \forall 1 \le i \le N; \\
& \text{(ii) } n_i \cdot n_{i+1} = 0, \forall 1 \le i \le N-1; \\
& \text{(iii) } l_{i-1}' = L \cdot (n_{i-1} \times n_i), \forall 2 \le i \le N; \\
& \text{(iv) } \sum_{i=0}^{N+1} Q_i - \sum_{i=0}^{N+1} P_i' = 0.
\end{aligned}$$

The constrained nonlinear optimization problem can be solve by standard gradient-descent algorithms such as MATLAB's built-in function `fmincon`. For the sidewiding

gaits we proposed in this work, we experimentally verified that solving the nonlinear optimization using MATLAB is feasible for the real-time implementation in the quasi-static motions. However, a limitation of this method is that optimization problems might not be solved fast enough in the scenarios where the robot has to execute the gaits with complex backbone curves under high temporal frequencies. In such cases, pre-optimizing the configurations offline should be considered.

The optimization algorithm outputs the optimized coordinates $Q_0, Q_1, ..., Q_{N+1} \in \mathbb{R}^3$, which denote the optimal positions for N joints, and the anterior and the posterior endpoints of the robot in the work-space. To implement the optimized robot configuration on the physical robot, we must translate the coordinates to the robot joint angles in joint space: the absolute value of the i-th joint angle is achieved by the inner product of l'_i and l'_{i-1}, given the coordinates $Q_0, Q_1, ..., Q_{N+1}$; and the orientation of the i-th joint angle can be determined by the direction of the normal vector n_i of the rotation plane α_i, given the coordinates $Q_0, Q_1, ..., Q_{N+1}$.

Thus the optimized joint angles θ_i ($i = 1, ..., N$) are sent to the robot as joint angle set points.

Toroidal shape space

The basic framework of geometric mechanics introduced in previous chapters provides a foundation for describing locomotion through the relationship between body shape changes and net displacements. In sidewinding locomotion, this framework takes on a distinctive form because the two principal shape variables (the phases of the horizontal and vertical body waves) are both cyclic. As a result, the corresponding shape space is topologically toroidal. This section focuses on the unique geometric structure that arises from this toroidal shape space and explains how it informs gait design and motion planning for sidewinding.

In the sidewinding gait prescription, one of the shape variable represents the phase of

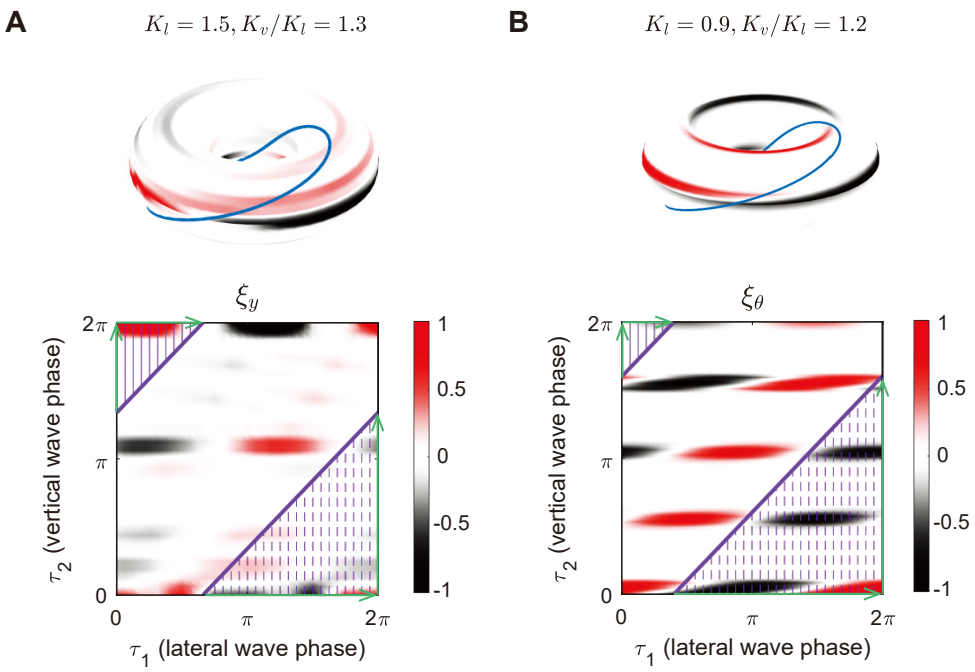

Figure 9.1: **Height functions for designing sidewinding gaits to produce motion in the desired direction.** Height functions on torus (top panel) and on unfolded Euclidean cover space (lower panel) are shown. The height function for (**A**) horizontal spatial frequency $K_l = 1.5$, V-L ratio $K_v/K_l = 1.3$ in lateral direction (the direction perpendicular to body axis) and (**B**) horizontal spatial frequency $K_l = 0.9$, V-L ratio $K_v/K_l = 1.2$ in rotational direction. The purple curve in each plot maximizes the surface integral enclosed in the upper left corner (marked in solid lines) minus the surface integral enclosed in the lower left corner (marked in the dashed lines). The assistive lines are shown as lines with green arrows. Figures are adapted from [106].

the horizontal wave ($\tau_1 \in S^1$), and the other shape variable represents the phase of the vertical wave ($\tau_2 \in S^1$). With both shape variables being cyclic, its shape space is toroidal, (T^2) [188]. Examples of height functions on toroidal shape spaces are shown in Figure 9.1. While the gait path (solid purple curve in Figure 9.1) is a closed curve in the toroidal shape space, there is no obvious surface enclosed by the gait path.

To form an enclosed surface, [189] introduced the notion of "assistive lines" in the Euclidean cover space of the toroidal shape space. As a result, the surface integral can be calculated as the surface enclosed in the upper left corner (see the surface labeled by solid lines in Figure 9.1) minus the surface enclosed in the lower right corner (see the surface labeled by dashed lines in Figure 9.1). We refer readers to [189] for a detailed derivation

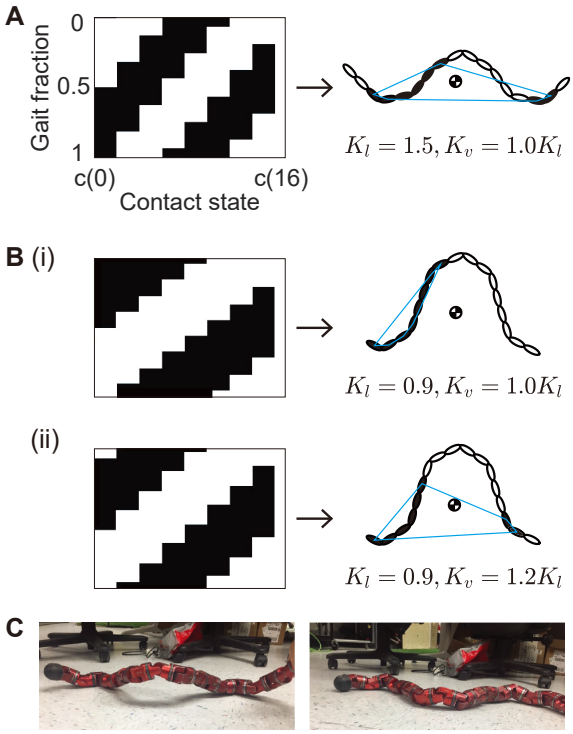

Figure 9.2: **Examples of statically stable and unstable configurations.** (**A**) The contact state pattern and an example of a statically stable configuration for gaits with high spatial frequency in both the horizontal wave and the vertical wave. (**B**) (i) The contact state pattern and an example of a statically unstable configuration for gaits with low spatial frequency in both the horizontal wave and the vertical wave. (ii) Stabilizing the statically unstable configuration by increasing the vertical spatial frequency. The label and the axis in panel (A) are the same as in (A). (**C**) Example of an unstable configuration (left) and an unexpected touchdown (right). Figures are adapted from [106].

and proof of motion planning in toroidal shape spaces.

9.3 Frequency modulation to optimize sidewinding gaits

Joint angle Prescription

We prescribe the joint angle using two methods, sine wave prescription (SWP) and Contact Pattern Realization (CPR). In SWP, we use Equation 9.3 and Equation 9.4 to directly prescribe the joint angle according to our choice of gait parameters. In CPR, we use the contact pattern realization method introduced in the previous section to calculate the joint angles for our choice of gait parameters. Note that in our robot, joint N (the last joint)

always orients link N (the tail link) into the air so the tether does not interfere with robot motion.

Static Stability

Static stability is defined as the fraction of a temporal undulation period that the center of mass is inside the support polygon. The support polygon is defined as the convex hull of all the links in contact with substrate. In Figure 9.2, we show examples of stable (Figure 9.2A) and unstable configurations (Figure 9.2B). We observe that gaits with large vertical spatial frequencies have more distinct body-environment contact patches, and are therefore more statically stable than gaits with low spatial frequency in the vertical wave. Inspired by this observation, we will stabilize the originally unstable gaits by increasing the spatial frequencies of the vertical wave (*frequency modulation*).

Gait Stabilization

We stabilize the sidewinding gaits by increasing the spatial frequency of the vertical wave. In other words, we gradually increase the V-L ratio, K_v/K_l, until the satisfactory static stability is reached. As we increase the vertical spatial frequency, the vertical spatial period decreases. Thus, lower vertical spatial frequency represents shorter but more frequent contact patterns, which is more stable; whereas higher vertical spatial frequency represents longer but less frequent contact patterns, which is less stable. In this paper, we consider a gait as statically stable when its static stability is greater than 0.5. Note that this threshold is selected for our experiments on flat terrain. If necessitated by conditions such as uneven terrain, the static stability threshold may be raised to improve the capability of the robot to remain statically stable even when some modules fail to follow the prescribed contact states (e.g., perturbed by the environment).

Coordination of the Horizontal and the Vertical Waves

We decomposed the internal shape of sidewinder robots into two independent traveling waves: a horizontal traveling wave and a vertical traveling wave. The horizontal traveling wave is prescribed by:

$$\theta_l(j, \tau_1) = A_l \sin\left(2\pi K_l \frac{j}{N} + \tau_1\right), \tag{9.9}$$

where τ_1 is the phase of the horizontal wave. Similarly, the contact state is prescribed as:

$$c(2i-1, \tau_2) = c(2i, \tau_2) = \sigma\left(\sin\left(2\pi K_v \frac{i}{2N} + \tau_2\right)\right), \tag{9.10}$$

where τ_2 is the phase of the vertical wave that can uniquely determine the contact pattern. $c(i, \tau_2) = 0$ represents swinging-state and therefore no ground reaction force appears at link i at phase τ_2 .

The phases of the horizontal wave and the vertical wave then comprise the shape variable, $\boldsymbol{\tau} = [\tau_1,\ \tau_2]^T$. Using the geometric mechanics tool, we can calculate the height function and visualize the kinematics in the desired directions (translational and rotational).

A gait that coordinates the horizontal and vertical wave can be described as a function that maps τ_1 to τ_2. From the structure of the height functions (see Figure 9.1), we observed that in the Euclidean cover space of the torus (where the edges are properly identified with each other at 0 and 2π), a straight line path gives rise to a optimal path; this is seen by the integral of the surface in the upper left minus the integral of the surface in the lower right being maximized. In this way, we characterize the coordination of the horizontal and the vertical wave by the relative phase lag: $\phi_0 := (\tau_2 - \tau_1 \bmod 2\pi)$.

Numerical Simulation

We first performed numerical simulations to test our scheme's ability to predict locomotion. Specifically, in the simulation, we prescribed the horizontal amplitude and the contact state of the robot using Equation 9.3 and Equation 9.5. In other words, we take $\tau_1 = 2\pi ft$ and $\tau_2 = 2\pi f + \phi_0$. Thus, the shape variable and shape velocity can be prescribed as:

$$\boldsymbol{\tau} = \begin{bmatrix} 2\pi ft \\ 2\pi ft + \phi_0 \end{bmatrix}, \ \dot{\boldsymbol{\tau}} = \begin{bmatrix} 2\pi f \\ 2\pi f \end{bmatrix}. \tag{9.11}$$

Then we simulate the locomotion with the standard ordinary differential equation [161]:

$$\begin{aligned} g(T) &= \int_0^T T_e L_{g(t)} A(\boldsymbol{\tau}) \dot{\boldsymbol{\tau}} \boldsymbol{d}t \\ &= \int_0^T T_e L_{g(t)} A \left(\begin{bmatrix} 2\pi ft \\ 2\pi ft + \phi_0 \end{bmatrix} \right) \begin{bmatrix} 2\pi f \\ 2\pi f \end{bmatrix} \boldsymbol{d}t, \end{aligned} \tag{9.12}$$

where $g = (x, y, \alpha) \in SE(2)$ represents the body frame position and rotation ([165]), $T_e L_g = \begin{bmatrix} \cos(\alpha) & -\sin(\alpha) & 0 \\ \sin(\alpha) & \cos(\alpha) & 0 \\ 0 & 0 & 1 \end{bmatrix}$ is the left lifted action with respect to the coordinates of g. Rate independent kinetic Coulomb friction was used to derive the local connection matrix, A, where the ground reaction forces are related to the body velocity by:

$$F^i = F_m \frac{v}{|v|}, \tag{9.13}$$

where F^i is the ground reaction force experienced on $i-th$ module, v is the body velocity, and F_m is the magnitude of the friction force.

Solving the differential equation Equation 9.12 throughout one period (from $t = 0$ to $t = 1/f$), we obtain the trajectory of the locomotor and can thus determine the predicted displacements in the forward, lateral, and rotational directions over one gait cycle.

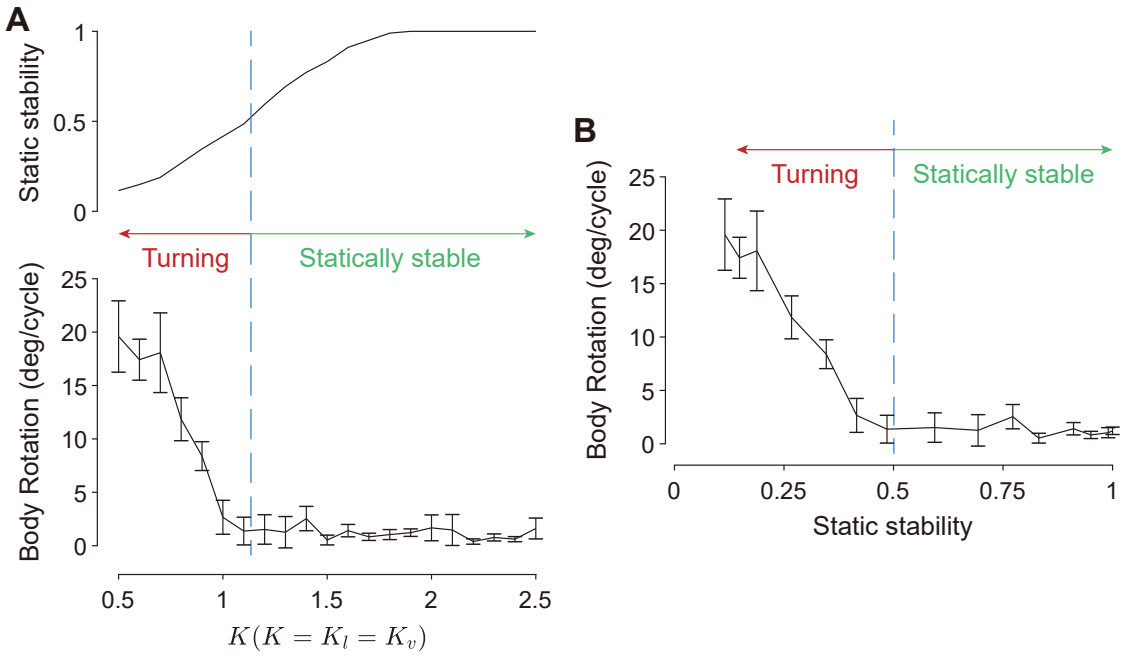

Figure 9.3: **Effect of spatial frequency on static stability.** (**A**) (*Top*) The relationship between the spatial frequency ($K_v = K_l = K$) and the static stability. (*Bottom*) Robot experiments showed that significant turning was observed in gaits with low static stability and the turning vanished at gaits with high static stability. (**B**) The relationship between the body rotation and static stability. The curve appeared to be a piece-wise linear function. In the range where the static stability is less than 0.5, the body rotation grows almost linearly with the loss of static stability (R = 0.99). Whereas in the range where the static stability is higher than 0.5, the body rotation is almost negligible. Figures are adapted from [106].

Note that we assume that the friction force dominates the motion and we neglect inertia in the simulation. However, inertia can be important in gait stability. That is, when the statically unstable gaits are implemented on robots with low temporal frequency (i.e., no dynamic stability), the robot often cannot reach the prescribed configuration; therefore, simulation-experiment discrepancy is expected (see Figure 9.3A). On the other hand, when operated at high temporal frequency, inertial effects can make the statically unstable gaits dynamically stable. In the case where the gait can be stably (either statically stable or dynamically stable) implemented on robots, inertia has a relatively small contribution to the motion (i.e., friction dominates the motion), as we show in Figure 9.3B.

Robot experiments

We conducted experiments with CMU SEA snake robot [164]. The robot (mass 3.7 kg, length 1.2 m) is a modular series elastic actuated robot composed of a chain of 16 identical modules that are capable of precise torque, velocity and position control. The arrangement of modules in the robot ensures that the rotation axes of neighbouring modules were 90° off along the longitudinal axis. Thus, the joints were divided into two groups: yaw joints (odd modules from head to tail), which control the horizontal body wave, and pitch joints (even modules), which control the vertical body wave. Note that during the experiments, the connection wire was lifted to avoid the additional force.

Experiments were conducted on flat hard ground, where we assume the ground reaction forces are given by rate independent kinetic Coulomb friction. The robot was controlled directly by joint angle commands. For each sidewinder gait tested, we conducted 5 trials. In each trial, we commanded the robot to execute two complete gait cycles and collected the robot motion data starting from the first command being sent out until the robot stop moving.

To track the motion of the robot in the environment, we uniformly attached 17 IR reflective markers along the body. An OptiTrack motion capture system was employed, and 4 OptiTrack Flex 13 cameras were installed to track the three-dimensional positions of the markers at a frame rate of 120 FPS. We recorded the trajectory of the markers over two cycles, from which we calculate the forward, lateral and rotational displacements. Examples of the robot experiments can be found in the supplementary video.

We summarize our steps to stabilize the sidewinding gaits in algorithm 1.

9.4 Verification of contact pattern realization

In this subsection, we compare the locomotion performance using Equation 9.3–Equation 9.4 (sine wave prescription, SWP) and the contact pattern realization method (CPR) to pre-

Algorithm 1: Stabilizing sidewinding and turning gaits

```
Initialization: K_v/K_l = 1.0;
while Static Stability < 0.5 do
    K_v/K_l ← K_v/K_l + 0.1;
    CPR;
    Calculate height function (HF);
    Take φ_0 to maximize HF surface integral;
end
Perform numerical simulation
Implement robot experiments
```

scribe the joint angles. We compare three gaits: high-stability (HS), intermediate-stability (IS), and low-stability (LS).

In our experiments, we compared these three representative sidewinding gaits that span a range of static stability levels. The gaits differ primarily in their horizontal spatial frequency K_l. Specifically, the HS gait used $K_l = 1.5$, the IS gait used $K_l = 1.2$, and the LS gait used $K_l = 0.5$. For all gaits, we kept $K_v/K_l = 1, A_l/K_l = 0.7, A_v/K_v = 0.15, \phi_0 = \pi/2$, and $f = 2.0$ Hz. We characterized gait stability using the ratio of the projected center of mass within the support polygon, yielding normalized stability values of 1.00, 0.60, and 0.12 for the HS, IS, and LS gaits, respectively. Note that in all three gaits, the expected rotation is zero with effective translational displacement.

In the HS experiments, both methods can lead to almost no rotation with effective lateral displacements. This is as expected from previous experiments.

In the IS experiments, we notice that there is significant body rotation in SWP, whereas in CPR, the body rotation is almost negligible. We hypothesize that SWP does not give accurate configurations as expected, which causes the discrepancy in contact patterns. To test our hypothesis, we measure the body contact and compare the empirically collected contact pattern data with the expectation given by Equation 9.5. Interestingly, we observe that in SWP, the actual contact pattern in robot experiments (Figure 9.4E-ii) is clearly different from the expectation (Figure 9.4E-i). In contrast, in CPR, the actual contact pattern in robot experiments (Figure 9.4E-iii) is almost identical to the expectation. Therefore, the

discrepancy in contact pattern is at least one of the reasons for the unexpected turning in SWP robot experiments.

Finally, in the LS experiments, both methods display significant rotation. We suspect that this body rotation is caused by the low stability contact pattern. We will evaluate in details in later sections.

From the observations in this section, we showed that contact pattern with at least intermediate static stability can be reliably realized, allowing us to directly modulate the contact pattern to stabilize gaits based on contact patterns prescribed by Equation 9.5.

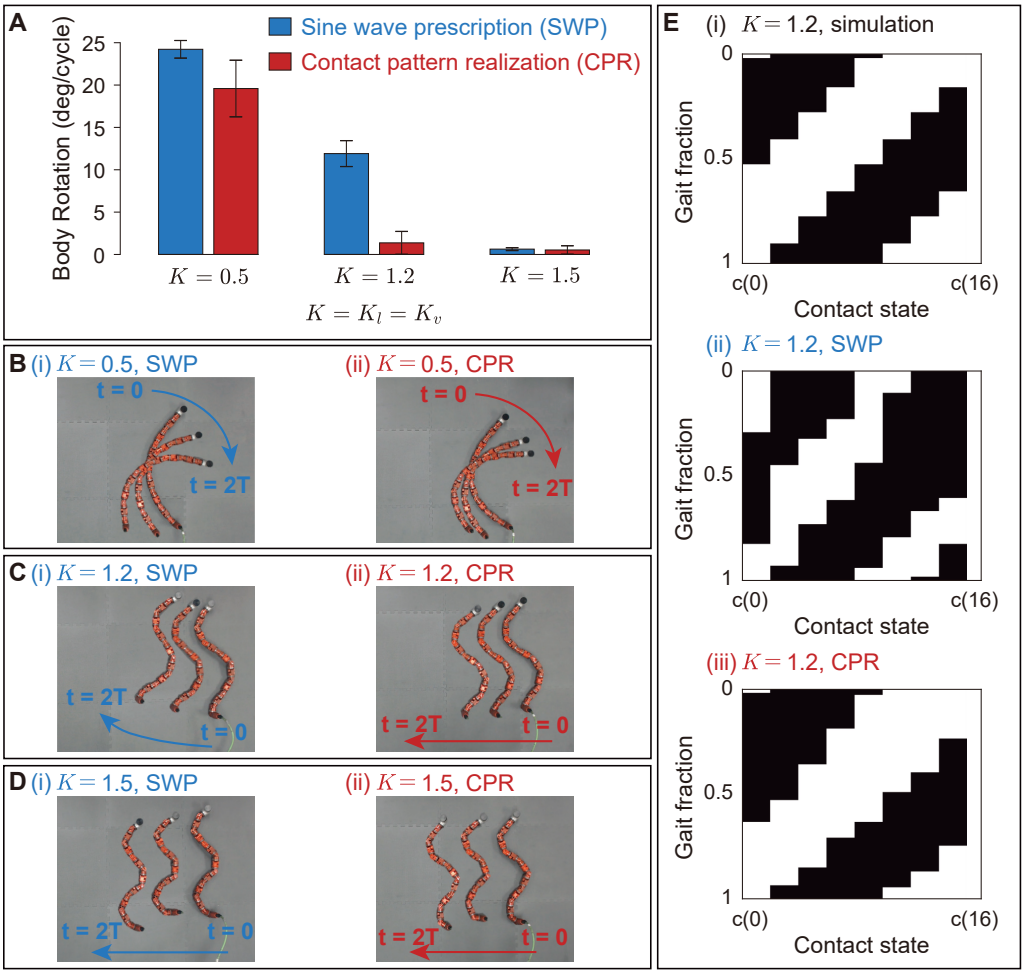

Figure 9.4: **Contact pattern comparison of the sine wave prescription (SWP) and the contact pattern realization method (CPR).** (**A**) Comparison of body rotations in low-stability (LS, $K = 0.5$), intermediate-stability (IS, $K = 1.2$), and high-stability (HS, $K = 1.5$). Both SWP and CPR cause low body rotations in LS case and high body rotations in HS; whereas in IS case, significant body rotation is only observed in the SWP. (**B-D**) Snapshots of robot experiments implementing gaits using SWP (i) and CPR (ii). (**E**) The comparison of IS body contact pattern from simulation (i), SWP (ii) and CPR (iii). Figures are adapted from [106].

9.5 Gait stability analysis

We calculate the static stability for sidewinding gaits with different spatial frequencies ($K_v = K_l = K$) in Figure 9.3. High spatial frequencies lead to a dense distribution of short contact patches (Figure 9.2A) and are often statically stable. In contrast, low spatial frequencies lead to sparse distribution of long contact patches (Figure 9.2B-i) and are often

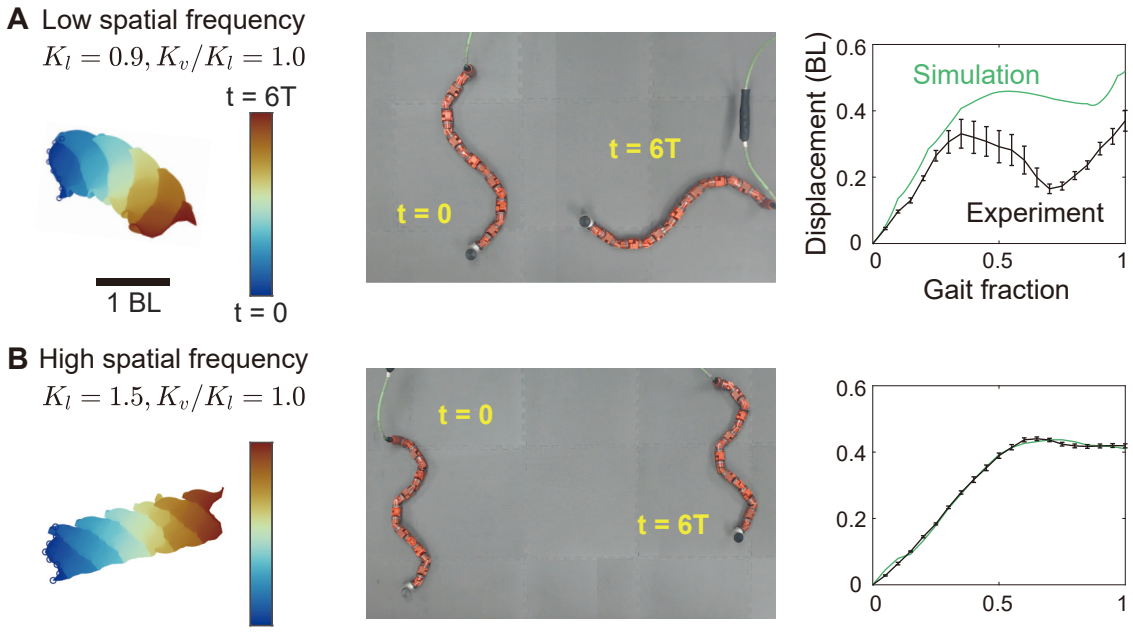

Figure 9.5: **Discrepancy between robot experiments and simulation at low spatial frequency.** We compared the low spatial frequency gait (**A**) and high spatial frequency gait (**B**). (*Left*) Trajectories of body motion in 6 gait cycles. The colors represent gait periods. Initial positions of the robot indicated by the black circles. (*Middle*) Comparisons of time evolution of displacement of the simulation and robot experiments. (*Right*) The simulation-experiment discrepancy. Large discrepancies occur in low spatial frequency gaits. The unit and the axis labels in all panels are the same. Figures are adapted from [106].

not statically stable.

To investigate the behavior of statically unstable sidewinding gaits, we perform similar experiments on sidewinding gaits with 0.9 spatial wave and 1.5 waves on our robot. We set horizontal amplitude $A_l = 40K_l$ (unit of amplitudes: degree), vertical amplitude $A_v = 8.5K_v$, and a temporal frequency $f = 2.0$ Hz for all the robot experiments unless otherwise stated. Snapshots of the robot implementing such gaits are shown in Figure 9.5. Good agreement between experiment and theory is observed in the sidewinding gait with 1.5 spatial waves. However, we observe significant discrepancies between the simulation and robot experiments the sidewinding gait with 0.9 spatial waves (Figure 9.5). We hypothesize that at low spatial frequency, the configuration of the robot is not statically stable (static stability = 0.34 for 0.9 spatial wave, static stability = 0.83 for 1.5 spatial waves), which

leads to the robot falling down (Figure 9.2B, C) and causes contact patterns different from expectation. The unexpected touchdown can change the distribution of ground reaction forces and therefore lead to motions in other directions (in this case, turning).

We further conducted robot experiments across a range of spatial frequencies. Those robot experiments showed that such discrepancies (stability related turning) vanished at high spatial frequencies. We observed that, the cut-off static stability that leads to unexpected behavior is around 0.5. In this way, we use 0.5 as the threshold to determine the static stability in later analysis.

9.6 Dynamic effect of temporal frequency on performance

Despite being statically stable, it is possible that, when operated at high temporal frequency, the acquired dynamic stability can compensate for the loss of static stability. Following this idea, we test the effect of the temporal frequency on the performance of gaits.

We first evaluate the effect of temporal frequency on the translational sidewinding gait with 0.9 spatial wave ($K_l = 0.9, K_v/K_l = 1$). We set $A_l = 50^\circ$ and $A_v = 75^\circ$ for all the robot experiments. From our static stability analysis, this translational sidewinding gait is not statically stable (static stability = 0.35). At low temporal frequency (see Figure 9.6A), significant rotations are observed in robot experiments, whereas at high temporal frequency, the magnitude of rotation reduces but the robot rotates in a different direction. Our experiments show that the locomotion performance for statically unstable gaits is not predictable and controllable when operated at different temporal frequencies. However, the magnitude of rotation significantly decreases when the robot was operated at high temporal frequency, which suggests that the loss of static stability can be compensated by emergent dynamic stability at high speed.

Next, we evaluate the temporal frequency dependence of the rotational sidewinding gait: $K_l = 1.5$, $K_v/K_l = 0.6$, $\phi_0 = \pi/2$. From our static stability analysis, the rotational sidewinding gait is not statically stable (static stability = 0.46). In addition, numerical sim-

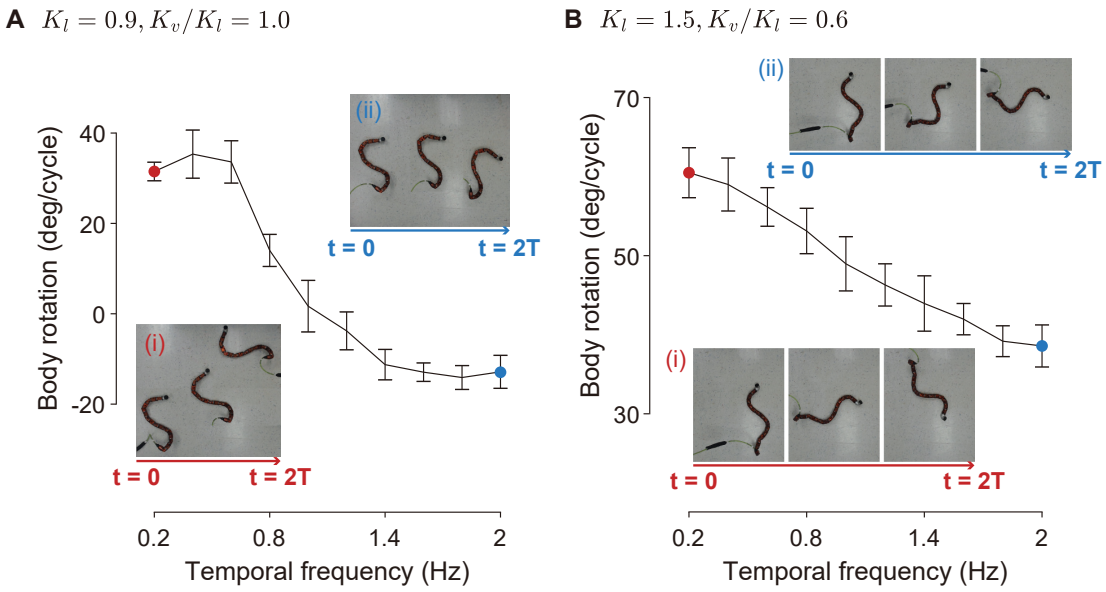

Figure 9.6: **Temporal frequency dependency of unstable gaits.** Dependence of the rotation angle (per cycle) on the temporal frequency of (**A**) statically unstable translational sidewinding gaits and (**B**) statically unstable rotational sidewinding gaits on robot experiments. The subplots (i) and (ii) show the snapshots of the robot implementing gaits in low temporal frequency (0.2 Hz, red) and high temporal frequency (2.0 Hz, blue) over three gait cycles. Figures are adapted from [106].

ulation predicts that the rotational sidewinding gaits should lead to counterclockwise rotation. Therefore we suspect that the rotational sidewinding gait is driven by the unexpected touchdowns and therefore will be strongly temporal frequency dependent. Robot experiments verified that locomotion performance (Figure 9.6B) in the rotational sidewinding gait is strongly correlated with the temporal frequency. Higher rotation angles are achieved when the robot operated at low temporal frequency.

9.7 Contact modulation for gait stabilization

We use algorithm 1 to stabilize the statically unstable translational and rotational sidewinding gaits. As discussed earlier, the translational sidewinding gait with 0.9 spatial wave is not statically stable. We show that we can stabilize this gait by increasing the V-L ratio K_v/K_l to 1.2. From the lateral height function (Figure 9.1B), we take $\phi_0 = 1.076$ to optimize the surface enclosed in the lateral height function. The static stability analysis

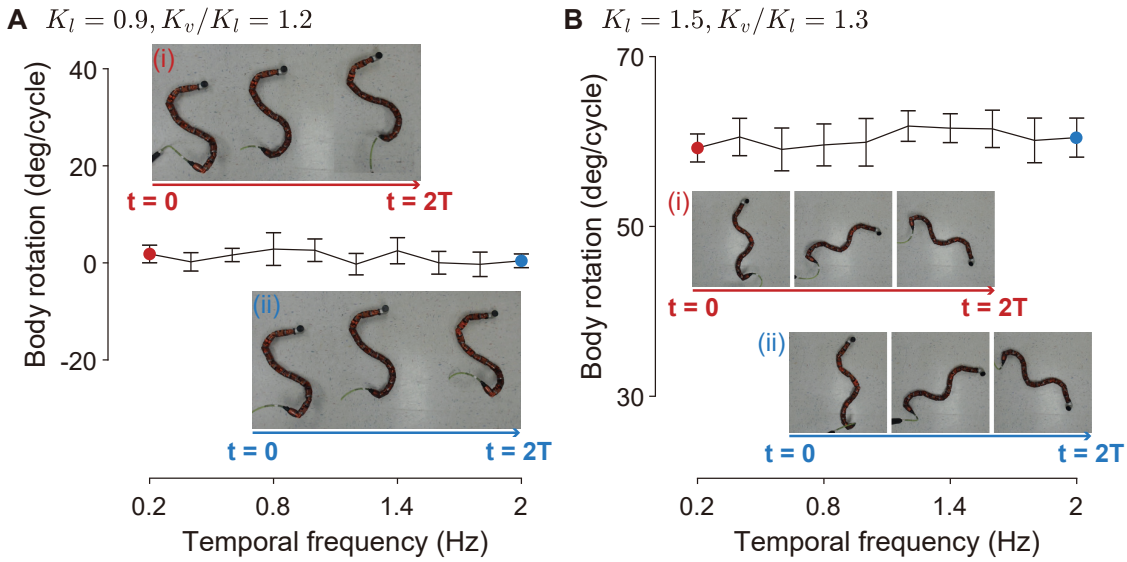

Figure 9.7: **Robustness of statically stable gaits as a function of temporal frequency.** Dependence of the rotation angle (per cycle) on the temporal frequency of (**A**) the stabilized translational sidewinding gaits and (**B**) the stabilized rotational sidewinding gaits on robot experiments. In both cases, the rotation angle is steady over a range of temporal frequencies. The unit and the axis labels in all panels are the same. The subplots (i) and (ii) show the snapshots of the robot implementing gaits in low temporal frequency (0.2 Hz, red) and high temporal frequency (2.0 Hz, blue) over three gait cycles. Figures are adapted from [106].

suggests that this gait is statically stable (static stability = 0.5). We implement this gait in robot experiments (Figure 9.7A), which show that no significant turning was observed over our range of temporal frequencies.

Note that the stabilized translational sidewinding gait ($K_l = 0.9$, $K_v/K_l = 1.2$) exhibited effective lateral displacement. robot experiments demonstrate that the average lateral displacement per gait cycle is 0.69 ± 0.02 body lengths per cycle, significantly greater than the displacement (0.42 ± 0.01 body length per gait cycle) of the translational sidewinding gait with 1.5 spatial waves ($K_l = 1.5$, $K_v/K_l = 1$).

We next stabilize the rotational sidewinding gait with 1.5 spatial waves, $K_l = 1.5$. We show that we can stabilize this gait by raising the V-L ratio K_v/K_l to 1.3. From the rotational height function (Figure 9.1A), we take $\phi_0 = 1.02$ to optimize the surface enclosed in the rotational height function. The static stability analysis suggests that this gait is statically

stable (static stability = 0.62). We implement this gait on the robot (Figure 9.7B), revealing that the locomotion performance (rotation per gait cycle) is robust over a range of temporal frequencies.

9.8 Discussion

This chapter expanded the sidewinding gait family through a combination of geometric mechanics analysis and configuration optimization. By systematically varying the ratio K_v/K_l between the vertical and horizontal spatial frequencies, we revealed that the balance between speed and stability in sidewinding can be tuned continuously: smaller V-L ratios generally yield faster but less stable motion, whereas larger ratios produce slower yet more statically stable gaits. This finding not only broadens the accessible gait space but also highlights that stability and speed are inherently coupled through spatial wave coordination.

The introduction of frequency-tuned turning gaits further illustrates how the modulation of shape-space parameters can generate rotation without explicit steering inputs. Our analysis shows that frequency turning gaits with V-L ratios greater than one maintain static stability and exhibit directionally consistent motion across temporal frequencies. In contrast, those with V-L ratios less than one are statically unstable and prone to unpredictable ground reaction forces, explaining the observed mismatch between model predictions and experimental behavior. These results emphasize that static stability serves as a necessary foundation for achieving predictable, repeatable sidewinding motion at low temporal frequencies.

More broadly, the combination of 3D configuration optimization and geometric mechanics enables contact pattern realization, an approach that can be generalized beyond sidewinding. This approach naturally extends to cable-driven limbless platforms such as Morphing MILR, where cable actuation can be further optimized regarding energy consumption while realizing the optimized contact patterns. In such systems, the control complexity associated with contact regulation can be offloaded to mechanical and morphologi-

cal design, providing stability, and even energy efficiency through mechanical intelligence.

In summary, this work establishes a unified framework linking geometric mechanics, contact pattern realization, and morphological embodiment. By expanding the sidewinding gait family and revealing how spatial frequency modulation governs stability, we lay the groundwork for applying similar principles to general limbless robots. These insights contribute to the broader goal of designing mechanically intelligent robots capable of achieving stable and versatile locomotion across diverse environments.

Part III

Extending mechanical intelligence principles to aquatic settings and incorporating high-level computational intelligence for amphibious autonomy

The exploration of mechanical intelligence in terrestrial environments has revealed the remarkable capacity of limbless robots to exploit their intrinsic body mechanics and environmental interactions for effective locomotion without requiring prior knowledge of the surroundings. Through systematic gait design and optimization, we demonstrated that open-loop performance can be further enhanced by leveraging computational frameworks. Building on these insights, Part III transfers mechanical intelligence to aquatic environments and integrates high-level computational intelligence toward amphibious autonomy.

In aquatic settings, locomotion emerges from the intricate interplay among fluid dynamics, buoyancy, and drag. In contrast to conventional swimming robots that prioritize high-speed motion in open water, this thesis emphasizes achieving robust and adaptive mobility in rheologically complex underwater settings, where hydrodynamic and terradynamic effects coexist. Using the AquaMILR series as model systems, this part examines how mechanical intelligence principles extend to underwater environments and how decentralized sensing and feedback control can further enhance locomotor robustness. Ultimately, this approach broadens the operational envelope of limbless robots across land-water interfaces and illustrates how the synergy between mechanical and computational intelligence allows these systems to evolve toward fully autonomous amphibious locomotion.

CHAPTER 10

AQUAMILR: DESIGN OF A CLASS OF MECHANICALLY INTELLIGENT LIMBLESS ROBOT FOR COMPLEX AQUATIC TERRAIN NAVIGATION

10.1 Introduction

The exploration of mechanical intelligence in terrestrial environments has shown that physical body design and environmental interaction can jointly produce robust locomotion without reliance on complex control or perception. Extending these principles into aquatic settings presents new challenges and opportunities, as locomotion becomes dominated by the coupled effects of fluid dynamics, buoyancy, and drag. The development of novel underwater robots offers promising solutions for diverse applications such as deep-sea exploration, search and rescue, infrastructure inspection, environmental monitoring, and underwater construction. Among these, autonomous underwater vehicles (AUVs) have demonstrated reliability and effectiveness in open-water tasks; however, their rigid structures often limit maneuverability in confined, cluttered, or dynamically changing environments [190].

Beyond traditional AUVs, numerous alternative robotic platforms have been explored to enhance mobility and adaptability across a range of aquatic applications [191, 192, 193, 194, 195, 196]. Bio-inspired designs, in particular, have greatly advanced swimming performance through the emulation of fish, eel, and cephalopod morphologies [197, 19, 198, 199, 200, 201]. Yet, despite these innovations, many underwater robots still struggle with agility and robustness when operating in rheologically complex or obstacle-rich environments [190, 202].

Limbless robots, with their continuous and hyper-redundant body structures, provide a promising foundation for addressing these challenges [89, 100, 76]. Inspired by anguilliform swimmers such as eels and sea snakes, such robots are capable of distributed body

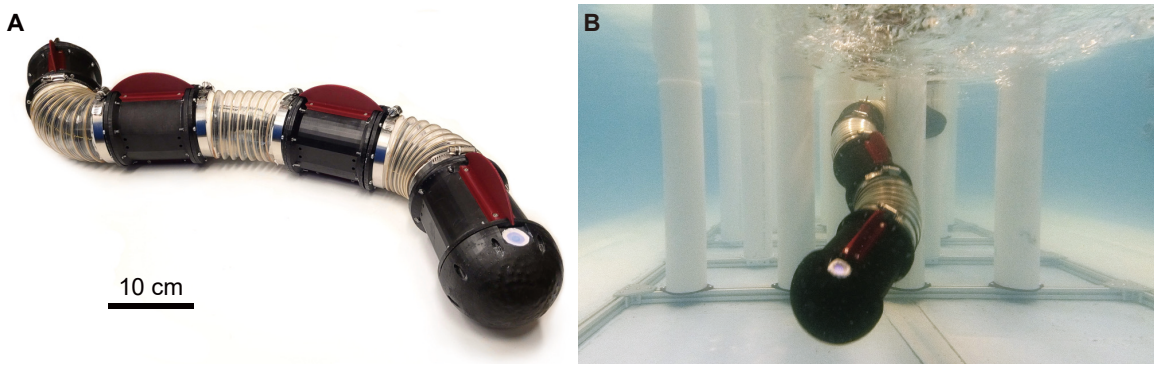

Figure 10.1: **The aquatic limbless robot AquaMILR+ designed for locomotion in complex and cluttered environments.** (**A**) Full robot assembly, featuring a modular self-contained untethered architecture. (**B**) AquaMILR+ navigating a laboratory obstacle-rich environment (vertical posts). Figures are adapted from [107].

modulation and can, in principle, adapt to environmental constraints through shape reconfiguration [18, 203, 204, 27, 205]. However, most existing limbless underwater systems lack passive body compliance, which has been proved to be essential for robust locomotion in unstructured terrestrial environments.

Building upon the concept of mechanical intelligence established in earlier chapters, this chapter introduces the design of a class of underwater limbless robot, Aquatic Mechanically Intelligent Limbless Robot (AquaMILR). As shown in Figure 10.1, we present AquaMILR+: an limbless underwater robot that extends the design philosophy of MILR to aquatic motion. AquaMILR+ employs a bilateral cable-driven actuation system inspired by the musculoskeletal structure of anguilliform swimmers, enabling open-loop adaptation to obstacles via anisotropic compliance. The robot integrates a fully waterproof modular architecture with a dedicated depth control system, allowing submersion and controlled locomotion.

This chapter is adapted from my previously published peer-reviewed work [107].

10.2 Robot design

AquaMILR+ is an untethered cable-driven undulatory robot with full control over body shape and depth, featuring programmable body compliance (Figure 10.2A). It has a body

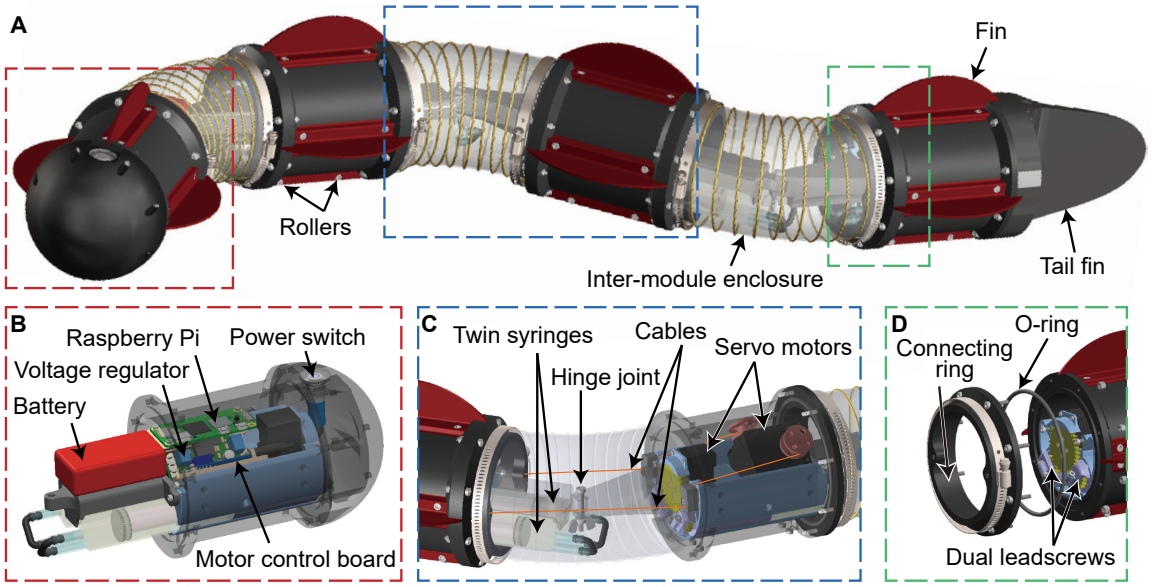

Figure 10.2: **Detailed design of AquaMILR+.** (**A**) An assembly of 4 modules with 3 joints. (**B**) The electronics module contained within the head module, features onboard power, a single-board computer, and a waterproof power switch. (**C**) An internal diagram of each module and inter-module enclosure, including the depth control and cable-driving servo motors, cable routing, and revolute joint. (**D**) The primary waterproofing method between modules, including a gasket seal to clamp modules with in between O-ring. Figures are adapted from [107].

length of 1 m, with 4 primary modules and 3 joints. The robot's fully waterproof design includes completely onboard power and communication enclosed in the head module, and a distributed depth control system in each module. It also holds appendages including multiple fins, a tail, and ventral rollers for effective in-water propulsion and stability.

Module components

Each of the primary resin-printed modules is 100 cm in length and 10.8 cm in diameter. Inside each module lays a PLA insert which serves as the attachment point to all components in the module assembly. This insert is hollowed out, filled with 2-mm-diameter lead balls, and sealed, creating a form-fitting weight to achieve neutral buoyancy. Additionally, the insert has bottom-side cutouts for twin syringe-leadscrew assemblies for depth control. On the top-side, it has mounts for the cable-driving servo motor and the depth-control servo

motor (Figure 10.2C).

On the outside of the modules, each side has four mounting holes in the resin holding screw-to-expand threaded inserts allowing for easy fastening of fins on all sides. On the bottom side, a set of four low-profile acrylic rollers are attached to provide anisotropic ventral friction allowing AquaMILR+ to effectively move on the seabed and hard ground [206]. The pectoral fins on the sides are helpful for robot stability and pitch control in relatively open-water areas but can be removed to allow dense obstacle navigation.

Waterproofing

AquaMILR+ features a robust, waterproof design which allows for safe operation at depth. External module casings and mating parts were made from resin on the Elegoo Saturn 3 Ultra MSLA 3D printer, preventing the possibility of water seepage through layer lines. The primary sealing method is a flange-gasket system, where each side of the module casings has a gland to hold an 8.9-cm-diameter O-ring (Figure 10.2D). The connecting ring includes an 8-screw circular pattern which clamps against the O-ring, providing even pressure.

These connecting rings are a part of the inter-module enclosure, which includes an 8.9-cm-diameter PVC flex-duct ventilation tubing fixed to the resin connecting ring on each side for a total length of 15 cm (Figure 10.2A). These parts are fixed and sealed together using 3M Marine Adhesive Sealant 5200 at their intersection. On top of these seals, an 8.9-cm stainless steel hose clamp is fastened as a mechanical constraint taking any potential load off of the sealant. Flex-duct tubing was selected because of its extensibility, essential to allow the collapse of one side and the extension of another as the joint bends. Its spring steel reinforcement maintains the structure of this flexible membrane, resulting in a relatively constant volume through different depths to not dramatically influence buoyancy. This inter-module enclosure offers a simple watertight solution for wiring between modules as well as joint actuation solution does add volume (and thus requires extra mass

for neutral buoyancy) to the system, the extra space allows for the depth control system, weight storage, and a reliable static seal.

Bilateral cable actuation

To enable locomotion, AquaMILR+ includes a bilateral actuation mechanism, leveraging a dual pulley-cable system at each joint (Figure 10.2C). Each module contains a Robotis Dynamixel 2XL430-W250-T dual-axis servo motor with a 10-mm-diameter pulley connected to each axis. In between each module is a single-degree-of-freedom revolute joint, where a male and female PLA component are fastened to their respective module inserts and held together by an M4 shoulder bolt with wingnut. Additionally, this joint assembly features detachable PLA cable guides to relieve tension on the resin components. Rikimaru braided fishing line (800 N strength) is tied to each pulley and routed through their respective joint's cable guide and connecting rings, ensuring the calculated cable path. The cable is finally tied to the opposite connecting ring on the next module allowing the two cables to control the angle of the revolute joint between each module.

Power and communication

Different from the other modules, the head module contains all of the power and communication components (Figure 10.2B). When combining this with the RS-485 serial communication protocol used by all of the Dynamixel servo motors, AquaMILR+ maintains 3 wires running along its body length with a simple disconnect at each joint. This structure enforces the modularity of the design, where to extend the robot length or disassemble it for servicing, modules can be simply connected in series to one another.

On this electronics tray, there are four main boards tightly packed in the head with an 11.1 V 1000 mAh LiPo battery fixed to the first joint. This battery provides its full voltage to the servo motors through the Robotis power distribution board and then splits off to a voltage regulator that outputs 5 V, protecting the rest of the electronics. From here, 5 V is

provided to a Raspberry Pi Zero 2W which serves as the main computer for AquaMILR+, containing the relevant libraries and sequences. The Raspberry Pi is then connected to the Robotis U2D2 motor control board, which handles the bulk motor reading and writing commands with RS-485 serial communication protocol. With this power setup and consumption of around 1.0 A under normal operation, AquaMILR+ can run continuously for one hour before requiring battery replacement. External to AquaMILR+, the Raspberry Pi connects through Wi-Fi to an external computer so that the operator can remotely control the untethered robot via remote desktop (RealVNC) Finally, the battery is wired in series with the main power switch mounted on the outside top surface of the rounded head attachment (Figure 10.2B). This switch also includes a visible LED allowing visual confirmation of activation and battery life. On top of this switch, there is a silicone cover cast from Smooth-On ECOFLEX 00-35 Fast. This is sealed over the switch with J-B Weld Marine Epoxy allowing the switch to be externally activated without compromising AquaMILR+'s seals.

Depth control system

Through the use of local fluid exchange with surrounding waters [200, 207], AquaMILR+ features a self-contained depth control system that maintains a constant external volume. This is accomplished through the use of a dual-syringe water exchange system in every module which connects to open water just underneath the modules (Figure 10.3B). The robot mass was carefully calibrated to achieve neutral buoyancy, allowing a small volume of fluid displacement to impact the robot's acceleration. This calibration was achieved by adding sealed packets of 2-mm-diameter lead balls in each module and inter-module enclosure, allowing easy adjustments based on environment or attachment changes. Syringes were chosen due to their preferred form factor, simple actuation, and limited inertial consequences as a result of their inextensibility. These syringes each have a 35-mL internal volume with a 24-mm diameter, maximizing the available module space.

Despite pre-existing architectures on syringe actuation [191], traditional linear actuation systems struggle to remain volume efficient, where the primary actuator is often longer than the stroke length needed. To avoid this and allow a greater maximum depth acceleration of AquaMILR+, a novel FDM printed telescopic leadscrew mechanism was developed (Figure 10.3A). This leadscrew mechanism operates similarly to traditional leadscrews but with a cascading secondary stage allowing a 60% increase in stroke length in comparison. In this design, the primary leadscrew (yellow) has a slotted key with the secondary leadscrew (orange), effectively making them rotationally coupled while allowing motion linearly. From here, similarly to standard leadscrews, the primary leadscrew is threaded into the primary stage (green). This primary stage has 3 tabs along its circumference that mate with slots on the outer casing (lavender), which constrains the primary stage to move linearly upon rotation of the primary leadscrew. The secondary leadscrew is then able to travel linearly with the primary stage, and a secondary stage (pink) is constrained similarly as it is threaded with the secondary leadscrew and slotted with the primary stage. When combined, the driving of the primary leadscrew results in the telescoping of the mechanism's two stages for a greater overall stroke.

To adapt to the syringe, the outer casing is press-fit into the syringe's inner diameter and the secondary stage is adapted to hold the silicone plunger (black) from the syringe. The primary leadscrew is axially constrained with the outer casing to keep the mechanism stable, and two of these leadscrew assemblies are slotted and locked into each module insert. Finally, the two leadscrew assemblies in each module are driven by a Robotis Dynamixel XC330-T288-T servo motor attached to a 36-tooth spur gear (Figure 10.2C). This spur gear meshes with the 16-tooth spur gear at the end of each primary leadscrew, controlling both syringes.

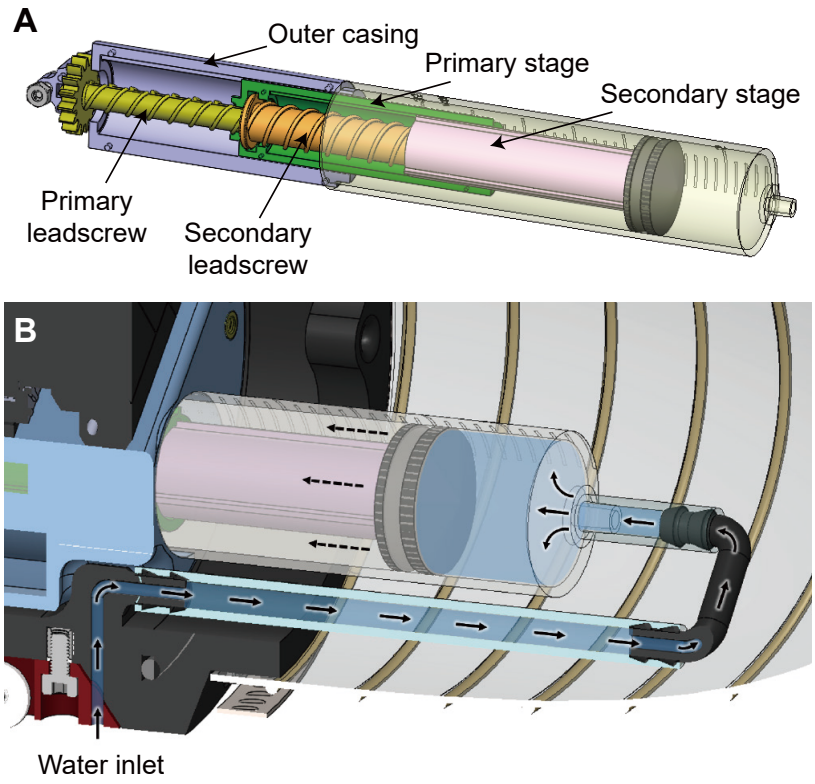

Figure 10.3: **Self-contained depth control system.** (**A**) A telescopic leadscrew design for syringe activation, granting extra stroke in a compact space. (**B**) The water channel used by the syringes to change AquaMILR+'s buoyancy. Figures are adapted from [107].

10.3 Robot control

Bilateral body actuation

AquaMILR+ employs the same bilateral cable-driven actuation framework introduced for the terrestrial MILR in Chapter 1, extending it for undulatory swimming in water. Each joint is actuated by antagonistic cable pairs to realize body shapes prescribed by the serpenoid gait template [11],

$$\alpha_i(t) = A \sin\left(2\pi\xi\frac{i}{N} - 2\pi\omega t\right) + \varphi, \tag{10.1}$$

where A, ξ, ω, and φ denote the amplitude, spatial frequency, temporal frequency, and offset, respectively. The mapping between desired joint angles and cable lengths follows the

same geometric relations derived in Chapter 1, ensuring accurate wave propagation along the body. This open-loop control scheme enables forward propulsion through continuous shape change and body-fluid interaction

Programmable body compliance

The cable-driven mechanism in AquaMILR+ retains the programmable joint-level compliance originally established in MILR [89]. By modulating the relative lengths of bilateral cables, the robot can adjust how strictly each joint follows the prescribed gait template. The generalized compliance parameter G (as defined in Chapter 1, Equation 2.2 and Equation 2.11) determines the effective stiffness of each joint, enabling transitions among characteristic compliance states illustrated in Figure 2.5: bidirectionally non-compliant ($G = 0$), directionally compliant ($G = 0.5$), and bidirectionally compliant ($G = 1$). In aquatic environments, this tunable compliance allows AquaMILR+ to passively conform to hydrodynamic loads and nearby obstacles, improving locomotor stability, energy efficiency, and robustness in cluttered or dynamic underwater settings.

Depth and pitch control

As displayed in Figure 10.2C and D, each of AquaMILR+'s modules is equipped with a dual leadscrew system attached to twin syringes which allows for swift and precise control of the robot's overall depth and pitch, independent from the main body undulation. AquaMILR+'s net mass was carefully calibrated to be neutrally buoyant when the syringes hold 50% of their stroke length, allowing equal capability in diving and ascension as the syringes exchange water. Throughout this exchange, the robot volume is assumed constant with a changing mass. This leads to a change of weight in each module, resulting in individual forces (weight or buoyancy) in the respective directions. When the total mass is greater than the neutrally buoyant mass, the robot will accelerate downward and vice versa. This resulting motion is opposed by drag as the robot dives through the water column.

Additionally, AquaMILR+ has the ability to pitch its body due to having per-module mass control. By altering the syringe actuation percentages, the full body center of mass can move along the major axis of the robot, creating a moment with the buoyant force. This moment rotates the robot until the center of mass is positioned below the centroid. These relationships allow for both acceleration of the robot vertically in the water column and fine-tuned pitch control due to the precision of the servo motors that actuate the syringes.

10.4 Swimming performance evaluation in simple, controlled open water

Open water locomotion

We first evaluated AquaMILR+'s performance in an open water environment with a 3 m $\times$ 2 m $\times$ 0.5 m ($L \times W \times H$) indoor pool. In open water tests, we kept gait parameters consistent with $A = 30°$, $\xi = 0.5$, $\omega = 0.2$, and $\varphi = 0$ in Equation 10.1, and we set $G = 0$ (noncompliant). We found that AquaMILR+ is capable of generating propulsion through this gait (Figure 10.4A), where the robot maintained a straight trajectory moving at 0.062 ± 0.006 m/s (mean $\pm$ standard deviation) and 0.305 ± 0.031 BL/cycle. Note the gaits shown have been optimized for consistent direction and obstacle navigation, but greater speeds can be achieved by increasing the robot's amplitude and temporal frequency.

To achieve turning behavior (Figure 10.4A), we set the offset $\varphi = 20°$ in Equation 10.1 to enable the robot to do a right offset turn where the remaining gait parameters unchanged as in the straight undulation evaluations. AquaMILR+ can turn in place with 6.21°/s (32.1°/cycle) within a sweeping area of an estimated radius of 0.6 m. Note that this in-place turning performance can be further improved by either increasing the offset or employing more efficient gaits such as omega turns [103].

Depth control experiments

The depth control system of AquaMILR+ is independent of the body actuation system, allowing us to tune the robot's depth and body pitch without the concern of gait interference.

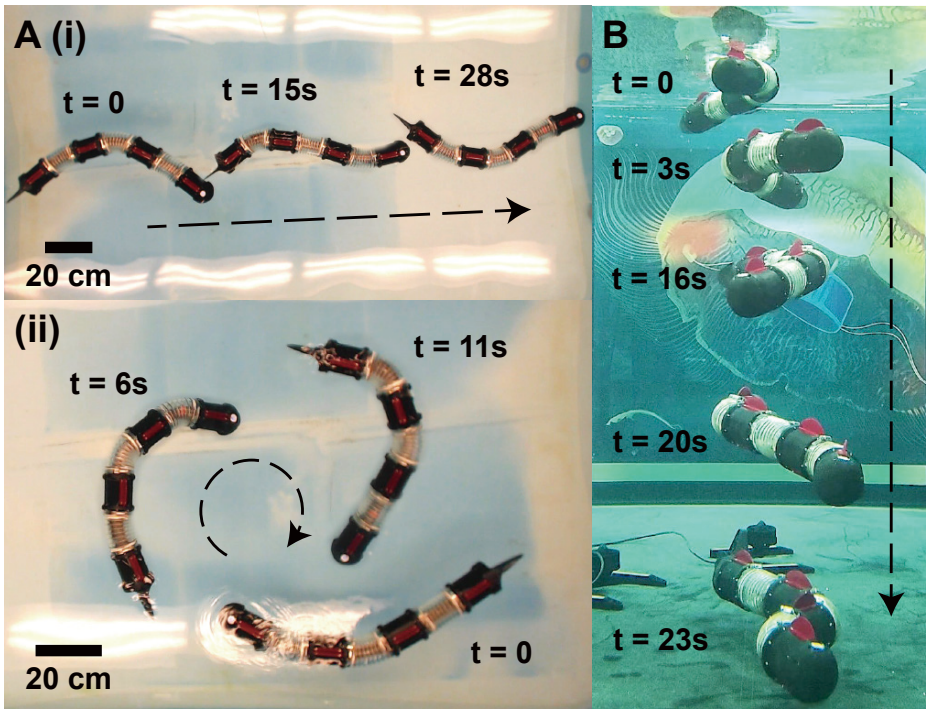

Figure 10.4: **Demonstration of locomotion and depth control capabilities of AquaMILR+.** (**A**)(i) Straight locomotion across a 3-m-long pool; (ii) implementation of a turning gait, where the robot can turn with a tight sweeping area. (**B**) A demonstration of a controlled, slow descent to 1.52 m deep while locomoting forward 1 m. Figures are adapted from [107].

We first evaluated the depth control system alone within a 4.88 m $\times$ 1.82 m $\times$ 1.82 m ($L \times W \times H$) water tank. During the evaluation, the syringes were slowly controlled from empty to full of water over 20 seconds (Figure 10.4B) in which the robot was able to reach a controlled descent to a depth of 1.52 m. This was done while the robot was locomoting forward, as this continuous change in volume during the gait proves essential to consider, altering the buoyancy characteristics compared to the straightened position. At this depth, the robot was still able to quickly ascend again with no compromise in seal integrity. Note that the 1.52 m depth is the maximum depth we could test with the facility; the full capability of AquaMILR+ is yet to be determined. This demonstrated the effectiveness of the depth-control system independent of the locomotion task at hand.

We then evaluated the robot's ability to follow more complex 3D trajectories to verify general open water performance applicable to navigation in cluttered environments. To test

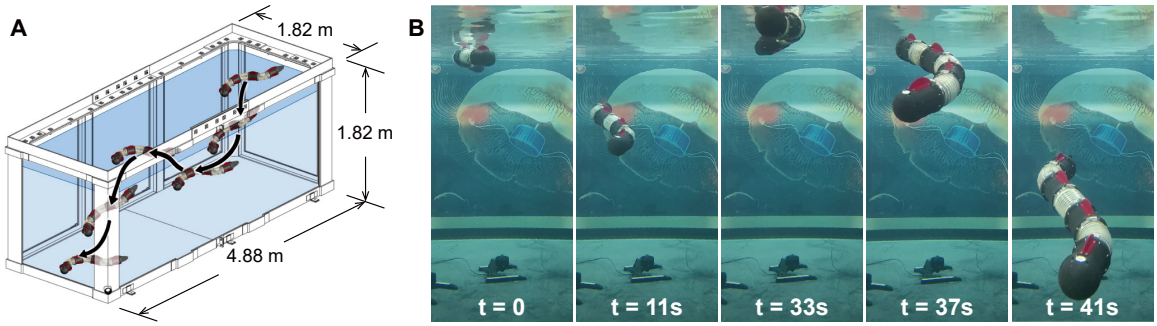

Figure 10.5: **Evaluation of AquaMILR+ locomotor capabilities, with independent depth control during undulation.** (**A**) The path of the robot in the tank, showing control authority over movement direction. (**B**) Video frames throughout the locomotion from a front-camera view. Figures are adapted from [107].

this, a sequence of syringe positions was commanded during the instructed undulation gait, resulting in a forward motion with changing depth to follow a complex path (Figure 10.5). With these tests, AquaMILR+ demonstrated effective open-loop locomotion in 3D aquatic environments through independent depth and gait control.

10.5 Discussion

The progression from MILR to AquaMILR illustrates a systematic evolution of the mechanical intelligence framework from terrestrial to aquatic environments. The first version, AquaMILR [108], represented an initial proof of concept for adapting cable-driven limbless robots to water (Figure 10.6A). Built upon the terrestrial MILR platform, it featured an untethered design encased in a waterproof coat (a tube-shaped polyethylene plastic sleeve), enabling surface swimming. However, its motion was limited to two-dimensional locomotion at the water-air interface. Despite this constraint, the system successfully demonstrated that body-compliance-based mechanical intelligence could be extended to amphibious regimes without additional control complexity.

The second-generation design presented in this chapter, AquaMILR+ (Figure 10.6B), advances this concept by introducing full submersion capability and independent depth control while preserving the morphologically intelligent actuation architecture of MILR.

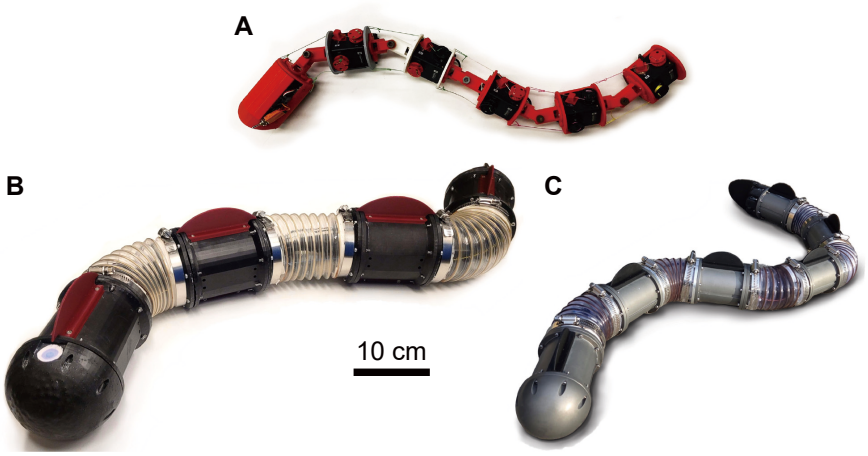

Figure 10.6: **A scale comparison of three generations of AquaMILR:** (**A**) AquaMILR without the waterproof coat, (**B**) AquaMILR+, and (**C**) a refined version of AquaMILR+. Figures are adapted from [108, 107].

The addition of a modular buoyancy system, telescopic leadscrew actuators, and robust waterproofing allowed AquaMILR+ to perform controlled three-dimensional swimming. This design established the foundation for studying mechanical intelligence in rheologically complex aquatic environments, where water currents, submerged obstacles, and fluid–structure interactions significantly influence locomotion.

Most recently, a refined version of AquaMILR+ (Figure 10.6C) incorporates several key upgrades for improved robustness. A reliable metal gasket system enhances sealing integrity for field operation, while a reduced body diameter yields finer body-wave resolution and increased maneuverability in dense obstacle environments. The decreased overall mass further promises easier transition between terrestrial and amphibious experiments, expanding the range of environments accessible to the robot.

The following chapter builds upon these developments by examining robophysical experiments conducted in a range of aquatic terrains. Using different AquaMILR models as representative implementations, these studies investigate how body compliance, actuation patterns, and environmental rheology interact to produce robust and adaptive locomotion under varying physical conditions.

CHAPTER 11
INVESTIGATION OF MECHANICAL INTELLIGENCE PRINCIPLES IN AQUATIC SETTINGS

11.1 Introduction

This chapter investigates whether the mechanical intelligence (MI) principles identified in terrestrial environments can be preserved, transformed, or newly manifested in aquatic settings. Building on the design and modeling framework established in Chapter 10, where the AquaMILR was developed as a cable-driven and compliance-programmable limbless robot, we now employ robophysical experiments to examine how body compliance and environmental interaction shape locomotion in water.

Biologically inspired swimming robots have been widely explored for their versatility in aquatic locomotion [200, 201, 19, 199, 197]. Among them, elongate limbless robots inspired by anguilliform swimmers, such as eels and sea snakes, exhibit high maneuverability and adaptability due to their continuous body undulation and redundancy [205, 27, 204]. While extensive studies have clarified the propulsion principles of these robots in homogeneous hydrodynamic conditions, far less is known about their behaviors in heterogeneous or cluttered aquatic terrains, where the body interacts continuously with obstacles and suspended materials.

In contrast to feedback-driven avoidance strategies [71, 208], MI leverages passive body mechanics and morphological compliance to adapt to environmental complexity without explicit sensing [89]. Terrestrial studies in earlier chapters demonstrated that such embodied mechanics allow spontaneous and robust obstacle negotiation. The question we now address is whether these same principles remain effective once the dominant physical regime shifts from frictional to hydrodynamic, where inertia and coasting fundamentally

alter locomotor dynamics. At intermediate Reynolds numbers, typically on the order of 10^2 to 10^3, inertial effects allow the swimmer to retain momentum between strokes, leading to coasting behavior that decouples instantaneous body deformation from instantaneous environmental reaction. This breaks the quasi-static assumption that underlies many terrestrial models and introduces time-dependent fluid-structure coupling, making the relationship between body shape change and net displacement rate-dependent [209, 127, 210, 110].

This chapter explores AquaMILR's locomotion across a spectrum of aquatic terrains, ranging from homogeneous fluids to cluttered and turbulent underwater environments. Through systematic variations in body compliance, gait pattern, and environmental disorder, we seek to determine (1) whether MI principles from terrestrial systems can persist in hydrodynamic conditions, (2) how these principles are modified by fluid-mediated interactions, and (3) whether new forms of MI arise uniquely in water. The findings presented here aim to expand the scope of MI beyond land, revealing how they evolve across physical media.

Note that all experiments in this chapter were conducted at the water surface unless otherwise specified. Because surface locomotion is primarily governed by the interaction between body undulation and near-surface hydrodynamics, the choice of robot platform does not significantly influence the observed behaviors. Accordingly, different AquaMILR models were employed across experiments depending on availability and setup compatibility, while all were treated as equivalent embodiments of the same underlying mechanical principles.

This chapter is adapted from my previously published peer-reviewed work [108] and [107].

11.2 Robophysical experiment setup

A laboratory-scale aquatic environment was constructed to evaluate AquaMILR's locomotion under controlled hydrodynamic and cluttered conditions. The test arena consisted of an indoor pool measuring 3 m $\times$ 2 m $\times$ 0.5 m ($L \times W \times H$).

The first environment, referred to as the *rigid lattice*, was composed of PVC pipes 9 cm in diameter, each mounted on suction cups to ensure firm attachment to a submerged plexiglass base. The obstacles were arranged in a triangular grid with 25 cm spacing, forming a 2 m $\times$ 2 m terrain area. The suction-mounted bases prevented obstacle displacement upon collisions, maintaining a fixed and repeatable geometry for all experiments. This setup provided a controlled environment to study locomotion through rigid, immobile clutter.

In addition to the rigid lattice, a *flexible lattice* configuration was tested using vertically mounted pool noodles of 6 cm diameter. These obstacles were partially submerged and anchored to the pool floor by a lightweight frame that allowed bending upon contact. The flexible lattice introduced a compliant environment that emulated aquatic clutter such as vegetation or suspended debris, allowing investigation of how environmental compliance influences body-obstacle interactions and locomotor stability.

To further explore locomotion in unanchored cluttered environments, a terrain composed of freely floating obstacles was introduced. The obstacles were 3D-printed spheres and cylindrical tubes with 6.3 cm diameter, designed to remain partially submerged and mobile on the water surface. Their random initial distribution generated a dynamic and continuously reconfiguring environment that changed as the robot moved through it. This setup simulated floating debris, enabling the study of locomotion through disordered and mobile clutter.

Finally, to examine performance under flow-induced disturbances, a weak turbulent current was generated using four 80 GPH (300 L/h, 4 W) mini submersible pumps placed in a row at one end of the pool. The pump produced turbulence and a mild unidirectional stream, and the robot was commanded to swim upstream toward the source. This configuration allowed assessment of how the robot interact with unsteady hydrodynamic forces.

Together, these four environments progress from rigid to flexible, fixed to floating, and static to flowing conditions. They represent a collection of physical models that approximate the diverse types of obstacles a limbless robot may encounter in realistic aquatic

applications, such as inspection, environmental monitoring, or search operations. By systematically varying both the mechanical properties of the environment and the robot's internal compliance, these experiments provide a comprehensive view of how embodied design principles influence locomotion across increasing levels of environmental complexity.

11.3 Performance in diverse aquatic complex environments

Rigid lattice

In this section, we present the results of our robophysical experiments. By varying the parameters of generalized compliance (G), gait amplitude (A), spatial frequency (ξ), and temporal frequency (ω), we conducted repeated trials with AquaMILR operating under purely feedforward, open-loop control, where the robot executed prescribed undulation motions without sensing-based active adjustments. These experiments enabled us to examine how these parameters influence AquaMILR's behavior and performance within the lattice and to quantify the conditions under which body compliance facilitates spontaneous movement through obstacles.

Generalized compliance G: Previous chapters have demonstrated that in the terradynamic regime, the robot exhibited the highest capability to navigate lattices at a mid-range of generalized compliance (G). A small G often led to jamming between obstacles, while a large G resulted in insufficient thrust for forward movement. Jamming occurs when the robot's motion is restricted either by excessive strain from obstacles, exceeding compliance limits and causing immobilization, or by excessive compliance, which prevents the robot from maintaining its undulatory body shape and generating thrust against obstacles. To verify whether this principle extends to the hydrodynamic regime, we experimented with the robot under varied G values, using a fixed gait template that resulted in the same body wavelength-to-post spacing ratio as in the terrestrial case ($A = 55°, \xi = 0.6, \omega = 0.05$ Hz). Figure 11.1A shows the survival rate as a function of the distance traveled by the robot. The results indicate that a mid-level G remains optimal for navigating obstacles, as reflected by

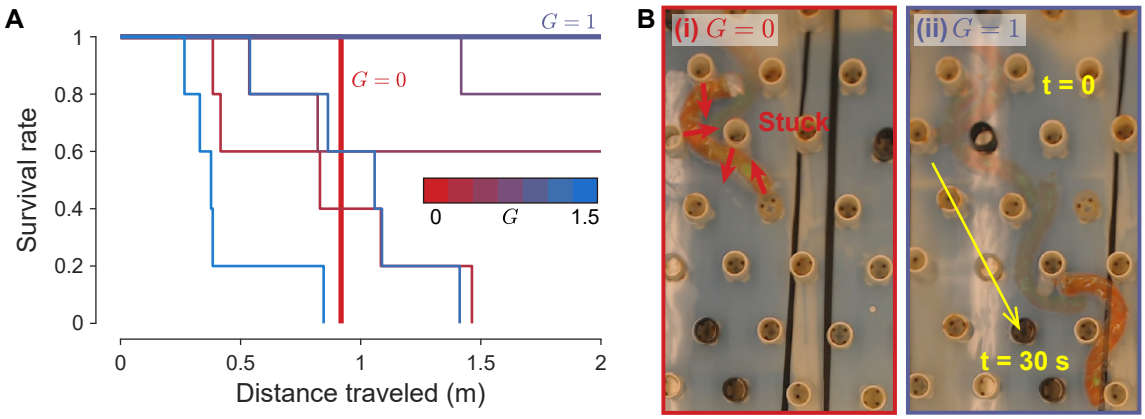

Figure 11.1: **The effect of the generalized compliance parameter (G) on locomotion performance.** (**A**) The survivor function for varied G values with respect to distance traveled. (**B**) Time-lapsed frames showing examples of (i) the robot becoming stuck at $G = 0$ and (ii) the robot successfully traversing the lattice at $G = 1$. Figures are adapted from [108].

the highest survival rates over distance traveled. Specifically, $G = 1$ emerged as the most appropriate value, enabling the robot to traverse the lattice in all trials (Figure 11.1B-ii), demonstrating a manifestation of mechanical intelligence. Our experiments showed that with a low level of $G < 0.75$, the robot body was too rigid, and when combined with coasting dynamics in the lattice, it often ended up in jamming configurations (Figure 11.1B-i). At a high level of $G > 1$, the robot became too compliant, and the inability to maintain the desired body curvature significantly hampered propulsion through the lattice.

Gait spatial frequency and amplitude: By varying gait parameters in the template Equation 10.1, we investigated the robustness of the emergent obstacle navigation over a wide range of gaits. In this set of experiments, we tested the robot with $G = 0$ and $G = 1$, where $G = 1$ was identified previously as the optimal value for successful lattice traversal.

First, we fixed $A = 55°$ and varied the spatial frequency. Figure 11.2A depicts the successful traverse rate as a function of spatial frequency for both the noncompliant robot ($G = 0$) and the mechanically intelligent robot ($G = 1$). The results show that $G = 1$ allows the robot to traverse the lattice over a wider range of spatial frequencies than $G = 0$. Also note that the robot was unable to navigate through spatial frequency values above 0.9,

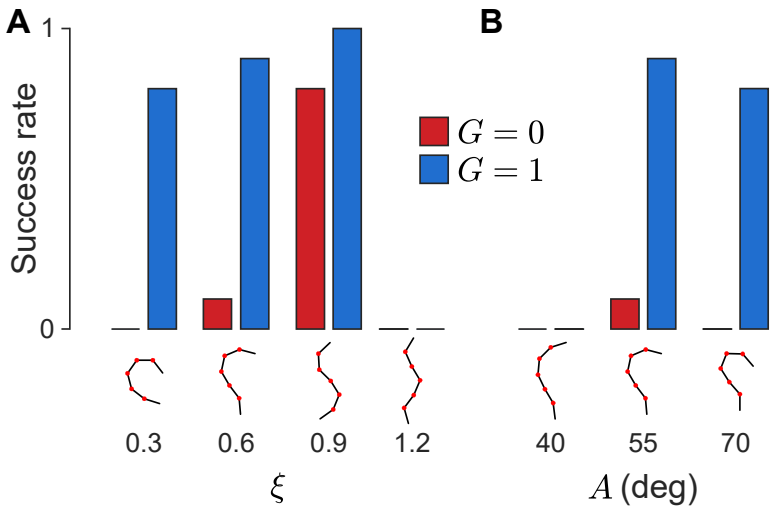

Figure 11.2: **The effect of gait parameters on locomotion performance.** (**A**) Success traversal rate as a function of spatial frequency (ξ). (**B**) Success traversal rate as a function of amplitude (A). Figures are adapted from [108].

even with $G = 1$. This is likely due to the insufficient curvature in the wave shape, which hinders the robot's ability to latch around obstacles and propel itself forward.

We then fixed $\xi = 0.9$ and varied the amplitude. Similar to the results above, Figure 11.2B reveals that $G = 1$ allows the robot to traverse the lattice over a wider range of amplitudes than $G = 0$. Overall, although for a specific lattice there is a combination of gait parameters that allows the non-compliant robot to traverse (in this case, $A = 55°, \xi = 0.9$), an appropriate level of body compliance can reduce the sensitivity of robot performance to parameter selection, allowing a wider range of gaits to be effective.

Undulation frequency: Previous sections have verified that principles of mechanical intelligence in terrestrial environments can be extended to aquatic environments. However, the largest difference in locomotion between terradynamic and hydrodynamic regimes is the effect of inertia. In the terradynamic regime, locomotion can be assumed quasi-static, making performance insensitive to undulation frequency. Conversely, in the hydrodynamic regime, the coasting effect influences performance with increased undulation frequency leading to increased coasting. Thus, to study the effect of undulation frequency on performance, we varied the temporal frequency (ω) in the gait template Equation 10.1, while

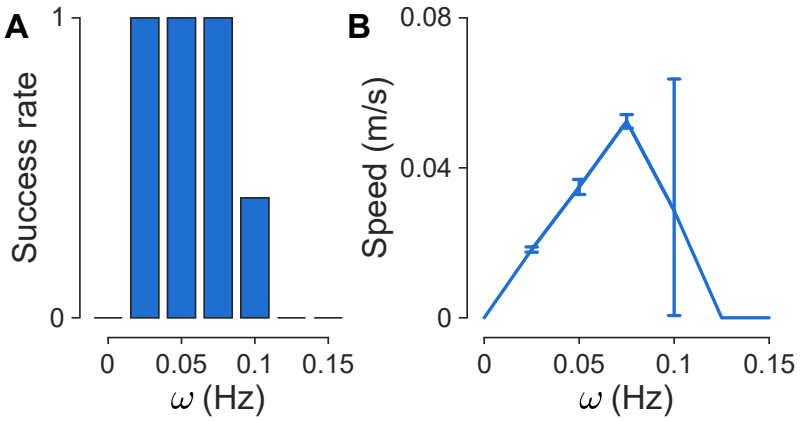

Figure 11.3: **The effect of undulation temporal frequency (ω) on locomotion performance.** (**A**) Success rate as a function of temporal frequency. (**B**) Averaged absolute speed of the robot as a function of temporal frequency. Error bars indicate standard deviations. Figures are adapted from [108].

keeping other parameters fixed ($A = 55°$, $\xi = 0.6$, $G = 1$). Figure 10.3 showcases the results for the successful traverse rate and the absolute speed as functions of temporal frequency. The results first showed a linear relationship in speed from 0.025 Hz to 0.075 Hz, peaking at 0.062 m/s. When $\omega > 0.075$, jamming events started to emerge at $\omega = 0.1$ Hz, resulting in a large standard deviation in speed, and became dominant at higher ω. Higher undulation frequency induced more unpredictable collisions, leading to abrupt deviations in the robot's trajectory. These collisions increased the probability of jamming instances in the lattice. These findings indicate that at high undulation frequencies in hydrodynamic environments, passive body mechanics alone can no longer effectively mitigate harsh collisions, leading to increased jamming and instability. Consequently, relying solely on mechanical intelligence is insufficient for high-frequency operation and achieving higher absolute speeds in obstacle-rich environments. To enhance performance in cluttered fluid settings, computational intelligence (incorporating sensing and decision-making for active adaptation to perturbations) must be integrated with mechanical intelligence to improve speed and autonomy.

Inertia-induced body flipping in high undulation frequency regimes: When the undulation frequency was further increased beyond 0.15 Hz, reaching approximately 0.2 Hz, an

unexpected behavior emerged in the rigid lattice experiments. Even with minimal or zero generalized compliance ($G = 0$), the robot was occasionally able to traverse the lattice successfully. As shown in Figure 11.4, when the robot approached a near-jamming configuration, the interaction between its body and the surrounding obstacles generated a sudden torque that flipped the body about its longitudinal axis. Rather than causing failure, this inertial body flip enabled the robot to reorient and continue forward locomotion.

This phenomenon demonstrates an inertia-induced mechanism that effectively resolves potential jamming events in cluttered aquatic environments. The body flip arises from momentum accumulation during high-frequency undulation, which leads to transient lift and rotational impulses when the body is compressed by the lattice. Once flipped, the robot resumes undulation in the new orientation, maintaining propulsion without external intervention. Such behavior reveals a new form of mechanical intelligence unique to high-coasting, three-dimensional motion regimes. Unlike terrestrial conditions, where friction-dominated interactions prevent out-of-plane maneuvers, the feature of aquatic settings enable the robot to exploit body-environment coupling dynamically to escape confinement. This result suggests that, in aquatic systems, mechanical intelligence can manifest through inertially mediated body reorientation, extending its domain beyond compliance-driven adaptations observed in low-coasting terrestrial environments.

Flexible lattice

To examine how environmental compliance influences locomotion performance, experiments were conducted in the flexible lattice environment (Figure 11.5). The robot was placed in random initial positions, and flexible obstacles were installed at approximately the same spacing as the rigid lattice but with small perturbations in their placement to introduce stochastic variations. The compliant obstacles could bend under contact, allowing dynamic interactions between the robot body and the deformable terrain.

For each test, the robot was driven at different undulation frequencies and general-

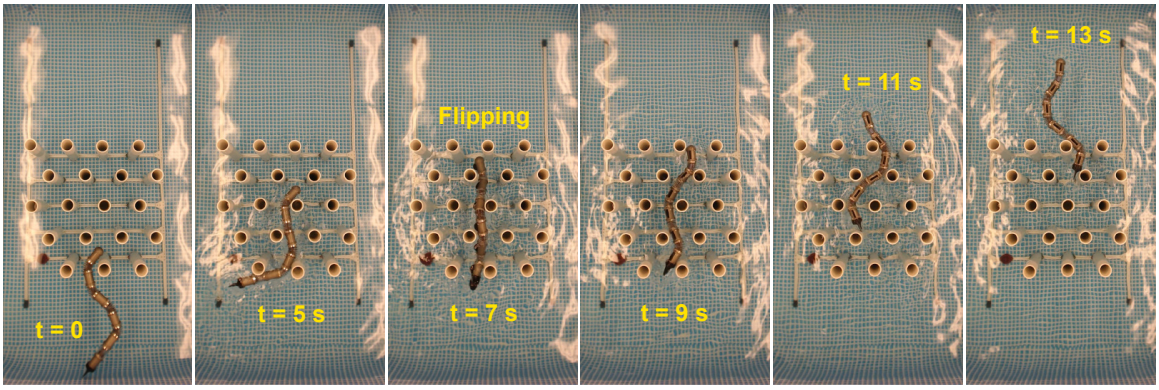

Figure 11.4: **Inertia-induced body flipping observed in the rigid lattice at high undulation frequency ($\omega = 0.2$ Hz, $G = 0$).** When the robot approaches a near-jamming configuration, accumulated momentum and obstacle reaction forces generate a torque that flips the body about its longitudinal axis. The flip reorients the robot and enables continued forward locomotion, demonstrating a new mechanical intelligence principle unique to high-coasting, three-dimensional movement regimes.

ized compliance (G). The expected speed was calculated as the product of the average speed in successful traversals and the corresponding traverse success rate. As shown in Figure 11.5A, locomotion performance exhibited a strong co-dependence between G and ω. At low frequencies ($\omega = 0.1$ Hz), robots with rigid bodies ($G = 0$) failed to generate sufficient thrust to overcome obstacle resistance, whereas intermediate compliance values ($G = 0.5$ and 1) enabled stable propulsion through body-environment adaptation. As the undulation frequency increased, inertial effects began to contribute to locomotion, and even robots with $G = 0$ started to traverse the lattice successfully, consistent with the inertia-induced flipping principle discussed in the previous section.

However, when the undulation frequency was further increased to $\omega = 0.4$ Hz, high-compliance robots ($G = 1$) lost their ability to maintain the prescribed body curvature as joints could no longer reach the target amplitude due to the slackness of the cables, reducing thrust generation and leading to performance degradation. At very high frequencies ($\omega \geq 0.6$ Hz), all configurations failed to produce coordinated undulation due to amplitude loss. The optimal performance occurred at $\omega = 0.4$ Hz and $G = 0.5$, where the expected speed reached 0.028 m/s.

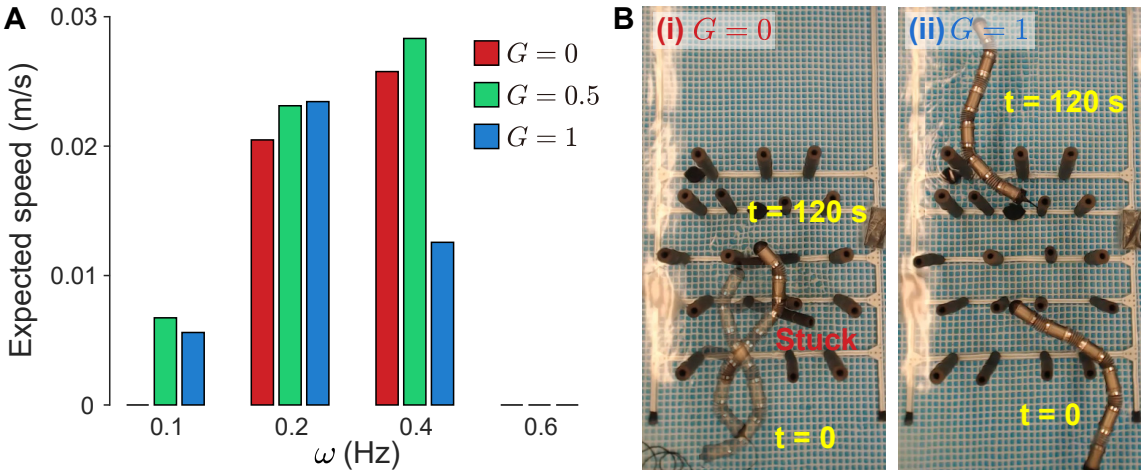

Figure 11.5: **Locomotion performance in the flexible lattice environment.** (**A**) Expected speed as a function of undulation frequency ω for three body compliance levels. The expected speed was computed as the product of average successful speed and traverse success rate. (**B**) Representative time-lapse images comparing performance between $G = 0$ (i) and $G = 1$ (ii) at $\omega = 0.1$ Hz. The rigid body failed to progress through the deformable terrain, whereas moderate compliance enabled continuous propulsion and successful traversal.

These results reveal that environmental compliance introduces new coupling effects between internal and external mechanics. In the flexible lattice, appropriate body compliance enhances stability and adaptability at low frequency, while at higher frequencies, inertial effects can compensate for the lack of compliance. This co-effect of G and ω demonstrates the extended range of mechanical intelligence achievable in deformable aquatic terrains.

Floating clutter

To assess how AquaMILR performs in unanchored and dynamically changing environments, we conducted experiments in the floating clutter field (Figure 11.6). In each trial, the robot was placed at a fixed initial position, while the floating spherical and cylindrical obstacles were randomly distributed over the water surface. These obstacles were free to drift and reconfigure as the robot moved, creating continuously evolving contact and flow conditions. The experiments were performed with $\omega = 0.2$ Hz, which corresponded to the optimal frequency range identified in the flexible lattice tests.

Figure 11.6A shows the averaged locomotion speed as a function of body compliance

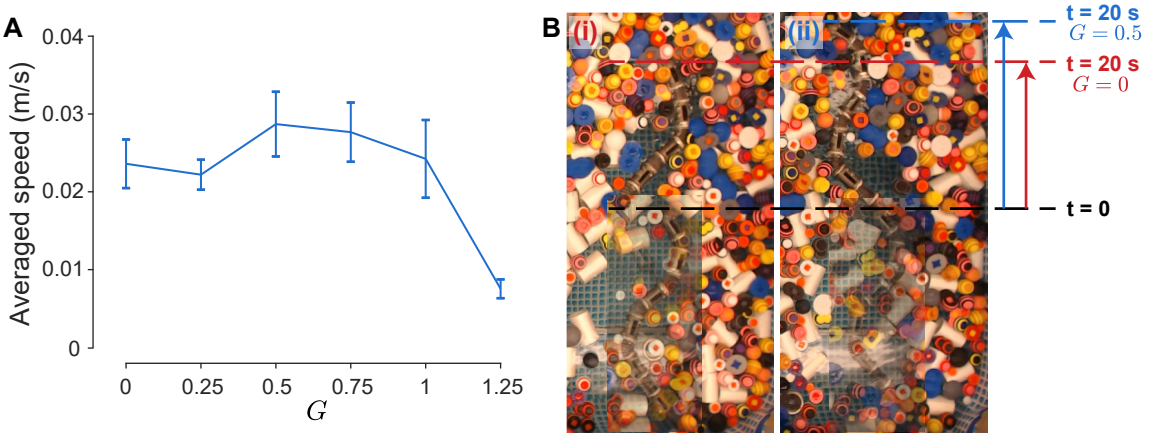

Figure 11.6: **Locomotor performance in the floating clutter environment.** (**A**) Averaged speed as a function of body compliance G at $\omega = 0.2$ Hz. Each data point represents the mean of three traversals, and error bars denote standard deviation. (**B**) Representative trajectories comparing robots with $G = 0$ and $G = 0.5$.

G. Each data point represents the mean of three trials, with error bars denoting standard deviation. The results indicate that performance remains relatively stable for $0 \leq G \leq 0.75$, suggesting that a moderate range of compliance provides adequate adaptability to the continuously shifting environment. The highest average speed of approximately 0.029 m/s was achieved at $G = 0.5$. When G exceeded 1, performance dropped sharply because excessive compliance weakened body curvature, reducing thrust generation and causing energy loss through body deformation. Representative trajectories in Figure 11.6B illustrate that both rigid ($G = 0$) and directionally compliant ($G = 0.5$) robots could advance through the clutter. These results show that moderate body compliance enables the robot to absorb and redistribute impact forces efficiently while maintaining directional stability in disordered, mobile environments.

Turbulent flow

To evaluate AquaMILR's capability under unsteady hydrodynamic disturbances, a demonstration was conducted in the turbulent flow environment (Figure 11.7). The robot was commanded to swim upstream toward the flow source using the gait parameters $G = 0.5$ and $\omega = 0.4$ Hz, corresponding to the best-performing configuration identified in previous

Figure 11.7: **Demonstration of AquaMILR swimming upstream in a turbulent flow environment ($G = 0.5$, $\omega = 0.4$ Hz).** Despite the unsteady hydrodynamic disturbances produced by the pumps, the robot maintained stable forward progression.

sections.

Despite the presence of surface disturbances and unsteady vortices, the robot maintained a stable upstream trajectory and continuous forward propulsion. The body oscillations remained regular, and the robot's heading was minimally affected by fluctuating flow. This result demonstrates that the combination of moderate compliance and appropriate gait frequency provides sufficient passive stability to counteract transient hydrodynamic perturbations.

Although this test was primarily qualitative, it highlights the robustness of the AquaMILR's embodied design in turbulent conditions. The robot's ability to maintain upstream locomotion without active feedback control suggests that the same mechanical intelligence principles governing adaptability in cluttered environments also contribute to stability in unsteady flow regimes.

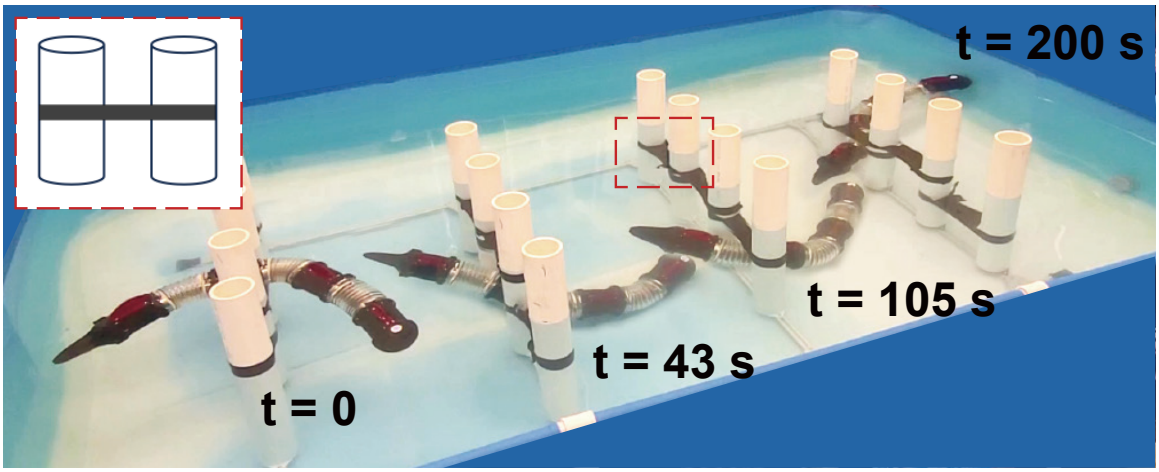

Figure 11.8: **Demonstration of AquaMILR navigating a 3D obstacle terrain using open-loop depth modulation.** The robot alternated between ascending and descending motions while performing undulatory swimming with bidirectional compliance ($G = 1$). This strategy enabled it to bypass both vertical and lateral obstacles without feedback control, showcasing the extension of mechanical intelligence into 3D aquatic environments. The figure is adapted from [108].

3D lattice

Further experiments were conducted to evaluate AquaMILR's capability to navigate complex three-dimensional environments (Figure 11.8). The terrain was constructed using rows of PVC cylinders mounted on an aluminum frame, similar to the rigid lattice configuration but with increased spacing between rows and the addition of lateral obstacles. This arrangement required the robot to coordinate horizontal locomotion with vertical motion to escape from confinement.

During these trials, AquaMILR employed an open-loop depth modulation sequence that alternated between ascending and descending phases while performing body undulation. The combination of depth variation and lateral undulation enabled the robot to move around or beneath obstacles without feedback control. Bidirectional body compliance ($G = 1$) was applied, along with the same gait parameters used in the two-dimensional lattice experiments.

As shown in Figure 11.8, the robot successfully navigated through multiple layers of

obstacles by continuously adjusting its depth while maintaining forward progression. The results demonstrate that the integration of independent depth control and programmable compliance allows AquaMILR to extend its mechanical intelligence into three-dimensional aquatic spaces. Through this capability, the robot can exploit its passive body mechanics to manage contact forces and buoyant lift simultaneously, enabling locomotion through volumetric terrains where traditional planar strategies are ineffective.

11.4 Conclusion

This chapter examined how gait parameters and body compliance jointly influence locomotion performance in cluttered aquatic environments. Through systematic robophysical experiments, we demonstrated that the coupling between undulation frequency, body compliance, and environmental resistance produces qualitatively different locomotor behaviors. At low undulation frequencies, locomotion is dominated by quasi-static interactions in which appropriate body compliance is essential to maintain propulsion and prevent jamming. As frequency increases, inertial effects emerge and begin to supplement or even replace the role of compliance, allowing successful traversal even in robots with rigid bodies.

A key discovery in this study is the inertia-induced body flipping mechanism, observed when the robot operates in the high-frequency, high-coasting regime. In this regime, accumulated momentum and obstacle reaction forces generate sufficient torque to reorient the robot's body in three dimensions, resolving potential jamming events and restoring forward progression. This behavior represents a new form of mechanical intelligence that arises only in fluid environments, where inertia and buoyancy enable body reorientation and recovery from constrained states without sensing or control intervention.

Overall, the results presented in this chapter expand the understanding of mechanical intelligence by showing how inertial and compliant effects can coexist to sustain robust locomotion in cluttered aquatic terrains. The transition from compliance-driven adaptation

at low frequency to inertia-driven self-recovery at high frequency highlights the versatility of embodied mechanics as a basis for intelligent behavior.

CHAPTER 12
INCORPORATE COMPUTATIONAL INTELLIGENCE TOWARDS AMPHIBIOUS AUTONOMY

12.1 Introduction

Building upon the hierarchical framework of mechanical intelligence established throughout this thesis, this final chapter focuses on the high-level computational layer, where sensing, decision-making, and control interact to enable autonomy across diverse environments. While earlier chapters have shown how passive body mechanics and tunable compliance can yield spontaneous adaptation on land and underwater, this chapter extends these principles toward amphibious autonomy, referring to the ability of a single robotic platform to operate adaptively across both terrestrial and aquatic domains through embedded sensing and decentralized feedback control.

Two representative studies demonstrate how computational intelligence (CI) can augment mechanical intelligence (MI) to achieve this goal. The first study investigates a worm-inspired reversal behavior in MILR, where head-contact sensing triggers an active reversal maneuver analogous to the collision-evoked escape response in *C. elegans* [89]. Through this closed-loop sensory reflex, the robot achieves robust obstacle negotiation by coupling local proprioceptive feedback with motor commands, showing how minimal sensing can transform passive locomotion into context-responsive behavior.

The second study extends the CI augmenting MI concept into aquatic environments using AquaMILR. By continuously adjusting the generalized compliance parameter G based on joint-level torque feedback, AquaMILR dynamically reshapes its joint mechanical properties to accommodate hydrodynamic interactions and environmental disturbances [108]. This distributed feedback mechanism enables body-wide self-regulation, allowing the robot

to maintain effective propulsion and maneuverability.

Together, these studies mark a transition from mechanically intelligent locomotion to computationally enhanced mechanical intelligence, advancing toward true amphibious autonomy. Through integrated sensing, feedback, and local computation, the robots presented here illustrate how physical intelligence and algorithmic adaptation can work in synergy to achieve robust performance across land-water interfaces and other complex terrains.

This chapter is adapted from my previously published peer-reviewed work [89] and [108].

12.2 Bio-inspired reversals triggered by head contact sensing

In addition to the passive body-environment interactions in MILR discussed in early chapters, nematodes such as *C. elegans* exhibit an active reversal behavior triggered by head collisions, which serves as an effective escape response [211]. During this behavior, the worm transiently reverses the direction of its traveling body wave before resuming forward motion. Such active responses to environmental heterogeneities can augment the animal's obstacle navigation by providing an additional means of modulating its body orientation and collision angle.

We hypothesized that similar active reversals could enhance locomotor performance in limbless robots by complementing passive mechanical adaptation with a simple closed-loop feedback mechanism. To do so, we developed a head collision sensor for MILR to allow real-time collision angle and force estimation.

The head collision sensor is an add-on structure in MILR. We designed and 3D-printed a head for the robot that is capable of sensing the collision angle (discrete) and the approximate magnitude of collision forces. Five force-sensing resistors (FSR, Interlink Electronics FSR Model 408) were attached in parallel on the curved head surface (Figure 12.1A). The feedback analog signals were collected using an Arduino micro-controller (Seeeduino XIAO SAMD21). Each FSR covered a distinct collision angle range: approximately $65°$–$75°$, $75°$–$85°$, $85°$–$95°$, $95°$–$105°$, and $105°$–$115°$. The thresholds used to trigger re-

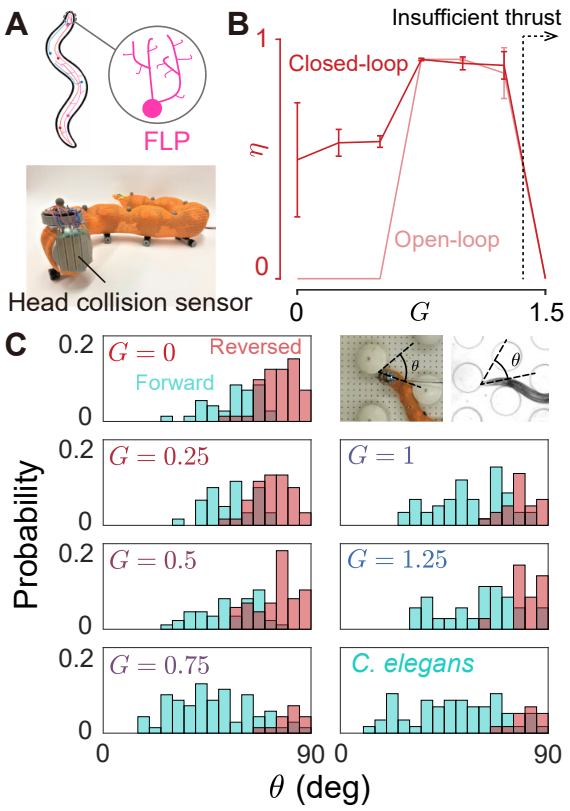

Figure 12.1: **Active reversals augment mechanical intelligence in MILR.** (**A**) The FLP dendrite structure in nematodes and the head collision sensor in the robot. (**B**) Wave efficiency η (normalized speed) as a function of generalized compliance G for open-loop and closed-loop MILR, showing that reversals expand the range of effective locomotion. (**C**) Head collision angle probability distributions classified by post-collision direction (forward or reverse) in the robot across different G values, compared with *C. elegans*. Figures are adapted from [89].

versal behavior in the closed-loop control were set to 3 N for the third (center) FSR and 5 N for the second and fourth (left and right middle) FSRs. When collision forces exceeded the set thresholds, the robot initiated a reversal behavior, where the reverse duration was fixed at 0.125 gait cycle.

We studied the closed-loop robot with reversal capability in the dense environment and compared its locomotor performance to open-loop results. Reversals enabled the robot to traverse the environment in the low generalized compliance regime, which the open-loop strategy failed to (Figure 12.1B), improving η in the range $0 \leq G \leq 0.5$. The reversal behaviors robustified the locomotion by increasing the range of G that allows the model to

effectively locomote in the most challenging environment.

Furthermore, the kinematic similarity between the closed-loop robot and nematodes motivated a comparative analysis of head-collision statistics. The probability distributions of head collision angles and post-collision movement directions (forward or reverse) were strikingly consistent between the robot ($G = 0.75$) and nematodes (Figure 12.1C). These results indicate that simple feedback control based on head sensing can reproduce emergent behavioral features observed in biological organisms. Robophysical experiments revealed the function of reversal behaviors in undulatory locomotors: by not simply repeating the same movement back and forth in place, reversals allow the locomotor to take advantage of mechanically intelligent dynamics—passively adjusting body postures and spontaneously finding favorable position and orientation to generate effective thrust for locomoting further.

Overall, the reversal-capable robot exemplifies the synergistic integration of mechanical and computational intelligence. The implementation of minimal sensing and feedback transforms otherwise passive dynamics into context-dependent adaptive behaviors, revealing a pathway toward embodied autonomy. The close agreement in both locomotor efficiency and behavioral statistics between the robot and *C. elegans* also provides insight into the functional role of mechanosensory neurons such as FLP [212, 213], whose spatial structure may facilitate angular discrimination during head collisions. This work thus demonstrates how local feedback control can augment embodied intelligence and serves as a foundation for developing higher-level autonomous behaviors in limbless robots.

12.3 Decentralized real-time compliance tuning based on joint torque feedback

The previous section demonstrated how head-collision-triggered reversals can augment mechanical intelligence through closed-loop sensory feedback on land. To extend the concept of CI augmenting MI into aquatic environments, we next developed a decentralized control mechanism that enables local adaptation of body compliance in real time. This approach

aims to further integrate CI into AquaMILR, allowing it to navigate complex aquatic environments where spatial heterogeneities challenge open-loop control.

We developed a feedback controller that dynamically modulates G in real time based on the torque experienced at each joint (Figure 12.2A). Instead of assigning a constant G value to all joints, this controller operates in a decentralized manner by locally tuning each joint's compliance according to sensed torque feedback. The G value of the i-th joint is modulated following

$$G_i(\tau) = 1 + 0.2H(\tau_i - 0.3T) + 0.2H(\tau_i - 0.5T) + 0.2H(\tau_i - 0.7T), \tag{12.1}$$

where τ_i is the torque estimated at the servo motors controlling the left or right cable in the i-th joint, and T is the maximum stall torque of the servo motor (1.4 N·m). The step function $H(\cdot)$ implements a three-level torque thresholding mechanism:

$$H(x) = \begin{cases} 0 & x < 0, \\ 1 & x \geq 0, \end{cases} \tag{12.2}$$

realizing the logic shown in Figure 12.2A. Starting from a baseline value of $G = 1$, the controller increases G in 0.2 increments as joint torque exceeds predefined thresholds. Once an increase occurs, the new G value is maintained for 0.5 s or until the sensed torque drops below the threshold, ensuring stability while preserving responsiveness. This real-time mechanism effectively distributes computational intelligence across the robot's body, allowing local joints to adapt to transient loading without centralized control.

To evaluate the controller's effect on locomotor performance, we first tested AquaMILR in a randomly distributed lattice, generated by perturbing a regular obstacle grid to better represent natural underwater irregularities (Figure 12.2B). The decentralized controller enabled the robot to achieve a 100% successful traverse rate through the random lattice.

An example trajectory is shown in Figure 12.2B, with corresponding time-varying G

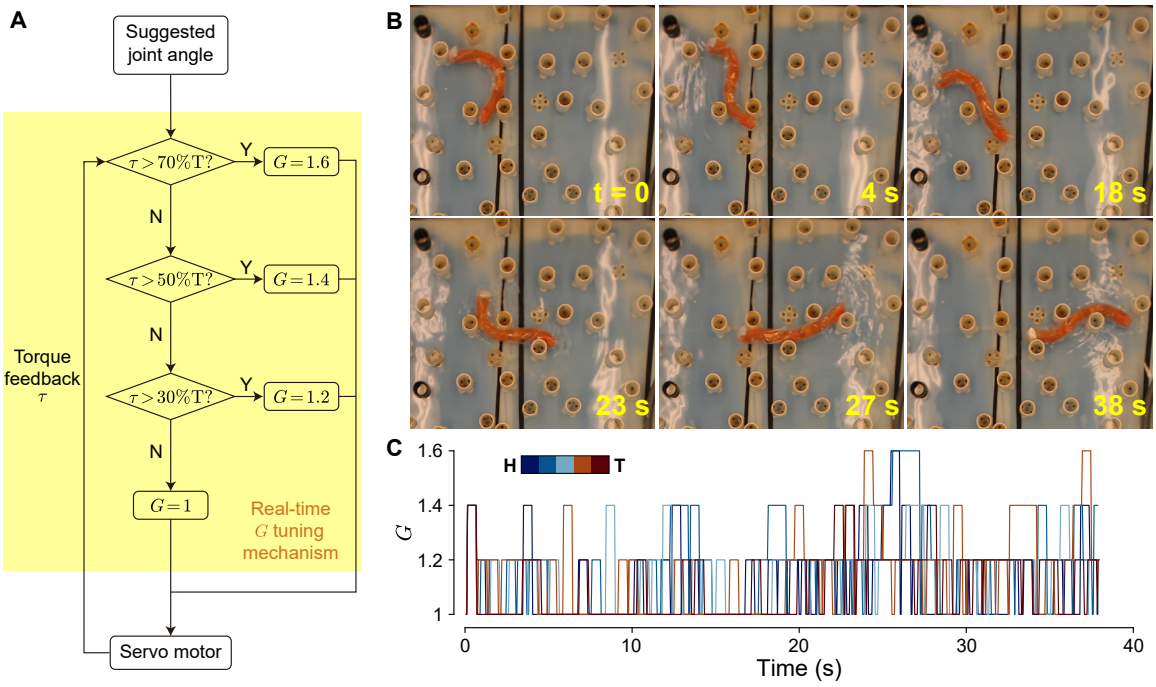

Figure 12.2: **Decentralized real-time compliance tuning enhances aquatic locomotion robustness in AquaMILR.** (**A**) Block diagram of the decentralized feedback controller implementing real-time local G tuning based on torque feedback. (**B**) Video snapshots illustrating the robot navigating a randomly distributed lattice. (**C**) Time evolution of local G values along the body, from head (H) to tail (T). Figures are adapted from [108].

values of individual joints plotted in Figure 12.2C. During the experiment, when the robot experienced local jamming or increased resistive forces, the corresponding joints automatically adjusted their G values, thereby facilitating escape and restoring forward motion. This adaptive compliance tuning significantly enhanced robustness in disordered environments where passive mechanical intelligence alone was insufficient. These results demonstrate that real-time decentralized feedback control can complement mechanical intelligence and improve locomotor performance under high environmental uncertainty.

To further demonstrate the generality of this control mechanism, we implemented the G controller in a terrain transition scenario where AquaMILR navigated from a rigid lattice into a layer of floating clutter (Figure 12.3). As discussed in the previous chapter, $G = 0.5$ was found to be optimal for locomotion on floating clutter, and thus we set this value as the baseline compliance for this experiment. When the robot entered the lattice region, the local

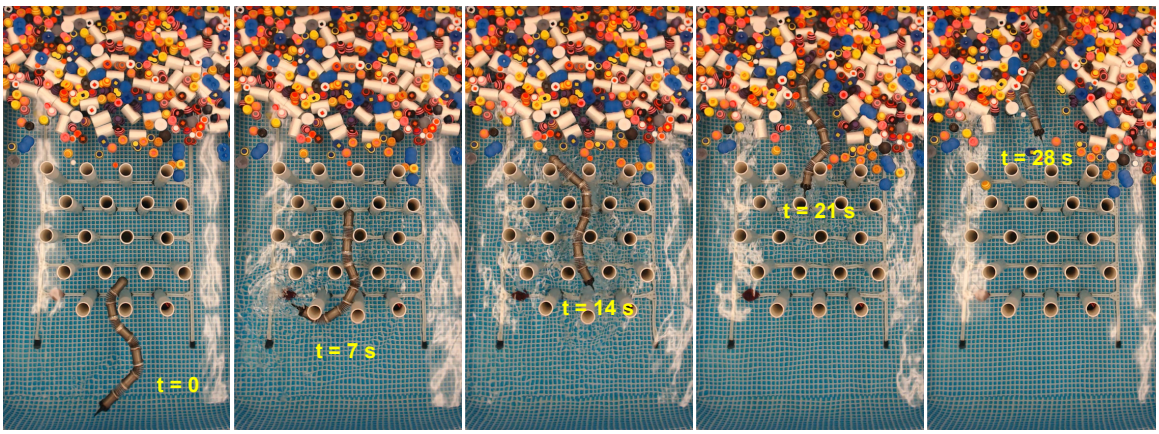

Figure 12.3: **Implementation of the decentralized G controller in transitioning aquatic terrain.** AquaMILR navigates from a rigid lattice into floating clutter while maintaining forward progression.

torque feedback triggered increases in G to overcome the higher resistance and contact constraints. This experiment illustrates how the same decentralized G-tuning strategy can support adaptive transitions between distinct aquatic environments, providing a promising pathway toward robust amphibious operation.

In addition to improving locomotion robustness, this control mechanism provided the robot with a sensing capability that effectively allowed it to probe the density of its surrounding environment. For instance, during the time period from $t = 23$ s to $t = 27$ s in Figure 12.2C, we observed an emergent increase in G values, corresponding to regions of higher obstacle density. Due to the decentralized nature of the controller, it was also possible to identify which body segments experienced the greatest environmental resistance. Such distributed proprioceptive sensing not only improves adaptive locomotion but also provides a foundation for environmental characterization.

Future integration with onboard localization and mapping systems could enable AquaMILR to operate as a mobile probe, capable of both locomoting through and sensing heterogeneous aquatic environments. This capability represents a further step toward amphibious autonomy, where mechanical and computational intelligence jointly support adaptive and informative interactions with the environment.

12.4 Conclusion

This chapter demonstrated how computational intelligence can augment mechanical intelligence to achieve robust locomotion across both terrestrial and aquatic environments. Building upon the principles of mechanical intelligence established in earlier chapters, the studies presented here focused on implementing feedback mechanisms that enable context-dependent adaptation in situations where pure MI is insufficient.

The first study showed that head-collision-triggered reversals provide a simple yet effective form of closed-loop feedback that enhances obstacle negotiation on land. By coupling proprioceptive sensing with local motor responses, MILR reproduced the reversal behavior observed in *C. elegans*, extending mechanically intelligent dynamics with a biologically inspired reflex that improves locomotor robustness in dense environments.

The second study demonstrated a decentralized real-time compliance controller that allows each joint of AquaMILR to modulate its mechanical properties based on local torque feedback. This distributed computational mechanism significantly improved the robot's ability to traverse disordered environments, where open-loop strategies alone could fail. The results highlight that local sensing and real-time adaptation can amplify the benefits of mechanical intelligence, allowing the robot to maintain performance under environmental uncertainty.

Together, these findings establish that simple feedback architectures can effectively bridge local passive dynamics with higher-level behavioral computation. The combination of reflexive sensing and decentralized control provides a scalable strategy for achieving amphibious autonomy, allowing a robot to continuously adapt its interaction with the environment through both physical embodiment and sensory feedback. This integration of mechanical and computational intelligence represents the final layer of the hierarchical framework introduced in this thesis and points toward future robotic systems capable of self-organized, environmentally responsive behaviors across diverse and dynamic terrains.

CHAPTER 13
CONCLUSION AND FUTURE WORK

13.1 Conclusion

This thesis establishes a comprehensive framework for the design, modeling, and control of limbless robots that integrate mechanical and computational intelligence to achieve adaptive and robust locomotion across complex environments. The central contribution of this work is the development of a novel actuation method for limbless robots that embeds the principles of mechanical intelligence (MI) directly into their physical structure. By leveraging bilateral cable-driven actuation and programmable body compliance, the proposed mechanism allows the robot body to spontaneously manage local perturbations through emergent, reflex-like mechanical responses, without the need for high-level sensing or computation. This ability to offload control to the body itself represents a fundamental shift in how locomotor robustness can be achieved.

Through systematic robophysical experiments on MILR, we identified key principles of MI: (1) morphological and material properties can offload control by shaping how robots interact with their environment; (2) programmable compliance provides a quantitative knob for tuning body property; and (3) locomotor robustness can emerge naturally from the interplay between internal actuation dynamics and external resistance. These principles together form the physical basis of embodied adaptability.

Building upon these foundations, the thesis expanded from planar motion to multi-dimensional and multi-modal locomotion. Sidewinding MILR introduced directional modulation through coordinated shape waves in orthogonal planes, revealing how distributed compliance enables smooth turning and stability over uneven terrains. Morphing MILR further extended these capabilities by introducing rolling joints that allow real-time body re-

configuration, enabling continuous transitions between planar and three-dimensional gaits. Together, these platforms demonstrated that the MI principle brought by bilateral actuation can support diverse locomotor modes.

Extending these principles to aquatic environments led to the development of AquaMILR, a waterproof, bilaterally actuated system capable of swimming through complex aquatic terrains. Experiments revealed that MI principles persist underwater but interact with inertia and buoyancy in new ways, giving rise to phenomena such as inertia-induced self-righting and three-dimensional obstacle negotiation through depth modulation. These studies demonstrated that the same principles enabling robustness on land can be reinterpreted to achieve stability and adaptability in fluidic environments.

Finally, by incorporating computational intelligence (CI), the thesis advanced toward amphibious autonomy. Two representative studies illustrated how sensing and decentralized control can augment MI: (1) a head-contact-triggered reversal reflex in MILR that mimics biological escape responses, and (2) a decentralized, real-time compliance controller in AquaMILR that enables local torque-based adaptation. Together, these works showed that even minimal feedback architectures can bridge physical embodiment and decision-making, producing systems capable of self-organized and environmentally responsive behaviors across land–water interfaces.

Collectively, the studies presented in this dissertation contribute to a hierarchical understanding of locomotor intelligence: from MI at the lowest layer, through environment-specific gait optimization at the intermediate layer, to high-level feedback autonomy at the top. This hierarchical framework not only advances the design of limbless robots but also provides physical models for studying how animals exploit mechanical intelligence to simplify neural control. The integration of MI and CI demonstrated here outlines a pathway toward future robotic systems that extend beyond limbless locomotion, offering a general strategy for achieving adaptive, efficient, and resilient movement across complex and dynamic environments.

13.2 Future work

Extend Morphing MILR to richer terresrial applications

Morphing MILR has demonstrated that distributed actuation and body compliance enable smooth transitions between planar and three-dimensional gaits in controlled settings. A next step is to deploy Morphing MILR in real environments, where surface irregularities, frictional variation, and unpredictable perturbations demand robust body-environment interaction.

Future development will further explore rolling-joint motion as an effective means for locomotion on complex terrains. Recent examples such as NASA JPL's EELS robot [214], which employs screw-like body rotation for traversing icy slopes, and Northeastern University's COBRA platform [215], which transitions between sidewinding and tumbling through head-tail reconfiguration, demonstrate the versatility of articulated systems in challenging environments. Building on these concepts, Morphing MILR's cable-driven joints can be coordinated to realize hybrid gaits that merge undulation, twisting, and screw-like body rotation for climbing, rolling, or traversing soft and granular media.

Beyond existing gait templates, Morphing MILR can physically implement arbitrary three-dimensional body curves, removing the constraints of predefined gait patterns. This capability opens the door to embody locomotion strategies developed through reinforcement learning frameworks [216], which generate complex, high-dimensional movement patterns that conventional snake robots cannot achieve due to kinematic and actuation limitations.

For practical applications, Morphing MILR will be equipped with onboard power, sensing, and computation modules for untethered operation, targeting confined-space inspection, subsurface exploration, and cluttered-field search and rescue. These efforts will validate Morphing MILR as a robust and reconfigurable platform capable of extending mechanical intelligence from laboratory demonstrations to real-world tasks.

Advance AquaMILR toward practical underwater applications

AquaMILR has demonstrated that mechanical intelligence can enable quiet, propulsion-free swimming through body undulation alone. Future efforts will advance this platform toward practical underwater applications such as environmental monitoring in fish farms, flooded agricultural fields, and natural water-land interfaces. Compared with conventional underwater vehicles, AquaMILR's body-driven locomotion produces minimal hydrodynamic disturbance and acoustic noise, offering advantages for observing aquatic organisms and sampling fragile ecosystems.

To enhance underwater and amphibious locomotion, we will develop CI-driven approaches for buoyancy control, posture adjustment, and multimodal navigation. A hierarchical control architecture will integrate feedforward shape-based gait generation with feedback-driven adjustments of buoyancy and compliance. Variable buoyancy control, implemented through multi-module depth-adjusting mechanisms, will enable precise positioning and stable transitions between surface swimming, mid-water movement, near-bottom locomotion, and terrestrial crawling. PID-regulated depth control will maintain vertical stability, while force-based compliance control, driven by torque and strain feedback, will adapt body flexibility to changing hydrodynamic forces or contact with submerged structures.

An onboard vision system will provide perception for path finding and environmental observation [78, 71]. It will detect terrain transitions and visual cues such as water edges, submerged obstacles, and land exits, enabling the robot to autonomously plan and execute mode transitions. Depth sensors will be incorporated to achieve closed-loop depth regulation and fine-grained control of three-dimensional trajectories. The resulting system will allow AquaMILR to perform fully autonomous navigation in unstructured aquatic terrains, maintaining stability, efficiency, and environmental safety across both water and land domains.

Toward viscoelastic and muscle-inspired cable-driven actuation

The cable-driven model developed in this thesis captures the fundamental properties of bilateral actuation and tunable compliance, providing a minimal framework for mechanical intelligence. However, real biological systems exhibit far richer mechanical behaviors arising from the viscoelastic nature of muscles and tendons, as well as their tight coupling with neural feedback. Future work will seek to incorporate these biophysical principles into cable-driven actuation, exploiting its mechanisms to improve robot locomotor performance.

We aim to develop robots (robophysical models) that capture the dynamic interplay between elastic storage, viscous damping, and active control. By introducing materials and mechanisms with controllable viscoelastic properties, cable-driven robots could achieve smoother energy transfer, faster recovery from perturbations, and enhanced stability. Incorporating neuromuscular analogs such as variable-stiffness actuation, proprioceptive sensing, and central pattern generator (CPG)-based coordination [183, 20] could allow real-time adaptation of stiffness and damping, mirroring how animals coordinate muscle tone to balance speed, precision, and energy efficiency.

This line of research will bridge the gap between purely mechanical compliance and biologically inspired adaptability. Through such models, mechanical intelligence can evolve from static structural properties into a dynamic, feedback-driven embodiment of control, enabling future robots to achieve levels of resilience and versatility approaching those of living organisms.

Develop intelligent appendages for improved mobility and task capability

While undulatory locomotion provides a foundation for effective mobility, its performance depends strongly on how the body interacts with the surrounding medium. Generating and tuning drag anisotropy on land remains a major challenge, and similar limitations exist in aquatic environments where body-only propulsion constrains thrust and maneuverability.

Future work will therefore focus on developing intelligent appendages: modular, passively or actively controlled structures that dynamically regulate contact, drag, and interaction forces across diverse environments.

On land, adaptive appendages such as foldable legs [217] and frictional skins [218] could provide tunable anisotropy for improved traction, stability, and terrain adaptability. In aquatic environments, fin-like appendages [219] could complement body undulation to enhance propulsion efficiency, maneuverability, and control, functioning analogously to pectoral or dorsal fins in fish. Each appendage can be actuated and modulated individually in response to local flow, pressure, or contact feedback, enabling distributed interaction control that can operate either independently or in coordination with higher-level commands.

Beyond locomotion, intelligent appendages can serve broader functional roles. Gripper-like or anchoring modules could be integrated for object manipulation, sampling, or temporary attachment during environmental monitoring. By embedding sensing and control within each module, these appendages can act as distributed end effectors that extend the robot's task capability. This direction ultimately expands the scope of mechanical intelligence from improving mobility to enabling task execution, paving the way for a new generation of undulatory robots that integrate mobility, perception, and manipulation to realize their potential in diverse real-world applications.

REFERENCES

[1] R. M. Alexander, *Principles of animal locomotion*. Princeton University Press, 2003.

[2] J. Gau, R. Gemilere, L.-V. (subteam), J. Lynch, N. Gravish, and S. Sponberg, "Rapid frequency modulation in a resonant system: Aerial perturbation recovery in hawkmoths," *Proceedings of the Royal Society B*, vol. 288, no. 1951, p. 20 210 352, 2021.

[3] R. D. Estes, "The comparative behavior of grant's and thomson's gazelles," *Journal of Mammalogy*, pp. 189–209, 1967.

[4] P. E. Schiebel, J. M. Rieser, A. M. Hubbard, L. Chen, D. Z. Rocklin, and D. I. Goldman, "Mechanical diffraction reveals the role of passive dynamics in a slithering snake," *Proceedings of the National Academy of Sciences*, vol. 116, no. 11, pp. 4798–4803, 2019.

[5] C. Fang-Yen *et al.*, "Biomechanical analysis of gait adaptation in the nematode caenorhabditis elegans," *Proceedings of the National Academy of Sciences*, vol. 107, no. 47, pp. 20 323–20 328, 2010.

[6] J. G. White, E. Southgate, J. N. Thomson, S. Brenner, *et al.*, "The structure of the nervous system of the nematode caenorhabditis elegans," *Philos Trans R Soc Lond B Biol Sci*, vol. 314, no. 1165, pp. 1–340, 1986.

[7] A.-S. Chiang *et al.*, "Three-dimensional reconstruction of brain-wide wiring networks in drosophila at single-cell resolution," *Current biology*, vol. 21, no. 1, pp. 1–11, 2011.

[8] S. W. Oh *et al.*, "A mesoscale connectome of the mouse brain," *Nature*, vol. 508, no. 7495, pp. 207–214, 2014.

[9] S. Sponberg and R. Full, "Neuromechanical response of musculo-skeletal structures in cockroaches during rapid running on rough terrain," *Journal of Experimental Biology*, vol. 211, no. 3, pp. 433–446, 2008.

[10] D. A. Winter, *Biomechanics and motor control of human movement*. John Wiley & Sons, 2009.

[11] S. Hirose, "Biologically inspired robots," *Snake-Like Locomotors and Manipulators*, 1993.

[12] S. Hirose and M. Mori, "Biologically inspired snake-like robots," in *2004 IEEE International Conference on Robotics and Biomimetics*, IEEE, 2004, pp. 1–7.

[13] A. A. Transeth, R. I. Leine, C. Glocker, K. Y. Pettersen, and P. Liljebäck, "Snake robot obstacle-aided locomotion: Modeling, simulations, and experiments," *IEEE Transactions on Robotics*, vol. 24, no. 1, pp. 88–104, 2008.

[14] C. Wright *et al.*, "Design and architecture of the unified modular snake robot," in *2012 IEEE international conference on robotics and automation*, Ieee, 2012, pp. 4347–4354.

[15] P. E. Schiebel, J. M. Rieser, A. M. Hubbard, L. Chen, and D. I. Goldman, "Collisional diffraction emerges from simple control of limbless locomotion," in *Conference on Biomimetic and Biohybrid Systems*, Springer, 2017, pp. 611–618.

[16] T. Takemori, M. Tanaka, and F. Matsuno, "Ladder climbing with a snake robot," in *2018 IEEE/RSJ International Conference on Intelligent Robots and Systems (IROS)*, IEEE, 2018, pp. 1–9.

[17] Q. Fu and C. Li, "Robotic modelling of snake traversing large, smooth obstacles reveals stability benefits of body compliance," *Royal Society open science*, vol. 7, no. 2, p. 191 192, 2020.

[18] H. Yamada and S. Hirose, "Study of a 2-dof joint for the small active cord mechanism," in *2009 IEEE international conference on robotics and automation*, IEEE, 2009, pp. 3827–3832.

[19] R. Thandiackal *et al.*, "Emergence of robust self-organized undulatory swimming based on local hydrodynamic force sensing," *Science Robotics*, vol. 6, no. 57, eabf6354, 2021.

[20] X. Liu *et al.*, "Artificial embodied circuits uncover neural architectures of vertebrate visuomotor behaviors," *Science Robotics*, vol. 10, no. 107, eadv4408, 2025.

[21] B. C. Jayne, "Kinematics of terrestrial snake locomotion," *Copeia*, pp. 915–927, 1986.

[22] B. C. Jayne, "Muscular mechanisms of snake locomotion: An electromyographic study of lateral undulation of the florida banded water snake (nerodia fasciata) and the yellow rat snake (elaphe obsoleta)," *Journal of Morphology*, vol. 197, no. 2, pp. 159–181, 1988.

[23] A. T. Jones, "The Gliding of a Snake," *Physics*, vol. 4, no. 4, pp. 164–165, Apr. 1933, Number: 4.

[24] G. J. Stephens, B. Johnson-Kerner, W. Bialek, and W. S. Ryu, "Dimensionality and dynamics in the behavior of c. elegans," *PLoS computational biology*, vol. 4, no. 4, e1000028, 2008.

[25] C. L. Johnson, T. J. Lewis, and R. Guy, "Neuromechanical mechanisms of gait adaptation in c. elegans: Relative roles of neural and mechanical coupling," *SIAM Journal on Applied Dynamical Systems*, vol. 20, no. 2, pp. 1022–1052, 2021.

[26] M.-A. Félix and C. Braendle, "The natural history of caenorhabditis elegans," *Current biology*, vol. 20, no. 22, R965–R969, 2010.

[27] A. Crespi and A. J. Ijspeert, "Online optimization of swimming and crawling in an amphibious snake robot," *IEEE Transactions on robotics*, vol. 24, no. 1, pp. 75–87, 2008.

[28] C. Wright *et al.*, "Design of a modular snake robot," in *2007 IEEE/RSJ International Conference on Intelligent Robots and Systems*, IEEE, 2007, pp. 2609–2614.

[29] M. Luo, M. Agheli, and C. D. Onal, "Theoretical modeling and experimental analysis of a pressure-operated soft robotic snake," *Soft Robotics*, vol. 1, no. 2, pp. 136–146, 2014.

[30] C. Branyan *et al.*, "Soft snake robots: Mechanical design and geometric gait implementation," in *2017 IEEE International Conference on Robotics and Biomimetics (ROBIO)*, IEEE, 2017, pp. 282–289.

[31] X. Qi, T. Gao, and X. Tan, "Bioinspired 3d-printed snakeskins enable effective serpentine locomotion of a soft robotic snake," *Soft Robotics*, 2022.

[32] G. Endo, K. Togawa, and S. Hirose, "Study on self-contained and terrain adaptive active cord mechanism," *Journal of the Robotics Society of Japan*, vol. 18, no. 3, pp. 419–425, 2000.

[33] S. Ma, H. Araya, and L. Li, "Development of a creeping snake-robot," in *Proceedings 2001 IEEE International Symposium on Computational Intelligence in Robotics and Automation (Cat. No. 01EX515)*, IEEE, 2001, pp. 77–82.

[34] P. Wiriyacharoensunthorn and S. Laowattana, "Analysis and design of a multi-link mobile robot (serpentine)," in *2002 IEEE International Conference on Industrial Technology, 2002. IEEE ICIT'02.*, IEEE, vol. 2, 2002, pp. 694–699.

[35] M. Tanaka and K. Tanaka, "Control of a Snake Robot for Ascending and Descending Steps," *IEEE Transactions on Robotics*, vol. 31, no. 2, pp. 511–520, Apr. 2015, Number: 2 Conference Name: IEEE Transactions on Robotics.

[36] S. Yu, S. Ma, B. Li, and Y. Wang, "An amphibious snake-like robot with terrestrial and aquatic gaits," in *2011 IEEE International Conference on Robotics and Automation*, IEEE, 2011, pp. 2960–2961.

[37] M. J. Travers, J. Whitman, P. E. Schiebel, D. I. Goldman, and H. Choset, "Shape-based compliance in locomotion.," in *Robotics: Science and Systems*, vol. 12, 2016.

[38] H. Marvi *et al.*, "Sidewinding with minimal slip: Snake and robot ascent of sandy slopes," *Science*, vol. 346, no. 6206, pp. 224–229, Oct. 2014, Number: 6206.

[39] J. Burdick, J. Radford, and G. Chirikjian, "A 'sidewinding' locomotion gait for hyper-redundant robots," in *[1993] Proceedings IEEE International Conference on Robotics and Automation*, May 1993, 101–106 vol.3.

[40] H. C. Astley *et al.*, "Modulation of orthogonal body waves enables high maneuverability in sidewinding locomotion," *Proceedings of the National Academy of Sciences*, vol. 112, no. 19, pp. 6200–6205, May 2015, Number: 19.

[41] B. Zhong, T. Wang, J. Rieser, A. Kaba, H. Choset, and D. Goldman, "Frequency Modulation of Body Waves to Improve Performance of Limbless Robots," Jul. 2020.

[42] T. Takemori, M. Tanaka, and F. Matsuno, "Gait design for a snake robot by connecting curve segments and experimental demonstration," *IEEE Transactions on Robotics*, vol. 34, no. 5, pp. 1384–1391, 2018.

[43] T. Takemori, M. Tanaka, and F. Matsuno, "Gait design of a snake robot by connecting simple shapes," in *2016 IEEE International Symposium on Safety, Security, and Rescue Robotics (SSRR)*, IEEE, 2016, pp. 189–194.

[44] C. D. Onal and D. Rus, "Autonomous undulatory serpentine locomotion utilizing body dynamics of a fluidic soft robot," *Bioinspiration & Biomimetics*, vol. 8, no. 2, p. 026 003, Jun. 2013, Number: 2.

[45] X. Qi, H. Shi, T. Pinto, and X. Tan, "A novel pneumatic soft snake robot using traveling-wave locomotion in constrained environments," *IEEE Robotics and Automation Letters*, vol. 5, no. 2, pp. 1610–1617, 2020.

[46] A. Parra Rubio *et al.*, "Modular Morphing Lattices for Large-Scale Underwater Continuum Robotic Structures," *Soft Robotics*, vol. 10, no. 4, pp. 724–736, Aug. 2023, Publisher: Mary Ann Liebert, Inc., publishers.

[47] A. Rafsanjani, Y. Zhang, B. Liu, S. M. Rubinstein, and K. Bertoldi, "Kirigami skins make a simple soft actuator crawl," *Science Robotics*, vol. 3, no. 15, eaar7555, Feb. 2018, Number: 15.

[48] B. Seyidoğlu and A. Rafsanjani, "A textile origami snake robot for rectilinear locomotion," *Device*, vol. 2, no. 2, p. 100 226, Feb. 2024.

[49] B. C. Jayne, "What Defines Different Modes of Snake Locomotion?" *Integrative and Comparative Biology*, vol. 60, no. 1, pp. 156–170, Jul. 2020.

[50] M. Tesch *et al.*, "Parameterized and scripted gaits for modular snake robots," *Advanced Robotics*, vol. 23, no. 9, pp. 1131–1158, 2009.

[51] Y. Ohmameuda and S. Ma, "Control of a 3-dimensional snake-like robot for analysis of sinus-lifting motion," in *Proceedings of the 41st SICE Annual Conference. SICE 2002.*, vol. 3, Aug. 2002, 1487–1491 vol.3.

[52] S. Toyoshima, M. Tanaka, and F. Matsuno, "A Study on Sinus-Lifting Motion of a Snake Robot With Sequential Optimization of a Hybrid System," *IEEE Transactions on Automation Science and Engineering*, vol. 11, no. 1, pp. 139–144, Jan. 2014, Number: 1 Conference Name: IEEE Transactions on Automation Science and Engineering.

[53] K. Dowling, "Limbless locomotion: Learning to crawl," in *Proceedings 1999 IEEE International Conference on Robotics and Automation (Cat. No.99CH36288C)*, ISSN: 1050-4729, vol. 4, May 1999, 3001–3006 vol.4.

[54] H. Ohno and S. Hirose, "Design of slim slime robot and its gait of locomotion," in *Proceedings 2001 IEEE/RSJ International Conference on Intelligent Robots and Systems. Expanding the Societal Role of Robotics in the the Next Millennium (Cat. No.01CH37180)*, vol. 2, Oct. 2001, 707–715 vol.2.

[55] G. Poi, C. Scarabeo, and B. Allotta, "Traveling wave locomotion hyper-redundant mobile robot," in *Proceedings. 1998 IEEE International Conference on Robotics and Automation (Cat. No.98CH36146)*, ISSN: 1050-4729, vol. 1, May 1998, 418–423 vol.1.

[56] S. Chen and A. M. Roth, "Gait Design and Analysis of an Arboreal Concertina Locomotion for a Snake Robot,"

[57] I. Virgala, M. Dovica, M. Kelemen, E. Prada, and Z. Bobovský, "Snake Robot Movement in the Pipe Using Concertina Locomotion," *Applied Mechanics and Materials*, vol. 611, pp. 121–129, Aug. 2014.

[58] Weikun Zhen, C. Gong, and H. Choset, "Modeling rolling gaits of a snake robot," in *2015 IEEE International Conference on Robotics and Automation (ICRA)*, Seattle, WA, USA: IEEE, May 2015, pp. 3741–3746, ISBN: 978-1-4799-6923-4.

[59] T. Takemori, M. Tanaka, and F. Matsuno, "Adaptive helical rolling of a snake robot to a straight pipe with irregular cross-sectional shape," *IEEE Transactions on Robotics*, 2022.

[60] M. Nilsson, "Snake robot-free climbing," *IEEE Control Systems Magazine*, vol. 18, no. 1, pp. 21–26, Feb. 1998, Number: 1 Conference Name: IEEE Control Systems Magazine.

[61] T. Takemori, M. Tanaka, and F. Matsuno, "Hoop-passing motion for a snake robot to realize motion transition across different environments," *IEEE Transactions on Robotics*, vol. 37, no. 5, pp. 1696–1711, 2021.

[62] R. Hatton and H. Choset, "Nonconservativity and noncommutativity in locomotion: Geometric mechanics in minimum-perturbation coordinates," *The European Physical Journal Special Topics*, vol. 224, no. 17-18, pp. 3141–3174, Dec. 2015, Number: 17-18.

[63] R. L. Hatton and H. Choset, "Geometric motion planning: The local connection, Stokes' theorem, and the importance of coordinate choice," *The International Journal of Robotics Research*, vol. 30, no. 8, pp. 988–1014, Jul. 2011, Number: 8.

[64] J. Dai, H. Faraji, C. Gong, R. L. Hatton, D. I. Goldman, and H. Choset, "Geometric Swimming on a Granular Surface," in *Robotics: Science and Systems XII*, Robotics: Science and Systems Foundation, 2016, ISBN: 978-0-9923747-2-3.

[65] B. Chong *et al.*, "A Hierarchical Geometric Framework to Design Locomotive Gaits for Highly Articulated Robots," in *Robotics: Science and Systems*, 2019.

[66] P. Liljebäck, K. Y. Pettersen, Ø. Stavdahl, and J. T. Gravdahl, "A review on modelling, implementation, and control of snake robots," *Robotics and Autonomous systems*, vol. 60, no. 1, pp. 29–40, 2012.

[67] M. Saito, M. Fukaya, T. Iwasaki, *et al.*, "Modeling, analysis, and synthesis of serpentine locomotion with a multilink robotic snake," *IEEE control systems magazine*, vol. 22, no. 1, pp. 64–81, 2002.

[68] R. L. Hatton and H. Choset, "Generating gaits for snake robots: Annealed chain fitting and keyframe wave extraction," *Autonomous Robots*, vol. 28, no. 3, pp. 271–281, Apr. 2010, Number: 3.

[69] C. Tang, L. Sun, G. Zhou, X. Shu, H. Tang, and H. Wu, "Gait generation method of snake robot based on main characteristic curve fitting," *Biomimetics*, vol. 8, no. 1, p. 105, 2023.

[70] T. Wang *et al.*, "Reconstruction of Backbone Curves for Snake Robots," *IEEE Robotics and Automation Letters*, vol. 6, no. 2, pp. 3264–3270, Apr. 2021, Conference Name: IEEE Robotics and Automation Letters.

[71] F. Sanfilippo, J. Azpiazu, G. Marafioti, A. A. Transeth, Ø. Stavdahl, and P. Liljebäck, "Perception-driven obstacle-aided locomotion for snake robots: The state of the art, challenges and possibilities," *Applied Sciences*, vol. 7, no. 4, p. 336, 2017.

[72] P. Liljebäck, I. U. Haugstuen, and K. Y. Pettersen, "Path following control of planar snake robots using a cascaded approach," in *49th IEEE Conference on Decision and Control (CDC)*, ISSN: 0191-2216, Dec. 2010, pp. 1969–1976.

[73] D. Li, Z. Pan, H. Deng, and L. Hu, "Adaptive Path Following Controller of a Multijoint Snake Robot Based on the Improved Serpenoid Curve," *IEEE Transactions on Industrial Electronics*, vol. 69, no. 4, pp. 3831–3842, Apr. 2022, Conference Name: IEEE Transactions on Industrial Electronics.

[74] M. Tanaka, K. Kon, and K. Tanaka, "Range-Sensor-Based Semiautonomous Whole-Body Collision Avoidance of a Snake Robot," *IEEE Transactions on Control Systems Technology*, vol. 23, no. 5, pp. 1927–1934, Sep. 2015, Number: 5 Conference Name: IEEE Transactions on Control Systems Technology.

[75] C. Ye, D. Hu, S. Ma, and H. Li, "Motion planning of a snake-like robot based on artificial potential method," in *2010 IEEE International Conference on Robotics and Biomimetics*, Dec. 2010, pp. 1496–1501.

[76] T. Wang, J. Whitman, M. Travers, and H. Choset, "Directional compliance in obstacle-aided navigation for snake robots," in *2020 American Control Conference (ACC)*, IEEE, 2020, pp. 2458–2463.

[77] F. Ruscelli, G. Sartoretti, J. Nan, Z. Feng, M. Travers, and H. Choset, "Proprioceptive-Inertial Autonomous Locomotion for Articulated Robots," in *2018 IEEE International Conference on Robotics and Automation (ICRA)*, Brisbane, QLD: IEEE, May 2018, pp. 3436–3441, ISBN: 978-1-5386-3081-5.

[78] G. Sartoretti, T. Wang, G. Chuang, Q. Li, and H. Choset, "Autonomous decentralized shape-based navigation for snake robots in dense environments," in *2021 IEEE International Conference on Robotics and Automation (ICRA)*, IEEE, 2021, pp. 9276–9282.

[79] T. Baba, Y. Kameyama, T. Kamegawa, and A. Gofuku, "A snake robot propelling inside of a pipe with helical rolling motion," in *Proceedings of SICE Annual Conference 2010*, Aug. 2010, pp. 2319–2325.

[80] R. J. Webster III and B. A. Jones, "Design and kinematic modeling of constant curvature continuum robots: A review," *The International Journal of Robotics Research*, vol. 29, no. 13, pp. 1661–1683, 2010.

[81] B. A. Jones and I. D. Walker, "Kinematics for multisection continuum robots," *IEEE Transactions on Robotics*, vol. 22, no. 1, pp. 43–55, 2006.

[82] J. Burgner-Kahrs, D. C. Rucker, and H. Choset, "Continuum robots for medical applications: A survey," *IEEE transactions on robotics*, vol. 31, no. 6, pp. 1261–1280, 2015.

[83] P. E. Dupont, J. Lock, B. Itkowitz, and E. Butler, "Design and control of concentric-tube robots," *IEEE Transactions on Robotics*, vol. 26, no. 2, pp. 209–225, 2009.

[84] M. W. Hannan and I. D. Walker, "Kinematics and the implementation of an elephant's trunk manipulator and other continuum style robots," *Journal of robotic systems*, vol. 20, no. 2, pp. 45–63, 2003.

[85] D. C. Rucker and R. J. Webster III, "Mechanics of continuum robots with external loading and general tendon routing," in *Experimental Robotics: The 12th International Symposium on Experimental Robotics*, Springer, 2014, pp. 645–654.

[86] S. Qian, B. Zi, W.-W. Shang, and Q.-S. Xu, "A review on cable-driven parallel robots," *Chinese Journal of Mechanical Engineering*, vol. 31, no. 1, pp. 1–11, 2018.

[87] A. Pott and T. Bruckmann, *Cable-driven parallel robots*. Springer, 2013.

[88] H. B. Lillywhite, *How snakes work: structure, function and behavior of the world's snakes*. Oxford ; New York: Oxford University Press, 2014, ISBN: 978-0-19-538037-8.

[89] T. Wang *et al.*, "Mechanical intelligence simplifies control in terrestrial limbless locomotion," *Science Robotics*, vol. 8, no. 85, eadi2243, 2023.

[90] Z. Altun, L. Herndon, C. Wolkow, C. Crocker, R. Lints, and D. Hall, *Wormatlas*.

[91] D. H. Hall and E. M. Hedgecock, "Kinesin-related gene unc-104 is required for axonal transport of synaptic vesicles in c. elegans," *Cell*, vol. 65, no. 5, pp. 837–847, 1991.

[92] M. Sitti, "Physical intelligence as a new paradigm," *Extreme Mechanics Letters*, vol. 46, p. 101 340, 2021.

[93] S. Freyberg and H. Hauser, "The morphological paradigm in robotics," *Studies in History and Philosophy of Science*, vol. 100, pp. 1–11, 2023.

[94] Z. Zhao, Q. Wu, J. Wang, B. Zhang, C. Zhong, and A. A. Zhilenkov, "Exploring embodied intelligence in soft robotics: A review," *Biomimetics*, vol. 9, no. 4, p. 248, 2024.

[95] C. Chen *et al.*, "Advancing physical intelligence for autonomous soft robots," *Science Robotics*, vol. 10, no. 102, eads1292, 2025.

[96] H. Chen and M. Sitti, "Physical intelligence in small-scale robots and machines," *Advanced Materials*, e10332, 2025.

[97] R. Pfeifer, M. Lungarella, and F. Iida, "Self-organization, embodiment, and biologically inspired robotics," *science*, vol. 318, no. 5853, pp. 1088–1093, 2007.

[98] C. Laschi, *The multifaceted approach to embodied intelligence in robotics*, 2025.

[99] F. Iida and F. Giardina, "On the timescales of embodied intelligence for autonomous adaptive systems," *Annual Review of Control, Robotics, and Autonomous Systems*, vol. 6, no. 1, pp. 95–122, 2023.

[100] V. Kojouharov, T. Wang, M. Fernandez, J. Maeng, and D. I. Goldman, "Anisotropic body compliance facilitates robotic sidewinding in complex environments," in *2024 IEEE International Conference on Robotics and Automation (ICRA)*, IEEE, 2024, pp. 11 691–11 697.

[101] J. Lin, T. Wang, B. Chong, M. Fernandez, Z. Xu, and D. I. Goldman, "Optimal swimming with body compliance in an overdamped medium," *arXiv preprint arXiv:2510.03457*, 2025.

[102] T. Wang *et al.*, "The omega turn: A biologically-inspired turning strategy for elongated limbless robots," in *2020 IEEE/RSJ International Conference on Intelligent Robots and Systems (IROS)*, IEEE, 2020, pp. 7766–7771.

[103] T. Wang, B. Chong, Y. Deng, R. Fu, H. Choset, and D. I. Goldman, "Generalized omega turn gait enables agile limbless robot turning in complex environments," in *2022 International Conference on Robotics and Automation (ICRA)*, IEEE, 2022, pp. 01–07.

[104] B. Chong *et al.*, "Gait design for limbless obstacle aided locomotion using geometric mechanics," in *Robotics: Science and Systems*, 2023.

[105] B. Zhong, T. Wang, J. Rieser, A. Kaba, H. Choset, and D. Goldman, "Frequency modulation of body waves to improve performance of limbless robots," *Robotics: Science and Systems 2020*, 2020.

[106] B. Chong *et al.*, "Frequency modulation of body waves to improve performance of sidewinding robots," *The International Journal of Robotics Research*, vol. 40, no. 12-14, pp. 1547–1562, 2021.

[107] M. Fernandez *et al.*, "Aquamilr+: Design of an untethered limbless robot for complex aquatic terrain navigation," in *2025 IEEE International Conference on Robotics and Automation (ICRA)*, IEEE, 2025, pp. 12 316–12 322.

[108] T. Wang, N. Mankame, M. Fernandez, V. Kojouharov, and D. I. Goldman, "Aquamilr: Mechanical intelligence simplifies control of undulatory robots in cluttered fluid environments," in *2025 IEEE International Conference on Robotics and Automation (ICRA)*, IEEE, 2025, pp. 14 671–14 677.

[109] D. M. Eisenmann, *Wormbook*.

[110] J. M. Rieser *et al.*, "Geometric phase predicts locomotion performance in undulating living systems across scales," *Proceedings of the National Academy of Sciences*, vol. 121, no. 24, e2320517121, 2024.

[111] B. Chong, T. Wang, E. Erickson, P. J. Bergmann, and D. I. Goldman, "Coordinating tiny limbs and long bodies: Geometric mechanics of lizard terrestrial swimming," *Proceedings of the National Academy of Sciences*, vol. 119, no. 27, e2118456119, 2022.

[112] J. M. Rieser *et al.*, "Geometric phase predicts locomotion performance in undulating living systems across scales," *Proceedings of the National Academy of Sciences*, vol. 121, no. 24, e2320517121, Jun. 2024, Publisher: Proceedings of the National Academy of Sciences.

[113] J. Aguilar *et al.*, "A review on locomotion robophysics: The study of movement at the intersection of robotics, soft matter and dynamical systems," *Reports on Progress in Physics*, vol. 79, no. 11, p. 110 001, 2016.

[114] T. Kano and A. Ishiguro, "Obstacles are beneficial to me! scaffold-based locomotion of a snake-like robot using decentralized control," in *2013 IEEE/RSJ International Conference on Intelligent Robots and Systems*, IEEE, 2013, pp. 3273–3278.

[115] Z. Bing *et al.*, "Perception-action coupling target tracking control for a snake robot via reinforcement learning," *Frontiers in Neurorobotics*, vol. 14, p. 591 128, 2020.

[116] K. G. Hanssen, A. A. Transeth, F. Sanfilippo, P. Liljebäck, and Ø. Stavdahl, "Path planning for perception-driven obstacle-aided snake robot locomotion," in *2020 IEEE 16th International Workshop on Advanced Motion Control (AMC)*, IEEE, 2020, pp. 98–104.

[117] G. Gabrielli, "What price speed?" *Mech. Eng.(ASME)*, vol. 72, no. 10, pp. 775–781, 1950.

[118] S. Collins, A. Ruina, R. Tedrake, and M. Wisse, "Efficient bipedal robots based on passive-dynamic walkers," *Science*, vol. 307, no. 5712, pp. 1082–1085, 2005.

[119] S. Seok, A. Wang, M. Y. Chuah, D. Otten, J. Lang, and S. Kim, "Design principles for highly efficient quadrupeds and implementation on the mit cheetah robot," in *2013 IEEE International Conference on Robotics and Automation*, IEEE, 2013, pp. 3307–3312.

[120] U. Saranli, M. Buehler, and D. E. Koditschek, "Rhex: A simple and highly mobile hexapod robot," *The International Journal of Robotics Research*, vol. 20, no. 7, pp. 616–631, 2001.

[121] R. D. Maladen, Y. Ding, P. B. Umbanhowar, and D. I. Goldman, "Undulatory swimming in sand: Experimental and simulation studies of a robotic sandfish," *The International Journal of Robotics Research*, vol. 30, no. 7, pp. 793–805, 2011.

[122] R. L. Hatton, Y. Ding, H. Choset, and D. I. Goldman, "Geometric visualization of self-propulsion in a complex medium," *Physical review letters*, vol. 110, no. 7, p. 078 101, 2013.

[123] A. Parashar, R. Lycke, J. A. Carr, and S. Pandey, "Amplitude-modulated sinusoidal microchannels for observing adaptability in c. elegans locomotion," *Biomicrofluidics*, vol. 5, no. 2, p. 024 112, 2011.

[124] J. Yuan, D. M. Raizen, and H. H. Bau, "Gait synchronization in caenorhabditis elegans," *Proceedings of the National Academy of Sciences*, vol. 111, no. 19, pp. 6865–6870, 2014.

[125] J. H. Long Jr, "Muscles, elastic energy, and the dynamics of body stiffness in swimming eels," *American zoologist*, vol. 38, no. 4, pp. 771–792, 1998.

[126] M. Backholm, W. S. Ryu, and K. Dalnoki-Veress, "Viscoelastic properties of the nematode caenorhabditis elegans, a self-similar, shear-thinning worm," *Proceedings of the National Academy of Sciences*, vol. 110, no. 12, pp. 4528–4533, 2013.

[127] M. Gazzola, M. Argentina, and L. Mahadevan, "Gait and speed selection in slender inertial swimmers," *Proceedings of the National Academy of Sciences*, vol. 112, no. 13, pp. 3874–3879, 2015.

[128] J. H. Boyle, S. Berri, and N. Cohen, "Gait modulation in c. elegans: An integrated neuromechanical model," *Frontiers in computational neuroscience*, vol. 6, p. 10, 2012.

[129] J. E. Denham, T. Ranner, and N. Cohen, "Signatures of proprioceptive control in caenorhabditis elegans locomotion," *Philosophical Transactions of the Royal Society B: Biological Sciences*, vol. 373, no. 1758, p. 20 180 208, 2018.

[130] G. Haspel, K. E. Severi, L. J. Fauci, N. Cohen, E. D. Tytell, and J. R. Morgan, "Resilience of neural networks for locomotion," *The Journal of Physiology*, vol. 599, no. 16, pp. 3825–3840, 2021.

[131] T. Majmudar, E. E. Keaveny, J. Zhang, and M. J. Shelley, "Experiments and theory of undulatory locomotion in a simple structured medium," *Journal of the Royal Society Interface*, vol. 9, no. 73, pp. 1809–1823, 2012.

[132] A. J. Ijspeert, "Central pattern generators for locomotion control in animals and robots: A review," *Neural networks*, vol. 21, no. 4, pp. 642–653, 2008.

[133] G. Bellegarda and A. Ijspeert, "Cpg-rl: Learning central pattern generators for quadruped locomotion," *IEEE Robotics and Automation Letters*, vol. 7, no. 4, pp. 12 547–12 554, 2022.

[134] T. Haarnoja, H. Tang, P. Abbeel, and S. Levine, "Reinforcement learning with deep energy-based policies," in *International conference on machine learning*, PMLR, 2017, pp. 1352–1361.

[135] S. Ramasamy and R. L. Hatton, "Optimal gaits for drag-dominated swimmers with passive elastic joints," *Physical Review E*, vol. 103, no. 3, p. 032 605, 2021.

[136] W. Mosauer, "Adaptive convergence in the sand reptiles of the sahara and of california: A study in structure and behavior," *Copeia*, vol. 1932, no. 2, pp. 72–78, 1932.

[137] C. Brain, "Observations on the locomotion of the south west african adder, bitis perinqueyi (boulenger), with speculations on the origin of sidewinding," *Annals of the Transvaal Museum*, vol. 24, no. 1, pp. 19–24, 1960.

[138] C. Gans and H. Mendelssohn, "Sidewinding and jumping progression of vipers," *Toxins of animal and plant origin*, pp. 17–38, 1972.

[139] J. L. Tingle, "Facultatively sidewinding snakes and the origins of locomotor specialization," *Integrative and Comparative Biology*, vol. 60, no. 1, pp. 202–214, 2020.

[140] J. W. Burdick, J. Radford, and G. S. Chirikjian, "A'sidewinding'locomotion gait for hyper-redundant robots," *Advanced Robotics*, vol. 9, no. 3, pp. 195–216, 1994.

[141] K. Lipkin *et al.*, "Differentiable and piecewise differentiable gaits for snake robots," in *2007 IEEE/RSJ international conference on intelligent robots and systems*, IEEE, 2007, pp. 1864–1869.

[142] R. Ariizumi and F. Matsuno, "Dynamic analysis of three snake robot gaits," *IEEE Transactions on Robotics*, vol. 33, no. 5, pp. 1075–1087, 2017.

[143] F. Rozaidi, E. Waters, O. Dawes, J. Yang, J. R. Davidson, and R. L. Hatton, "Hissbot: Sidewinding with a soft snake robot," in *2023 IEEE International Conference on Soft Robotics (RoboSoft)*, IEEE, 2023, pp. 1–7.

[144] H. C. Astley *et al.*, "Side-impact collision: Mechanics of obstacle negotiation in sidewinding snakes," *Bioinspiration & Biomimetics*, vol. 15, no. 6, p. 065 005, 2020.

[145] H. C. Astley *et al.*, "Modulation of orthogonal body waves enables high maneuverability in sidewinding locomotion," *Proceedings of the National Academy of Sciences*, vol. 112, no. 19, pp. 6200–6205, 2015.

[146] H. Marvi *et al.*, "Sidewinding with minimal slip: Snake and robot ascent of sandy slopes," *Science*, vol. 346, no. 6206, pp. 224–229, 2014.

[147] E. M. Purcell, "Life at low reynolds number," *American Journal of Physics*, vol. 45, no. 1, pp. 3–11, Jan. 1977.

[148] H. C. Astley *et al.*, "Surprising simplicities and syntheses in limbless self-propulsion in sand," *Journal of Experimental Biology*, vol. 223, no. 5, jeb103564, 2020.

[149] D. L. Hu, J. Nirody, T. Scott, and M. J. Shelley, "The mechanics of slithering locomotion," *Proceedings of the National Academy of Sciences*, vol. 106, no. 25, pp. 10 081–10 085, 2009.

[150] M. Travers, J. Whitman, and H. Choset, "Shape-based coordination in locomotion control," *The International Journal of Robotics Research*, vol. 37, no. 10, pp. 1253–1268, 2018.

[151] C. Gong, M. Travers, H. C. Astley, D. I. Goldman, and H. Choset, "Limbless locomotors that turn in place," in *2015 IEEE International Conference on Robotics and Automation (ICRA)*, IEEE, 2015, pp. 3747–3754.

[152] C. Ye, S. Ma, B. Li, and Y. Wang, "Turning and side motion of snake-like robot," in *IEEE International Conference on Robotics and Automation, 2004. Proceedings. ICRA'04. 2004*, IEEE, vol. 5, 2004, pp. 5075–5080.

[153] J. Dai, H. Faraji, C. Gong, R. L. Hatton, D. I. Goldman, and H. Choset, "Geometric swimming on a granular surface.," in *Robotics: Science and Systems*, 2016.

[154] N. A. Croll, "Components and patterns in the behaviour of the nematode *Caenorhabditis elegans*," *Journal of zoology*, vol. 176, no. 2, pp. 159–176, 1975.

[155] O. D. Broekmans, J. B. Rodgers, W. S. Ryu, and G. J. Stephens, "Resolving coiled shapes reveals new reorientation behaviors in *C. elegans*," *Elife*, vol. 5, e17227, 2016.

[156] L. C. Salvador, F. Bartumeus, S. A. Levin, and W. S. Ryu, "Mechanistic analysis of the search behaviour of *Caenorhabditis elegans*," *Journal of The Royal Society Interface*, vol. 11, no. 92, p. 20 131 092, 2014.

[157] A. Mohammadi, J. B. Rodgers, I. Kotera, and W. S. Ryu, "Behavioral response of *Caenorhabditis elegans* to localized thermal stimuli," *BMC neuroscience*, vol. 14, no. 1, p. 66, 2013.

[158] B. Chong *et al.*, "A hierarchical geometric framework to design locomotive gaits for highly articulated robots," in *Robotics: science and systems*, 2019.

[159] S. Ramasamy and R. L. Hatton, "Soap-bubble optimization of gaits," in *2016 IEEE 55th Conference on Decision and Control (CDC)*, IEEE, 2016, pp. 1056–1062.

[160] Shugen, "Analysis of creeping locomotion of a snake-like robot," *Advanced Robotics*, vol. 15, no. 2, pp. 205–224, 2001.

[161] R. L. Hatton and H. Choset, "Nonconservativity and noncommutativity in locomotion," *The European Physical Journal Special Topics*, vol. 224, no. 17, pp. 3141–3174, 2015.

[162] B. Chong *et al.*, "Coordination of lateral body bending and leg movements for sprawled posture quadrupedal locomotion," *The International Journal of Robotics Research*, vol. 40, no. 4-5, pp. 747–763, 2021.

[163] J. M. Rieser *et al.*, "Geometric phase and dimensionality reduction in locomoting living systems," *arXiv preprint arXiv:1906.11374*, 2019.

[164] D. Rollinson *et al.*, "Design and architecture of a series elastic snake robot," in *2014 IEEE/RSJ International Conference on Intelligent Robots and Systems*, IEEE, 2014, pp. 4630–4636.

[165] R. M. Murray, Z. Li, and S. S. Sastry, *A mathematical introduction to robotic manipulation*. CRC press, 2017.

[166] O. Rieppel, "A review of the origin of snakes," *Evolutionary biology*, pp. 37–130, 1988.

[167] B. F. Simões *et al.*, "Visual system evolution and the nature of the ancestral snake," *Journal of evolutionary biology*, vol. 28, no. 7, pp. 1309–1320, 2015.

[168] P. Liljeback, K. Y. Pettersen, Ø. Stavdahl, and J. T. Gravdahl, "Experimental investigation of obstacle-aided locomotion with a snake robot," *IEEE Transactions on Robotics*, vol. 27, no. 4, pp. 792–800, 2011.

[169] K. Kelley, S. Arnold, and J. Gladstone, "The effects of substrate and vertebral number on locomotion in the garter snake thamnophis elegans," *Functional Ecology*, vol. 11, no. 2, pp. 189–198, 1997.

[170] C. E. Collins, J. D. Self, R. A. Anderson, and L. D. McBrayer, "Rock-dwelling lizards exhibit less sensitivity of sprint speed to increases in substrate rugosity," *Zoology*, vol. 116, no. 3, pp. 151–158, 2013.

[171] S. E. Parker and L. D. McBrayer, "The effects of multiple obstacles on the locomotor behavior and performance of a terrestrial lizard," *Journal of Experimental Biology*, vol. 219, no. 7, pp. 1004–1013, 2016.

[172] K. Gast, R. Kram, and R. Riemer, "Preferred walking speed on rough terrain: Is it all about energetics?" *Journal of experimental biology*, vol. 222, no. 9, jeb185447, 2019.

[173] F. Wilczek and A. Shapere, *Geometric phases in physics*. World Scientific, 1989, vol. 5.

[174] C. Li, T. Zhang, and D. I. Goldman, "A terradynamics of legged locomotion on granular media," *Science*, vol. 339, no. 6126, pp. 1408–1412, 2013.

[175] S. S. Sharpe *et al.*, "Locomotor benefits of being a slender and slick sand swimmer," *Journal of Experimental Biology*, vol. 218, no. 3, pp. 440–450, 2015.

[176] T. Zhang and D. I. Goldman, "The effectiveness of resistive force theory in granular locomotion," *Physics of Fluids*, vol. 26, no. 10, 2014.

[177] J. E. Marsden and T. S. Ratiu, *Introduction to mechanics and symmetry: a basic exposition of classical mechanical systems*. Springer Science & Business Media, 2013, vol. 17.

[178] C. Gong, D. I. Goldman, and H. Choset, "Simplifying gait design via shape basis optimization.," in *Robotics: Science and Systems*, Michigan, USA, vol. 655, 2016.

[179] B. Lin *et al.*, "Optimizing coordinate choice for locomotion systems with toroidal shape spaces," in *2020 IEEE/RSJ International Conference on Intelligent Robots and Systems (IROS)*, 2020, pp. 7501–7506.

[180] P. Liljebäck, K. Y. Pettersen, Ø. Stavdahl, and J. T. Gravdahl, "Lateral undulation of snake robots: A simplified model and fundamental properties," *Robotica*, vol. 31, no. 7, pp. 1005–1036, 2013.

[181] S. Alben, "Efficient sliding locomotion with isotropic friction," *Physical Review E*, vol. 99, no. 6, p. 062 402, 2019.

[182] R. Sedgewick and K. Wayne, *Algorithms: Algorithms_4*. Pearson Education, 2011, ISBN: 9780132762564.

[183] A. J. Ijspeert, A. Crespi, D. Ryczko, and J.-M. Cabelguen, "From swimming to walking with a salamander robot driven by a spinal cord model," *science*, vol. 315, no. 5817, pp. 1416–1420, 2007.

[184] D. Pongas, M. Mistry, and S. Schaal, "A robust quadruped walking gait for traversing rough terrain," in *Proceedings 2007 IEEE International Conference on Robotics and Automation*, IEEE, 2007, pp. 1474–1479.

[185] C. Li, P. B. Umbanhowar, H. Komsuoglu, D. E. Koditschek, and D. I. Goldman, "Sensitive dependence of the motion of a legged robot on granular media," *Proceedings of the National Academy of Sciences*, vol. 106, no. 9, pp. 3029–3034, 2009.

[186] B. Ponton, M. Khadiv, A. Meduri, and L. Righetti, "Efficient multicontact pattern generation with sequential convex approximations of the centroidal dynamics," *IEEE Transactions on Robotics*, vol. 37, no. 5, pp. 1661–1679, 2021.

[187] T. Wang *et al.*, "Reconstruction of backbone curves for snake robots," *IEEE Robotics and Automation Letters*, vol. 6, no. 2, pp. 3264–3270, 2021.

[188] S. Kobayashi and K. Nomizu, *Foundations of differential geometry*. Interscience publishers New York, 1963, vol. 1.

[189] C. Gong, J. Whitman, J. Grover, B. Chong, R. Ren, and H. Choset, "Geometric motion planning for systems with toroidal and cylindrical shape spaces," in *Dynamic Systems and Control Conference*, 2018.

[190] S. Watson, D. A. Duecker, and K. Groves, "Localisation of unmanned underwater vehicles (uuvs) in complex and confined environments: A review," *Sensors*, vol. 20, no. 21, p. 6203, 2020.

[191] P. Spino and D. Rus, "Towards centimeter-scale underwater mobile robots: An architecture for capable μauvs," in *2024 IEEE International Conference on Robotics and Automation (ICRA)*, IEEE, 2024, pp. 1484–1490.

[192] W.-S. Chu *et al.*, "Review of biomimetic underwater robots using smart actuators," *International journal of precision engineering and manufacturing*, vol. 13, pp. 1281–1292, 2012.

[193] J. Qu *et al.*, "Recent advances on underwater soft robots," *Advanced Intelligent Systems*, vol. 6, no. 2, p. 2 300 299, 2024.

[194] R. Wang, S. Wang, Y. Wang, L. Cheng, and M. Tan, "Development and motion control of biomimetic underwater robots: A survey," *IEEE Transactions on Systems, Man, and Cybernetics: Systems*, vol. 52, no. 2, pp. 833–844, 2020.

[195] A. Raj and A. Thakur, "Fish-inspired robots: Design, sensing, actuation, and autonomy—a review of research," *Bioinspiration & biomimetics*, vol. 11, no. 3, p. 031 001, 2016.

[196] R. Bogue, "Underwater robots: A review of technologies and applications," *Industrial Robot: An International Journal*, vol. 42, no. 3, pp. 186–191, 2015.

[197] T. Wang, H.-J. Joo, S. Song, W. Hu, C. Keplinger, and M. Sitti, "A versatile jellyfish-like robotic platform for effective underwater propulsion and manipulation," *Science Advances*, vol. 9, no. 15, eadg0292, 2023.

[198] K. Ren and J. Yu, "Research status of bionic amphibious robots: A review," *Ocean Engineering*, vol. 227, p. 108 862, 2021.

[199] R. Baines *et al.*, "Multi-environment robotic transitions through adaptive morphogenesis," *Nature*, vol. 610, no. 7931, pp. 283–289, 2022.

[200] R. K. Katzschmann, J. DelPreto, R. MacCurdy, and D. Rus, "Exploration of underwater life with an acoustically controlled soft robotic fish," *Science Robotics*, vol. 3, no. 16, eaar3449, 2018.

[201] J. Zhu, C. White, D. K. Wainwright, V. Di Santo, G. V. Lauder, and H. Bart-Smith, "Tuna robotics: A high-frequency experimental platform exploring the performance space of swimming fishes," *Science Robotics*, vol. 4, no. 34, eaax4615, 2019.

[202] C. Wong, E. Yang, X.-T. Yan, and D. Gu, "Autonomous robots for harsh environments: A holistic overview of current solutions and ongoing challenges," *Systems Science & Control Engineering*, vol. 6, no. 1, pp. 213–219, 2018.

[203] H. Yamada, S. Chigisaki, M. Mori, K. Takita, K. Ogami, and S. Hirose, "Development of amphibious snake-like robot acm-r5, isr2005," *Proceedings of ISR*, p. 133, 2005.

[204] P. Liljebäck, Ø. Stavdahl, K. Y. Pettersen, and J. T. Gravdahl, "Mamba-a waterproof snake robot with tactile sensing," in *2014 IEEE/RSJ International Conference on Intelligent Robots and Systems*, IEEE, 2014, pp. 294–301.

[205] G. Li, G. Liu, D. Leng, X. Fang, G. Li, and W. Wang, "Underwater undulating propulsion biomimetic robots: A review," *Biomimetics*, vol. 8, no. 3, p. 318, 2023.

[206] J. M. Rieser *et al.*, "Dynamics of scattering in undulatory active collisions," *Physical Review E*, vol. 99, no. 2, p. 022 606, 2019.

[207] B. K. Tiwari and R. Sharma, "Design and analysis of a variable buoyancy system for efficient hovering control of underwater vehicles with state feedback controller," *Journal of Marine Science and Engineering*, vol. 8, no. 4, p. 263, 2020.

[208] E. Kelasidi, S. Moe, K. Y. Pettersen, A. M. Kohl, P. Liljebäck, and J. T. Gravdahl, "Path following, obstacle detection and obstacle avoidance for thrusted underwater snake robots," *Frontiers in Robotics and AI*, vol. 6, p. 57, 2019.

[209] J. Carling, T. L. Williams, and G. Bowtell, "Self-propelled anguilliform swimming: Simultaneous solution of the two-dimensional navier–stokes equations and newton's laws of motion," *Journal of experimental biology*, vol. 201, no. 23, pp. 3143–3166, 1998.

[210] N. Justus and R. Hatton, "Optimal gaits for inertia-dominated swimmers with passive elastic joints," *Physical Review E*, vol. 109, no. 3, p. 034 602, 2024.

[211] B. Zhao, P. Khare, L. Feldman, and J. A. Dent, "Reversal frequency in caenorhabditis elegans represents an integrated response to the state of the animal and its environment," *Journal of Neuroscience*, vol. 23, no. 12, pp. 5319–5328, 2003.

[212] D. B. Doroquez, C. Berciu, J. R. Anderson, P. Sengupta, and D. Nicastro, "A high-resolution morphological and ultrastructural map of anterior sensory cilia and glia in caenorhabditis elegans," *Elife*, vol. 3, e01948, 2014.

[213] M. Chatzigeorgiou and W. R. Schafer, "Lateral facilitation between primary mechanosensory neurons controls nose touch perception in c. elegans," *Neuron*, vol. 70, no. 2, pp. 299–309, 2011.

[214] T. S. Vaquero *et al.*, "Eels: Autonomous snake-like robot with task and motion planning capabilities for ice world exploration," *Science robotics*, vol. 9, no. 88, eadh8332, 2024.

[215] A. Salagame, H. Noyes, E. Sihite, A. Kalantari, and A. Ramezani, "Crater observing bioinspired rolling articulator (cobra)," *Advanced Intelligent Systems*, p. 2 500 352, 2025.

[216] Y. Zhang, Y. Niu, X. Liu, and D. Zhao, "Composer: Scalable and robust modular policies for snake robots," in *2024 IEEE International Conference on Robotics and Automation (ICRA)*, IEEE, 2024, pp. 10 800–10 806.

[217] B. Chong *et al.*, "Multilegged matter transport: A framework for locomotion on noisy landscapes," *Science*, vol. 380, no. 6644, pp. 509–515, 2023.

[218] J. M. Rieser, T.-D. Li, J. L. Tingle, D. I. Goldman, and J. R. Mendelson III, "Functional consequences of convergently evolved microscopic skin features on snake locomotion," *Proceedings of the National Academy of Sciences*, vol. 118, no. 6, e2018264118, 2021.

[219] Festo, *Bionicfinwave*.